НАУЧНОМ ВЕЋУ ИНСТИТУТА ЗА ФИЗИКУ

Предмет: Молба за покретање поступка за стицање звања <u>научни сарадник</u>

С обзиром да испуњавам критеријуме потписане од стране Министарства просвете, науке и технолошког развоја за стицање звања научни сарадник, молим Научно веће Института за физику покрене поступак за мој избор у наведено звање.

У прилогу достављам:

1. Мишљење руководиоца пројекта са предлогом комисије за избор у звање
2. Стручну биографију
3. Преглед научне активности
4. Елементе за квалитативну и квантитативну оцену научног доприноса
5. Списак објављених радова и њихове копије
6. Податке о цитираности са Web of Science и Google Scholar
7. Уверење о одбрањеној докторској тези

Београд, 16. јануар 2018.

С поштовањем

др Наташа Томић
истраживач сарадник

НАУЧНОМ ВЕЋУ ИНСТИТУТА ЗА ФИЗИКУ

Београд 29. децембар 2017.

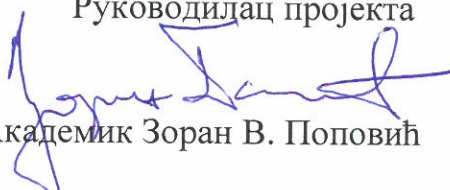Предмет: Мишљење руководиоца пројекта о избору др Наташе Томић у звање <u>научни сарадник</u>

Др Наташа Томић је запослена у Центру за физику чврстог стања и нове материјале, Центру изврсности Института за физку у Београду. Ангажована је на пројекту ИИИ45018 "Наноструктурни мултифункционални материјали и нанокомпозити" Министарства просвете, науке и технолошког развоја Републике Србије. На овом пројекту ангажована је на потпројекту "Нанооксидни материјали за примене у технологијама заштите животне средине" на темама синтезе, карактеризације и испитивања адсорпционих и фотокаталитичких својстава наноматеријала.

С обзиром да испуњава све предвиђене услове у складу са Правилником о поступку, начину вредновања и квантитативном исказивању научно истраживачких резултата истраживача МПНТР, сагласан сам са покретањем избора др Наташе Томић у звање научни сарадник.

За састав Комисије за избор у звање др Наташе Томић предлажем:

1) др Маја Шћепановић, научни саветник, Институт за физику
2) др Мирјана Грујић-Бројчин, научни саветник, Институт за физику
3) др Вера Дондур, редовни професор у пензији, Факултет за физичку хемију, Универзитет у Београду
4) др Мирослав Кузмановић, ванредни професор, Факултет за физичку хемију, Универзитет у Београду

Руководилац пројекта

Академик Зоран В. Поповић

Биографија др Наташе Томић

Наташа Томић је рођена 20.02.1981. године у Београду, општина Савски Венац, Република Србија. Основну школу и гимназију (V београдска гимназија) природно-математичког смера похађала је у Београду.

Основне студије на Факултету за Физичку Хемију, Универзитет у Београду, уписала је 2001. године. У фебруару 2011. године дипломирала је са просечном оценом 9.60 и оценом 10 на дипломском испиту са темом "Примена (0,0) спектралне траке Свановог система за одређивање температуре гаса" код др Мирослава Кузмановића, ванредног професора на Факулету за физичку хемију.

У марту 2011. године уписала је докторске студије на Факултету за Физичку Хемију, Универзитет у Београду. Од 1.09.2011. године запослена је у Центру за физику чврстог стања и нове материјале Института за физику Београд у Београду, као истраживач-приправник на пројекту ON 171032 "Физика наноструктурних оксидних материјала и јако корелисаних система" које финансира Министарство просвете, науке и технолошког развоја Републике Србије, а чији је руководилац др Зорана Дохчевић-Митровић. У марту 2014. године је изабрана у звање истраживач - сарадник.

Члан је Српског керамичког друштва. Од 2013. до 2015. године је учествовала на билатералном пројекту са Италијом - "Нове оксидне наноструктуре за пречишћавање воде", под руководством др Зоране Дохчевић - Митровић.

Од 1.11.2017. године ангажована је на пројекту ИИИ45018 "Наноструктурни мултифункционални материјали и нанокомпозити" Министарства просвете, науке и технолошког развоја Републике Србије, чији је руководилац др Зоран В. Поповић.

Током досадашњег рада Наташа Томић има укупно 9 радова објављених у међународним часописима од којих је осам објављено у врхунским међународним часописима категорије М21 и један рад у међународном часопису категорије М23. Такође има 9 саопштења на међународним научним скуповима.

Докторску дисертацију под насловом **„Адсорпциона и фотокаталитичка својства наноматеријала на бази церијум(IV)-оксида и титан(IV)-оксида"**, одбранила је 28.12.2017. године на Факултету за Физичку хемију, Универзитета у Београду.

Преглед научне активности др Наташе Томић

Током свог досадашњег научно-истраживачког рада, др Наташа Томић се првенствено бавила проблемима везаним за различите методе синтезе (сол-гел и хидротермална синтеза, метода преципитације и самопропагирајућа метода синтезе на собној температури-SPRT) оксидних нанопрахова TiO_2 и CeO_2, како недопираних тако и допираних елементима ретких земаља. Њен рад је такође обухватао испитивање утицаја избора методе и појединих параметара синтезе (време и температура третмана, различити прекурсори) на фазни састав, структурна и морфолошка својства синтетисаних нанопрахова, са крајњим циљем да се испитају адсорпциона и фотокаталитичка својства ових наноматеријала када је реч о уклањању различитих органских загађивача. Најзначајнији део истраживачког рада и научних резултата које је до сада остварила др Наташе Томић може се груписати у две теме:

- синтеза и фотокаталитичка својства TiO_2

- синтеза и адсорпциона својства CeO_2

Синтеза и фотокаталитичка својства TiO_2

Први део научне активности др Наташе Томић односи се на проучавање нанопрахова базираних на TiO_2.

За потребе синтезе TiO_2 нанопрахова у којима је као главна добијена анатас фаза кандидаткиња је користила две методе: сол-гел и хидротермалну методу. Као прекурсор код обе методе синтезе коришћен је $TiCl_4$ и NH_4OH. Допирање ових нанопрахова вршено је помоћу $LaCl_3 \cdot 7H_2O$. Упоређиване су кристалне структуре добијене различитим методама синтезе као и утицај допирања лантаном. Др Наташа Томић је била укључена у синтезу и карактеризацију TiO_2 нанопрахова (чистих и допираних са La^{3+} у различитим концентрацијама) добијених сол-гел и хидротермалном методом, при чему је пратила утицај услова синтезе и/или допирања на њихову фотокаталитичку активност и кинетику процеса разградње алпразолама у UV области. Добијени резултати су објављени у једном раду у међународном часопису изузетних вредности и 1 раду у врхунском међународном часопису, као и представљени на 2 конференције:

- M. Grujić-Brojčin, S. Armaković, **N. Tomić**, B. Abramović, A. Golubović, B. Stojadinović, A. Kremenović, B. Babić, Z. Dohčević-Mitrović, M. Šćepanović, *Surface modification of sol-gel synthesized TiO$_2$ nanoparticles induced by La-doping*, Materials Characterization 88 (2014) 30-41.

- A. Golubović, **N. Tomić**, N. Finčur, B. Abramović, I. Veljković, J. Zdravković, M. Grujić-Brojčin, B. Babić, B. Stojadinović, M.Šćepanović, *Synthesis of pure and La-doped anatase nanopowders by sol-gel and hydrothermal methods and their efficiency in photocatalytic degradation of alprazolam*, Ceramics International 40 (2014) 13409-13418.

- **Nataša Tomić**, Aleksandar Golubović, Marko Radović, Jelena Tanasijević, Ivana Veljković, *Influence of La^{3+}-dopant on anatase nanopowders synthesized by sol-gel and hydrothermal methods*, First International Conference on Processing, characterization and application of nanostructured materials and nanotechnology Nano Belgrade, Belgrade, Serbia, P-15, page 93, September 2012.

- **Nataša Tomić**, Nina Finčur, Ivana Veljković, Maja Šćepanović, Aleksandar Golubović, Biljana Abramović, *The efficiency of pure and La-doped anatase nanopowders synthesized by sol-gel and hydrothermal method in photocatalytic degradation of alprazolam,* 2nd Conference of The Serbian Ceramic Society, Belgrade, Serbia, P-20, page 71, June 2013.

Када је реч о фотокаталитичкој деградацији различитих органских загађивача, фотоактивност и процеси оксидације се најчешће везују за анатас фазу. Како би се пратио утицај услова синтезе на кристална, порозна и фотокаталитичка својства ове фазе, анатас TiO$_2$ нанопрахови у којима није детектовано присуство осталих TiO$_2$ фаза су синтетисани сол-гел методом, при чему је као прекурсор коришћен Ti(OBu)$_4$ (титан бутоксид). Варирањем параметара синтезе (температура и време калцинације) добијени су нанопрахови чија је фотоактивност и кинетика (у присуству UV зрачења) праћена кроз процес деградације азо боје Reactive Orange 16, карбофурана и фенола. Резултати су објављени у раду у међународном часопису:

- Aleksandar Golubović, Ivana Veljković, Maja Šćepanović, Mirjana Grujić-Brojčin, **Nataša Tomić**, Dušan Mijin, Biljana Babić, *Influence of some sol-gel synthesis parameters of mesoporous TiO$_2$ on photocatalytic degradation of pollutants*, Chem. Ind. Chem. Eng. Q. 22(1) (2016) 65-73.

Брукит је најмање испитана (природна) кристална форма TiO$_2$, првенствено због строго дефинисаних услова који су потребни за његову синтезу. Последњих година он привлачи све већу пажњу као потенцијални материјал за фотокаталитичке примене. Др Наташа Томић је у циљу добијања чисте брукитне фазе користила хидротермалну методу. Избором pH вредности (базна средина) и уз присуство Na$^+$ јона у почетној смеши, која се након стајања трансформише у гел, као и температуре и трајања хидротермалног третмана, кандидаткиња је синтетисала серију нанопрахова са различитим уделом TiO$_2$ фаза и успела да пронађе оптималне услове за синтезу чисте

брукитне фазе. Фотокаталитичка активност добијених нанопрахова испитана је кроз процес деградације алпразолама у присуству UV зрачења, при чему је најбоља каталитичка својства од свих испитаних синтетисаних и комерцијалних TiO$_2$ нанопрахова показао управо катализатор са чистом брукитном фазом. Резултати су објављени у једном раду у врхунском међународном часопису и представљени на конференцији:

- **N. Tomić**, M. Grujić-Brojčin, N. Finčur, B. Abramović, B. Simović, J. Krstić, B. Matović, M. Šćepanović, *Photocatalytic degradation of alprazolam in water suspension of brookite type TiO2 nanopowders prepared using hydrothermal route*, Materials Chemistry and Physics 163 (2015) 518-528.

- Nina L. Finčur, **Nataša M. Tomić**, Mirjana U. Grujić-Brojčin, Maja J. Šćepanović, Biljana F. Abramović, *Efikasnost brukitnih TiO$_2$ nanoprahova u fotokatalitičkoj razgradnji alprazolama primenom UVA zračenja*, 52. Savetovanje Srpskog Hemijskog Društva, Novi Sad, HŽS P 11, страна 80, 29. и 30. мај 2015.

Синтеза и адсорпциона својства CeO$_2$

Други део научне активности др Наташе Томић обухвата синтезу наноматеријала церијум-диоксида. За те потребе кандидаткиња је користила (развијала) три различите методе синтезе: хидротермалну методу, методу преципитације и самопропагирајућу методу на собној температури (SPRT). Различите методе дају различите величине нанокристала CeO$_2$ (23, 4 и 6 nm, редом). Такође је радила и на допирању нанопраха добијеног SPRT методом користећи Nd (елемент ретких земаља у различитим процентима), при чему је калцинација овог праха вршена на две температуте (T = 600, 800° C) ради постизања боље кристалиничности. Зависно од методе синтезе, CeO$_2$ може имати различиту примену. Управо, нанопрах синтетисан SPRT методом се показао као потенцијални адсорбент. Сходно томе, кандидаткиња је радила на испитивању адсорпционих капацитета овог CeO$_2$ нанопраха у присуству азо боја (Reactive Orange 16, Methyl Orange и Mordant Blue 9) као органских загађивача и проучавању кинетике и механизама адсорпционих процеса. Резултати описаних истраживања објављени су у 3 рада у врхунским међународним часописима и представљени на конференцији:

- **Nataša M. Tomić**, Zorana D. Dohčević-Mitrović, Novica M. Paunović, Dušan Ž. Mijin, Nenad D. Radić, Boško V. Grbić, Sonja M. Aškrabić, Biljana M. Babić, and Danica V. Bajuk-Bogdanović, *Nanocrystalline CeO$_{2-\delta}$ as Effective Adsorbent of Azo Dyes*, Langmuir 30 (2014) 11582-11590.

- M. Radović, B. Stojadinović, **N. Tomić**, A. Golubović, B. Matović, I. Veljković, Z. Dohčević-Mitrović, *Investigation of surface defect states in CeO$_{2-y}$ nanocrystals by Scanning-tunneling microscopy/spectroscopy and ellipsometry*, J. Appl. Phys. 116 (2014) 234305.

- M. Radović, Z. Dohčević-Mitrović, N. Paunović, S. Bošković, **N. Tomić**, N. Tadić, I. Belča, *Infrared study of plasmon-phonon coupling in pure and Nd doped CeO$_{2-y}$ nanocrystals*, J. Phys. D: Appl. Phys. 48 (2015) 065301 (8pp).

- M. Radović, B. Stojadinović, **N. Tomić**, I. Veljković, S. Aškrabić, A. Golubović, B. Matović, Z. Dohčević-Mitrović, *Investigation of defect electronic states in CeO$_2$ nanocrystals synthesized by SPRT, Hydrothermal and Precipitation method*, 2nd Conference of The Serbian Ceramic Society, Belgrade, Serbia, O-3, page 42, June 2013.

Поред главне активности, која се односила на испитивање поменутих TiO$_2$ и CeO$_2$ наноматеријала, кандидаткиња је учествовала у испитивању фотокаталитичких својстава и других нанопрахова (Pr(OH)$_3$) и композита (TiO$_2$/WO$_3$ композитних превлака на титанијумској подлози).

Што се тиче нанопрахова Pr(OH)$_3$, др Наташа Томић је учествовала у испитивању њихових адсорпционих и фотокаталитичких својстава (како чистих тако и допираних са Eu^{3+}) у присуству азо боје Reactive Orange 16 (при чему је коришћено UV зрачење), као и испитивању кинетике ових реакција. Резултати су објављени у једном раду у врхунском међународном часопису и приказани на конференцији:

- S. Aškrabić, V. D. Araujo, M. Passacantando, M. I. B. Bernardi, **N. Tomić**, B. Dojčinović, D. Manojlović, B. Čalija, M. Miletić, Z. D. Dohčević-Mitrović, *Nitrate-assisted photocatalytic efficiency of defective Eu-doped Pr(OH)$_3$ nanostructures*, Phys. Chem. Chem. Phys. 19 (2017) 31756-31765.

- **Nataša Tomić**, Sonja Aškrabić, Vinicius Dantas de Araújo, Marijana Milićević, Saša Lazović, Zoran Petrović, Zorana Dohčević-Mitrović, *Efficient photocatalytic degradation of azo-dye RO16 by pure and Eu-doped Pr(OH)$_3$ nanostructures*, 3rd Conference of The Serbian Society for Ceramic Materials, Belgrade, Serbia, P-14, page 89, June (15-17), 2015.

У случају композита праћен је фотокаталитички процес разградње азо боје Mordant Blue 9 у присуству UV зрачења, користећи TiO$_2$/WO$_3$ композитне превлаке на титанијумској подлози. Поред испитивања кинетике ових реакција др Наташа Томић радила је и на експериментима који се тичу одређивања (праћења) концентрације OH$^{\bullet}$ радикала као најважније врсте за потпуну деградацију различитих органских загађивача. Резултати су објављени у раду у врхунском међународном часопису:

- Zorana Dohčević-Mitrović, Stevan Stojadinović, Luca Lozzi, Sonja Aškrabić, Milena Rosić, **Nataša Tomić**, Novica Paunović, Saša Lazović, Marko G. Nikolić, Sandro Santucci, *WO3/TiO2 composite coatings: Structural, optical and photocatalytic properties*, Materials Research Bulletin 83 (2016) 217-224.

Такође, др Наташа Томић је имала допринос у експерименталном раду који се односио на испитивање утицаја неравнотежних атмосферских плазми на деградацију азо боја и кинетику ових процеса. Резултати ових анализа приказани су на више међународних конференција:

- Sasa Lazovic, Dejan Maletic, **Natasa Tomic**, Gordana Malovic, Uros Cvelbar, Zorana Dohcevic-Mitrovic, Zoran LJ. Petrovic, *Decolorization of azodyes using the atmospheric pressure plasma jet*, 66th Annual Gaseous Electronics Conference, Princeton, New Jersey, CT1 68, page 29, September-October, 2013.

- Tatjana Mitrović, Dejan Maletić, **Nataša Tomić**, Saša Lazović, Gordana Malović, Tanja Nenin, Uroš Cvelbar, Zorana Dohčević –Mitrović, Z. Lj. Petrović, *Removal of reactive orange 16 from water by plasma needle*, 27th Summer School and International Symposium on the Physics of Ionized Gases (SPIG 2014), Belgrade, Serbia, 26.8.- 29.8.2014. pp 443-446.

- U. Cvelbar, S. Lazović, **N. Tomić**, T. Mitrović, D. Maletić, T. Nenin, G. Malovic, Z. Dohčević-Mitrović, Z. Lj. Petrović, *Removal of azo dyes from water by two advanced oxidation processes*, COST TD1208 Annual meeting, "Electrical dis-charges with liquids for future applications", Lisboa, 10-13 March 2014, WG:4-1

- S. Lazović, **N. Tomić**, T. Mitrović, D. Maletić, T. Nenin, G. Malović, U. Cvelbar, Z. Dohčević-Mitrović, Z. Lj. Petrović, *Removal of Organic Pollutants from Water by two Advanced Oxidation Processes*, 9th EU-Japan Joint Symposium on Plasma Processing (JSPP2014) and EU COST MP1101 Workshop on Atmospheric Plasma Processes and Sources, 19-23 January 2014, Bohinjska Bistrica, Slovenia, p 1

- Tatjana Mitrović, Nikola Božović, **Nataša Tomić**, Zorana Dohčević-Mitrović, Dejan Maletić, Saša Lazović, Gordana Malović, Uroš Cvelbar and Zoran Lj. Petrović, *Plasma needle decolourisation of direct red (DR28) diazo dye*, 20th Symposium on Application of Plasma Processes and COST TD1208 Workshop on Application of Gaseous Plasma with Liquids, Slovakia, Tatranská Lomnica, 17.1. - 22.1.2015. pp 245-247 (ISSN: 978-80-8147-027-1).

Др Наташа Томић је дала допринос у изради докторске дисертације др Марка Радовића на Физичком факултету, Универзитета у Београду о чему је приложен доказ (захвалница).

Елементи за квалитативну оцену научног доприноса

1 Квалитет научних резултата

1.1 Значај научних резултата

Др Наташа Томић је до сада учествовала у изради 9 научних радова од којих је на два као први аутор дала кључан допринос. Један рад је објављен у међународном часопису изузетних вредности категорије М21а, седам радова је објављено у врхунским међународним часописима категорије М21, док је један рад објављен у међународном часопису М23. Такође, до сада је учествовала на више међународних и националних конференција.

1.2 Параметри квалитета часописа

Кандидаткиња др Наташа Томић је објавила укупно девет радова у међународним часописима и то:

- 1 рад у међународном часопису изузетних вредности *Materials Characterization* (IF = 1.925)

- 1 рад у врхунском међународном часопису *Langmuir* (IF = 4.457)

- 1 рад у врхунском међународном часопису *Physical Chemistry Chemical Physics* (IF = 4.449)

- 1 рад у врхунском међународном часопису *Journal of Physics. D: Applied Physics* (IF = 2.772)

- 1 рад у врхунском међународном часопису *Ceramics International* (IF = 2.605)

- 1 рад у врхунском међународном часопису *Materials Research Bulletin* (IF = 2.435)

- 1 рад у врхунском међународном часопису *Journal of Applied Physics* (IF = 2.210)

- 1 рад у врхунском међународном часопису *Materials Chemistry and Physics* (IF = 2.259)

- 1 рад у међународном часопису *Chemical Industry and Chemical Engineering Quarterly* (IF = 0.892)

1.3 Подаци о цитираности

Према бази *Web of Science*, радови др Наташе Томић су цитирани укупно 50 пута, од чега 47 пута изузимајући аутоцитате. Према бази *Google Scholar* укупан број цитата је 90.

2 Нормирање броја коауторских радова, патената и техничких решења

Сви радови др Наташе Томић су експерименталне природе који подразумевају сарадњу више институција. Имајући то у виду број коаутора је на појединим радовима већи од 7. Нормирање М бодова у складу са Правилником Министарства о поступку и начину вредновања, и квантитативном исказивању научноистраживачких резултата истраживача је кандидаткињин укупан збир умањило на око 63 бода, што је и даље знатно (скоро 4 пута) више од захтеваног минимума (16) за избор у звање научни сарадник.

3 Учешће у пројектима, потпројектима и пројектним задацима

Кандидаткиња је од 1.09.2011. до 31.10.2017. учествовала на пројекту Министарства просвете, науке и технолошког развоја Републике Србије ОН 171032 “Физика наноструктурних оксидних материјала и јако корелисаних система”. Од 1.11.2017. године ангажована је на пројекту ИИИ45018 “Наноструктурни мултифункционални материјали и нанокомпозити” Министарства просвете, науке и технолошког развоја Републике Србије, чији руководилац је академик Зоран В. Поповић.

4 Утицај научних резултата

Списак радова и цитата дат је у прилогу.

5 Конкретан допринос кандидата у реализацији радова у научним центрима у земљи и иностранству

Кандидаткиња је све своје истраживачке активности реализовала у Институту за физику Београд. Значајно је допринела сваком раду на коме је учествовала. Њен допринос се огледа у синтези наноматеријала (CeO_2 и TiO_2), испитивању примене ових наноматеријала у процесима адсорпције и фотокаталитичке деградације када су у питању различити органски (канцерогени) молекули, као и у писању радова.

Елементи за квантитативну оцену научног доприноса

Остварени М-бодови по категоријама публикација

Категорија	М-бодова по публикацији	Број публикација	Укупно М-бодова
М21а	10	1	10
М21	8	7	56
М23	3	1	3
М33	1	1	1
М34	0.5	8	4
М64	0.2	1	0.2
М70	6	1	6

Поређење оствареног броја М-бодова са минималним условима потребним за избор у звање научног сарадника

	Потребно	Остварено
Укупно	16	80.2
М10+М20+М31+М32+М33+М41+М42	10	70
М11+М12+М21+М22+М23	6	69

Списак радова Наташе Томић

Рад у међународном часопису изузетних вредности (M21a):

1. M. Grujić-Brojčin, S. Armaković, **N. Tomić**, B. Abramović, A. Golubović, B. Stojadinović, A. Kremenović, B. Babić, Z. Dohčević-Mitrović, M. Šćepanović, *Surface modification of sol-gel synthesized TiO_2 nanoparticles induced by La-doping*, Materials Characterization 88 (2014) 30-41.

Радови у врхунским међународним часописима (M21):

1. A. Golubović, **N. Tomić**, N. Finčur, B. Abramović, I. Veljković, J. Zdravković, M. Grujić-Brojčin, B. Babić, B. Stojadinović, M.Šćepanović, *Synthesis of pure and La-doped anatase nanopowders by sol-gel and hydrothermal methods and their efficiency in photocatalytic degradation of alprazolam*, Ceramics International 40 (2014) 13409-13418.

2. **Nataša M. Tomić**, Zorana D. Dohčević-Mitrović, Novica M. Paunović, Dušan Ž. Mijin, Nenad D. Radić, Boško V. Grbić, Sonja M. Aškrabić, Biljana M. Babić, and Danica V. Bajuk-Bogdanović, *Nanocrystalline $CeO_{2-\delta}$ as Effective Adsorbent of Azo Dyes*, Langmuir 30 (2014) 11582-11590.

3. M. Radović, B. Stojadinović, **N. Tomić**, A. Golubović, B. Matović, I. Veljković, Z. Dohčević-Mitrović, *Investigation of surface defect states in CeO_{2-y} nanocrystals by Scanning-tunneling microscopy/spectroscopy and ellipsometry*, J. Appl. Phys. 116 (2014) 234305.

4. M. Radović, Z. Dohčević-Mitrović, N. Paunović, S. Bošković, **N. Tomić**, N. Tadić, I. Belča, *Infrared study of plasmon-phonon coupling in pure and Nd doped CeO_{2-y} nanocrystals*, J. Phys. D: Appl. Phys. 48 (2015) 065301 (8pp).

5. **N. Tomić**, M. Grujić-Brojčin, N. Finčur, B. Abramović, B. Simović, J. Krstić, B. Matović, M. Šćepanović, *Photocatalytic degradation of alprazolam in water suspension of brookite type TiO2 nanopowders prepared using hydrothermal route*, Materials Chemistry and Physics 163 (2015) 518-528.

6. Zorana Dohčević-Mitrović, Stevan Stojadinović, Luca Lozzi, Sonja Aškrabić, Milena Rosić, **Nataša Tomić**, Novica Paunović, Saša Lazović, Marko G. Nikolić, Sandro Santucci, *WO3/TiO2 composite coatings: Structural, optical and photocatalytic properties*, Materials Research Bulletin 83 (2016) 217-224.

7. S. Aškrabić, V. D. Araujo, M. Passacantando, M. I. B. Bernardi, **N. Tomić**, B. Dojčinović, D. Manojlović, B. Čalija, M. Miletić, Z. D. Dohčević-Mitrović, *Nitrate-assisted photocatalytic efficiency of defective Eu-doped $Pr(OH)_3$ nanostructures*, Phys. Chem. Chem. Phys. 19 (2017) 31756-31765.

Рад у међународном часопису (М23):

1. Aleksandar Golubović, Ivana Veljković, Maja Šćepanović, Mirjana Grujić-Brojčin, **Nataša Tomić**, Dušan Mijin, Biljana Babić, *Influence of some sol-gel synthesis parameters of mesoporous TiO₂ on photocatalytic degradation of pollutants*, Chem. Ind. Chem. Eng. Q. 22(1) (2016) 65-73.

Саопштење са међународног скупа штампано у целини (М33):

1. Tatjana Mitrović, Dejan Maletić, **Nataša Tomić**, Saša Lazović, Gordana Malović, Tanja Nenin, Uroš Cvelbar, Zorana Dohčević –Mitrović, Z. Lj. Petrović, *Removal of reactive orange 16 from water by plasma needle*, 27th Summer School and International Symposium on the Physics of Ionized Gases (SPIG 2014), Belgrade, Serbia, 26.8.- 29.8.2014. pp 443-446

Саопштење са међународног скупа штампано у изводу (М34):

1. **Nataša Tomić**, Aleksandar Golubović, Marko Radović, Jelena Tanasijević, Ivana Veljković, *Influence of La³⁺-dopant on anatase nanopowders synthesized by sol-gel and hydrothermal methods*, First International Conference on Processing, characterization and application of nanostructured materials and nanotechnology Nano Belgrade, Belgrade, Serbia, P-15, page 93, September 2012.

2. M. Radović, B. Stojadinović, **N. Tomić**, I. Veljković, S. Aškrabić, A. Golubović, B. Matović, Z. Dohčević-Mitrović, *Investigation of defect electronic states in CeO₂ nanocrystals synthesized by SPRT, Hydrothermal and Precipitation method*, 2ⁿᵈ Conference of The Serbian Ceramic Society, Belgrade, Serbia, O-3, page 42, June 2013.

3. **Nataša Tomić**, Nina Finčur, Ivana Veljković, Maja Šćepanović, Aleksandar Golubović, Biljana Abramović, *The efficiency of pure and La-doped anatase nanopowders synthesized by sol-gel and hydrothermal method in photocatalytic degradation of alprazolam*, 2ⁿᵈ Conference of The Serbian Ceramic Society, Belgrade, Serbia, P-20, page 71, June 2013.

4. Sasa Lazovic, Dejan Maletic, **Natasa Tomic**, Gordana Malovic, Uros Cvelbar, Zorana Dohcevic-Mitrovic, Zoran LJ. Petrovic, *Decolorization of azodyes using the atmospheric pressure plasma jet*, 66th Annual Gaseous Electronics Conference, Princeton, New Jersey, CT1 68, page 29, September-October, 2013.

5. U. Cvelbar, S. Lazović, **N. Tomić**, T. Mitrović, D. Maletić, T. Nenin, G. Malovic, Z. Dohčević-Mitrović, Z. Lj. Petrović, *Removal of azo dyes from water by two advanced oxidation processes*, COST TD1208 Annual meeting, "Electrical discharges with liquids for future applications," Lisboa, 10-13 March 2014, WG:4-1

6. S. Lazović, **N. Tomić**, T. Mitrović, D. Maletić, T. Nenin, G. Malović, U. Cvelbar, Z. Dohčević-Mitrović, Z. Lj. Petrović, *Removal of Organic Pollutants from Water by two Advanced Oxidation Processes*, 9th EU-Japan Joint Symposium on Plasma Processing (JSPP2014) and EU COST MP1101 Workshop on Atmospheric Plasma Processes and Sources, 19-23 January 2014, Bohinjska Bistrica, Slovenia, p 1

7. Tatjana Mitrović, Nikola Božović, **Nataša Tomić**, Zorana Dohčević-Mitrović, Dejan Maletić, Saša Lazović, Gordana Malović, Uroš Cvelbar and Zoran Lj. Petrović, *Plasma needle decolourisation of direct red (DR28) diazo dye*, 20th Symposium on Application of Plasma Processes and COST TD1208 Workshop on Application of Gaseous Plasma with Liquids, Slovakia, Tatranská Lomnica, 17.1. - 22.1.2015. pp 245-247 (ISSN: 978-80-8147-027-1)

8. **Nataša Tomić**, Sonja Aškrabić, Vinicius Dantas de Araújo, Marijana Milićević, Saša Lazović, Zoran Petrović, Zorana Dohčević-Mitrović, *Efficient photocatalytic degradation of azo-dye RO16 by pure and Eu-doped Pr(OH)$_3$ nanostructures*, 3rd Conference of The Serbian Society for Ceramic Materials, Belgrade, Serbia, P-14, page 89, June (15-17), 2015.

Саопштење са скупа националног значаја штампано у изводу (M64)

1. Nina L. Finčur, **Nataša M. Tomić**, Mirjana U. Grujić-Brojčin, Maja J. Šćepanović, Biljana F. Abramović, *Efikasnost brukitinih TiO$_2$ nanoprahova u fotokatalitičkoj razgradnji alprazolama primenom UVA zračenja*, 52. Savetovanje Srpskog Hemijskog Društva, Novi Sad, HŽS P 11, strana 80, 29. i 30. maj 2015.

Одбрањена докторска дисертација (M70)

Наташа Томић

Адсорпциона и фотокаталитичка својства наноматеријала на бази церијум(IV)-оксида и титан(IV)-оксида, Универзитет у Београду, Факултет за Физичку хемију (2017).

Web of Science

| Search | Search Results | | My Tools ▼ | Search History | Marked List | 9 |

Citation report for **9** results from Web of Science Core Collection between `1996` ▼ and `2018` ▼   Go

You searched for: **From Marked List: ...More**

This report reflects citations to source items indexed within Web of Science Core Collection. Perform a Cited Reference Search to include citations to items not indexed within Web of Science Core Collection.

Export Data: Save to Text File ▼

Total Publications
9
1998   2017

h-index
4

Average citations per item
5.56

Sum of Times Cited
50
Without self citations
47

Citing articles
46
Without self citations
44

Sum of Times Cited per Year

Sort by: **Times Cited**   Date   More ▼   Page 1 of 1

	2014 ◀	2015	2016	2017	2018 ▶	Total	Average Citations per Year
Use the checkboxes to remove individual items from this Citation Report	1	8	19	19	3	50	10.00

or restrict to items published between 1996 ▼ and 2018 ▼   **Go**

☐ 1. ☑ **Surface modification of sol-gel synthesized TiO2 nanoparticles induced by La-doping** By: Grujic-Brojcin, M.; Armakovic, S.; Tomic, N.; et al. MATERIALS CHARACTERIZATION Volume: 88 Pages: 30-41 Published: FEB 2014	1	6	6	4	1	18	3.60
☐ 2. ☑ **Nanocrystalline CeO2-delta as Effective Adsorbent of Azo Dyes** By: Tomic, Natasa M.; Dohcevic-Mitrovic, Zorana D.; Paunovic, Novica M.; et al. LANGMUIR Volume: 30 Issue: 39 Pages: 11582-11590 Published: OCT 7 2014	0	1	7	5	1	14	2.80
☐ 3. ☑ **Photocatalytic degradation of alprazolam in water suspension of brookite type TiO2 nanopowders prepared using hydrothermal route** By: Tomic, N.; Grujic-Brojcin, M.; Fincur, N.; et al. MATERIALS CHEMISTRY AND PHYSICS Volume: 163 Pages: 518-528 Published: AUG 1 2015	0	0	2	6	0	8	2.00
☐ 4. ☑ **Synthesis of pure and La-doped anatase nanopowders by sol-gel and hydrothermal methods and their efficiency in photocatalytic degradation of alprazolam** By: Golubovic, A.; Tomic, N.; Fincur, N.; et al. CERAMICS INTERNATIONAL Volume: 40 Issue: 8 Pages: 13409-13418 Part: B Published: SEP 2014	0	1	2	1	0	4	0.80
☐ 5. ☑ **WO3/TiO2 composite coatings: Structural, optical and photocatalytic properties** By: Dohcevic-Mitrovic, Zorana; Stojadinovic, Stevan; Lozzi, Luca; et al. MATERIALS RESEARCH BULLETIN Volume: 83 Pages: 217-224 Published: NOV 2016	0	0	0	1	1	2	0.67
☐ 6. ☑ **Investigation of surface defect states in CeO2-y nanocrystals by Scanning-tunneling microscopy/spectroscopy and ellipsometry** By: Radovic, Marko; Stojadinovic, Bojan; Tomic, Natasa; et al. JOURNAL OF APPLIED PHYSICS Volume: 116 Issue: 23 Article Number: 234305 Published: DEC 21 2014	0	0	1	1	0	2	0.40
☐ 7. ☑ **INFLUENCE OF SOME SOL-GEL SYNTHESIS PARAMETERS OF MESOPOROUS TIO2 ON PHOTOCATALYTIC DEGRADATION OF POLLUTANTS** By: Golubovic, Aleksandar; Veljkovic, Ivana; Scepanovic, Maja; et al. CHEMICAL INDUSTRY & CHEMICAL ENGINEERING QUARTERLY Volume: 22 Issue: 1 Pages: 65-73 Published: JAN-MAR 2016	0	0	0	1	0	1	0.33
☐ 8. ☑ **Infrared study of plasmon-phonon coupling in pure and Nd-doped CeO2-y nanocrystals** By: Radovic, M.; Dohcevic-Mitrovic, Z.; Paunovic, N.; et al. JOURNAL OF PHYSICS D-APPLIED PHYSICS Volume: 48 Issue: 6 Article Number: 065301 Published: FEB 18 2015	0	0	1	0	0	1	0.25

9.   **Nitrate-assisted photocatalytic efficiency of defective Eu-doped Pr(OH)(3) nanostructures**

By: Askrabic, S.; Araujo, V. D.; Passacantando, M.; et al.
PHYSICAL CHEMISTRY CHEMICAL PHYSICS   Volume: 19   Issue: 47
Pages: 31756-31765   Published: DEC 21 2017

0	0	0	0	0	0	0.00

☐ Select Page   Save to Text File ▾

Sort by: **Times Cited**   Date   More ▾   Page 1   of 1

9 records matched your query of the 39,646,300 in the data limits you selected.
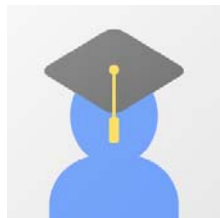
Natasa Tomic

Institute of Physics

	All	Since 2013
Citations	90	90
h-index	5	5
i10-index	4	4

TITLE	CITED BY	YEAR
Surface modification of sol–gel synthesized TiO 2 nanoparticles induced by La-doping M Grujić-Brojčin, S Armaković, N Tomić, B Abramović, A Golubović, ... Materials Characterization 88, 30-41	31	2014
TiO 2/WO 3 photocatalytic composite coatings prepared by spray pyrolysis B Grbić, N Radić, S Stojadinović, R Vasilić, Z Dohčević-Mitrović, ... Surface and Coatings Technology 258, 763-771	22	2014
Nanocrystalline CeO2− δ as effective adsorbent of azo dyes NM Tomić, ZD Dohčević-Mitrović, NM Paunović, DZ Mijin, ND Radić, ... Langmuir 30 (39), 11582-11590	16	2014
Photocatalytic degradation of alprazolam in water suspension of brookite type TiO 2 nanopowders prepared using hydrothermal route N Tomić, M Grujić-Brojčin, N Finčur, B Abramović, B Simović, J Krstić, ... Materials Chemistry and Physics 163, 518-528	10	2015
Synthesis of pure and La-doped anatase nanopowders by sol–gel and hydrothermal methods and their efficiency in photocatalytic degradation of alprazolam A Golubović, N Tomić, N Finčur, B Abramović, I Veljković, J Zdravković, ... Ceramics International 40 (8), 13409-13418	5	2014
Influence of some sol-gel synthesis parameters of mesoporous TiO2 on photocatalytic degradation of pollutants A Golubović, I Veljković, M Šćepanović, M Grujić-Brojčin, N Tomić, D Mijin, ... Chemical Industry and Chemical Engineering Quarterly 22 (1), 65-73	4	2016
Investigation of surface defect states in CeO2-y nanocrystals by Scanning−tunneling microscopy/spectroscopy and ellipsometry M Radović, B Stojadinović, N Tomić, A Golubović, B Matović, I Veljković, ... Journal of Applied Physics 116 (23), 234305	2	2014
Adsorpciona i fotokatalitička svojstva nanomaterijala na bazi cerijum (IV) oksida i titan (IV) oksida NM Tomić Univerzitet u Beogradu-Fakultet za fizičku hemiju		2017
Nitrate-assisted photocatalytic efficiency of defective Eu-doped Pr (OH) 3 nanostructures S Aškrabić, VD Araújo, M Passacantando, MIB Bernardi, N Tomić, ... Physical Chemistry Chemical Physics 19 (47), 31756-31765		2017

TITLE	CITED BY	YEAR
[Infrared study of plasmon–phonon coupling in pure and Nd-doped CeO2− y nanocrystals](#) M Radović, Z Dohčević-Mitrović, N Paunović, S Bošković, N Tomić, ... Journal of Physics D: Applied Physics 48 (6), 065301		2015
[PLASMA NEEDLE DECOLOURISATION OF DIRECT RED (DR 28) DIAZO DYE](#) T Mitrović, N Božović, N Tomić, Z Dohčević-Mitrović, D Maletić, S Lazović, ... 20 th Symposium on Application of Plasma Processes, 245		2015
[Decolorization of azodyes using the atmospheric pressure plasma jet](#) S Lazovic, D Maletic, N Tomic, G Malovic, U Cvelbar, Z Dohcevic-Mitrovic, ... APS Meeting Abstracts		2013
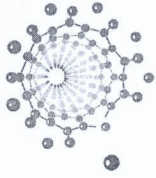
Универзитет у Београду
Факултет за физичку хемију
Број индекса: 2010/0320
Број: Д1252018
Датум: 29.12.2017.

На основу члана 161 Закона о општем управном поступку ("Службени лист СРЈ", бр. 33/97, 31/2001 и "Службени гласник РС", бр. 30/2010), дозволе за рад број 612-00-00564/2009-04 од 11.06.2009. године коју је издало Министарство просвете Републике Србије и службене евиденције, Универзитет у Београду - Факултет за физичку хемију, издаје

УВЕРЕЊЕ

Наташа Томић

име једног родитеља Миодраг, ЈМБГ 2002981715276, рођена 20.02.1981. године, Београд, општина Београд-Савски Венац, Република Србија, уписана школске 2010/11. године, дана 28.12.2017. године завршила је докторске академске студије на студијском програму Физичка хемија, у трајању од три године, обима 180 (сто осамдесет) ЕСПБ бодова, са просечном оценом 9,86 (девет и 86/100).

На основу наведеног издаје јој се ово уверење о стеченом високом образовању и научном називу **доктор наука – физичкохемијске науке.**

Декан

Проф. др Гордана Ћирић-Марјановић

CrossMark

Surface modification of sol–gel synthesized TiO₂ nanoparticles induced by La-doping

M. Grujić-Brojčin[a],*, S. Armaković[b], N. Tomić[a], B. Abramović[b], A. Golubović[a], B. Stojadinović[a], A. Kremenović[c], B. Babić[d], Z. Dohčević-Mitrović[a], M. Šćepanović[a]

[a]Institute of Physics, University of Belgrade, Pregrevica 118, 11080 Belgrade, Serbia
[b]Department of Chemistry, Biochemistry and Environmental Protection, Faculty of Sciences, University of Novi Sad, Trg D. Obradovića 3, 21000 Novi Sad, Serbia
[c]Faculty of Mining and Geology, Laboratory for Crystallography, University of Belgrade, Đušina 7, 11000 Belgrade, Serbia
[d]Institute of Nuclear Sciences "Vinča", University of Belgrade, 11001 Belgrade, Serbia

ARTICLE DATA

ABSTRACT

The influence of La-doping in the range of 0.5–6.0 mol% on structural and morphological properties of TiO₂ nanopowders synthesized by sol–gel routine has been investigated by XRPD, AFM, EDS and BET measurements, as well as Raman spectroscopy. The XRPD and Raman measurements have revealed the anatase phase as dominant in all nanopowders, with crystallite size decreasing from ~15 nm in pure TiO₂ to ~12 nm in La-doped samples. The BET data suggest that all samples are fully mesoporous, with mean pore diameters in the range of ~6–8 nm. The specific surface area and the complexity of pore structure are greater in doped samples than in pure TiO₂ sample. The spectroscopic ellipsometry has apparently shown that the band gap has been gradually increased with the increase of La content. The STM and STS techniques have been used successfully to evaluate the surface morphology and electronic properties of La-doped nanopowders. All investigated properties have been related to photocatalytic activity, tested in degradation of a metoprolol tartrate salt (0.05 mM), and induced by UV-radiation. All doped samples showed increased photocatalytic activity compared to pure TiO₂, among which the 0.65 mol% La-doped sample appeared to be the most efficient.

1. Introduction

Among the semiconductors investigated for the purpose of the degradation of pollutants in the water, titanium dioxide (TiO₂) is the most preferable material for the photocatalytic processes, due to its high photosensitivity, non-toxic nature, large band gap and stability ([1] and the references therein). In recent research, doping TiO₂ with lanthanum (La³⁺) ions has been found to improve the activity of TiO₂ photocatalysts [2–4]. The reasons for such improvement in photocatalytic activity have been generally related to increasing surface area and pore volume, capacity for adsorption of organic compounds, as well as suppressing electron–hole recombination rates in La-doped TiO₂ photocatalyst during the photocatalytic reaction [2–4]. However, the variety of experimental conditions, sample preparation and determination of photoreactivity, as well as a lack of information on electronic structure, still make it difficult to explain the formation mechanism of lanthanum oxides and the changing of band gap energy with La-doping [5,6]. Namely, most of the literature is in agreement with the fact that La-doping is able to red shift the adsorption edges of TiO₂ to longer wavelengths, usually attributed to the La³⁺ replacing Ti⁴⁺

---

* Corresponding author at: Institute of Physics, University of Belgrade, Pregrevica 118, 11080 Belgrade, Serbia. Tel.: +381 113713023; fax: +381 113162190.
E-mail address: myramyra@ipb.ac.rs (M. Grujić-Brojčin).

ions in the TiO_2 lattice [6,7], but some recent studies have reported either a blue shift [8] or an absence of any shift [6]. This may be due to different synthesis conditions, and more insight is needed to determine which conditions are responsible for the specific behavior of the adsorption edge.

The sol–gel process appears to be the most popular doping technique since it is a low-cost, simple, and versatile method that can be easily manipulated. However, this process, followed by calcination at high temperature, can allow for lanthanum ions either to form oxides dispersed on the surface of the TiO_2 nanoparticles, or to incorporate in the titania lattice, as a less frequent outcome [7]. Therefore one of the goals of this research was to estimate which form of La^{3+} ions is dominant in TiO_2 nanopowders synthesized under the specified sol–gel synthesis conditions.

The TiO_2 mesoporous nanopowders, pure and doped with La^{3+} in the range of 0.5 to 6.0 mol% have been prepared by sol–gel routine using titanium tetrachloride ($TiCl_4$) as a precursor [9–11]. The effects of La-doping on the crystallite size, structure and phase composition of the synthesized samples have been investigated by X-ray powder diffraction (XRPD), energy-dispersive X-ray spectroscopy (EDS), and Raman scattering measurements.

The morphological properties have been studied by atomic force microscopy (AFM) and the Brunauer–Emmett–Teller (BET) measurements. The BET data have been analyzed by BJH (Barrett–Joyner–Halenda) and CPSM (corrugated pore structure model) methods to estimate the specific surface area and pore size distribution. Also, the pore structure tortuosity factor, as a feature of primary importance in catalysis, has been calculated by CPSM to obtain the information on the connectivity among the pores, which is essential to describe transport dynamics in porous media, and consequently determine the time of the catalytic reaction [12,13].

The electronic properties of nanopowders have been studied by scanning tunneling spectroscopy (STS) and spectroscopic ellipsometry (SE), to reveal the influence of doping on band gap energy and the energies of electronic transitions.

Experimentally observed structural, morphological and surface modifications of TiO_2 nanoparticles induced by La-doping have been related to the photocatalytic activity under ultraviolet (UV) irradiation. The efficiency of La-doped TiO_2 nanopowders have been tested in photocatalytic degradation of metoprolol tartrate salt, and compared to the performance of pure nanopowder under the same conditions [10,11,14]. Metoprolol tartrate salt (1-[4-(2-methoxyethyl) phenoxy]-3-(propan-2-ylamino)propan-2-ol tartrate (2:1), CAS no. 56392-17-7, $(C_{15}H_{25}NO_3)_2$ $C_4H_6O_6$, $M_r = 684.81$, MET) is commonly used as selective β_1-blocker in treatment of cardiovascular diseases. Its continuous input and persistence in the aqueous system, even in trace concentrations, may result in an emerging environmental pollution [15].

2. Experimental Details

2.1. Synthesis

Anatase nanoparticles have been prepared by using a sol–gel procedure with $TiCl_4$ (99.0% pure, Merck) as a titanium precursor.

The 5 ml of $TiCl_4$ was dissolved in 150 ml of distilled water under vigorous stirring on the ice-bath. In order to obtain the hydrogel, the aqueous solution of ammonium hydroxide (29%, Carlo Erba) has been added under careful control of the pH value of the solution (9.3). After aging in the mother liquor for 5 h, as-prepared hydrogel has been filtered and washed out with distilled water until complete removal of chloride ions. Obtained hydrogel has been converted to alcogel by repeated exchange with anhydrous ethanol for several times. To convert into nanoparticles, the alcogel was placed in a vessel, dried at 280 °C and calcined at a temperature of 550 °C for 7 h [9]. Also, an appropriate amount of $LaCl_3 \cdot 7H_2O$ (Merck) had been dissolved in water prior to the hydrolysis of $TiCl_4$, to obtain La-doped TiO_2 nanoparticles. The pure TiO_2 nanopowder and those doped with 0.5, 0.65, 1, 2, 3, 4, 5, and 6 mol% of La are labeled as TL(0), TL(0.5), TL(0.65) and from TL(1) to TL(6), respectively.

2.2. Characterization Methods

Powder X-ray diffraction has been used for the identification of crystalline phases, quantitative phase analysis and estimation of crystallite size and strain. The XRPD patterns for pure titanium dioxide nanopowder and those doped with 0.65 and 1 mol% of lanthanum ions have been collected on a Philips diffractometer (PW1710) employing Cu $K_{\alpha1,2}$, in the scanning range of 2θ between 20 and 80° with the step size of 0.06° and the counting time of 41 s/step. The patterns of the samples doped with higher La concentration have been collected in the same range by using a Stoe Stadi MP diffractometer (Cu $K_{\alpha1}$ radiation, primary beam Ge monochromator, linear PSD detector, Bragg–Brentano geometry), at every 0.01°, with a counting time of 80 s/step. The Fullprof computer program was used for the structure refinements, quantitative phase analysis and estimation of average crystallite sizes and strains [16]. For size-strain analysis the instrumental resolution function was obtained by parameterizing the profiles of the diffraction pattern of a LaB_6 (NIST SRM660a) standard specimen.

Composition/quality of TiO_2 has been analyzed on a SEM (JEOL JSM-6460LV, with the operating voltage of 20 keV) equipped with an EDS (INCAx-sight) detector and "INAx-stream" pulse processor (Oxford Instruments).

Non-contact atomic force microscopy (NC-AFM) measurements were carried out using an Omicron B002645 SPM probe VT AFM 25.

The porous structure of catalysts has been evaluated from adsorption/desorption isotherms of N_2 measured on TiO_2 samples, at −196 °C, using the gravimetric McBain method. The main parameters of the porosity such as specific surface area and pore volume have been estimated by BET method and α_s-plot ([17] and references therein). The pore size distributions have been estimated from experimental nitrogen sorption data by BJH and CPSM methods [11,18].

The Raman scattering measurements of TiO_2 samples were performed in the backscattering geometry at room temperature in the air using a Jobin-Yvon T64000 triple spectrometer, equipped with a confocal microscope and a nitrogen-cooled charge coupled device detector. The spectra have been excited by a 514.5 nm line of Ar^+/Kr^+ ion laser with an output power of less than 5 mW to avoid local heating due to laser irradiation.

The ellipsometric spectra of the TiO_2 nanopowders were measured using a SOPRA GES-5 variable angle ellipsometer in rotating polarizer configuration. The data were collected at room temperature, in the range from 1.5 to 6.5 eV with a resolution of 0.02 eV, for the incidence angle of 65°. Bulk calculations have been used to analyze the ellipsometric spectra and determine the dielectric functions of synthesized anatase nanopowders from measured SE data. The critical point (CP) method [19–21] has been applied to identify and evaluate the energy of the electronic transitions in nanopowders.

Scanning tunneling microscopy and spectroscopy (STM/STS) were employed to study the formation of La_2O_3 on an anatase nanoparticle surface. The measurements were performed at room temperature using the Omicron VT UHV system. Topography images were taken at several bias voltages in the range of 2.0–2.3 V and set-point currents with typical value of 200 pA, or less. Spectroscopic data were acquired at various locations of the tungsten tip above chosen nanoparticles in the range of ±4 V. The data represent an average of 100 measurements performed consecutively.

2.3. Measurements of Photocatalytic Activity

The photocatalytic activity of the TiO_2 powders doped with different amounts of La was evaluated by the degradation of the solution of metoprolol tartrate salt (≥99%, Sigma-Aldrich). The photocatalytic degradation was carried out as described in our previous research [10,11]. The initial MET concentration was 0.05 mM and the TiO_2 loading was 1.0 mg ml^{-1}. All experiments were performed at the natural pH. Kinetics of the MET photodegradation was monitored with liquid chromatography with diode array detection (LC–DAD) at 225 nm (wavelength of MET maximum absorption) [10]. The use of the gradient mode to follow the degradation kinetics of MET was necessary in order to separate the peaks originating from MET and intermediates, and shorten the time of the LC–DAD analysis. In order to determine the reproducibility of the results, at least duplicated runs were carried out for each condition for averaging the results, and reproducibility of kinetic measurements were 3–10%.

3. Experimental Results

3.1. X-ray Powder Diffraction

The XRPD patterns of pure and some La-doped TiO_2 nanopowders, are shown in Fig. 1. The most intensive diffraction peaks can be ascribed to the anatase crystal structure (JCPDS card 78-2486). Structure refinements have been performed by Rietveld method, and the lattice parameters, unit cell volume, average crystallite size and average strain in anatase are summarized in Table 1. The value of the anatase parameter a varies around its reference value ($a_0 = 0.378479(3)$ nm), whereas the value of the c parameter is slightly smaller than the reference one ($c_0 = 0.951237(1)$ nm). The unit cell volume of all samples is also smaller in comparison to the reference value, except in the pure TiO_2. The structural refinement has revealed that the anatase crystallite size of doped samples is decreased from ~15 nm in pure TL(0) to ~12 nm in La-doped samples, whereas the strain is slightly increased with doping (Table 1).
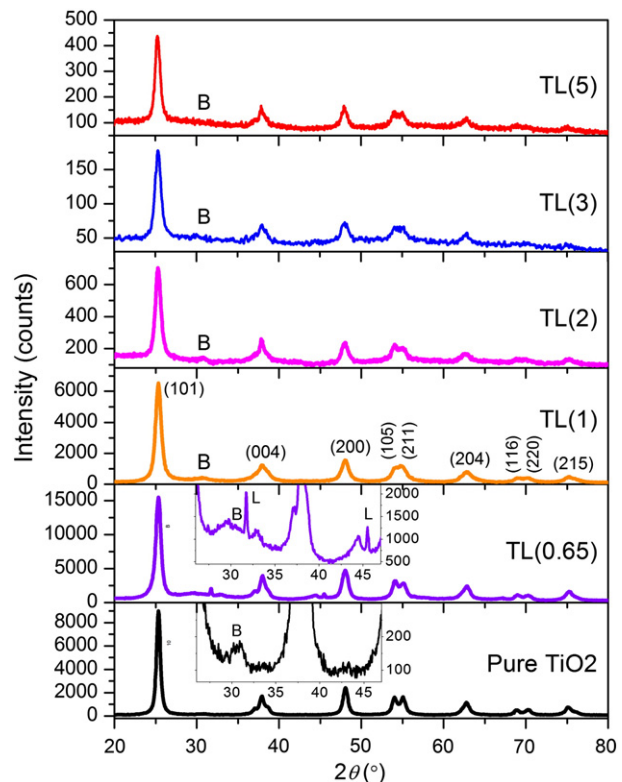
Fig. 1 – XRPD patterns of pure and selected La-doped TiO_2 nanopowders, with characteristic reflections of anatase phase given in the parentheses. The enlarged parts of diffractograms of the samples TL(0.65) and pure TiO_2 are shown in the insets. Characteristic reflections of brookite and La_2O_3 are denoted by "B" and "L", respectively.

The presence of a low intensity diffraction peak at $2\theta \approx 30.8°$ (denoted by "B" in Fig. 1), observed in all XRPD patterns, points to the brookite phase (JCPDS card 29-1360). The average crystallite size, the average strain, and the content of brookite phase have been also summarized in Table 1. The small crystallite size (down to 2 nm in TL(0.65)), as well as large values of the average strain in brookite phase indicate that this phase is highly disordered in all the samples. Therefore any attempt to obtain reliable unit cell parameters of brookite during the Rietveld refinement has failed. It also can be seen from Table 1 that brookite content, estimated from quantitative phase analysis, is greater in doped samples. A relatively large error in estimation of brookite content (defined as triple value of standard deviation, Table 1) is a consequence of the very low crystallinity of this phase followed by wide brookite diffraction peaks. Also, the lower intensity of brookite diffraction peaks in comparison to those of anatase, as well as a number of anatase and brookite reflections at very close values of diffraction angle, convoluting to one diffraction maximum, make the estimation of brookite presence even more complicated.

Moreover, very broad peaks at around 13.0, 29.5, 33.0 and 44.0° (as could be noticed from the pattern of the sample TL(0.65) shown in the upper inset of Fig. 1), which probably point to the presence of amorphous TiO_2 phase, as well as low signal intensity and great noise (samples TL(2), TL(3) and TL(5)), are

Table 1 – The results of the Rietveld analyses (the unit cell parameters and unit cell volume of anatase, average crystallite size and average strain in anatase and brookite phase and content of brookite phase) for pure and La-doped TiO$_2$ (the values in parentheses represent estimated standard deviations).

Sample	Anatase					Brookite		
	a (nm)	c (nm)	V (10^{-3} nm^3)	Crystallite size (nm)	Strain ($\times 10^{-3}$)	Content (%)	Crystallite size (nm)	Strain (10^{-3})
TL(0)	0.37884(1)	0.94980(5)	136.31(1)	15	3	10(2)	58	17
TL(0.65)	0.37895(2)	0.9485(1)	136.21(2)	12	4	42(5)	2	29
TL(1)	0.37880(2)	0.94780(1)	136.01(2)	10	5	24(3)	26	22
TL(2)	0.37853(2)	0.94908(9)	135.99(2)	12	8	21(1)	12	8
TL(3)	0.37823(6)	0.9471(3)	135.49(5)	12	8	21(4)	12	8
TL(5)	0.37874(3)	0.9485(1)	136.06(2)	12	8	22(2)	12	8

Reference values: a_0 = 0.378479(3) nm, c_0 = 0.951237(1) nm, and V_0 = 136.26(1) (10^{-3} nm^3).

confirming that the crystallinity of synthesized materials is of extremely low degree. It seems that La-doping induces additional disorder in both anatase and brookite phases.

The diffraction peaks at ~31.7 and 45.5°, characteristic for crystalline La$_2$O$_3$, have been found only in the pattern of the sample doped with 0.65 mol% La (the upper inset in Fig. 1). However, it does not exclude the presence of La-oxide in the amorphous phase in the samples doped with higher La concentration.

3.2. Atomic Force Microscopy

The NC-AFM images of pure, 1 mol% and 6 mol% La-doped TiO$_2$ samples are shown in Fig. 2. Note that images (a) and (c) are
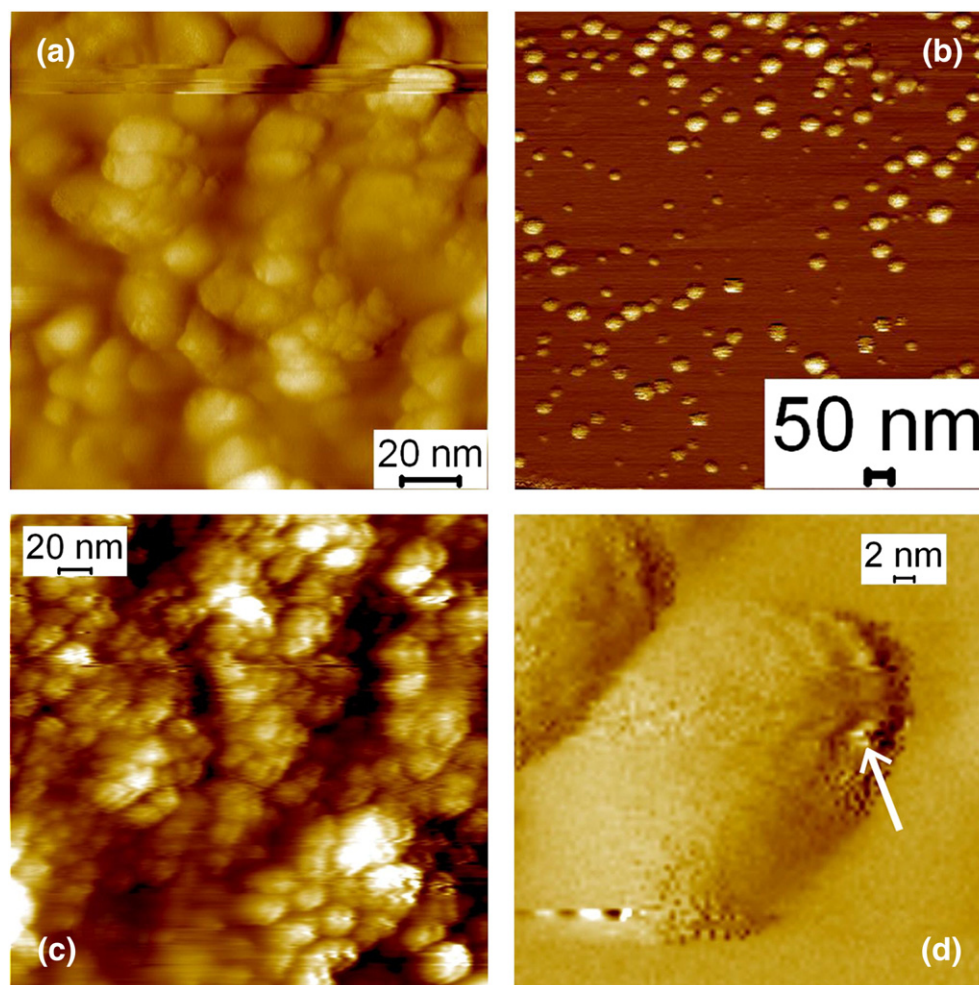
Fig. 2 – NC-AFM images of pure (a) and La-doped TiO$_2$ samples: 1 mol% La (b), 6 mol% La (c) and close-up image of the sample with 6 mol% La (d).

Table 2 – EDS results for pure and some La-doped TiO$_2$ nanopowders.

Sample	La (mol%)	EDS data			
		O (wt.%)	Ti (wt.%)	La (wt.%)	Total (wt.%)
TL(0)	0	39.46	60.54	0	100
TL(0.65)	0.65	42.91	57.09	0	100
TL(1)	1	49.71	49.44	0.85	100
TL(2)	2	44.59	53.45	1.96	100
TL(6)	6	41.71	52.39	5.91	100

agglomerated particles. However, in the close-up image of the sample with 6 mol% La, as the most interesting, one could observe a granular structure (up to 2 nm) covering the surface of some nanoparticles.

3.3. EDS

The chemical composition of pure and some La-doped nanopowders has been estimated by EDS method (Table 2). The micrographs of chosen samples (pure TL(0) and doped TL(0.65), TL(1) and TL(6)) are shown in Fig. 3(a), whereas the EDS spectra of pure and maximally doped sample are presented in Fig. 3(b). The oxygen weight percent in pure TiO$_2$ nanopowder sample is close to stoichiometric TiO$_2$ (40 wt.%), whereas the percent of oxygen is higher in the La-doped samples. The final molar La/Ti ratio calculated from EDS data is lower than at the beginning of the synthesis process. It is estimated at around 63% of the starting value, except in the case of the sample doped with

taken from the pure and 6 mol% La doped nanopowders, respectively, pressed into the pellets, whereas the image (b) is recorded on nanopowder TL(1), previously dispersed in ethanol, deposited on freshly cleaved HOPG (highly oriented prolific graphite). From these images we can observe that samples consist of very small nanocrystals (up to 20 nm) and greater
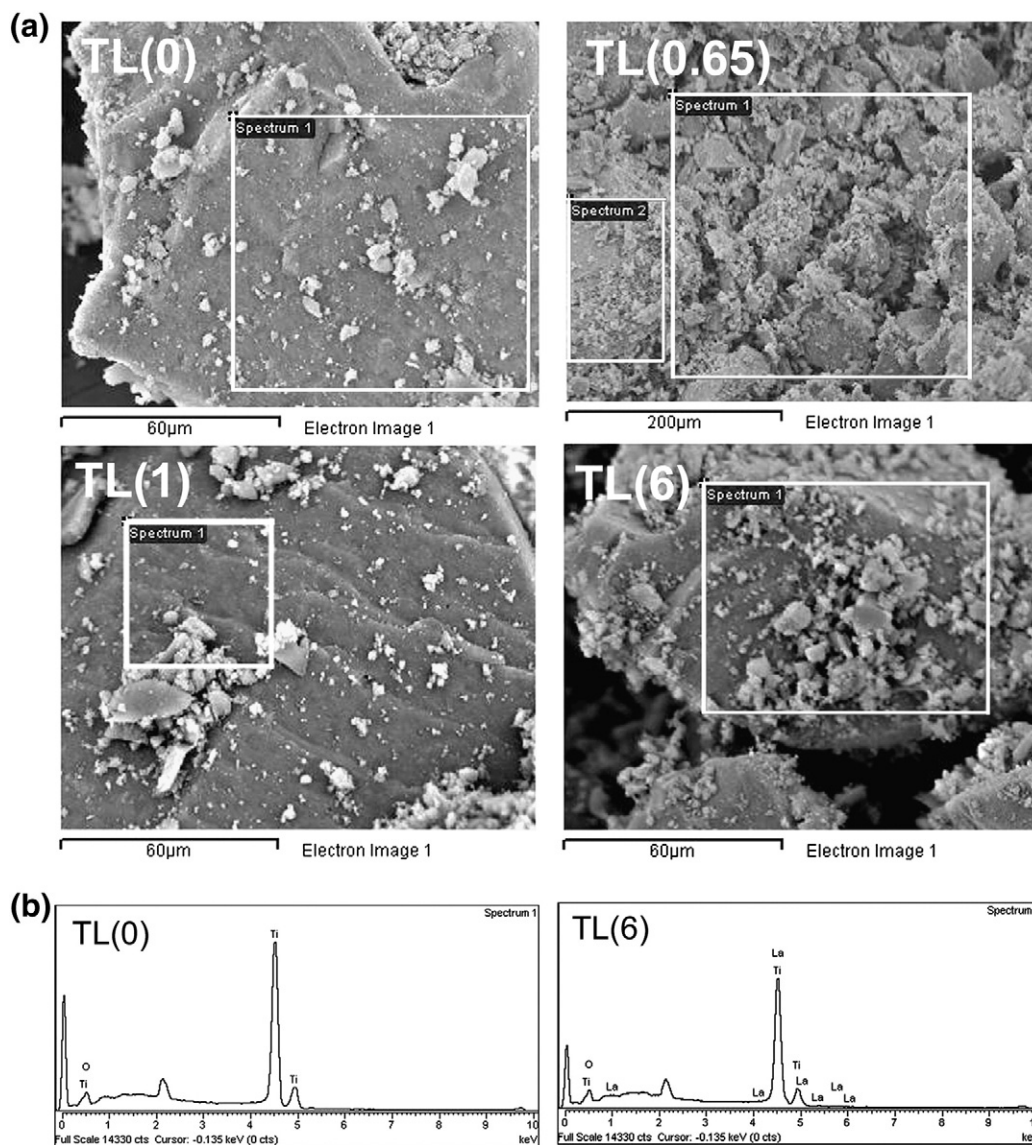
Fig. 3 – (a) The SEM images of pure TL(0) and some La-doped nanopowders TL(0.65), TL(1) and TL(6); (b) EDS spectra of pure TiO$_2$, TL(0), and nanopowder doped with the highest percent of La, TL(6).

0.65 wt.% of La, where such low content of La could not be detected by EDS method.

3.4. BET

To investigate the effects of lanthanum doping on the pore structure and adsorption abilities of TiO$_2$ nanopowders, the nitrogen sorption isotherm measurements have been carried out. The parameters of porosity, determined from the α_s-plots [17] obtained from the standard nitrogen adsorption isotherms suggest that the samples are fully mesoporous. The specific surface area (S$_{BET}$) and pore volume (V$_p$) obtained by BET method, and mesopore diameter calculated from both BET and BJH ($\overline{D}_{BET}$, $\overline{D}_{BJH}$, respectively) for chosen samples are listed in Table 3. The values of S$_{BET}$ in La-doped samples (~80 m^2 g^{-1}) are higher than those in pure nanopowder (58 m^2 g^{-1}). Mean pore diameters, obtained from BET results as $\overline{D}_{BET} = 4V_p/S_{BET}$ are in good agreement with the diameters obtained by BJH method.

The pore size distribution (PSD) is estimated from the desorption branch of the hysteresis isotherm loops by usually used BJH method [18]. The mean pore diameters obtained by BJH method, listed in Table 3, are comparable to the corresponding diameters obtained by BET method. The CPSM method [12,22] for PSD evaluation has been also applied. In this method the pore structure is considered as a statistically large number of independent, nonintersected corrugated pores, made of a series of N$_S$ cylindrical segments of equal length, with randomly distributed diameters of mesopores [11,12,22]. The pore volume distributions obtained by CPSM are shown in Fig. 4 (thick lines). Note that the distributions calculated by this method are somewhat wider than those obtained by BJH, although corresponding mean pore diameters are in good agreement (Table 3). The CPSM fitting parameter N$_S$, mentioned above, is also listed in Table 3: higher values of N$_S$ have been obtained for doped samples, which can be associated with a more complex pore structure in doped samples [12]. As a result of CPSM, the pore tortuosity factor τ is also estimated (Table 3), as a measure of diffusion through porous media based on nitrogen sorption hysteresis data [11,12]. The dependence of tortuosity factor on the La-content in doped samples shows the same tendency as N$_S$: higher values of τ are obtained for doped samples, with the maximum in the sample TL(0.65) ($\tau = 5.3$), pointing to the most
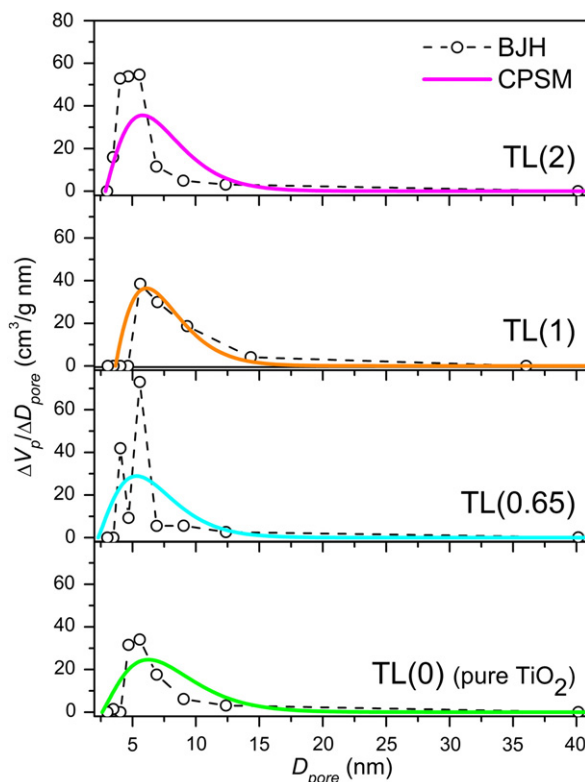
Fig. 4 – The pore size distribution for pure TiO$_2$ and some La-doped nanopowders obtained by BJH (symbols with thin dashed lines) and CPSM (thick lines) methods.

complex pore structure consisting of interconnected pore segments with different diameters in this sample.

3.5. Raman Scattering

The Raman spectra of all synthesized nanopowders are dominated by anatase Raman modes [11,23]: $E_{g(1)}$ (~143 cm^{-1}), $E_{g(2)}$ (~199 cm^{-1}), B_{1g} (~399 cm^{-1}), $A_{1g} + B_{1g}$ (~518 cm^{-1}), and $E_{g(3)}$ (~639 cm^{-1}), as can be seen from the spectrum of TiO$_2$ nanopowder doped with 0.65 mol% La shown in Fig. 5. The $E_{g(1)}$ Raman mode is shifted and broadened in all synthesized nanopowders in comparison with corresponding bulk value [10,11]. By applying the phonon confinement model [24] on those experimental results, the anatase crystallite size has been estimated as ~12 nm in samples with 1–4 mol% of La, and ~15 nm in the other doped samples, as well as pure TiO$_2$ nanopowder, which is in good accordance with XRPD results. The broadening of the experimental Raman modes, which exceed the values ascribed to the phonon confinement effect only, also suggests the presence of defects and nonstoichiometry [11,24,25].

Additional Raman features, detected in the spectra of all samples, in the range from 210 to 380 cm^{-1} (shown enlarged in Fig. 7), can be ascribed to the brookite phase: A_{1g} (~247 cm^{-1}), B_{3g} (~288 cm^{-1}), B_{1g} (~322 cm^{-1}), and B_{2g} (~366 cm^{-1}) [10,11,25]. Low intensities and large linewidths of these modes indicate great disorder and partial amorphization of brookite in all the samples [10,11,25].

Table 3 – The porous properties of TiO$_2$ samples (TL(0), TL(0.65), TL(1), and TL(2)): specific surface area (S$_{BET}$), pore volume (V$_p$), mean pore diameters obtained from different methods ($\overline{D}_{BET}$, $\overline{D}_{BJH}$, $\overline{D}_{CPSM}$), CPSM fitting parameter N$_S$ and predicted tortuosity factor τ.
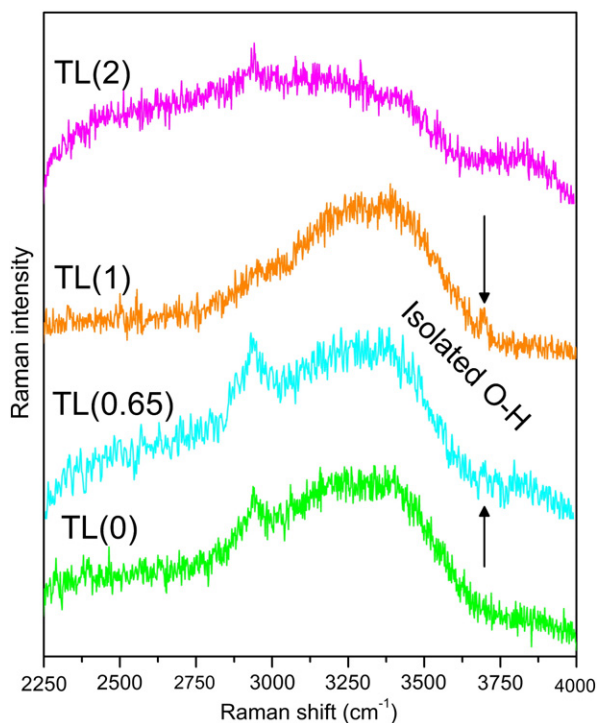
	Sample			
	TL(0)	TL(0.65)	TL(1)	TL(2)
S$_{BET}$ (m^2 g^{-1})	58	79	84	78
V$_p$ (cm^3 g^{-1})	0.160	0.185	0.258	0.215
S$_{BJH}$ (m^2 g^{-1})	58.2	79.4	83.8	78.1
$\overline{D}_{BET}$ (nm)	7.1	6.0	7.9	7.1
$\overline{D}_{BJH}$ (nm)	7.1	6.3	7.7	7.5
$\overline{D}_{CPSM}$ (nm)	8.1	6.9	7.7	7.5
N$_S$	8	13	12	11
τ	4.1	5.3	4.4	4.6
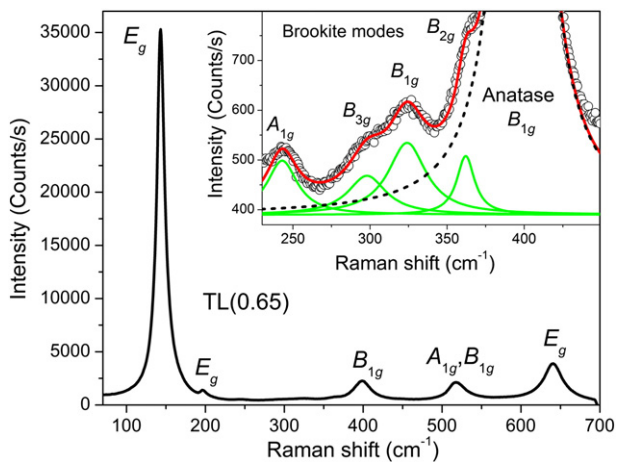
Fig. 5 – The Raman spectrum of doped TiO_2 nanopowdered sample TL(0.65) with anatase modes denoted. Inset: the region of 230–450 cm^{-1} with characteristic brookite modes.

The Raman spectra of pure and representative La-doped TiO_2 nanopowders (TL(0.65), TL(1) and TL(2)) in the C–H and O–H spectral region (2300–4000 cm^{-1}) are shown in Fig. 6. Few broad features have been noticed in this region. According to many other vibrational studies, carried out to determine the characteristics of water molecules and hydroxyl groups adsorbed on anatase surfaces ([26] and references therein), broad Raman structure in the frequency range of 2800–3800 cm^{-1} can be assigned to O–H stretching vibration of water molecules

Fig. 6 – The Raman spectra of pure TiO_2 and selected La-doped TiO_2 nanopowders in the C–H and O–H spectral region (2300–4000 cm^{-1}). The mode ascribed to isolated OH groups in samples TL(0.65) and TL(1) is marked by the arrows. The spectra of doped samples are upshifted for clarity.

adsorbed on the surface of the particles and condensed in the pores of TiO_2 nanopowders [10,27], whereas the peak at ~ 2940 cm^{-1} can be assigned to the stretching mode characteristic for CH– species [10,28]. Moreover, a low intensity peak located at ~ 3700 cm^{-1} is noticed in the samples doped with low La content (TL(0.65) and TL(1)). This peak is assigned to the O–H stretching mode of isolated (free) hydroxyls [10,26], and can be related to the ability of the anatase samples to form the surface O–H groups with the important influence on their catalytic activity [10,29].

3.6. Spectroscopic Ellipsometry

The optical band gap energy has been estimated by means of the extinction coefficient k, obtained from SE data of pure and doped TiO_2 nanopowders, by using a so-called two phase model. In a case of large band gap semiconductors, in a small energy range in the vicinity of the optical band gap energy E_g, the absorption coefficient α is assumed to follow the well-known dependence $\alpha h\nu \approx A(h\nu - E_g)^\gamma$, where A is a sample-dependent constant parameter, γ is a constant equal to 1/2 and 2 for direct and indirect allowed transitions, respectively, and $h\nu$ is the photon energy. Then, E_g can be graphically estimated by a linear fit of the high energy tail of $(\alpha h\nu)1/\gamma$ [30]. The absorption coefficient has been evaluated from the extinction coefficient k of pure and doped anatase nanopowders, as $\alpha = 4\pi k / \lambda$, where λ is the wavelength of incident light. In the literature, both direct and indirect band to band transitions of nanocrystalline anatase titania are reported (1[30] and references therein). To establish the type of electronic transition of the synthesized samples, the absorption coefficient data were fitted to the equation for both indirect and direct band gap transitions. Fig. 7(a) shows the $(\alpha h\nu)^{1/2}$ plots versus the photon energy $h\nu$ for an indirect transition, whereas the $(\alpha h\nu)^2$ plots for a direct transition are given in Fig. 7(b). The dispersions of $(\alpha h\nu)^{1/2}$ of the samples under examination do not show an asymptotic linear behavior in the near-UV region (Fig. 7(a)). This finding confirms that, contrary to bulk anatase, synthesized TiO_2 nanoparticles do not exhibit an indirect type of band to band transition. In Fig. 7(b) the dispersions of $(\alpha h\nu)^2$ clearly show an asymptotic linear behavior in the near-UV region, and the intercepts of the linear-fit extrapolations with the horizontal axes led us to estimate the energy of the optical band gap corresponding to the direct electronic transition. The dependence of the optical band gap energy on mol% of La is presented in the inset of Fig. 7(b). The band gap values, found in the range from 3.62 to 3.82 eV, are higher than that of bulk anatase TiO_2 (3.2 eV) [30], and gradually increase with the increase of molar percent of La in titania nanopowders.

Spectroscopic ellipsometry has been also used to determine the room temperature pseudodielectric function spectra of pure and doped anatase nanopowders. The features observed in the range from 2 to 6 eV of the $\varepsilon(\omega)$ spectra are ascribed to interband critical points (CPs) [19,20,31], which are related to regions of the band structure with large or singular point electronic density of states [19]. Those structures are analyzed by standard analytic line shapes [20]: $\varepsilon(\omega) = C - A \exp(i\varphi)(\omega - E + i\gamma)^m$, where a CP is described by the amplitude A, threshold energy E, broadening γ and phase angle φ. The exponent m takes the values of $-1/2$ and $1/2$ for one- (1D) and three-dimensional (3D) CPs, respectively. Two dimensional (2D) CPs are described with $m = 0$

Fig. 7 – (a) The plot of $(\alpha E)^{1/2}$ versus E for indirect band gap transition in pure and selected La-doped TiO$_2$ nanopowders; (b) the plot of $(\alpha E)^2$ versus E for direct band gap transition in the same samples with characteristic tangent lines. Inset: the dependence of estimated direct band gap energy on mol% of La.

and corresponding analytical line shape is given by $\varepsilon(\omega) = C - A \exp(i\varphi)\ln(\omega - E + i\gamma)$. Discrete excitons with a Lorentzian line shape (0D) are represented by $m = -1$. The values of the CP energy thresholds have been determined by theoretical fitting of both the second derivative and the module of the first derivative.

The 2nd derivative spectra of the complex dielectric function, $d^2\varepsilon(\omega)/d\omega^2$, have been calculated by a standard technique of smoothing polynomials to obtain the CP parameters [19]. It is given in analytic form as follows [21]:

$$\frac{d^2\varepsilon}{d\omega^2} = A'\Omega^{(m-2)/2} \left(\begin{array}{c} \cos\left((m-2)\arccos\left(\frac{\omega-E}{\Omega^{1/2}}\right) + \varphi\right) \\ + i\sin\left((m-2)\arccos\left(\frac{\omega-E}{\Omega^{1/2}}\right) + \varphi\right) \end{array} \right), \quad (1)$$

with $\Omega = (\omega - E)^2 + \gamma^2$. Note that for $\omega \neq 0$, $A' = -m(m-1)A$, but for $m = 0$, A' must be equal to A. The parameters A, E, γ and φ have been calculated for all investigated nanopowders by fitting the numerically obtained second derivative spectra of the experimental $\varepsilon(\omega)$ to Eq. (1), considering the CPs of 2D and 3D types [31]. The 2nd derivatives of the real and imaginary parts ($\varepsilon_1(\omega)$ and $\varepsilon_2(\omega)$ respectively) of the complex dielectric function $\varepsilon(\omega)$ of pure (TL(0)) and one doped TiO$_2$ nanopowder (TL(1)), obtained from SE experimental data, are shown in Fig. 8(a). Corresponding fitting curves, taking into account the electronic transitions in the range from 2 to 6 eV, according to Eq. (1) are also shown. According to this procedure, the electronic transitions with energies at about 2.72, 3.35, 3.80, 4.20 and 4.93 eV have been registered in all samples, whereas the transition at about 5.5 eV has been noticed in doped nanopowders only. Thereby, the energies of the first three transitions listed above are gradually increasing with the molar percent of lanthanum.

The module of the first derivative of dielectric function $\varepsilon(\omega)$ for pure and several La-doped nanopowders, defined as $|d\varepsilon/d\omega|^2 = (d\varepsilon_1/d\omega)^2 + (d\varepsilon_2/d\omega)^2$, is shown in Fig. 8(b). Generally, the module of the first derivative of dielectric function shows peaks that correspond to CPs of energy transitions of the

Fig. 8 – (a) The second derivatives of the real ($\varepsilon_1(\omega)$, denoted by circles) and imaginary ($\varepsilon_2(\omega)$, triangles) parts of the dielectric functions of TiO$_2$ nanopowders TL(0) and TL(1), obtained by SE measurements, together with the fitting curves (lines); (b) the module of the first derivative of dielectric function $\varepsilon(\omega)$ of pure and several La-doped anatase nanopowders.

electronic band structure [19]. The shift of the most intensive peak from 3.79 to 3.85 eV with the increase of mol% of La, is obvious from Fig. 8(b). Similar behavior is registered for the peak at 2.72–2.78 eV, whereas the peak at ~5.4 eV has approximately the same position in all doped samples. The position and behavior of other peaks denoted in Fig. 8(b) are hard to correlate with La content systematically, mostly because of the difficulties in precise evaluation of their energies in the spectra.

3.7.   STM/STS

The AFM results, shown in Fig. 2, point to the existence of a great number of nanoparticles with rough granular surface (Fig. 2(d)) in the sample with 6 mol% of La. Since TiO₂ nanoparticles with both smooth and rough surfaces in that sample have also been distinguished by the STM, STS measurements have been used to obtain information on the surface band gap in the nanoparticles with different surface morphologies.

The tunneling spectroscopy was performed by positioning the tip over different isolated TiO₂ nanoparticles and measuring their I–V characteristics. The measurements of I–V characteristics have been always repeated several times and the signal has been finally averaged for 100 runs. The dI/dV versus V characteristics, corresponding to the characteristic density of states, have been obtained by numerical differentiation of measured I–V curves. Fig. 9(a) shows a typical dI/dV versus V characteristic of isolated TiO₂ particles with smooth surface. The STM image of such particle from the sample TL(6) is given in the inset of Fig. 9(a). From the presented STS data, the surface band gap of those particles has been estimated as ~3.2 eV, a value close to the band gap of the anatase phase [30]. However, in the same sample, for isolated TiO₂ particles covered with rough granular structure (Fig. 9(b)), the higher value of surface band gap (~4 eV) has been found.

3.8.   Photocatalysis

The influence of different amounts of La³⁺ in the La-doped TiO₂ nanopowders on photocatalytic activity was studied

Fig. 10 – Kinetics of MET (0.05 mM) photodegradation under UV irradiation in the presence of La-doped TiO₂ nanopowders with various amounts of La, pure TiO₂, and direct photolysis. When present, the catalyst loading was 1 mg ml⁻³.

through the photocatalytic degradation of MET under UV light irradiation. Kinetic curves for all investigated samples are presented in Fig. 10, together with the results obtained using pure TiO₂ and direct photolysis. On the basis of these kinetic curves, a linear dependence of ln(c/c₀) on illumination time was obtained in the first period (30 min) of heterogeneous photocatalysis for all synthesized samples suggesting that the degradation reaction of the MET is of pseudo-first kinetic order (the linear correlation coefficients varied in the range 0.994–0.999).

As can be seen in Fig. 10, the photocatalytic activity of all doped samples with La³⁺ exhibited a significant increase in the MET photodegradation efficiency compared to pure TiO₂. It can be concluded (Fig. 11) that among all tested La-doped TiO₂ nanopowder samples the highest photocatalytic efficiency was exhibited by the sample TL(0.65), as it led to an 87% elimination of MET within 60 min. However, pure TiO₂ has eliminated only 55% of MET for the same time. These results

Fig. 9 – The dI/dV versus V characteristics of isolated TiO₂ nanoparticles of TL(6) sample, with smooth (a) and rough (b) surfaces obtained by STS, followed by corresponding STM images in the insets.
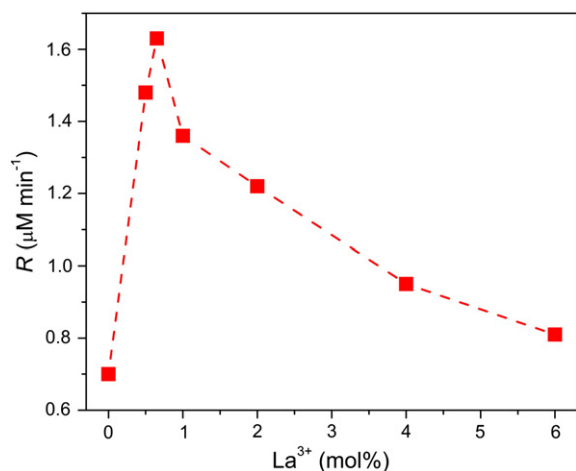
Fig. 11 – The influence of La doping content in TiO_2 nanopowders on MET (0.05 mM) photocatalytic degradation rate determined for the first 30 min of irradiation.

are in agreement with literature data [32]. Besides, as can be seen in Fig. 10, the addition of the photocatalysts, both undoped and doped with La^{3+} has markedly improved the degradation rate of MET in comparison to direct photolysis, i.e., in the absence of TiO_2.

4.   Discussion

The experimental results obtained from XRPD and Raman measurements, presented in previous paragraphs, have shown that synthesized TiO_2 nanopowders retain their anatase structure as the dominant phase, with the brookite content slightly varying with La-doping. Thereby, the anatase crystallites in doped samples are smaller than those in pure sample TL(0), with the strain slightly increasing with doping. The XRPD data confirmed the formation of crystalline La_2O_3 oxide only in the sample TL(0.65). The absence of the peaks characteristic for lanthanum oxide in XRPD data of other doped samples may indicate that this oxide is highly dispersed and/or mainly amorphized [33]. Also, retaining the position of the main diffraction peak of anatase with La-doping (within experimental error) stands in favor of the assumption that lanthanum has rather formed an oxide, than substituted titanium in the anatase lattice, due to the much greater ionic radius of La^{3+} ions (1.22 Å) than that of Ti^{4+} (0.69 Å) [3,8].

Although Raman spectroscopy has rarely been applied to study the surface complex formation of anatase nanoparticles [27], because the Raman features are hard to resolve due to intensive sample luminescence in C–H and O–H spectral region, we have demonstrated the applicability of Raman spectroscopy to identify specified surface groups. In addition to broad Raman feature between 2800 and 3800 cm^{-1}, assigned to OH stretching vibrations, and the peak at ~2940 cm^{-1} assigned to the stretching mode of CH-species, both present in the spectra of all samples, we have found a low intensity peak at ~3700 cm^{-1} in the spectra of the samples doped by low La content (TL(0.65) and TL(1)). The peak at ~3700 cm^{-1} is assigned to the O–H stretching mode of isolated (free) hydroxyls, which are, according to several

authors, the most photocatalytically active among all hydroxyl groups at the surface of TiO_2 nanoparticles [34].

The analysis of chemical composition by EDS method has shown that the ratio of Ti/O content is higher in doped samples in comparison to pure TiO_2. However, this method could not distinguish whether the excess oxygen participates in La_2O_3 or in interstitial oxygen, molecular oxygen at the surface and/or OH groups [10].

The morphological investigation of synthesized nanopowders, performed by nitrogen sorption isotherm measurements, has shown that doped samples are also fully mesoporous, and that La-doping increases the specific surface area to about 30%. Also, the total pore volume and pore structure complexity are increased in doped samples, which could be explained by the presence of La_2O_3 accumulated on the surface of TiO_2 nanoparticles, which inhibit the agglomeration of TiO_2 particles and produce more complex pores [35].

The analysis of SE data has shown that, contrary to bulk anatase, synthesized TiO_2 nanoparticles do not exhibit an indirect type of band to band transition, which confirms the findings of many authors, that TiO_2 nanoparticles with small crystalline domain exhibit a direct type of band to band transition [30]. These results have also shown that the energy of direct band gap transitions gradually increases with La-doping. The literature data have shown that the optical gap increases significantly with the increasing of La_2O_3 concentration in TiO_2 [8], whereas incorporation of La^{3+} in TiO_2 lattice usually leads to the slight shift of absorption edges of La-doped TiO_2 towards a longer wavelength (red shift) in comparison to pure TiO_2 [36]. So, the gradual increase of band gap registered in our doped samples can be related to increasing concentration of La_2O_3. Namely, when anatase TiO_2 is mixed with a larger band gap La_2O_3 (~5.5 eV [37]), the band gap of the composite semiconductor TiO_2/La_2O_3 should be shifted to a higher energy in comparison with pure TiO_2. Such conclusion is also supported by the results of the CP method. Namely, the electronic transition registered at ~5.4 eV has approximately the same energy for all doped samples, which implies that this transition may be related to the band gap of La_2O_3.

The STS data, recorded simultaneously with the STM topography, have provided direct experimental evidence for the modification of surface electronic properties by La-doping. The more prominent presence of granular structure at the surface of TiO_2 nanoparticles in the samples doped with a higher amount of La (6 mol%), as well as a higher value of surface band gap (~4 eV) in those particles, than in particles with smooth surface (~3.2 eV), most probably implies that the granular structure consisted of La_2O_3.

All these findings point out that, under specified sol–gel synthesis conditions, the La^{3+} ions rather form La_2O_3 oxide, mainly present in the surface layer of the doped TiO_2 nanopowders, than incorporate in the anatase lattice.

The investigations presented in this work have shown that La-doping does improve the photocatalytic activity of TiO_2 nanopowders, with higher efficiency obtained for lower La content. The kinetic analysis discussed here showed that an optimal La amount, with respect to the efficiency in photocatalytic degradation of MET, is 0.65 mol%, which is similar to the literature data obtained for the degradation of some other organic compounds ([38] and references therein). The improvement in

photocatalytic properties of La-doped samples can be ascribed to the formation of La_2O_3 at the grain boundaries of anatase nanoparticles. This effect inhibits the growth of crystal grains, decreases anatase crystallite size and produces a more complex pore structure [35], which is confirmed by the results of XRPD, Raman and BET measurements presented in this work. However, the presence of isolated hydroxyl groups on the surface of TiO_2 nanoparticles, which can represent a decisive factor in high photocatalytic activity of TiO_2 [39], has been registered only in the nanopowders with a low level of La-doping—0.65 and 1 mol%. This implies that reduction of photocatalytic activity of TiO_2 nanopowders with further increase of La-doping amount may be related to the blocking of the active centers due to the accumulation of excess La_2O_3 on the surface of anatase grains, registered by both AFM and STM measurements.

5. Conclusion

Mesoporous La-doped TiO_2 photocatalysts, prepared by sol–gel method, have been extensively characterized by various sophisticated techniques. The photocatalytic activity of La-doped TiO_2 nanopowders has been evaluated for the degradation of MET in an aqueous solution under UV light irradiation. Doped samples have shown a higher rate of degradation than pure TiO_2, synthesized under the same condition, with a maximum rate for 0.65 mol% La loading. The enhanced photocatalytic activity of La-doped TiO_2 is mainly due to the smaller particle size, larger specific surface area and total pore volume, as well as higher pore structure complexity. Moreover, the presence of isolated (free) hydroxyls, as the most photocatalytically active hydroxyl groups, has been registered in the TiO_2 photocatalysts with low La content, which exhibit the highest photocatalytic efficiency.

This study has also shown that the spectroscopic ellipsometry is able to determine the type of electronic transition in TiO_2 materials, as well as to resolve the dilemma of whether or not large La^{3+} ions replace smaller Ti^{4+} ions in the TiO_2 lattice. Presented analysis of SE results has shown gradual increase of direct band gap energy with La-doping, which can be attributed to the surface modification of TiO_2 nanoparticles, confirmed by the STM/STS measurements.

Acknowledgments

REFERENCES

[1] Chen W, Hua D, Jun-Ying T, Ji-Mei A. Photocatalytic activity enhancing for TiO_2 photocatalyst by doping with La. Trans Nonferrous Met Soc China 2006;16:s728–31.

[2] Kim HR, Lee TG, Shul YG. Photoluminescence of La/Ti mixed oxide prepared using sol–gel process and their pCBA photodecomposition. J Photochem Photobiol A 2007;185:156–60.

[3] Liqiang J, Xiaojun S, Baifu X, Baiqi W, Weimin C, Honggang F. The preparation and characterization of La doped TiO_2 nanoparticles and their photocatalytic activity. J Solid State Chem 2004;177:3375–82.

[4] Jin M, Nagaoka Y, Nishi K, Ogawa K, Nagahata S, Horikawa T, et al. Adsorption properties and photocatalytic activity of TiO_2 and La-doped TiO_2. Adsorption 2008;14:257–63.

[5] Zhao Z, Liu Q. Effects of lanthanide doping on electronic structures and optical properties of anatase TiO_2 from density functional theory calculations. J Phys D Appl Phys 2008;41:085417 [1–9].

[6] Sun L, Zhao X, Cheng X, Sun H, Li Y, Li P, et al. Synergistic effects in La/N codoped TiO_2 anatase (101) surface correlated with enhanced visible-light photocatalytic activity. Langmuir 2012;28:5882–91.

[7] Bingham S, Daoud WA. Recent advances in making nano-sized TiO_2 visible-light active through rare-earth metal doping. J Mater Chem 2011;21:2041–50.

[8] Zhang L, Sun Z-H, Yu F-M, Chen H-B. Bioinorganic chemistry and applications. Hindawi Publishing Corporation; 2001. http://dx.doi.org/10.1155/2011/853048.

[9] Golubović A, Šćepanović M, Kremenović A, Askrabić S, Berec V, Dohčević-Mitrović Z, et al. Raman study of the variation in anatase structure of TiO_2 nanopowders due to the changes of sol–gel synthesis conditions. J Sol Gel Sci Technol 2009;49:311–9.

[10] Šćepanović M, Abramović B, Golubović A, Kler S, Grujić-Brojčin M, Dohčević-Mitrović ZD, et al. Photocatalytic degradation of metoprolol in water suspension of TiO_2 nanopowders prepared using sol–gel route. J Sol–Gel Sci Technol 2012;61:390–402.

[11] Golubović A, Abramović B, Šćepanović M, Grujić-Brojčin M, Armaković S, Veljković I, et al. Improved efficiency of sol–gel synthesized mesoporous anatase nanopowders in photocatalytic degradation of metoprolol. Mater Res Bull 2012;48:1363–71.

[12] Salmas CE, Androutsopoulos GP. A novel pore structure tortuosity concept based on nitrogen sorption hysteresis data. Ind Eng Chem Res 2001;40:721–30.

[13] Zalc JM, Reyes SC, Iglesia E. The effects of diffusion mechanism and void structure on transport rates and tortuosity factors in complex porous structures. Chem Eng Sci 2004;59:2947–60.

[14] Šojić D, Despotović V, Orčić D, Szabó E, Arany E, Armaković S, et al. Degradation of thiamethoxam and metoprolol by UV, O_3 and UV/O_3 hybrid processes: kinetics, degradation intermediates and toxicity. J Hydrol 2012;472–473:314–27.

[15] Ikehata K, Naghashkar NJ, El-Din MG. Degradation of aqueous pharmaceuticals by ozonation and advanced oxidation processes: a review. Ozone Sci Eng 2006;28:353–414.

[16] Rodriguez-Carvajal J. FullProf computer program. http://www.ill.eu/sites/fullprof/index.html; 2008.

[17] Kaneko K, Ishii C, Kanoh H, Hanzawa Y, Setoyama N, Suzuki T. Characterization of porous carbons with high resolution α_s-analysis and low temperature magnetic susceptibility. Adv Coloid Interface Sci 1998;76–77:295–320.

[18] Barrett EP, Joyner LG, Halenda PP. The determination of pore volume and area distributions in porous substances. I. Computations from nitrogen isotherms. J Am Chem Soc 1951;73:373–80.

[19] Leòn M, Levcenko S, Nateprov A, Nicorici A, Merino JM, Serna R, et al. Dielectric functions and fundamental band gaps of $Cu_2In_4Se_7$, $CuGa_3Se_5$ and $CuGa_5Se_8$ crystals. J Phys D Appl Phys 2007;40:740–8.

[20] Lautenschlager P, Garriga M, Logothetidis S, Cardona M. Interband critical points of GaAs and their temperature dependence. Phys Rev B 1987;35:9174–89.

[21] Albornoz JG, Serna R, Leon M. Optical properties and electronic structure of polycrystalline $Ag_{1-x}Cu_xInSe_2$ alloys. J Appl Phys 2005;97:103515 [1–7].

[22] Androutsopoulos GP, Salmas CE. A new model for capillary condensation–evaporation hysteresis based on a random corrugated pore structure concept: prediction of intrinsic pore size distributions: part 1: model development. Ind Eng Chem Res 2000;39:3747–63.

[23] Ohsaka T, Izumi F, Fujiki Y. Raman spectrum of anatase, TiO_2. J Raman Spectrosc 1978;7:321–4.

[24] Šćepanović MJ, Grujić-Brojčin MU, Dohčević-Mitrović ZD, Popović ZV. Effects of confinement, strain and nonstoichiometry on Raman spectra of anatase TiO_2 nanopowders. Mater Sci Forum 2006;518:101–6.

[25] Šćepanović M, Aškrabić S, Berec V, Golubović A, Dohčević-Mitrović Z, Kremenović A, et al. Characterization of La-doped TiO_2 nanopowders by Raman spectroscopy. Acta Phys Pol A 2009;115:771–4.

[26] Soria J, Sanz J, Sobrados I, Coronado JM, Maira AJ, Hernandez-Alonso MD, et al. FTIR and NMR study of the adsorbed water on nanocrystalline anatase. J Phys Chem C 2007;111:10590–6.

[27] Watson S, Beydoun D, Scott J, Amal R. Preparation of nanosized crystalline TiO_2 particles at low temperature for photocatalysis. J Nanopart Res 2004;6:193–207.

[28] Brownson JRS, Tejedor-Tejedor MI, Anderson MA. Photoreactive anatase consolidation characterized by FTIR spectroscopy. Chem Mater 2005;17:6304–10.

[29] Yang D, Liu H, Zheng Z, Yuan Y, Zhao J, Waclawik ER, et al. An efficient photocatalyst structure: TiO_2(B) nanofibers with a shell of anatase nanocrystals. J Am Chem Soc 2009;131:17885–93.

[30] Ferrara MC, Pilloni L, Mazzarelli S, Tapfer L. Hydrophilic and optical properties of nanostructured titania prepared by sol–gel dip coating. J Phys D Appl Phys 2010;43:095301.

[31] Šćepanović M, Grujič-Brojčin M, Mirić M, Dohčević-Mitrović Z, Popović ZV. Optical characterization of laser-synthesized anatase TiO_2 nanopowders by spectroscopic ellipsometry and photoluminescence measurements. Acta Phys Pol A 2009;116:603–6.

[32] Wu H-H, Deng L-X, Wang S-R, Zhu B-L, Huang W-P, Wu S-H, et al. The preparation and characterization of La doped TiO_2 nanotubes and their photocatalytic activity. J Dispersion Sci Technol 2010;31:1311–6.

[33] Shi Z-L, Lai H, Yao S-H, Wang S-F. Preparation, characterization and photocatalytic activity of lanthanum doped mesoporous titanium dioxide. Chin J Chem Phys 2012;25:96–102.

[34] Bégin-Colin S, Gadalla A, Le Caer G, Humbert O, Thomas F, Barres O, et al. On the origin of the decay of the photocatalytic activity of TiO_2 powders ground at high energy. J Phys Chem C 2009;113:16589–602.

[35] Cao G, Li Y, Zhang Q, Wang H. Synthesis and characterization of $La_2O_3/TiO_{2-x}F_x$ and the visible light photocatalytic oxidation of 4-chlorophenol. J Hazard Mater 2010;178:440–9.

[36] Parida KM, Sahu N. Visible light induced photocatalytic activity of rare earth titania nanocomposites. J Mol Catal A Chem 2008;287:151–8.

[37] Yang C, Fan H, Qiu S, Xi Y, Fu Y. Microstructure and dielectric properties of La_2O_3 films prepared by ion beam assistant electron-beam evaporation. J Non-Cryst Solids 2009;355:33–7.

[38] Zhang S, Zheng Z, Wang J, Chen J. Heterogeneous photocatalytic decomposition of benzene on lanthanum-doped TiO_2 film at ambient temperature. Chemosphere 2006;65:2282–8.

[39] Liu G, Sun C, Cheng L, Jin Y, Lu H, Wang L, et al. Efficient promotion of anatase TiO_2 photocatalysis via bifunctional surface-terminating Ti–O–B–N structures. J Phys Chem C 2009;113:12317–24.

Synthesis of pure and La-doped anatase nanopowders by sol–gel and hydrothermal methods and their efficiency in photocatalytic degradation of alprazolam

A. Golubović[a], N. Tomić[a], N. Finčur[b], B. Abramović[b], I. Veljković[c], J. Zdravković[d], M. Grujić-Brojčin[a,*], B. Babić[e], B. Stojadinović[a], M. Šćepanović[a]

[a]Center for Solid State Physics and New Materials, Institute of Physics, University of Belgrade, Pregrevica 118, 11080 Belgrade-Zemun, Serbia
[b]Department of Chemistry, Biochemistry and Environmental Protection, Faculty of Sciences, University of Novi Sad, Trg D. Obradovića 3, 21000 Novi Sad, Serbia
[c]Institute for Multidisciplinary Research, University of Belgrade, Kneza Višeslava 1, 11000 Belgrade, Serbia
[d]Innovation Center, Faculty of Technology and Metallurgy, University of Belgrade, Karnegijeva 4, 11000 Belgrade, Serbia
[e]Institute of Nuclear Sciences "Vinča", University of Belgrade, 11001 Belgrade, Serbia

Abstract

Pure and La^{3+} doped titanium dioxide (TiO_2) nanopowders were obtained by sol–gel and hydrothermal methods. A precursor was titanium tetrachloride and concentrations of dopants were 0.5 and 1.0 mol%. Procedures of both methods were the same, up to the last part of synthesis (the transformation from the mother liquor to oxide nanopowders), in order to find the influence of applied methods on the properties of nanopowders. XRD results have shown that all synthesized nanopowders were in the anatase phase. It was seen from DSC measurements that anatase to rutile phase transition took place at a higher temperature with a higher concentration of dopant (La^{3+}). The samples obtained by the sol–gel method had a higher temperature of phase transition than related samples obtained by the hydrothermal method. Nanopowder properties have been related to the photocatalytic activity, tested in degradation of the pharmaceutical alprazolam.
© 2014 Elsevier Ltd and Techna Group S.r.l. All rights reserved.

Keywords: A. Powders: chemical preparation; B. Porosity; C. Optical properties; D. TiO_2

1. Introduction

Advanced Oxidation Processes (AOPs) have been developed to remove the contaminants of drinking water and industrial effluents [1,2]. Among them, heterogeneous photocatalysis using TiO_2 is regarded as a promising method for the purification and treatment of both contaminated air and water [3,4] due to its performance such as low cost, non-toxicity, chemical stability, availability and the strong oxidizing power of its photogenerated holes. The size of the titanium dioxide particles is an important factor affecting the photocatalytic

activity of this catalyst [5,6]. Therefore, it is not surprising that much research has been focused upon the reduction of the particle size. Nano-semiconductor materials doped with rare-earth elements have the ability of strong adsorption, good thermal stabilization, electron-type conductivity and high photocatalytic activity [7–9].

TiO_2 can be produced by many different methods and among them we are particularly interested for "wet" methods where the most representative are sol–gel and hydrothermal methods. Because of that, in this work pure and La-doped TiO_2 nanoparticles were prepared by sol–gel and hydrothermal methods. The content of La^{3+} in our investigation was 0.5 and 1 mol%, as these concentrations have been established as the most appropriate in photocatalytic applications [9,10].

*Corresponding author. Tel.: +38 1113713023; fax: +38 1113160531.
E-mail address: myramyra@ipb.ac.rs (M. Grujić-Brojčin).

In recent years, pharmaceuticals have been present in the aquatic environment as a consequence of their use in very high quantities throughout the world. Pharmaceuticals are large group of organic compounds which can enter the water system by means of direct disposal and excretion. They may be present in surface water at low concentration levels, depending on the efficiency of wastewater treatments. Despite these low concentrations, the ubiquity of pharmaceuticals in the aquatic environment together, with their persistent biological activities explains the concern over this specific group of water contaminants [11–13]. Until now, a large diversity of pharmaceuticals has been found in the environment: analgesics, antibiotics, antiepileptics, β-blockers, blood–lipid regulators, antidepressants, anxiolytics, sedatives, contraceptives, etc. [14].

Alprazolam (8-chloro-1-methyl-6-phenyl-4H-[1,2,4]triazole[4,3,-α]-[1,4]-benzodiazepine, CAS no. 28981-97-7, $C_{17}H_{13}ClN_4$, $M_r=308.765$) is a short-acting anxiolytic, which belongs to the benzodiazepine class of psychoactive drugs. It has unique clinical and neurochemical spectrum of action among benzodiazepine full agonists [15,16]. Alprazolam acts on the brain and central nervous system to produce a calming effect [17] and it is mainly used to treat anxiety disorders or anxiety associated to symptoms of depression [18]. The extensive use of alprazolam is a consequence of its antidepressant effect, its synergic action as an anxiolytic in combination with antidepressants in patients with advanced cancer, in the treatment of pathologies that imply anxiety disorders of chronic intensity as the social phobia and other psychosocial pathologies [16].

Since pharmaceuticals are being introduced into the environment on a continuous basis and its continuous input and persistence to the water system may result in a potential risk for aquatic and terrestrial organisms, special attention has recently been paid to the degradation of pharmaceuticals as a means of water decontamination. The aim of this work is to estimate the efficiency of pure and La^{3+} doped anatase nanopowders, synthesized by two different routes, in photocatalytic degradation of alprazolam, as well as to investigate the variations in anatase structure with La^{3+} doping.

2. Experimental details

2.1. Synthesis

All chemicals are used without further purifications.

2.2. Sol–gel method (SG)

$TiCl_4$ (99.0%, pure, Merck) was used as a precursor. An appropriate amount of $TiCl_4$ was dissolved in distilled water under vigorous stirring on an ice-bath. To obtain the hydrogel the aqueous solution of NH_4OH (29% Carlo Erba), was added under careful control of the pH value of the solution to achieve the alkaline conditions (pH~9). After aging in mother liquor for 5 h the hydrogel was filtered and washed out with distilled water until the complete removal of chloride ions (the common analytical procedure with $AgNO_3$). Afterwards the obtained hydrogel was converted to its ethanol–gel by anhydrous ethanol. Alcogel was placed in a vessel, dried at 280 °C and calcined at a temperature of 550 °C for 4 h.

2.3. Hydrothermal method (HT)

The whole procedure was the same as the sol–gel process until the hydrogel was obtained (including the aging in mother liquor for 5 h). Then hydrogel was placed in a steel pressure vessel (autoclave) under a controlled temperature. The reaction of hydrothermal synthesis was carried out at 200 °C for 24 h. After that, the vessel contains were filtered and washed with distilled water until complete removal of chloride ions. The last step to obtain TiO_2 nanoparticles was drying at 105.5 °C for 72 h.

2.4. Characterization methods

Samples of pure and La^{3+}-doped TiO_2 obtained by both methods were analyzed by XRD using a Stoe Stadi MP diffractometer (CuKα₁ radiation, primary beam Ge monochromator, linear PSD detector, Bragg–Brentano geometry). Data were collected at every 0.01° in the 10–90° 2θ angular range, using a counting time of 80 s/step. The Fullprof computer program was used. The Williamson–Hall Method [19] was applied for determination of the average microstrain and the mean crystallite sizes.

Composition/quality of TiO_2 has been analyzed on SEM (JEOL JSM-6460LV, with the operating voltage of 20 keV) equipped with an EDS (INCAx-sight) detector and "INAx-stream" pulse processor (Oxford Instruments).

Non-contact atomic force microscopy (NC-AFM) measurements were carried out using Omicron B002645 SPM probe VT AFM 25.

The TG/DSC analysis of samples consisted in pure and La-doped TiO_2 (anatase) synthesized by sol–gel method and hydrothermal method was carried out on an SDT Q600 instrument (TA Instruments) up to 1100 °C in N_2 atmosphere (flow rate: 100 $cm^3 min^{-1}$; heating rate: 10 °C min^{-1}). The pure indium and sapphire were used for the calibration of temperature and DSC signal, respectively.

The porous structure of anatase samples has been evaluated from adsorption/desorption isotherms of N_2 measured on TiO_2 samples, at −196 °C, using the gravimetric McBain method. The main parameters of the porosity such as specific surface area and pore volume have been estimated by the Brunauer–Emmett–Teller (BET) method and $α_s$-plot [20]. The pore size distribution has been estimated from hysteresis sorption data by the Barret–Joyner–Halenda (BJH) method [21].

Raman scattering measurements of TiO_2 samples was performed in the backscattering geometry at room temperature in the air using a Jobin-Yvon T64000 triple spectrometer, equipped with a confocal microscope and a nitrogen-cooled charge coupled device detector. The spectra were excited by 514.5 nm line of Ar^+/Kr^+ ion laser with output power less than 5 mW to avoid local heating due to laser irradiation.

2.5. Measurements of photocatalytic activity

The photocatalytic activity of the nanopowders was evaluated in the process of the degradation of the solution of alprazolam (Sigma-Aldrich). The photocatalytic degradation was carried out in a cell described previously [22]. A 125 W high-pressure mercury lamp (Philips, HPL-N, emission bands in the UV region at 304, 314, 335 and 366 nm, with maximum emission at 366 nm), together with an appropriate concave mirror, was used as the radiation source. Experiments were carried out using 20 cm^3 of 0.03 mmol dm^{-3} of alprazolam solution and the photocatalyst loading was 1.0 mg cm^{-3}. The aqueous suspension was sonicated (50 Hz) in the dark for 15 min before illumination, to uniformly disperse the photocatalyst particles and attain adsorption equilibrium. The suspension thus obtained was thermostated at 25 ± 0.5 °C in a stream of O$_2$ (3.0 cm^3 min^{-1}), and then irradiated. During irradiation, the mixture was stirred at a constant rate under continuous O$_2$ flow. In order to determine the reproducibility of the results, at least duplicated runs were carried out for each condition for averaging the results, and the reproducibility of kinetic measurements was 3–10%.

For the UFLC–DAD kinetic studies of alprazolam photodegradation, aliquots of 0.50 cm^3 were taken from the reaction mixture at the beginning of the experiment and at regular time intervals. Aliquot sampling caused a maximum volume variation of ca. 10% in the reaction mixture. The suspensions containing photocatalyst were filtered through a Millipore (Milex-GV, 0.22 μm) membrane filter. After that, a 10-μl sample was injected and analyzed on UFLC-Shimadzu equipped with an Eclypse XDB-C18 column (150 mm × 4.6 mm i.d., particle size 5 μm, 25 °C). The UV/vis DAD

detector was set at 222 nm (wavelength of alprazolam maximum absorption). The mobile phase (flow rate 1 cm^3 min^{-1}) was a mixture of acetonitrile (99.8%, J. T. Baker) and water (40:60, v/v), the water being acidified with 0.1% H$_3$PO$_4$ (85%, Sigma-Aldrich).

3. Results and discussion

3.1. Synthesis

In the sol–gel synthesis experimental parameters were the same as in our previous experiments [23] except the duration of calcination of 4 h. It was found that using the duration of 4 h to synthesize TiO$_2$ nanoparticles (anatase phase) have the best photocatalytic properties in photodegradation of metoprolol [22] within samples with various durations of calcination (from 1 to 7 h) and our samples have mentioned set-up of experimental parameters.

In the hydrothermal synthesis experimental parameters were temperature of 200 °C (as in [24,25], although Ti-butoxide was the precursor, and the duration was 24 h (as in [26]). The charge from the vessel in autoclave was the same as in the case of sol–gel synthesis before the processes of drying and calcination due to reveal a influence of type of synthesis on a properties of obtained TiO$_2$ nanoparticles.

3.2. X-ray diffraction

The XRD patterns of pure TiO$_2$ and doped with La^{3+} doped nanopowders, synthesized by sol–gel and hydrothermal
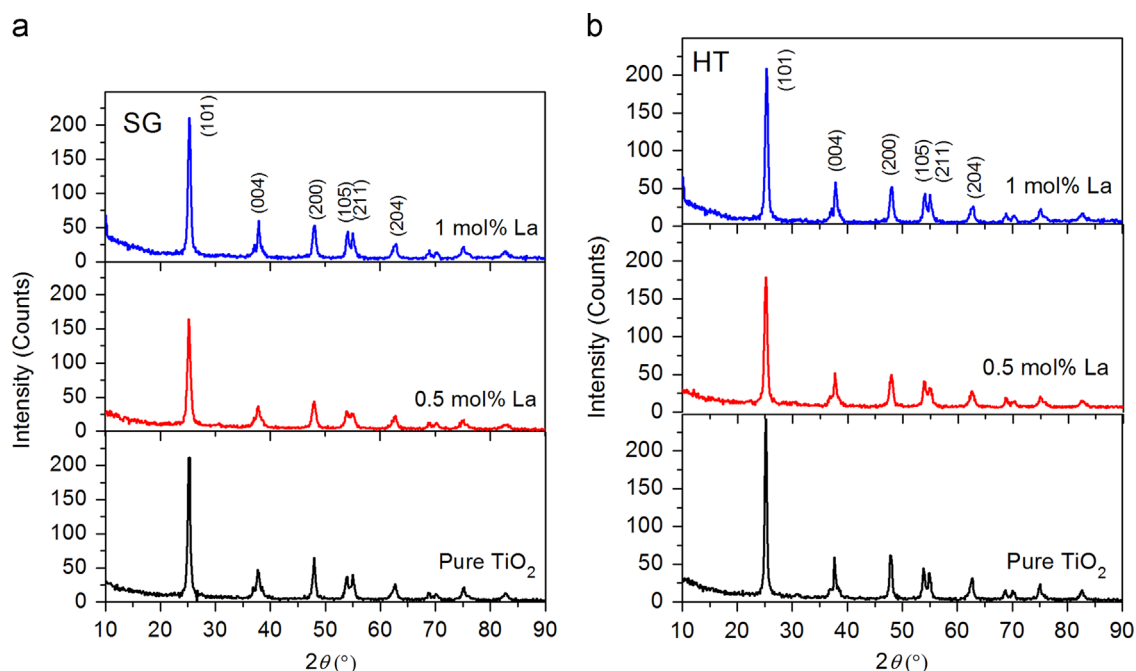
Fig. 1. XRD patterns of pure TiO$_2$ and La-doped TiO$_2$ nanopowders synthesized by sol–gel (a) and hydrothermal (b) methods. Characteristic diffractions of anatase phase given in parentheses.

Table 1
Crystallite size, lattice parameters, and average strain of pure and La^{3+} doped TiO$_2$ (anatase) obtained by sol–gel and hydrothermal methods.

	Crystallite size (nm)	Lattice parameters (nm)		Strain (%)
		a (=b)	c	
SG				
Pure TiO$_2$	16	0.3788 (6)	0.9526 (4)	0.12
0.5 mol% La	15	0.3795 (7)	0.9518 (9)	0.29
1 mol% La	15	0.3786 (5)	0.9462 (1)	0.86
HT				
Pure TiO$_2$	19	0.3796 (8)	0.9530 (0)	0.13
0.5 mol% La	17	0.3794 (4)	0.9536 (2)	0.24
1 mol% La	18	0.3791 (6)	0.9501 (6)	0.08

Fig. 2. DSC curves of pure and La-doped TiO$_2$ synthesized using sol–gel (a) and hydrothermal (b) methods.

method are presented in Fig. 1. The diffraction peaks present in all samples coincide to the anatase TiO$_2$ structure (JCPDS card 21-1272, space group I41/amd), which is clearly indicated by the main anatase reflection at $2\theta \sim 25°$. Their positions are slightly shifted, indicating a change in lattice parameters in comparison to the bulk values for anatase ($a_0=0.37852$ nm, $c_0=0.95139$ nm), as shown in Table 1.

The average crystallite size of anatase nanoparticles, estimated by the Williamson–Hall method, is slightly greater in samples obtained by the hydrothermal method than those obtained by the sol–gel method, as listed in Table 1. The crystallite size in the range from 15 to 19 nm has been estimated from all diffraction patterns. Significant difference in microstrain has not been found in pure TiO$_2$ samples synthesized by both methods. Similarly, for both samples doped with 0.5% La^{3+}, corresponding values of microstrain were close, whereas much smaller microstrain (0.08%) has been detected in the sample doped with 1% La^{3+} obtained by the hydrothermal method in comparison to the sample synthesized by the sol–gel method (0.86%).

3.3. TG/DSC analysis

The TG analysis of pure, 0.5 mol% La^{3+} doped TiO$_2$ and 1 mol% La^{3+} doped TiO$_2$ nanopowders, obtained by SG and HT method has been performed. After heating the sample, from the room temperature up to 1100 °C, the total mass loss for both pure TiO$_2$ was 3.5%, while for the 0.5 mol% La doped TiO$_2$ and 1 mol% La doped TiO$_2$ synthesized either using SG or HT method total weight loss was around 5%. Unlike pure TiO$_2$, the doped samples have a slightly larger mass loss. It could be found that there are two main stages for all samples, where the first step occurs from room temperature up to 200 °C for pure TiO$_2$ and for doped samples up to 180 °C. For this step the rate of mass loss is around 2.5% and it could be ascribed to the release of some adsorbed water. The second step occurs up to 450 °C and it ranges from 1% for pure up to 1.3% for all doped samples and it could mainly resulted from the combustion decomposition of some organic matters.
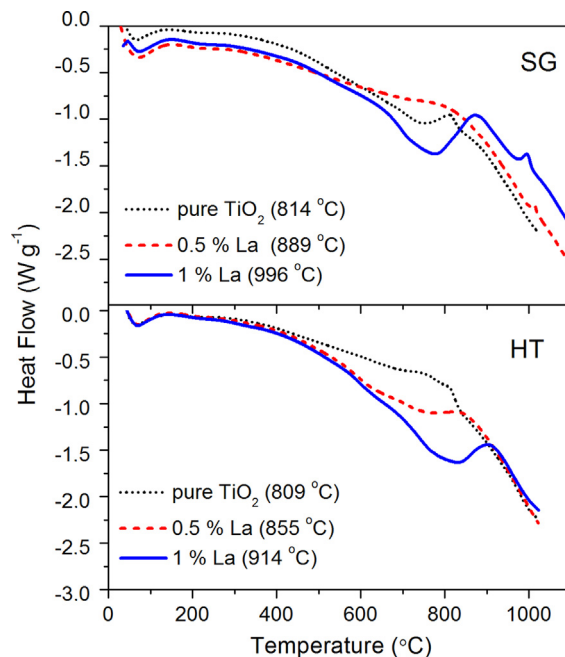
In Fig. 2 DSC curves containing two broad exothermic peaks in general are presented. According to these curves, a wide peak at about 100 °C could be found, corresponding to the earlier mentioned desorption of water, as well as one highly overlapped releasing thermal peak with maxima around 350 °C, corresponding to the combustion decomposition of the organic matters. The interval from $\sim$800 °C to 1000 °C has exhibited an obvious decalescence phenomena, possibly resulting from the phase transition from anatase to rutile [27]. Independently, in samples obtained both by SG or HT methods, the increasing of temperature of anatase to rutile the phase transition with increased La^{3+} concentration has been observed.

It can be concluded from the DSC curves of pure (undoped) TiO$_2$ nanopowders that the temperature of anatase to rutile phase transitions in these samples are almost the same, regardless of the process of synthesis. Also, the DSC peaks maxima are shifted towards higher temperatures with increasing concentration of La^{3+} in the samples synthesized by both methods. Samples obtained by the SG treatment (Fig. 3a) show higher increasing of temperature of anatase to rutile phase transition with increasing La^{3+} concentration, than samples obtained by the HT treatment (Fig. 3b). This phenomenon is directly related to the conditions of synthesis and the stoichiometric composition of the product, due to ability of La dopant to greatly inhibit anatase to rutile phase transition [28]. Generally, the temperature of the phase transition can be varied as a function of the preparation condition of the hydroxide gel (in our case, mother liquor). Namely, it has been found by studying XRD data of TiO$_2$ obtained by the sol–gel method that several weak peaks from the rutile phase appear in the sample calcined at 600 °C [29].
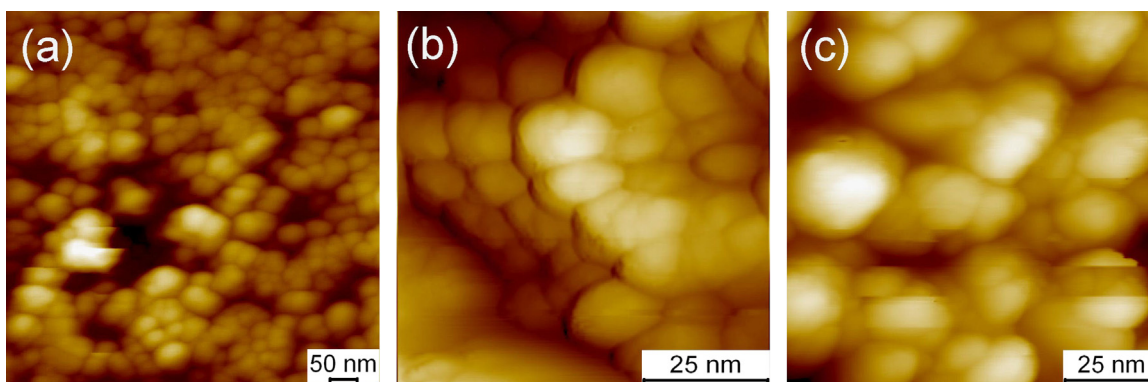
Fig. 3. The AFM images of (a) pure and (b) 0.5 wt% La doped TiO_2 synthesized by SG method, and (b) HT-synthesized TiO_2, nanopowder doped with 0.5 wt% La.

Table 2
EDS results for some TiO_2 nanopowders synthesized by SG and HT methods.

TiO_2 sample	O (wt%)	Ti (wt%)	La (wt%)	Total (wt%)
Sol–gel method				
Pure	43.28	56.72	0.00	100.00
0.5% La	47.99	52.01	0.00	100.00
1% La	43.56	55.97	0.47	100.00
Hydrothermal method				
Pure	43.16	56.84	0.00	100.00
0.5% La	43.02	56.98	0.00	100.00
1% La	43.03	56.17	0.80	100.00
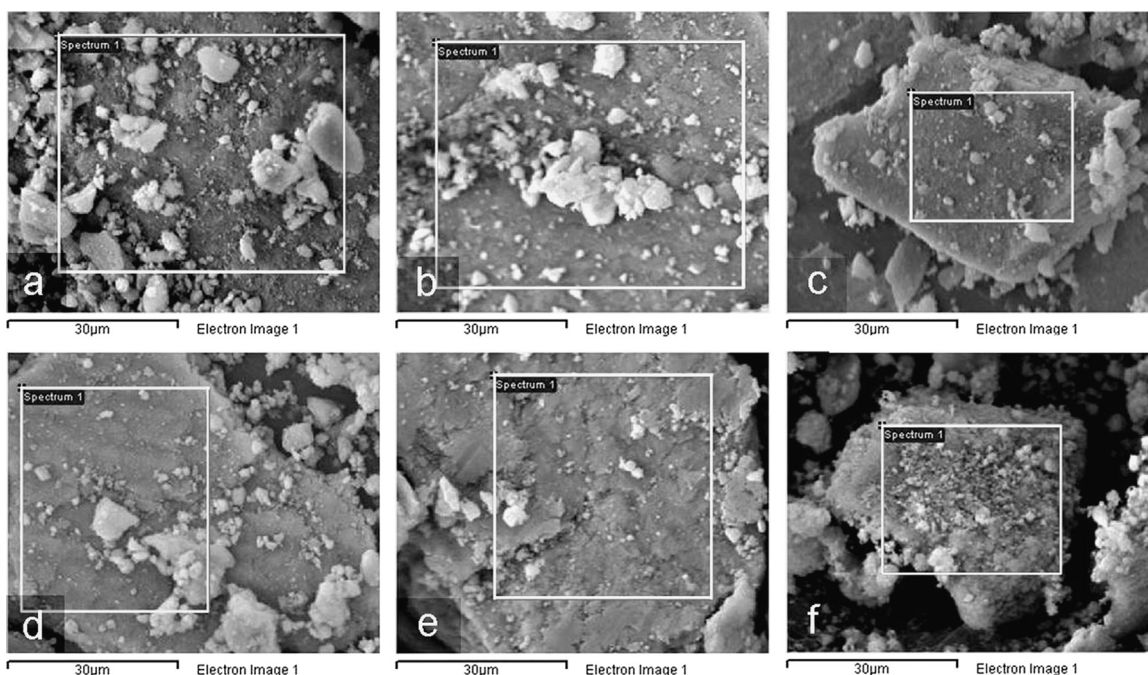
Fig. 4. The SEM images corresponding to EDS results of (a) pure, (b) 0.5 wt La doped and (c) 1 wt% La doped SG synthesized TiO_2 nanopowders; (d) pure, (e) 0.5 wt La doped and (f) 1 wt% La doped HT synthesized TiO_2 nanopowders.

3.4. Atomic force microscopy

The NC-AFM images of pure and 0.5 mol% La-doped TiO_2 samples synthesized by SG method are shown in Figs. 3(a)

and (b), respectively. In Fig. 3(c) the image of 0.5 mol% La-doped TiO_2 nanopowder synthesized by the HT method is presented. It can be observed from these images that samples consist of small, spherical nanoparticles ($\sim$15–20 nm), as well

as greater agglomerated particles, with slightly smaller particles in the SG synthesized doped sample. These results are in good agreement with size estimation obtained by XRD analysis (Table 1).

3.5. SEM-EDS

The chemical composition of pure and La-doped nanopowders synthesized by SG and HT methods has been estimated by the EDS method (Table 2). The micrographs of all synthesized samples are shown in Fig. 4, whereas the EDS spectra, collected from corresponding framed areas, are presented in Fig. 5. The oxygen weight percent is similar in SG and HT synthesized nanopowders ($\sim$43 wt%), and above the value in stoichiometric TiO$_2$ (40 wt%). The La content has been detected in the samples doped with 1 wt% of La: 0.47 wt%

in the SG synthesized sample, and 0.80 wt% in the HT synthesized sample. In the samples doped with 0.5 wt% of La, synthesized by both methods, the content of La could not be detected.

3.6. BET

In order to study the effects of synthesis method and La-doping on the pore structure and adsorption abilities of TiO$_2$ nanopowders, BET nitrogen sorption measurements have been carried out. The parameters of porosity, determined from the α_s-plots [20] obtained from the standard nitrogen adsorption isotherms have shown that the samples are fully mesoporous. In Fig. 6 the pore size distributions for pure and La-doped TiO$_2$ nanopowders synthesized by sol–gel and hydrothermal methods, obtained by the BJH model
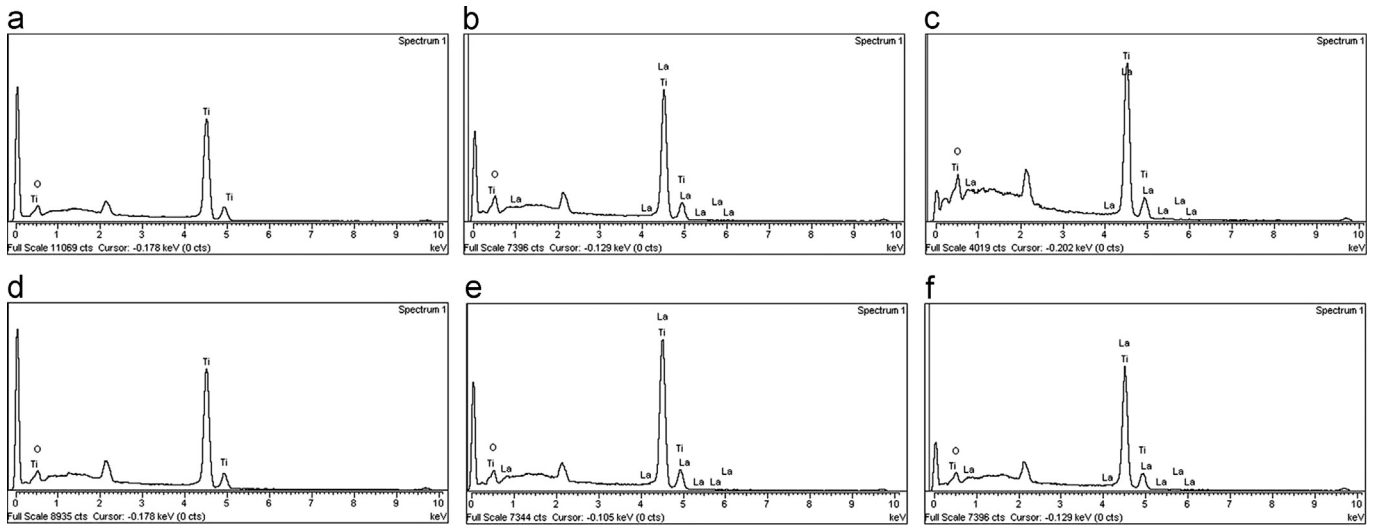
Fig. 5. The EDS spectra of (a) pure, (b) 0.5 wt% La doped and (c) 1 wt% La doped SG synthesized TiO$_2$ nanopowders; (d) pure, (e) 0.5 wt% La doped and (f) 1 wt% La doped HT synthesized TiO$_2$ nanopowders.
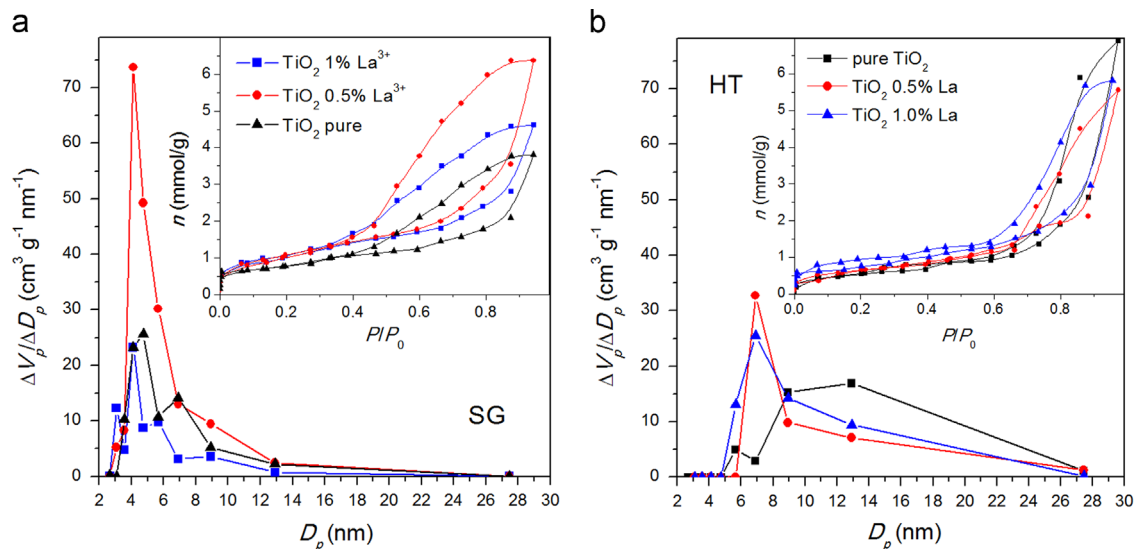
Fig. 6. The pore size distribution for pure and La-doped TiO$_2$ nanopowders synthesized by sol–gel (a) and hydrothermal (b) methods, obtained by BJH. Corresponding adsorption/desorption isotherm curves given in the insets.

[21], are shown, together with corresponding adsorption/desorption curves, given in the insets.

The pore parameters of the samples have been influenced by the synthesis method and the level of La-doping: in Table 3 the values of specific surface area (S_{BET}) and pore volume (V_p) for sol–gel and hydrothermally synthesized nanopowders, obtained by the BET method, are listed for comparison. Namely, in the sol–gel synthesized samples, the specific surface area is increasing with the increase of La content, from 60 m^2 g^{-1} in pure TiO$_2$ to ~ 80 m^2 g^{-1} in La-doped samples (see Table 3). In hydrothermally synthesized samples S_{BET} values are lower than in the sol–gel synthesized samples. In those samples, S_{BET} is also increasing, from 49 m^2 g^{-1} in pure TiO$_2$ nanopowder to 51 and 58 m^2 g^{-1} in samples doped

with 0.5 and 1 mol%, respectively (Table 3). Similar values of specific surface area have been obtained by the BJH method [21].

The mean diameters of mesopores, calculated from both BET and BJH (D_{BET}, D_{BJH}, respectively) for the samples obtained by both synthesis routes are also listed in Table 3. It may be noticed from these data that larger pore diameters have been registered in the hydrothermally synthesized sample.

3.7. Raman scattering measurements

The structure of synthesized pure and La-doped TiO$_2$ nanopowder samples have been analyzed by Raman

Table 3
The porous properties of pure and La-doped TiO$_2$ nanopowders synthesized by sol–gel and hydrothermal methods: specific surface area (S_{BET}, S_{BJH}), pore volume (V_p), and mean pore diameters (D_{BET}, D_{BJH}) obtained from BET and BJH methods.

	Sol–gel method			Hydrothermal method		
	Pure TiO$_2$	0.5% La	1% La	Pure TiO$_2$	0.5% La	1% La
S_{BET} (m^2 g^{-1})=S_{meso}	60	80	81	49	51	58
V_p (cm^3 g^{-1})	0.133	0.222	0.161	0.241	0.194	0.203
D_{BET} (nm)	5.7	7.2	5.1	12.6	9.8	9.0
S_{BJH} (m^2 g^{-1})	62	82	81	51	50	59
D_{BJH} (nm)	5.4	7.1	5.2	12.5	9.9	8.5
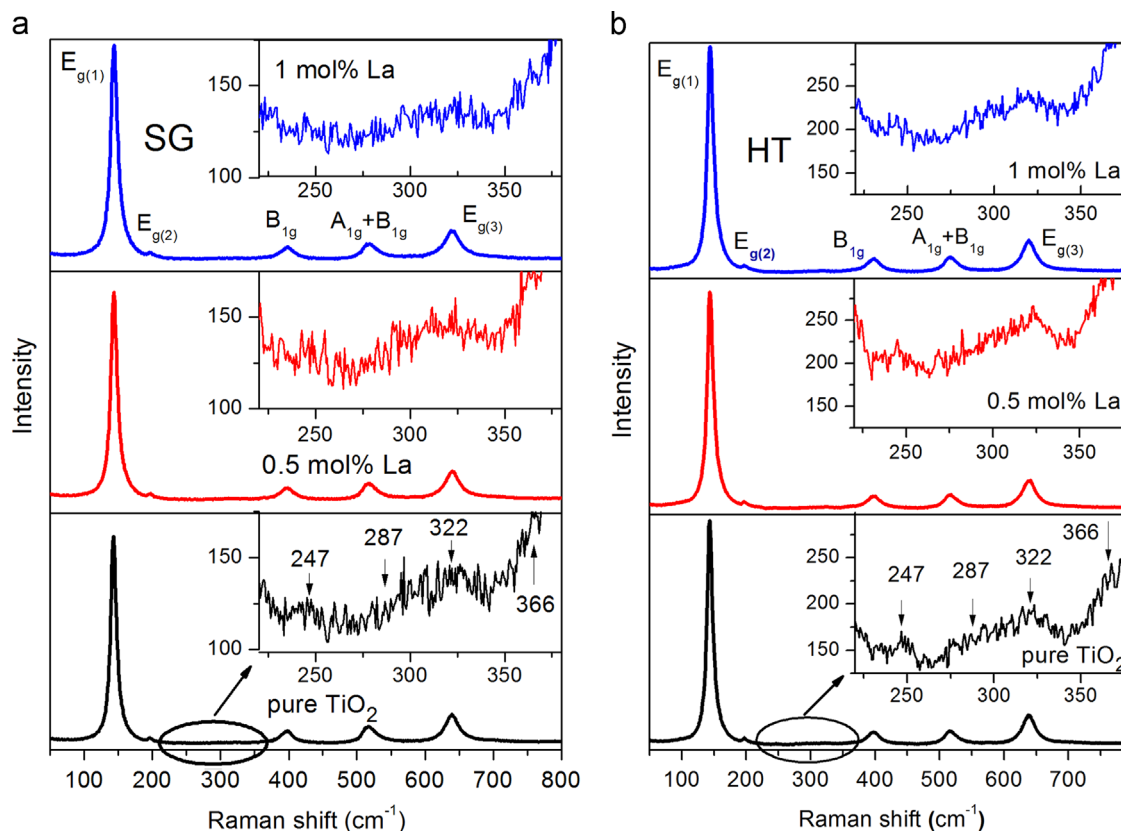
Fig. 7. The Raman spectrum of pure and La-doped TiO$_2$ nanopowders, synthesized by sol–gel (a) and hydrothermal (b) methods, with anatase modes denoted. Insets: the spectral region of 220–380 cm^{-1} with characteristic brookite modes.

spectroscopy, to reveal the influence of synthesis method and La-doping on measured Raman spectra. The most intensive Raman features in all spectra (Fig. 7) have been assigned to anatase [30]: $E_{g(1)}$ ($\sim$143 cm^{-1}), $E_{g(2)}$ ($\sim$199 cm^{-1}), B_{1g} ($\sim$399 cm^{-1}), $A_{1g}+B_{1g}$ ($\sim$518 cm^{-1}), and $E_{g(3)}$ ($\sim$639 cm^{-1}). Greater intensity of anatase modes, measured in the HT samples, points to better crystallinity in these samples in comparison to the SG synthesized samples. Besides anatase modes, some additional features of very low intensity have been detected in the range from 220 to 380 cm^{-1} in the Raman spectra of the samples synthesized by both sol–gel and hydrothermal method, as shown in the insets of Fig. 7(a) and (b). These features can be ascribed to the brookite phase [22]: A_{1g} ($\sim$247 cm^{-1}), B_{3g} ($\sim$287 cm^{-1}), B_{1g} ($\sim$322 cm^{-1}), and B_{2g} ($\sim$366 cm^{-1}). Low intensities and large linewidths of these modes should indicate a disorder and/or partial amorphization of the brookite phase [22,23], which is more pronounced in the sol–gel synthesized samples.

Table 4
Effect of type catalyst on reaction rate constant and reaction rate of photocatalytic degradation of alprazolam ($c_0=0.03$ mmol dm^{-3}).

	$k^a \times 10^2$ (min^{-1})	$R^b \times 10^6$ (mol dm^{-3} min^{-1})	r^c
SG			
Pure TiO$_2$	7.04	2.28	0.9991
0.5 mol% La	4.97	1.61	0.9966
1 mol% La	5.63	1.82	0.9995
HT			
Pure TiO$_2$	7.68	2.49	0.9938
0.5 mol% La	8.22	2.66	0.9960
1 mol% La	7.80	2.53	0.9948

[a]Reaction rate constant determined for the first 20 min of irradiation.
[b]Reaction rate determined for the first 20 min of irradiation.
[c]Linear regression coefficient.
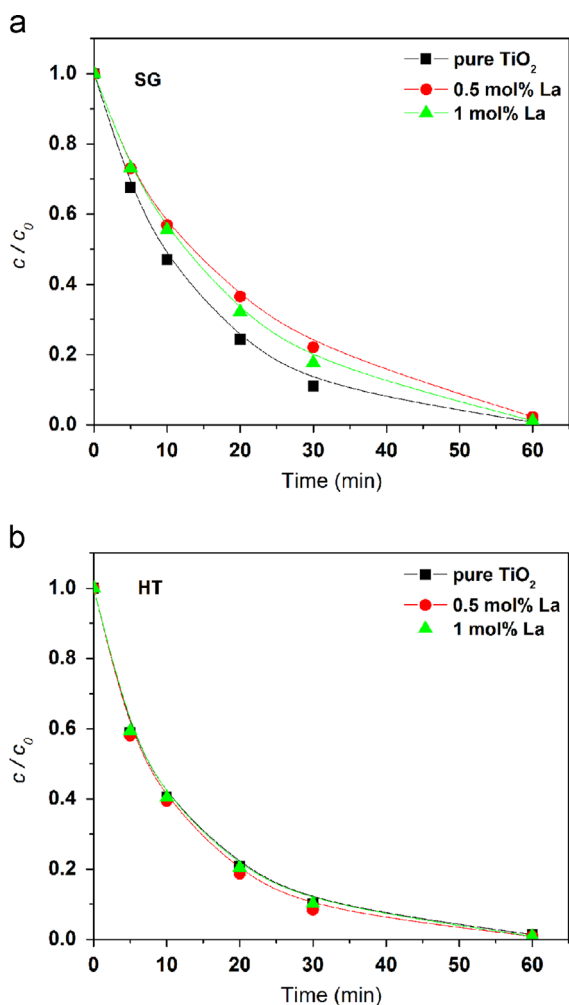
3.8. Photocatalysis

Influence of two different routes of synthesis and concentrations of La^{3+} on the photocatalytic activity of nanopowders was studied in photocatalytic degradation of alprazolam under UV light irradiation. The results are presented in Fig. 8. On the basis of these kinetic curves, a linear dependence of ln(c/c_0) on the illumination time was obtained in the first period of heterogeneous photocatalysis for all synthesized samples, suggesting that the degradation reaction of the alprazolam is pseudo-first order kinetics (the linear correlation coefficients varied in the range 0.994–0.999), as shown in Table 4.

As can be seen, the presence of La^{3+} has a negative effect on the photocatalytic efficiency of nanopowders synthesized by the sol–gel method (Fig. 8(a), Table 4), while in the case of hydrothermal synthesis method La^{3+} content practically has no impact (within experimental error) on the efficiency of nanopowders in photocatalytic degradation of alprazolam (Fig. 8(b), Table 4).

When comparing photocatalytic activity of nanopowders obtained by both methods of synthesis (Fig. 8, Table 4) it can be concluded that the alprazolam degradation rate was somewhat higher in the case of used catalysts synthesized by the hydrothermal method, although the crystallite size of nanoparticles in this case were a slightly greater than nanoparticles obtained by the sol–gel method (Table 1), while the specific surface areas were slightly lower (Table 2). However, the catalysts synthesized by the hydrothermal method have greater mean pore diameter (calculated by two different methods, Table 2) than the catalyst synthesized by the sol–gel method. These relationships confirm the crucial role of pore size distribution in efficient photocatalytic degradation of relatively large pollutant molecules such as alprazolam and probably this is the reason for a slightly higher efficiency of the catalyst synthesized by the hydrothermal method. Similar results were obtained in the study of photocatalytic degradation of metoprolol by using mesoporous anatase nanopowders [22].

Fig. 8. The kinetics of photocatalytic degradation of alprazolam ($c_0=0.03$ mmol dm^{-3}) in the presence of different types of catalyst (1 mg cm^{-3}) under UV irradiation: (a) sol–gel and (b) hydrothermally synthesizes samples of pure and La doped TiO$_2$ nanopowders.

4. Conclusion

Mesoporous TiO_2 nanopowders doped with La^{3+} were prepared by the sol–gel synthesis performed at 550 °C and hydrothermal method performed at 200 °C in order to compare structural, morphological and photocatalytic properties of synthesized samples. According to XRD and Raman measurements nanoparticles with a dominant anatase phase have been obtained by both synthesis methods. These measurements have shown that slightly larger crystallites, with better crystalline structure, have been produced by HT than by the SG method. It has been observed from DSC measurements that La-doping shifted anatase-to-rutile phase transformation to higher temperatures, giving better thermal stability to these nanomaterials for applications in advanced technologies. Photocatalytic activity of synthesized nanopowders has been tested in degradation of alprazolam in water solution under UV light irradiation. A higher degradation rate has been detected for the catalysts synthesized by the hydrothermal method, in spite of their slightly greater crystallite size and lower specific surface area, in comparison to the nanoparticles obtained by the sol–gel method. Such improvement of photocatalytic performance of hydrothermally synthesized nanopowders may rather be related to their better crystallinity of both TiO_2 phases (anatase and brookite), as well as greater mean pore size. Also, La-doping have slightly degraded photocatalytic efficiency of nanopowders obtained by the applied sol–gel route in degradation of alprazolam, whereas there was no impact of La-content on photocatalytic performance of hydrothermally synthesized samples.

Acknowledgments

References

[1] A. Fujishima, T.N. Rao, D.A. Tryk, Titanium dioxide photocatalysis, J. Photochem. Photobiol. C 1 (2000) 1–21.

[2] N. Daneshvar, A.R. Khataee, Removal of azo dye C.I. acid red 14 from contaminated water using Fenton, UV/H_2O_2, $UV/H_2O_2/Fe(II)$, $UV/H_2O_2/Fe(III)$ and $UV/H_2O_2/Fe(III)/oxalate$ processes: a comparative study, J. Environ. Sci. Health A 41 (2006) 315–328.

[3] K. Pirkanniemi, M. Sillanpää, Heterogeneous water phase catalysis as an environmental application: a review, Chemosphere 48 (2002) 1047–1060.

[4] N. Daneshvar, D. Salari, A.R. Khataee, Photocatalytic degradation of azo dye acid red14 in water: investigation of the effect of operational parameters, J. Photochem. Photobiol. A 157 (2003) 111–116.

[5] H. Jensen, A. Soloviev, Z. Li, E.G. Søgaard, XPS and FTIR investigation of the surface properties of different prepared titania nano-powders, Appl. Surf. Sci. 246 (2005) 239–249.

[6] K.L. Yeung, A.J. Maira, J. Stolz, E. Hung, N.K.-C. Ho, A.C. Wei, J. Soria, K.-J. Chao, P.L. Yue, Ensemble effects in nanostructured TiO_2 used in the gas-phase photooxidation of trichloroethylene, J. Phys. Chem. B106 (2002) 4608–4616.

[7] D. Xu, L. Feng, A. Lei, Characterization of lanthanum trivalent ions/TiO_2 nanopowders catalysis prepared by plasma spray, J. Colloid Interface Sci. 329 (2009) 395–403.

[8] K. Xu, G. Zhu, Preparation and characterization of nano-La (S, C)-TiO_2 oriented films by template hydrothermal synthesis, Appl. Surf. Sci. 255 (2009) 6691–6695.

[9] L. Jing, X. Sun, B. Xin, B. Wang, W. Cai, H. Fu, The preparation and characterization of La doped TiO_2 nanoparticles and their photocatalytic activity, J. Solid State Chem. 177 (2004) 3375–3382.

[10] S. Ahmed, M.G. Rasul, W.N. Martens, R. Brown, M.A. Hashib, Heterogeneous photocatalytic degradation of phenols in wastewater: a review on current status and developments, Desalination 261 (2010) 3–18.

[11] M. Huerta-Fontela, M.T. Galceran, F. Ventura, Fast liquid chromatography–quadrupole-linear ion trap mass spectrometry for the analysis of pharmaceuticals and hormones in water resources, J. Chromatogr. A 1217 (2010) 4212–4222.

[12] V. Calisto, V.I. Esteves, Psychiatric pharmaceuticals in the environment, Chemosphere 77 (2009) 1257–1274.

[13] A. Jurado, N. Mastroianni, E. Vàzquez-Suñé, J. Carrera, I. Tubau, E. Pujades, C. Postigo, M. López de Alda, D. Barceló, Drug of abuse in urban groundwater. A case study: Barcelona, Sci. Total Environ. 424 (2012) 280–288.

[14] O.A.H. Jones, N. Voulvoulis, J.N. Lester, Partitioning behavior of five pharmaceuticals compounds to activated sludge and river sediment, Arch. Environ. Contam. Toxicol. 50 (2006) 297–305.

[15] M. Reza Ganjali, H. Haji-Hashemi, F. Faridbod, P. Norouzi, M. Qomi, Potentiometric determination of alprazolam based on carbon paste and PVC membrane Electrodes, Int. J. Electrochem. Sci. 7 (2012) 1470–1481.

[16] B. Castañeda, W. Ortiz-Cala, C. Gallardo-Cabrera, N. Sbarbati Nudelman, Stability studies of alprazolam tablets: effect of chemical interactions with some excipients in pharmaceutical solid preparations, J. Phys. Org. Chem. 22 (2009) 807–814.

[17] G. Tulja Rani, D. Gowri Shankar, P. Kadgapathi, B. Satyanarayana, A validated RP HPLC method for simultaneous determination of propranolol hydrochloride and alprazolam in bulk and in pharmaceutical formulations, J. Pharm. Res. 4 (2011) 358–360.

[18] P. Pérez-Lozano, E. García-Montoya, A. Orriols, M. Miñarro, J.R. Ticó, J.M. Suñé-Negre, Development and validation of a new HPLC analytical method for the determination of alprazolam tablets, J. Pharm. Biomed. 34 (2004) 979–987.

[19] G.K. Williamson, W.H. Hall, X-ray line broadening from filed aluminium and wolfram, Acta Metall. 1 (1953) 22–31.

[20] K. Kaneko, C. Ishii, H. Kanoh, Y. Hanzawa, N. Setoyama, T. Suzuki, Characterization of porous carbons with high resolution α_S-analysis and low temperatures magnetic susceptibility, Adv. Colloid Interface 76–77 (1998) 295–320.

[21] E.P. Barret, L.G. Joyner, P.P. Halenda, The determination of pore volume and area distribution in porous substances. I. computation from nitrogen isotherms, J. Am. Chem. Soc. 73 (1951) 373–380.

[22] A. Golubović, B. Abramović, M. Šćepanović, M. Grujić-Brojčin, S. Armaković, I. Veljković, B. Babić, Z. Dohčević-Mitrović, Z.V. Popović, Improved efficiency of sol–gel synthesized mesoporous nanopowders in photocatalytic degradation of metoprolol, Mater. Res. Bull. 48 (2013) 1363–1371.

[23] A. Golubović, M. Šćepanović, A. Kremenović, S. Aškrabić, V. Berec, Z. Dohčević-Mitrović, Z.V. Popović, Raman study of the variation in anatase structure of TiO_2 nanopowders due to the changes of sol–gel synthesis conditions, J. Sol-Gel Sci. Technol. 49 (2009) 311–319.

[24] M. Akarsu, A. Asiltürk, F. Sayilkan, N. Kiraz, E. Arpaç, H. Sayilkan, A Novel, Approach to the hydrothermal synthesis of anatase titania nanoparticles and the photocatalytic degradation of rhodamine B, Turk. J. Chem. 30 (2006) 333–343.

[25] R.R. Djenadic, Lj.M. Nikolic, K.P. Giannakopoulos, B. Stojanovic, V.V. Srdic, One-dimensional titanate nanostructures: synthesis and characterization, J. Eur. Ceram. Soc. 27 (2007) 4339–4343.

[26] K. Yanagisawa, J. Overstone, Crystallization of anatase from amorphous titania using the hydrothermal technique: effects of starting material and temperature, J. Phys. Chem. B 103 (1999) 7781–7787.

[27] J. Liqiang, S. Xiaojun, C. Weimin, X. Zili, D. Yaoguo, F. Honggang, The preparation and characterization of nanoparticle TiO$_2$/Ti films and their photocatalytic activity, J. Phys. Chem. Solids 64 (2003) 615–623.

[28] J. Liqiang, S. Xiaojun, X. Baifu, W. Baiqi, C. Weimin, F. Honggang, The preparation and characterization of La doped TiO$_2$ nanoparticles and their photocatalytic activity, J. Solid State Chem. 177 (2004) 3375–3382.

[29] T. Sugimoto, X. Zhou, A. Muramatsu, Synthesis of uniform anatase TiO$_2$ nanoparticles by sol-gel method. 3. Formation process and size control, J. Colloid Interface Sci. 259 (2003) 43–52.

[30] T. Ohsaka, F. Izumi, Y. Fujiki, Raman spectra of anatase, TiO$_2$, J. Raman Spectrosc. 7 (1978) 321–324.

Nanocrystalline CeO$_{2-\delta}$ as Effective Adsorbent of Azo Dyes

Nataša M. Tomić,[†] Zorana D. Dohčević-Mitrović,*,[†] Novica M. Paunović,[†] Dušan Ž. Mijin,[‡] Nenad D. Radić,[§] Boško V. Grbić,[§] Sonja M. Aškrabić,[†] Biljana M. Babić,[∥] and Danica V. Bajuk-Bogdanović[⊥]

[†]Institute of Physics, University of Belgrade, Pregrevica 118, 11080 Belgrade, Serbia

[‡]Faculty of Technology and Metallurgy, University of Belgrade, Karnegijeva 4, 11000 Belgrade, Serbia

[§]IChTM, Department of Catalysis and Chemical Engineering, University of Belgrade, Njegoševa 12, 11000 Belgrade, Serbia

[∥]Institute of Nuclear Sciences "Vinča", University of Belgrade, 11001 Belgrade, Serbia

[⊥]Faculty of Physical Chemistry, University of Belgrade, Studentski Trg 12-16, 11000 Belgrade, Serbia

S *Supporting Information*

ABSTRACT: Ultrafine CeO$_{2-\delta}$ nanopowder, prepared by a simple and cost-effective self-propagating room temperature synthesis method (SPRT), showed high adsorption capability for removal of different azo dyes. Batch type of adsorption experiments with fixed initial pH value were conducted for the removal of Reactive Orange 16 (RO16), Methyl Orange (MO), and Mordant Blue 9 (MB9). The equilibrium adsorption data were evaluated using Freundlich and Langmuir isotherm models. The Langmuir model slightly better describes isotherm data for RO16 and MO, whereas the Freundlich model was found to best fit the isotherm data for MB9 over the whole concentration range. The maximum adsorption capacities, determined from isotherm data for MO, MB9, and RO16 were 113, 101, and 91 mg g^{-1} respectively. The adsorption process follows the pseudo-second-order kinetic model indicating the coexistence of chemisorption and physisorption. The mechanism of azo dye adsorption is also discussed.
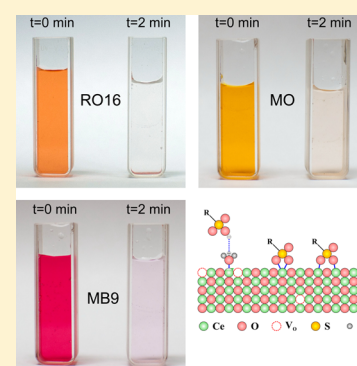
INTRODUCTION

Synthetic dyes are widely used in a number of industries such as textile and leather industries, paper printing, cosmetics, and pharmaceuticals. It is estimated to be more than 10 000 commercially available dyes with over 7×10^5 tons of dyestuff produced annually.[1,2] Azo dyes represent about 60−70% of the dyes used in the textile industry. Some of them show aquatic toxicity or allergenic effects, and under reductive conditions they produce aromatic amines that are carcinogenic.[2,3] Azo dyes represent a class of synthetic, colored, organic compounds, which are characterized by the presence of one or more azo bonds. These dyes belong to the most toxic ones compared to other forms of dyes.[1] Large quantities of these dyes (10−15% of the total world production) are released into the wastewater (typical concentration 10−200 mg L^{-1}), the presence of which poses a major threat to the aquatic organisms as well as animals and humans because of their nonbiodegradability, toxicity, and potential carcinogenic nature.[4−6]

Dye removal from textile effluents is a major environmental problem because of the difficulty to treat such streams by conventional physicochemical and biological treatment methods. The methods such as filtration, coagulation, flocculation, ion exchange, and photocatalytic degradation are unsatisfactory for wastewater treatment because they are expensive and may produce more toxic byproducts. Among the various available water treatment techniques, adsorption is the most reliable and efficient technique for dye removal, despite the fact that usually the adsorbent needs to be regenerated, which increases the cost of the process and can be a time-consuming procedure. The liquid phase adsorption has been shown to be an efficient way for removing the suspended solids, organic matter, and oil from aqueous solutions. Adsorption appears to offer the best perspective over all the other treatments because it can handle fairly large flow rates, producing a high quality effluent and does not result in the formation of harmful substances, such as ozone and free radicals which are present during the photodegradation process using UV.

Activated carbon is the most widely used adsorbent for this purpose, because it has a high surface area and high capacity for adsorption of organic matter, but its use is limited because of its high production cost and significant problems with the regeneration of the spent activated carbon.[7,8] A great variety of low-cost biomass materials[9−13] have been used to produce activated carbon for the treatment of wastewaters. In recent years, low cost agricultural wastes have been investigated as potential biosorbents,[14] but most of these cheap substitutes have to be subjected to the process of carbonization which increases process costs. Therefore, there is still a high demand for cheaper adsorbent materials with high adsorption capacity.

Nowadays, nanoscience and nanotechnology play important role in environmental protection. There is a strong need to develop simple and economical methods for producing nanomaterials with higher adsorption rates which can efficiently remove various contaminants. Nanomaterials with high surface area are the most promising candidates as adsorbents in organic dye removal.[5,15−19]

Among various metal oxide semiconductors, CeO_2 is widely used in many application areas such as catalysis, fuel cells, sensors, and UV shielding, owing to its outstanding physical and chemical properties. The application of ceria as effective sorbent is not so often studied. There are few reports in which it is demonstrated that ceria is effective sorbent for the removal of high toxic pollutants such as[17] As(V) and Cr(VI) and azo dyes such as Congo Red[18] or Acid Orange[4] from water. The adsorption experiments, performed to remove Reactive Orange 16 and Methyl Orange from wastewaters, mainly used as adsorbent waste biomass,[20] various types of sludge, and biosorbents.[1,13,14,20−26] Although most of these sorbents were relatively cheap and effective in dye removal, they showed modest and rarely high sorption capacities. On the other side, to the best of our knowledge there is almost no study which concerns the adsorption of Mordant Blue 9.

Herein we present the adsorption capability of ceria nanoparticles for removal of different azo dyes such as Reactive Orange 16, Methyl Orange, and Mordant Blue 9. Ceria nanopowder, obtained by a simple and cost-effective method, has shown very high efficiency toward azo dye removal and has been proven to be a promising alternative for wastewater treatment.

■ EXPERIMENTAL SECTION

1. Materials Preparation. The ultrafine $CeO_{2−\delta}$ nanopowder was fabricated via a simple and economical self-propagating room temperature synthesis method (SPRT).[27,28] Starting reactants were cerium nitrate hexahydrate $(Ce(NO_3)_3 \cdot 6H_2O)$ (Acros Organics 99.5%) and sodium hydroxide (Carlo Erba). Hand-mixing of nitrate with NaOH was performed in alumina mortar for ~10 min until the mixture turned light brown. After being exposed to air for 4 h, the mixture was suspended in water. Rinsing of $NaNO_3$ was performed in a centrifuge at 3500 rpm for 10 min. This procedure was performed four times with distilled water and twice with ethanol. The precipitate was dried at 60 °C overnight. The reaction based on the self-propagating room temperature method can be written as follows:

$$2[(Ce(NO_3)_3 \cdot 6H_2O) + 6NaOH + (1/2 − \delta)O_2$$
$$\rightarrow 2CeO_{2−\delta} + 6NaNO_3 + 15H_2O \qquad (1)$$
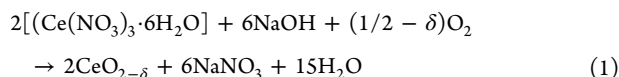
2. Characterization Methods. X-ray powder diffraction (XRD) data of the sample were collected on a Siemens D-5000 diffractometer with Cu $K\alpha$ radiation over the 2θ range from 20° to 80°. Atomic force microscope (AFM) images were taken using the Omicron B002645 SPM PROBE VT AFM 25 instrument in noncontact mode at room temperature. The powder specific surface area of the sample was calculated following the multipoint BET procedure on the Quantachrome ChemBet-3000 setup. The pore size distribution was derived from nitrogen adsorption-desorption isotherm obtained at 77 K. The infrared (IR) transmission spectra of $CeO_{2−\delta}$ pellets before and after dye adsorption were measured on a Thermo Nicolet 6700 Fourier transform infrared spectrophotometer at room temperature. Micro-Raman spectra were collected in the backscattering configuration using the TriVista 557 Raman system. The 488 nm line of an Ar^+/Kr^+ mixed gas laser was used as an excitation source. In order to avoid sample heating, the incident laser power on the samples was kept below 20 mW. Surface charge (zeta potential) of ceria nanoparticles at different pH was measured using Zetasizer Nano ZS90 (Malvern

Instruments) apparatus. Suspensions were prepared using deionized water as dispersing medium and were ultrasonicated for 15 min prior to the measurements using an ultrasonic bath. The pH values of suspensions were adjusted by adding HCl and NaOH solutions to the starting suspension of $CeO_{2−\delta}$ nanopowder.
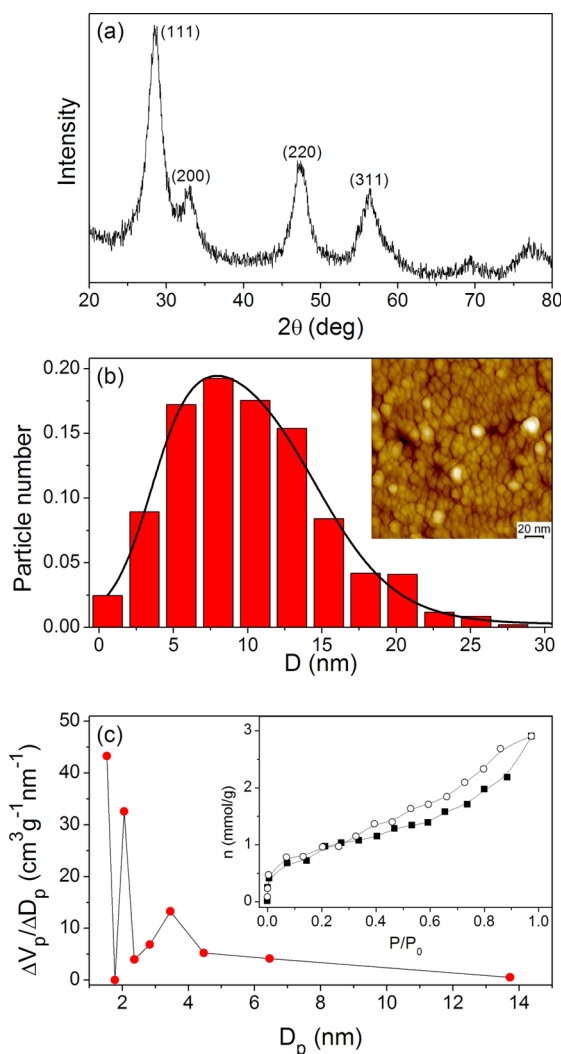
3. Adsorption Experiments. The adsorption experiments were carried out as batch tests in a magnetically stirred thermostated glass vessel with three different concentrations (50, 100, and 200 mg $L^{−1}$) of Reactive Orange 16 (RO16), Methyl Orange (MO), and Mordant Blue 9 (MB9). All measurements were performed at initial pH values of 6.2, 6, and 4.6 for MO, MB9, and RO16 dye solutions, respectively. The suspensions were stirred for 2 min at room temperature in the dark. The adsorption capacity (for the 200 mg $L^{−1}$ concentration of dyes) of coconut-based powdered activated carbon (PAC), of large specific surface area (1200 m²/g), was determined for comparison. The working volume (25 mL) and the quantity of ceria nanopowders and PAC (50 mg) were kept fixed in all adsorption experiments. At fixed contact time, the samples were taken, centrifuged, and analyzed on a Shimadzu 1700 UV-vis spectrophotometer within the spectral range where maximum absorption for each dye occurs. In Table S1 (see the Supporting Information) are given the chemical structure and the wavelength of maximal absorption (λ_{max}) for each dye.

■ RESULTS AND DISCUSSION

The powder XRD pattern of $CeO_{2−\delta}$ nanopowder is presented in Figure 1a. Diffraction peaks corresponding to cubic fluorite structure are clearly observed. All XRD peaks are broadened, indicating that the crystallite size is within the nanometer range. The average size of $CeO_{2−\delta}$ nanocrystals, estimated by the Wiliamson-Hall method,[29] is about 6 nm. The noncontact AFM image of $CeO_{2−\delta}$ sample (Inset of Figure 1b) shows small and agglomerated nonporous $CeO_{2−\delta}$ particles. The pores between agglomerated $CeO_{2−\delta}$ nanoparticles are also visible on the AFM image. Particle size distribution obtained from the AFM image of $CeO_{2−\delta}$ sample is presented in Figure 1b, and it was modeled by asymmetric double sigmoidal function. The average particle size is 11.4 nm.

To determine the surface area and pore size distribution, nitrogen adsorption−desorption isotherms at 77 K were recorded, and these are given in the inset of Figure 1c. According to the IUPAC classification,[30] the nitrogen adsorption−desorption isotherm is attributed to the Langmuir IV type. The pore size distribution was determined from the desorption branch of the isotherms using the BJH (Barrett−Joyner−Halenda) method and is shown in Figure 1c. It can be observed that the sample has bimodal pore size distribution in the mesoporous area with the first mode peak around 2 nm and the second one in the range 3−4 nm. The value of the BET specific surface area (S_{BET}) is 74 m² g$^{−1}$.

Further, we examined the performances of $CeO_{2−\delta}$ nanopowder as a potential adsorbent for removal of RO16, MO, and MB9. The adsorption measurements were carried out with three different concentrations of the dye solutions (50, 100, and 200 mg $L^{−1}$), and absorption spectra of the dye solutions were collected after certain time intervals. The UV−vis spectrum of RO16 is given in Figure 2a (blue line) for the concentration of 50 mg $L^{−1}$. The absorption spectrum of RO16 in the presence of $CeO_{2−\delta}$ nanoparticles after 2 min is also presented in Figure 2a (red line). As can be seen, the RO16 characteristic bands decreased promptly, indicating that RO16 was removed from the solution. The corresponding photo image (right panel of Figure 2a) shows that the solution is almost colorless. The absorption spectra of the MO and MB9 before (blue line) and after 2 min (red line) in the presence of $CeO_{2−\delta}$ nanoparticles are given in Figure 2b,c. Absorption spectra of these two dye

Figure 2. Absorption spectra with corresponding photo images of (a) RO16, (b) MO, and (c) MB9 dye solutions (50 mg L^{-1}) before and 2 min after introducing CeO$_{2-\delta}$ nanoparticles (2 g L^{-1}). Mass of adsorbent = 50 mg; solution volume = 25 mL.
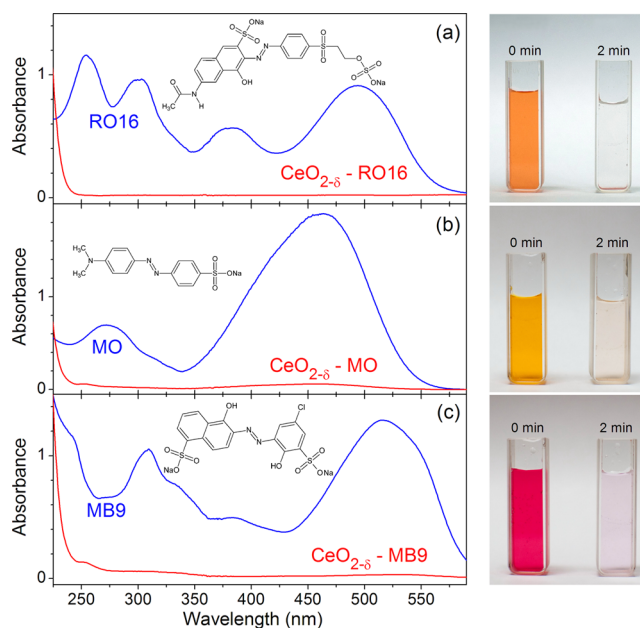
Figure 1. XRD spectrum (a), particle size distribution obtained from AFM (b), and pore size distribution curve obtained from the desorption branch of the isotherm (c) for CeO$_{2-\delta}$ nanopowder. Insets present the AFM image and the nitrogen adsorption–desorption isotherm of CeO$_{2-\delta}$ nanopowder.

solutions after 2 min showed that the dyes were present in a very low concentration. From the photo images (right panel of Figure 2b,c), it can be noticed that the solutions were almost colorless after 2 min. The experiment was repeated with an increased concentration for all three dyes (100 mg L^{-1}), and the obtained results were similar.

The concentration of RO16 in the solution was further increased to 200 mg L^{-1}. The absorption spectra of RO16 dye solution in the presence of CeO$_{2-\delta}$ nanoparticles, presented in Figure S1a (Supporting Information), demonstrate that CeO$_{2-\delta}$ quickly removes the RO16 from the solution. After 40 min, the equilibrium state was reached. The adsorption measurements were also performed on the solutions of MO and MB9 (200 mg L^{-1}) in the presence of CeO$_{2-\delta}$ nanopowder, in order to compare the efficiency of adsorption process onto ceria nanopowder for all three dyes. The adsorption capacity of CeO$_{2-\delta}$ nanopowder was determined from the mass balance relationship:[1,13,15,22]

$$q_e = \frac{(C_0 - C_e)V}{m} \tag{2}$$

where q_e represents the amount of dye adsorbed per unit mass of adsorbent (mg g^{-1}), C_0 and C_e are the initial and equilibrium liquid phase concentrations (mg L^{-1}), respectively, V is the volume of the solution (L), and m is the mass (g) of CeO$_{2-\delta}$ used.

The adsorption rate and the amount of adsorbed dye with contact time for the solutions of RO16, MO, and MB9 (200 mg L^{-1}) are illustrated in Figure 3a,b. As can be noticed from Figure 3, for all three curves, it is characteristic that the adsorption process is rapid in the initial stage, whereas in the later stage it becomes much slower. The adsorption rate for RO16 was higher at the beginning, but after 60 min much better elimination of MO from the solution was observed, whereas the adsorption rate of MB9 was still lower. The equilibrium was achieved after 40 (60) min for RO16 (MO), whereas for MB9 it was achieved after 180 min. The adsorption capacities of CeO$_{2-\delta}$ nanopowder in the case of MO, MB9, and RO16 were 100, 94, and 91 mg g^{-1}, respectively.

Further, the adsorption capacities of CeO$_{2-\delta}$ nanopowder and activated carbon were compared. The adsorption capacity of commercial activated carbon (50 mg) is presented in Figure 4 for MO (a), RO16 (b), and MB9 (c) solutions (200 mg L^{-1}). In the case of MO dye solution, it can be noticed that at the beginning of the adsorption process the activated carbon was slightly faster than CeO$_{2-\delta}$ nanopowder and reached the equilibrium state after 20 min. After 60 min, both curves overlapped. In the case of RO16 dye solution, activated carbon was much slower compared to CeO$_{2-\delta}$. After 40 min, CeO$_{2-\delta}$ nanopowder reached equilibrium and eliminated almost 90% of RO16 from the solution, whereas activated carbon needed 2 h to reach the final adsorption capacity of 85 mg g^{-1} which was still lower than that of ceria nanopowder (91 mg g^{-1}). The adsorption capability of CeO$_{2-\delta}$ for MB9 is lower than that for activated carbon, although after 2 h the final adsorption capacities were comparable.
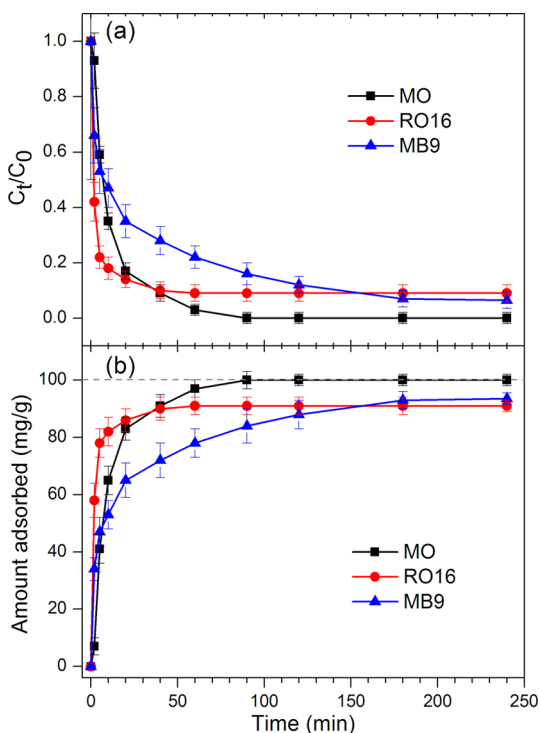
Figure 3. Adsorption rate (a) and amount of adsorbed dyes (b) for the solutions of MO, RO16, and MB9 (200 mg L^{-1}) in the presence of CeO$_{2-\delta}$ nanopowder. Mass of adsorbent = 50 mg; solution volume = 25 mL.

In Figure 5a−c are shown the IR transmission spectra of pure dyes and CeO$_{2-\delta}$ nanopowders after dye adsorption. For comparison, the IR spectrum of pure CeO$_{2-\delta}$ nanopowder is also given in Figure 5a−c.

The IR spectra of pure dyes have some common characteristic bands.[4,6,31−36] The bands at 1040/1120 cm^{-1} in MO, 1054/1139 cm^{-1} in RO16, and 1044/1136 cm^{-1} in MB9 originate from the symmetric stretching vibrations of the SO$_3^-$ group ($\nu_s(SO_3^-)$). The band at 1204 cm^{-1} in MO, 1236 cm^{-1} in RO16, and 1190 cm^{-1} in MB9 represents the asymmetric stretching vibrations of the SO$_3^-$ group ($\nu_{as}(SO_3^-)$). The band at 1368 cm^{-1} in MO and 1372 cm^{-1} in RO16 belongs to the C−N stretching vibrations. The bands at 1422, 1410, and 1409 cm^{-1} in MO, RO16, and MB9, respectively, are assigned to the N=N stretching vibrations. The bands at 1520/1608 cm^{-1} in MO and 1586 cm^{-1} in RO16 are from the aromatic ring stretching vibrations. The band at 1672 cm^{-1} in the spectra of RO16 originates from the stretching vibrations of the carbonyl C=O group.

In the IR spectrum of MO dye adsorbed on CeO$_{2-\delta}$ (shown in Figure 5a), the IR bands of the MO dye are of much lower intensity. The pronounced changes of the IR bands characteristic for sulfonate stretching vibration mode are observed. The $\nu_{as}(SO_3^-)$ band at 1204 cm^{-1} is much weaker after MO adsorption on CeO$_{2-\delta}$ and shifted to ~1193 cm^{-1} (marked with arrow in Figure 5a). The $\nu_s(SO_3^-)$ band at 1040 cm^{-1} in MO is slightly shifted to 1034 cm^{-1} (marked with arrow in Figure 5a) in the CeO$_2$−MO spectrum, the intensity of which is much lower after adsorption. All these changes can indicate that the sulfonate group is strongly involved in the adsorption of MO onto CeO$_{2-\delta}$.[34] In the IR spectrum of RO16 adsorbed onto CeO$_{2-\delta}$ (Figure 5b), a significant intensity decrease of the IR bands at 1054/1139 and 1500 cm^{-1}, characteristic for SO$_3^-$
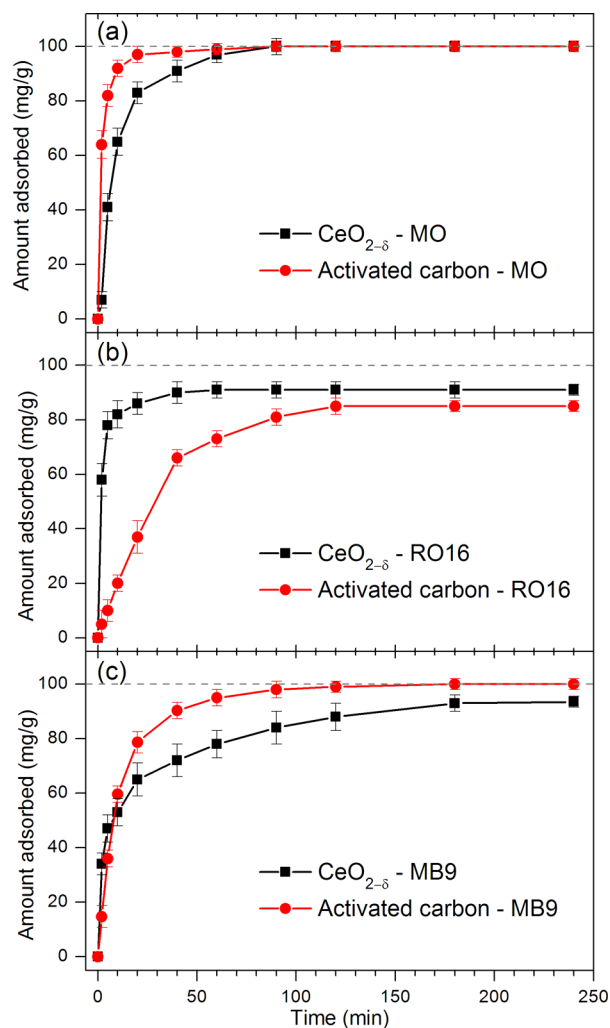
Figure 4. Comparison of adsorption capacities between CeO$_{2-\delta}$ nanopowder and activated carbon in the case of (a) MO, (b) RO16, and (c) MB9 dye solutions (200 mg L^{-1}). Mass of adsorbent = 50 mg; solution volume = 25 mL.

group and N−H bending vibrations,[4,6] is observed too. Many other bands which belong to pure RO16 dye are much weaker or barely visible in the CeO$_{2-\delta}$−RO16 spectrum, as for instance the band at 1410 cm^{-1} for N=N stretching vibrations. The carbonyl C=O peak at 1672 cm^{-1} in the IR spectrum of RO16, is almost absent from the CeO$_{2-\delta}$−RO16 spectrum. The $\nu_s(SO_3^-)$ band is shifted from 1139 to 1136 cm^{-1} in the CeO$_{2-\delta}$−RO16 spectrum. In the IR spectrum of CeO$_{2-\delta}$−MB9 (Figure 5c), a major decrease of the MB9 band intensity is observed and the slight shift of the asymmetric $\nu_s(SO_3^-)$ band is barely visible (marked with arrow in Figure 5c). All this indicates that RO16 and MB9 are also strongly adsorbed onto the CeO$_{2-\delta}$ surface. In Figure 5d is presented the IR transmission spectrum of pure CeO$_{2-\delta}$ in the extended spectral range. As can be seen, strong bands near 3400 and 1620 cm^{-1} are attributed to the adsorbed H$_2$O and hydroxyls.[37,38] The absorption band at 1384 cm^{-1} originates from CO$_2$ molecule vibrations.

Raman spectra, obtained on CeO$_{2-\delta}$ nanopowder before and after dye adsorption, are presented in Figure 6 and are consistent with the IR measurements. In the Raman spectra of nanocrystalline CeO$_{2-\delta}$ treated with dyes, besides the F$_{2g}$ mode of pure CeO$_{2-\delta}$ positioned at ~456.5 cm^{-1} and the mode at
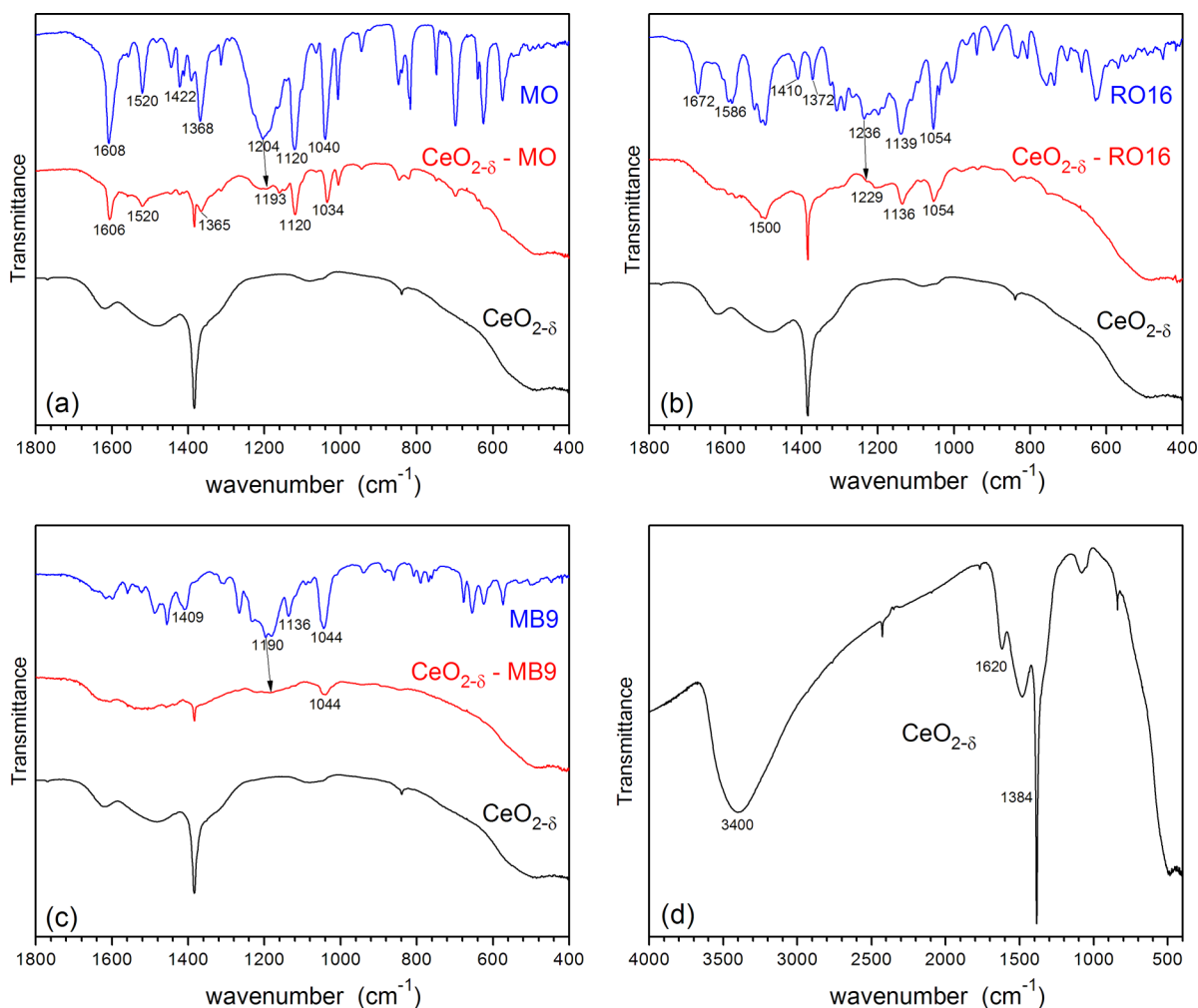
Figure 5. IR transmission spectra of (a) MO, (b) RO16, and (c) MB9 adsorbed on $CeO_{2-\delta}$ together with the transmission spectra of pure dyes and $CeO_{2-\delta}$ nanopowder. (d) IR transmission spectrum of $CeO_{2-\delta}$ nanopowder in the extended range.
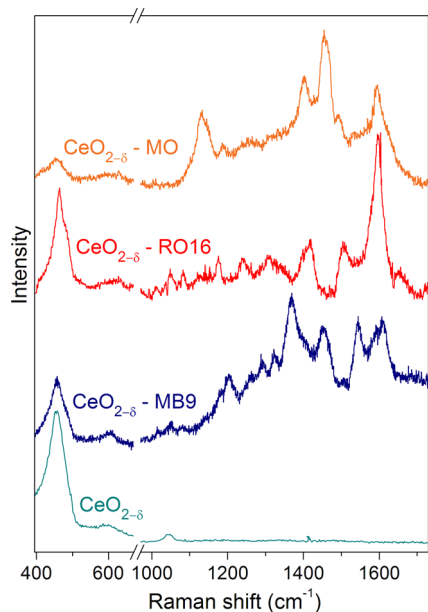
Figure 6. Room temperature Raman spectra of $CeO_{2-\delta}$ nanopowder before and after adsorption of MO, RO16, and MB9 dyes.

~600 cm^{-1} which belongs to intrinsic oxygen vacancies,[39] additional modes are observed. These new modes correspond to the vibrations of different atomic groups of dye molecules, such as $-N=N-$, $-C=O$, $-S=O$, $-O-H$, and aromatic ring vibrations. The most prominent mode frequencies deduced from the spectra of ceria treated with MO, RO16, and MB9 are summarized in the Table S2 (see the Supporting Information). As the majority of the atomic group vibrations characteristic for the dye molecules in question are observed in the Raman spectra of dyed ceria nanopowder, it can be concluded that in all three cases the adsorption of dye molecules took place.

The IR and Raman spectra unambiguously showed that MO, RO16, and MB9 are adsorbed on $CeO_{2-\delta}$ surface. In addition, from the IR spectra of three azo dyes adsorbed on $CeO_{2-\delta}$ nanopowders, we concluded that ν_{as} and ν_s bands of sulfonate groups are affected considerably. The intensity ratio of these bands ($\nu_{as}(SO_3^-)/\nu_s(SO_3^-) = 0.4$) for adsorbed MO onto ceria is different from the same ratio in the spectrum of isolated MO ($\nu_{as}(SO_3^-)/\nu_s(SO_3^-) = 0.9$). The changes of the ν_{as} and ν_s band intensities of sulfonate groups are also registered in the IR spectra of adsorbed RO16 and MB9 onto ceria. It is further worth mentioning that the frequency difference $\Delta\nu_{as-s}$ ($\nu_{as}(SO_3^-) - \nu_s(SO_3^-)$) in the MO, RO16, and MB9 spectra is higher than that in the corresponding spectra of adsorbed dyes on ceria (see Figure 5). This is characteristic of the

bidentate type coordination according to the Deacon and Phillips[40] empirical rule and the work of Bauer et al.,[41] formed when OH groups situated on the surface metal cations are substituted with oxygen atoms from azo dyes. Ji et al.[4] noticed similar changes to ours in the IR spectra of acid orange adsorbed onto CeO_2 surface and proposed that a bidentate type bridge is formed between sulfonate group and Ce^{4+} cations. According to the observed changes in the IR spectra of MO, RO16, and MB9 adsorbed on $CeO_{2-\delta}$ nanopowder, it is reasonable to assume that all three dyes form a bidentate type bridge on the ceria surface, where two oxygen atoms of the SO_3^- group are bound to one or two Ce^{4+} cations in a process that involves the substitution of surface coordinated OH groups on Ce^{4+} cations with oxygen atoms from azo dyes.

Another very important factor for dye removal concerns the capability of $CeO_{2-\delta}$ nanopowders to easily form oxygen vacancies on the surface which accompany functional groups. The surface functional groups can interact with dye molecules via hydrogen bonds and/or electrostatic forces promoting the adsorption of dye molecules. The first principle density functional theory calculations performed by Yang et al.[42] have shown that, in oxygen deficient ceria, the adsorbed water molecules prefer to decompose near the oxygen vacancy site, forming surface hydroxyls, where H atoms are bonded with surface oxygen atoms. Therefore, they concluded that in reduced ceria both adsorbed H_2O and surface hydroxyls coexist. Their calculations are in good agreement with experimental work of Kundakovic et al.[43] performed on oxidized and reduced CeO_2 thin films, who detected surface hydroxyls only in reduced ceria films.

Having in mind that our ceria is oxygen deficient, it is reasonable to assume that hydroxyl groups, already observed in the IR spectra, are present on the surface of $CeO_{2-\delta}$ nanopowder. The experimental determination of the pH value at zero point charge (pH_{ZPC}) revealed that $CeO_{2-\delta}$ has $pH_{ZPC} = 6.3$ (Figure S2 in the Supporting Information). As pH values of the dye solutions are lower than pH_{ZPC} of $CeO_{2-\delta}$ (see section 3 in Experimental Section), $CeO_{2-\delta}$ as adsorbent acts as a positive surface. The electrostatic attraction between ceria nanoparticles and negatively charged dye ions is an operable mechanism. In that case, the ceria surface hydroxyls are protonated:

$$Ce-OH + H^+ \rightarrow Ce-OH_2^+ \qquad (3)$$
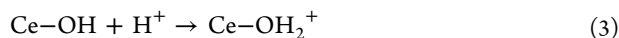
In aqueous solution, the sulfonate groups ($R-SO_3Na$) dissociate and are converted to anionic dye ions. The adsorption process further proceeds due to the electrostatic attraction between these two oppositely charged ions:

$$Ce-OH_2^+ + R-SO_3^- \rightleftharpoons Ce-OH_2^+ \cdots {}^-O_3S-R \qquad (4)$$
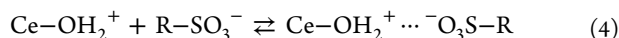
Illustration of the adsorption mechanisms between dye molecules and $CeO_{2-\delta}$ adsorbent is shown in Figure 7.

As we stated earlier, the adsorption rate at the beginning of the process (presented in Figure 3a) is higher for RO16 than for MO and MB9. The difference in removal efficiency between three dyes can be explained by the fact that the pH value of the RO16 solution is close to the pH value where ceria net positive charge surface has maximum, whereas the pH values of MO and MB9 dye solutions are close to the pH_{ZPC} value of $CeO_{2-\delta}$. Therefore, the electrostatic interaction between RO16 dye molecules and $CeO_{2-\delta}$ at the beginning will be stronger than that for MB9 and MO. It is important to emphasize that
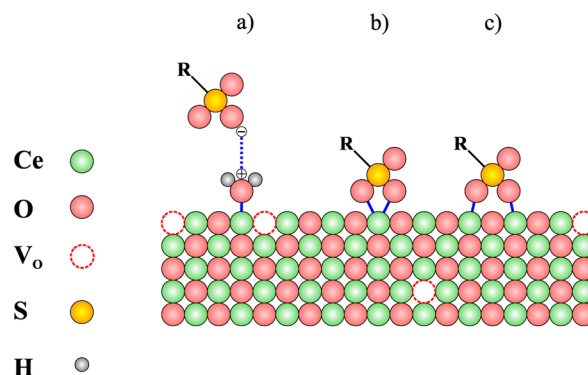

Figure 7. Schematic representation of RO16, MO, and MB9 adsorption on $CeO_{2-\delta}$ surface. (a) Electrostatic interaction between protonated ceria surface and sulfonate group in the dye molecule; (b, c) bidentate type structures between sulfonate group and Ce^{4+} cations.

sulfonic groups, which dissociate in aqueous solution and convert to $R-SO_3^-$ anions, are negatively charged even at higher acidic solutions, because their pK_a values are lower than zero.[44] Finally, the interaction between OH groups on the surface of $CeO_{2-\delta}$ and NH groups of the RO16 is also a possible mechanism for RO16 dye adsorption[19] and can explain the higher adsorption rate in the case of RO16 at the beginning of the process.

The study of the adsorption equilibrium isotherm is helpful in determining the maximum adsorption capacity of adsorbent for given adsorbate. These isotherms relate the dye uptake per unit mass of adsorbent, q_e, to the equilibrium liquid phase concentration C_e. In Figure 8 are presented the adsorption isotherms for RO16 (a), MO (b), and MB9 (c) dye solutions, measured at room temperature. Adsorption isotherms were analyzed according to Langmuir and Freundlich models in order to determine the best-fit model. Langmuir's model predicts the monolayer coverage of the adsorbate, assuming that all adsorption sites are identical and energetically equivalent, whereas the Freundlich's model assumes the adsorption on heterogeneous surface composed of nonidentical adsorption sites with different energy of adsorption. The isotherm equations and isotherm parameters for both models are listed in Supporting Information Table S3.

The adsorption isotherms of RO16 and MO from Figure 8a,b can be fitted by both the Langmuir and Freundlich equations. Both models give reasonable good fit in the case of MO and RO16, although the values of correlation coefficients (Supporting Information Table S3) are slightly higher for the Langmuir isotherm. The sorption data of MB9 are much better represented by the Freundlich model (Figure 8c and Supporting Information Table S3) which expresses adsorption in a multilayer manner on an energetically heterogeneous surface.

The parameter $1/n$ from the Freundlich equation characterizes the heterogeneity of the site energies and the adsorption intensity, that is, the degree of nonlinearity of adsorption isotherm. In their work, Tseng and Wu[45] have defined a favorable level for the adsorption isotherm curves and gave a classification for the values of parameter $1/n$. Despite the fact that the Langmuir model seems more suitable to describe the sorption of MO and RO16 onto ceria, according to Tseng's classification, the parameter $1/n$ (listed in Supporting Information Table S3) lies in the range of strongly favorable (for RO16 and MO) and favorable (for MB9) adsorption.
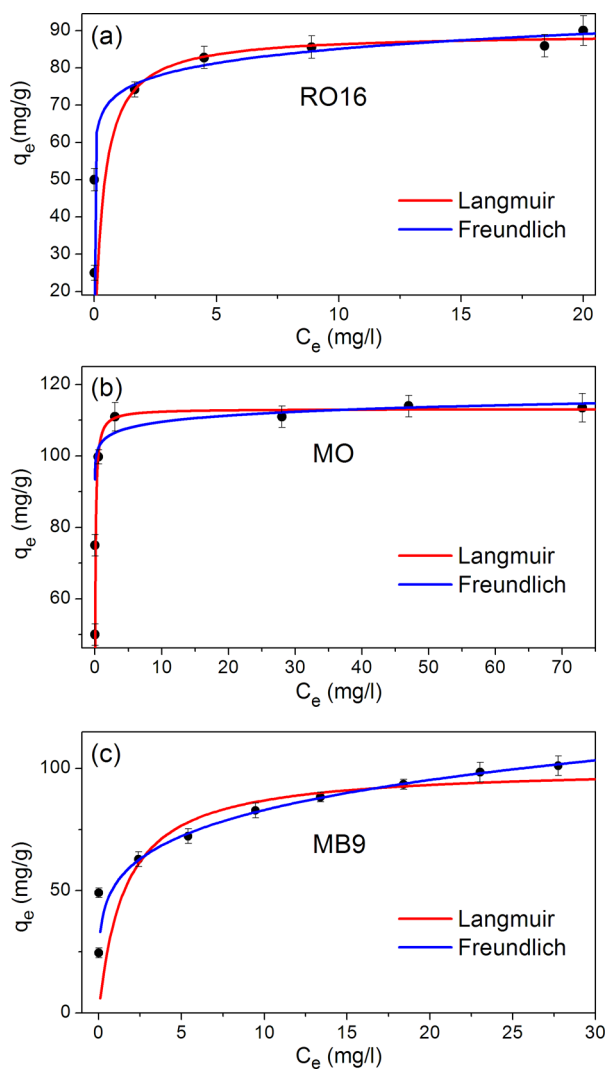
Figure 8. Adsorption isotherms of (a) RO16, (b) MO, and (c) MB9 dye solutions on $CeO_{2-\delta}$ at room temperature. Initial dye concentration = 50−230 mg L^{-1}; mass of adsorbent = 50 mg; solution volume = 25 mL.

Therefore, keeping in mind that oxygen-deficient surface of nanosized ceria is more heterogeneous than homogeneous, it is reasonable to conclude that adsorption of MB9, MO, and RO16 on $CeO_{2-\delta}$ nanopowders reflects the presence of more than one kind of adsorbent−adsorbate surface interaction. The maximal adsorption capacity values of $CeO_{2-\delta}$ nanopowder from isotherm data were found to be 113, 101, and 91 mg g^{-1} in the case of MO, MB9, and RO16 respectively.

To get further insight into the mechanism of adsorption, pseudo-first- and pseudo-second-order models were used to simulate the adsorption data for various contact times from Figure 3b. The pseudo-first-order model didn't give a good fit of the experimental data and will be omitted in further discussion. Kinetic data were further analyzed with the pseudo-second-order kinetic model shown in Figure 9. The linear form of the pseudo-second-order model is expressed as follows:

$$\frac{t}{q_t} = \frac{1}{k_2 q_e^2} + \frac{t}{q_e} \qquad (4)$$

where q_e and q_t refer to the amount of adsorbed dye at equilibrium and at time t, respectively, and k_2 is the equilibrium
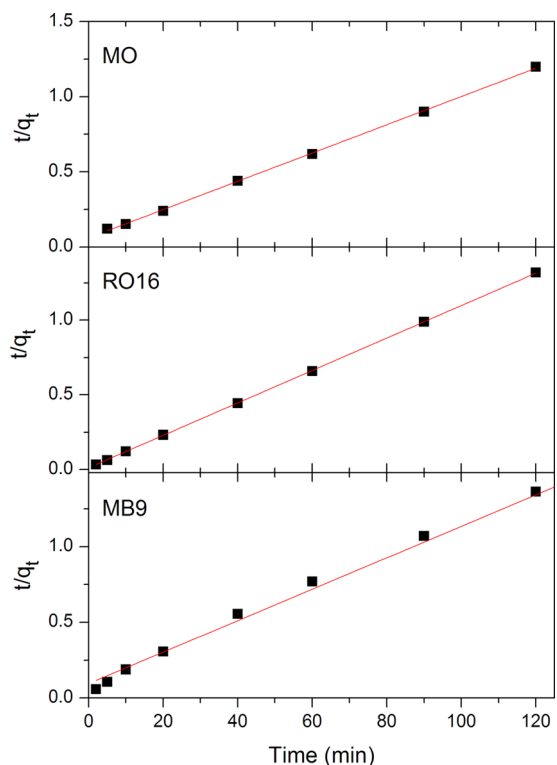
Figure 9. Pseudo-second-order kinetics of MO, RO16, and MB9 onto $CeO_{2-\delta}$ nanopowder. Initial dye concentration = 200 mg L^{-1}; mass of adsorbent = 50 mg; solution volume = 25 mL.

rate constant of the pseudo-second-order kinetic model. The linear plots of t/q_t vs t (Figure 9) show that the experimental data agree well with the pseudo-second-order kinetic model for all three dyes. The values of q_e and k_2 were calculated from the slope and intercept of eq 4, and their values are given in Table 1, together with experimental q_e values and correlation

Table 1. Pseudo-Second-Order Kinetic Model Parameters Together with Experimental q_e Values for Adsorption of Each Dye

	$q_{e,cal}$ (mg g^{-1})	$q_{e,exp}$ (mg g^{-1})	k_2 (g mg^{-1} min^{-1})	R^2
MO	106.3	100	1.44×10^{-3}	0.9994
RO16	100	91	9.09×10^{-3}	0.9999
MB9	96.3	93.6	1.13×10^{-3}	0.9977

coefficients. Calculated q_e values, tabulated in Table 1, are in quite good agreement with experimental ones and the correlation coefficients have large values ($R^2 > 0.99$). It can be concluded that the adsorption of MO, RO16, and MB9 on $CeO_{2-\delta}$ nanopowder follows the pseudo-second-order kinetic model which relies on the assumption that chemisorption and effective electrostatic interactions play a major role in the adsorption process.[46,47] Comparing the adsorption capacities of $CeO_{2-\delta}$ nanopowder with other adsorbents mentioned in the Introduction, we can conclude that $CeO_{2-\delta}$ nanopowder, produced by cost-effective SPRT method, shows efficient adsorption properties and is a promising candidate for environmentally friendly adsorbents in water treatment.

■ CONCLUSIONS

The $CeO_{2-\delta}$ nanopowder, synthesized by a facile and cost-effective SPRT method, appeared to be a very effective sorbent

for the MO, RO16, and MB9 azo dyes. The adsorption process was monitored at fixed initial pH value and varying dye concentration and contact time. Infrared and Raman spectroscopy measurements confirmed that the adsorption of azo dyes on the $CeO_{2-\delta}$ surface took place. The experimental adsorption data for the MO and RO16 were slightly better fitted with the Langmuir isotherm, whereas the Freundlich isotherm was a better fit for MB9 over the whole concentration range. According to the values of the Freundlich constant $(1/n)$, the adsorption of MB9, MO, and RO16 lies in a favorable and strongly favorable zone. The highest adsorption capacity of $CeO_{2-\delta}$ was obtained for MO (113 mg g^{-1}) and then for MB9 (101 mg g^{-1}) and RO16 (91 mg g^{-1}). The formation of a bidentate type bridge between sulfonate group and Ce^{4+} cations and the protonation of ceria surface hydroxyls can be responsible for effective adsorption process. Adsorption of MO, RO16, and MB9 dyes follows the pseudo-second-order equation with good correlation. These results imply that, besides strong electrostatic sorption, chemisorption mechanism may play an important role for the dye adsorption. Based on our results, ceria nanopowder prepared by the SPRT method represents an effective dye adsorbent and can be a promising substitute in wastewater treatment.

■ ASSOCIATED CONTENT

ⓢ Supporting Information

Figures showing absorption spectra of RO16 (200 mg L^{-1}) and photo image of RO16 solutions in the presence of $CeO_{2-\delta}$ nanopowders, and zeta potential of $CeO_{2-\delta}$ nanoparticles. Tables showing dye structures and their wavelengths of maximal absorption, values of the Raman shifts extracted from the experimental Raman spectra of $CeO_{2-\delta}$ nanopowder after adsorption of MO, RO16, and MB9, and isotherm equations and parameters for azo dyes at room temperature. This material is available free of charge via the Internet at http://pubs.acs.org.

■ AUTHOR INFORMATION

Corresponding Author
*E-mail: zordoh@ipb.ac.rs.
Notes
The authors declare no competing financial interest.

■ ACKNOWLEDGMENTS

■ REFERENCES

(1) Lee, J. W.; Choi, S. P.; Thiruvenkatachari, R.; Shim, W. G.; Moon, H. Evaluation of the performance of adsorption and coagulation processes for the maximum removal of reactive dyes. *Dyes Pigm.* **2006**, *69*, 196−203.
(2) Gomez, V.; Larrechi, M. S.; Callao, M. P. Kinetic and adsorption study of acid dye removal using activated carbon. *Chemosphere* **2007**, *69*, 1151−1158.
(3) Silva, J. P.; Sousa, S.; Rodrigues, J.; Antunes, H.; Porter, J. J.; Goncalves, I.; Ferreira-Dias, S. Adsorption of acid orange 7 dye in aqueous solutions by spent brewery grains. *Sep. Purif. Technol.* **2004**, *40*, 309−315.
(4) Ji, P. F.; Zhang, J. L.; Chen, F.; Anpo, M. Study of adsorption and degradation of acid orange 7 on the surface of CeO₂ under visible light irradiation. *Appl. Catal., B* **2009**, *85*, 148−154.
(5) Venkatesha, T. G.; Viswanatha, R.; Nayaka, Y. A.; Chethana, B. K. Kinetics and thermodynamics of reactive and vat dyes adsorption on MgO nanoparticles. *Chem. Eng. J.* **2012**, *198*, 1−10.
(6) Sahasrabudhe, M.; Pathade, G. Biodegradation of azo dye C.I. Reactive Orange 16 by an actinobacterium Georgenia sp. CC-NMPT-T3. *Int. J. Adv. Res.* **2013**, *1*, 91−99.
(7) Mohan, D.; Pittman, C. U., Jr Activated carbons and low cost adsorbents for remediation of tri- and hexavalent chromium from water. *J. Hazard. Mater.* **2006**, *137*, 762−811.
(8) Pollard, S. J. T.; Fowler, G. D.; Sollars, C. J.; Perry, R. Low-cost adsorbents for waste and wastewater treatment: a review. *Sci. Total Environ.* **1992**, *116*, 31−52.
(9) Amin, N. K. Removal of direct blue-106 dye from aqueous solution using new activated carbons developed from pomegranate peel: Adsorption equilibrium and kinetics. *J. Hazard. Mater.* **2009**, *165*, 52−62.
(10) Sharma, Y. C.; Uma; Upadhyay, S. N. Removal of a cationic dye from wastewaters by adsorption on activated carbon developed from coconut coir. *Energy Fuels* **2009**, *23*, 2983−2988.
(11) Aygün, A.; Yenisoy-Karakaş, S.; Duman, I. Production of granular activated carbon from fruit stones and nutshells and evaluation of their physical, chemical and adsorption properties. *Microporous Mesoporous Mater.* **2003**, *66*, 189−195.
(12) Kannan, N.; Sundaram, M. M. Kinetics and mechanism of removal of methylene blue by adsorption on various carbons—a comparative study. *Dyes Pigm.* **2001**, *51*, 25−40.
(13) Annadurai, G.; Juang, R. S.; Lee, D. J. Use of cellulose-based wastes for adsorption of dyes from aqueous solutions. *J. Hazard. Mater.* **2002**, *92*, 263−274.
(14) Haddadian, Z.; Shavandi, M. A.; Abidin, Z. Z.; Fakhru'l-Razi, A.; Ismail, M. H. S. Removal methyl orange from aqueous solutions using dragon fruit (Hylocereusundatus) foliage. *Chem. Sci. Trans.* **2013**, *2*, 900−910.
(15) Cheung, W. H.; Szeto, Y. S.; Mckay, G. Enhancing the adsorption capacities of acid dyes by chitosan nano particles. *Bioresour. Technol.* **2009**, *100*, 1143−1148.
(16) Wu, C. H. Adsorption of reactive dye onto carbon nanotubes: Equilibrium, kinetics and thermodynamics. *J. Hazard. Mater.* **2007**, *144*, 93−100.
(17) Zhong, L. S.; Hu, J. S.; Cao, A. M.; Liu, Q.; Song, W. G.; Wan, L. J. 3D flowerlike ceria micro/nanocomposite structure and its application for water treatment and CO removal. *Chem. Mater.* **2007**, *19*, 1648−1655.
(18) Ouyang, X. W.; Li, W.; Xie, S. L.; Zhai, T.; Yu, M. H.; Gan, J. Y.; Lu, X. H. Hierarchical CeO₂ nanospheres as highly-efficient adsorbents for dye removal. *New J. Chem.* **2013**, *37*, 585−588.
(19) Zhai, T.; Xie, S. L.; Lu, X. H.; Xiang, L.; Yu, M. H.; Li, W.; Liang, C. L.; Mo, C. H.; Zeng, F.; Luan, T. G.; Tong, Y. X. Porous Pr(OH)₃ nanostructures as high-efficiency adsorbents for dye removal. *Langmuir* **2012**, *28*, 11078−11085.
(20) Won, S. W.; Yun, H. J.; Yun, Y.-S. Effect of pH on the binding mechanisms in biosorption of Reactive Orange 16 by Corynebacterium glutamicum. *J. Colloid Interface Sci.* **2009**, *331*, 83−89.
(21) Won, S. W.; Choi, S. B.; Yun, Y.-S. Performance and mechanism in binding of Reactive Orange 16 to various types of sludge. *Biochem. Eng. J.* **2006**, *28*, 208−214.
(22) Janaki, V.; Vijayaraghavan, K.; Ramasamy, A. K.; Lee, K. J.; Oh, B. T.; Kamala-Kannan, S. Competitive adsorption of Reactive Orange 16 and Reactive Brilliant Blue R on polyaniline/bacterial extracellular polysaccharides composite-A novel eco-friendly polymer. *J. Hazard. Mater.* **2012**, *241*, 110−117.
(23) Suteu, D.; Zaharia, C.; Malutan, T. Removal of orange 16 reactive dye from aqueous solutions by waste sunflower seed shells. *J. Serb. Chem. Soc.* **2011**, *76*, 17.

(24) Zhao, D.; Zhang, W.; Chen, C.; Wang, X. Adsorption of Methyl Orange dye onto multiwalled carbon nanotubes. *Procedia Environ. Sci.* **2013**, *18*, 890−895.

(25) Saha, T. K.; Bhoumik, N. C.; Karmaker, S.; Ahmed, M. G.; Ichikawa, H.; Fukumori, Y. Adsorption of Methyl Orange onto Chitosan from Aqueous Solution. *J. Water Resour. Prot.* **2010**, *2*, 8.

(26) Ai, L.; Zhang, C.; Meng, L. Adsorption of Methyl Orange from Aqueous Solution on Hydrothermal Synthesized Mg−Al Layered Double Hydroxide. *J. Chem. Eng. Data* **2011**, *56*, 4217−4225.

(27) Yu, X.; Li, F.; Ye, X.; Xin, X.; Xue, Z. Synthesis of cerium(IV) oxide ultrafine particles by solid-state reactions. *J. Am. Ceram. Soc.* **2000**, *83*, 964−966.

(28) Boskovic, S.; Djurovic, D.; Dohcevic-Mitrovic, Z.; Popovic, Z.; Zinkevich, M.; Aldinger, F. Self-propagating room temperature synthesis of nanopowders for solid oxide fuel cells (SOFC). *J. Power Sources* **2005**, *145*, 237−242.

(29) Zhou, X.-D.; Huebner, W. Size-induced lattice relaxation in CeO_2 nanoparticles. *Appl. Phys. Lett.* **2001**, *79*, 3512−3514.

(30) Lowell, S. *Characterization of Porous Solids and Powders: Surface Area, Pore Size and Density*; Kluwer Academic Publishers: Dordrecht, The Netherlands, 2004.

(31) Jia, T.-J.; Song, G.; Li, P.-W.; He, T.-C.; Mo, Y.-J.; Cui, Y.-T. Vibrational modes study of methyl orange using SERS-measurement and the DFT method. *Mod. Phys. Lett. B* **2008**, *22*, 2869−2879.

(32) Sathiyabama, J.; Rajendran, S.; Selvi, J. A.; Amalraj, A. J. Methyl orange as corrosion inhibitor for carbon steel in well water. *Indian J. Chem. Technol.* **2008**, *15*, 462−466.

(33) Liu, Y.; Sun, D. Z. Development of Fe_2O_3-CeO_2-TiO_2/gamma-Al_2O_3 as catalyst for catalytic wet air oxidation of methyl orange azo dye under room condition. *Appl. Catal., B* **2007**, *72*, 205−211.

(34) Hua, Q.; Shi, F. C.; Chen, K.; Chang, S. J.; Ma, Y. S.; Jiang, Z. Q.; Pan, G. Q.; Huang, W. X. Cu_2O-Au nanocomposites with novel structures and remarkable chemisorption capacity and photocatalytic activity. *Nano Res.* **2011**, *4*, 948−962.

(35) Telke, A. A.; Kalyani, D. C.; Dawkar, V. V.; Govindwar, S. P. Influence of organic and inorganic compounds on oxidoreductive decolorization of sulfonated azo dye CI Reactive Orange 16. *J. Hazard. Mater.* **2009**, *172*, 298−309.

(36) Galindo, C.; Jacques, P.; Kalt, A. Photodegradation of the aminoazobenzene acid orange 52 by three advanced oxidation processes: UV/H_2O_2 UV/TiO_2 and VIS/TiO_2 - Comparative mechanistic and kinetic investigations. *J. Photochem. Photobiol., A* **2000**, *130*, 35−47.

(37) Yue, L.; Zhang, X.-M. Structural characterization and photocatalytic behaviors of doped CeO2 nanoparticles. *J. Alloys Compd.* **2009**, *475*, 702−705.

(38) Danish, M.; Hashim, R.; Ibrahim, M. N. M.; Sulaiman, O. Characterization of physically activated acacia mangium wood-based carbon for the removal of methyl orange dye. *BioResources* **2013**, *8*, 16.

(39) Dohčević-Mitrović, Z. D.; Šćepanović, M. J.; Grujić-Brojčin, M. U.; Popović, Z. V.; Bošković, S. B.; Matović, B. M.; Zinkevich, M. V.; Aldinger, F. The size and strain effects on the Raman spectra of $Ce_{1-x}Nd_xO_{2-d}$ ($0 \leq x \leq 0.25$) nanopowders. *Solid State Commun.* **2006**, *137*, 387−390.

(40) Deacon, G. B.; Phillips, R. J. Relationships between the carbon-oxygen stretching frequencies of carboxylato complexes and the type of carboxylate coordination. *Coord. Chem. Rev.* **1980**, *33*, 227−250.

(41) Bauer, C.; Jacques, P.; Kalt, A. Investigation of the interaction between a sulfonated azo dye (AO7) and a TiO_2 surface. *Chem. Phys. Lett.* **1999**, *307*, 397−406.

(42) Yang, Z.; Wang, Q.; Wei, S.; Ma, D.; Sun, Q. The effect of environment on the reaction of water on the ceria(111) surface: A DFT+U study. *J. Phys. Chem. C* **2010**, *114*, 14891−14899.

(43) Kundakovic, L.; Mullins, D. R.; Overbury, S. H. Adsorption and reaction of H_2O and CO on oxidized and reduced $Rh/CeO_x(111)$ surfaces. *Surf. Sci.* **2000**, *457*, 51−62.

(44) Lima, E. C.; Royer, B.; Vaghetti, J. C. P.; Simon, N. M.; da Cunha, B. M.; Pavan, F. A.; Benvenutti, E. V.; Cataluña-Veses, R.; Airoldi, C. Application of Brazilian pine-fruit shell as a biosorbent to removal of reactive red 194 textile dye from aqueous solution: Kinetics and equilibrium study. *J. Hazard. Mater.* **2008**, *155*, 536−550.

(45) Tseng, R.-L.; Wu, F.-C. Inferring the favorable adsorption level and the concurrent multi-stage process with the Freundlich constant. *J. Hazard. Mater.* **2008**, *155*, 277−287.

(46) Zhu, Y.-P.; Liu, Y.-L.; Ren, T.-Z.; Yuan, Z.-Y. Hollow manganese phosphonate microspheres with hierarchical porosity for efficient adsorption and separation. *Nanoscale* **2014**, *6*, 6627−6636.

(47) Yeddou-Mezenner, N. Kinetics and mechanism of dye biosorption onto an untreated antibiotic waste. *Desalination* **2010**, *262*, 251−259.

Investigation of surface defect states in CeO$_{2-y}$ nanocrystals by Scanning−tunneling microscopy/spectroscopy and ellipsometry

Marko Radović,[1] Bojan Stojadinović,[1] Nataša Tomić,[1] Aleksandar Golubović,[1] Branko Matović,[2] Ivana Veljković,[3] and Zorana Dohčević-Mitrović[1,a)]

[1]*Institute of Physics, Pregrevica 118, University of Belgrade, 11 000 Belgrade, Serbia*
[2]*Institute for Nuclear sciences "Vinča," Materials Science Laboratory, University of Belgrade, 11 000 Belgrade, Serbia*
[3]*Institute for Multidisciplinary Research, Kneza Viseslava 1a, University of Belgrade, 11 000 Belgrade, Serbia*

Synthesis process strongly influences the nanocrystalline CeO$_{2-y}$ defective structure. The presence of surface defects, in the form of oxygen vacancies in different charge states (F centers), can change the electronic properties of ceria nanocrystals. Nanocrystalline CeO$_{2-y}$ samples were synthesized using three different methods (precipitation, self-propagating room temperature, and hydrothermal synthesis). Raman spectroscopy was used to identify the presence of oxygen vacancies which presumably were formed at the nanoparticle surface. The defect concentration depended on the crystallite size of differently prepared CeO$_{2-y}$ samples. Scanning tunneling microscopy/spectroscopy and ellipsometry were employed to investigate the electronic band structure of defective CeO$_{2-y}$ nanocrystals. Scanning tunneling spectroscopy measurements demonstrated that inside the band gap of CeO$_{2-y}$ nanocrystals, besides the filled 4 f states, appeared additional states which were related to occupied and empty F center defect states. From the ellipsometric measurements, using the critical points model, the energy positions of different F centers states and the values of the reduced band gap energies were determined. The analysis of obtained data pointed out that depending on the synthesis method, different types of F centers (F^{+} and F^{0}) can be formed in the CeO$_{2-y}$ nanocrystals. The formation of different F center defect states inside the ceria gap have a strong impact on the electrical, optical, and magnetic properties of ceria nanocrystals. © 2014 AIP Publishing LLC. [http://dx.doi.org/10.1063/1.4904516]

I. INTRODUCTION

During the 20th century, CeO$_2$ based materials were widely applied in catalysis of automotive exhaust gases,[1,2] glass polishing,[3] high storage capacitors,[4] superconductor structures,[5] and gas sensors.[6] With significant expansion of nanotechnology, from the beginning of the 21st century, new areas of application emerged, such as solid oxide fuel cells[7,8] and spintronics.[9,10] Special interest was devoted to the optical properties of nanocrystalline ceria materials due to the appearance of new effects characteristic for nanosized materials. The application of ceria in the optical technologies, such as inorganic UV filters,[11] solar cells,[12,13] electrochromic smart windows,[14] and photocatalytic systems[15,16] requires precise control of the electronic band gap structure. For the ceria applications in oxide phosphorus materials[17] and optical conversion,[18] it is important to introduce additional electronic states inside the band gap. These electronic states can originate from the oxygen vacancies, whose concentration can be controlled by selecting the synthesis process or by a careful choice of the dopant.

In this paper, CeO$_{2-y}$ nanocrystals were synthesized by three different methods in order to investigate the influence of different synthesis methods on the formation of oxygen vacancies, which can be formed as abundant defects on the surface of ceria nanocrystals. The combined research performed by scanning tunneling microscopy (STM)/scanning tunneling spectroscopy (STS) and spectroscopic ellipsometry enabled to identify the electron trapping sites, i.e., F^{0} or F^{+} centers, and to obtain better insight into the electronic band gap structure of differently prepared CeO$_{2-y}$ nanopowders. The better knowledge of the electronic band gap structure of nanocrystalline ceria is crucial for the application of this material in the field of catalysis and spintronics.

## II. EXPERIMENT

A. Materials synthesis

1. Hydrothermal method

Cerium (III) nitrate hexahydrate (Ce(NO$_3$)$_3$ × 6H$_2$O), Acros Organics 99.5%) and Polyvinylpyrrolidone (PVP) (Aldrich) were used as starting materials. During a synthesis procedure, 1 g of PVP was mixed with 40 ml of distilled water under vigorous magnetic stirring at room temperature, until homogeneous solution was obtained. 3 mmol of cerium source was slowly added to the PVP solution (also under vigorous stirring at room temperature) in order to obtain a well-dissolved solution. No pH adjustment was made. Homogeneous solution was transferred into an autoclave and prepared at 200 °C for 6 h (T = 200 °C, t = 6 h). The precipitate was washed with distilled water and dried at 80 °C overnight.

a)Author to whom correspondence should be addressed. Electronic mail: zordoh@ipb.ac.rs

2. Self propagating room temperature synthesis (SPRT)

In this experiment, starting reactants were cerium nitrate hexahydrate $(Ce(NO_3)_3 \times 6H_2O)$ (Acros Organics 99.5%) and sodium hydroxide (Carlo Erba). Hand-mixing of nitrates with NaOH was performed in alumina mortar for approximately 10 min until mixture got light brown. After being exposed to air for 4 h, the mixture was suspended in water. Rinsing out of $NaNO_3$ (four times with distilled water and twice with ethanol) was performed in centrifuge at 3500 rpm for 10 min. The precipitate was dried at 60 °C overnight. The reaction can be written as follows:

$$2[(Ce(NO_3)_3 \times 6H_2O] + 6NaOH + (1/2 - y)O_2$$
$$\rightarrow 2CeO_{2-y} + 6NaNO_3 + 15H_2O. \qquad (1)$$
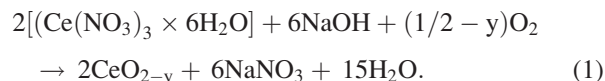
3. Precipitation method

The $Ce(SO_4)_2 \times 4H_2O$(Acros Organics) was dissolved in distilled water and formed a clear solution with a concentration of 0.4 M. The ammonia solution (Carlo Erba, 25%) was added drop-wise to the solution at room temperature (with continuous magnetic stirring) until the desired pH value was achieved ($\sim$9). Yellow suspension appeared and gradually became brown in color with continuous addition of the ammonium solution. The resulting room-temperature precipitate was filtered and washed with distilled water for several times, dried at 80 °C in air and calcinated at 200 °C for 4 h. The corresponding chemical reactions are

$$Ce(SO_4)_2 + 4NH_4OH \rightarrow Ce(OH)_4 \downarrow + 2(NH_4)_2SO_4 \quad (2)$$
$$Ce(OH)_4 \rightarrow CeO_2 + 2H_2O. \qquad (3)$$
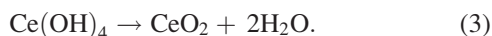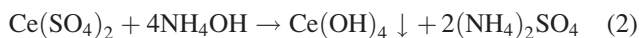
The samples produced by hydrothermal, SPRT, and precipitation methods are labeled as $H-CeO_{2-y}$, $S-CeO_{2-y}$, and $P-CeO_{2-y}$ for brevity.

4. Samples preparation

The X-ray diffraction (XRD) measurements were performed on powder samples. The Raman and ellipsometric measurements were performed on powder samples pressed into the pellets. For the STM/STS measurements, the synthesized ceria nanopowders were dispersed in ethanol and treated in the ultrasonic tub for 20 min in order to minimize the number of agglomerated particles. One drop of obtained suspension was deposited on a freshly cleaved, grounded highly ordered pyrolitic graphite (HOPG) surface, and after drying was loaded in the microscope chamber.

B. Materials characterization

The crystalline phase of cerium dioxide nanocrystals was studied by XRD method on a Siemens D-5000 diffractometer with Cu Kα radiation. The diffraction patterns were recorded over the 2θ range from 20° to 80°. The STM and STS measurements were carried out using Omicron scanning probe microscope (SPM) VT AFM 25. The micro-Raman spectra were collected in the backscattering configuration

using a Jobin Yvon T64000 spectrometer equipped with a nitrogen-cooled CCD detector. The argon ion (Ar$^+$) laser line at $\lambda = 514.5$ nm was used as an excitation source. Ellipsometric measurements were performed at $\theta_i = 70°$ incidence angle in the UV−V is spectral range, using variable angle spectroscopic ellipsometer (SOPRA GES5E–IRSE) of the rotating polarizer type. The high resolution spectra were collected with a step of 0.02 eV and prolonged exposure time.

III. RESULTS AND DISCUSSION

In Fig. 1 are shown the XRD patterns of the investigated samples with the Miller indices which correspond to the XRD peaks of CeO_2. All samples crystallized into fluorite type structure of CeO_2 and no amorphous or any other phase was detected. The average crystallite sizes (L_0) were calculated using Wiliamson-Hall method[19] and obtained values are also presented in Fig. 1. The diffraction peaks of CeO_2 samples, produced by SPRT and precipitation method, are broadened indicating that these samples are composed of very fine, nanometric size particles of lower crystallinity. The hydrothermal method produced significantly larger crystallites in comparison with SPRT and precipitation methods and consequently, the XRD pattern of this sample resembles to the XRD spectrum of well-crystallized sample.

Raman spectroscopy is more sensitive to structural disorder induced by oxygen vacancies than XRD method. In nonstoichiometric oxides like CeO_{2-y}, the oxygen vacancies are usually formed in the surface layer[20] and the presence of defects, as well as, defect concentration distribution can be
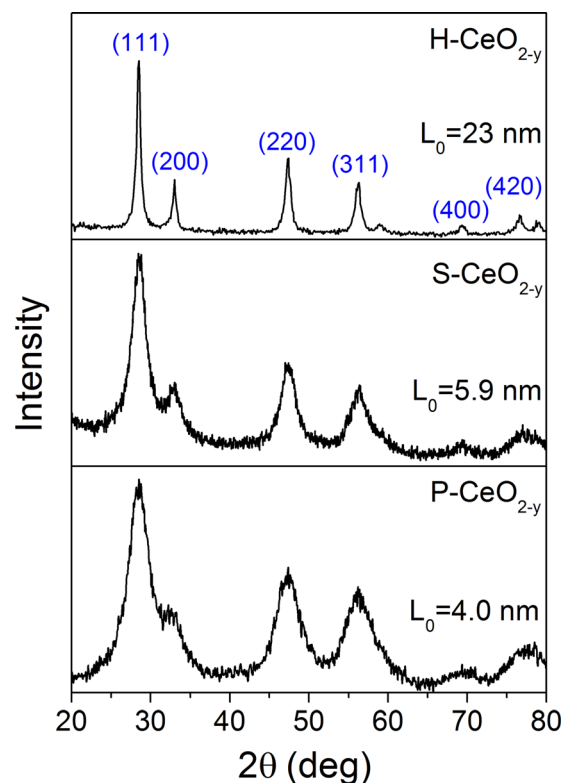

FIG. 1. XRD patterns of CeO_{2-y} nanopowders synthesized by hydrothermal ($H-CeO_{2-y}$), SPRT ($S-CeO_{2-y}$) and precipitation ($P-CeO_{2-y}$) method, together with a corresponding average crystallite size values.
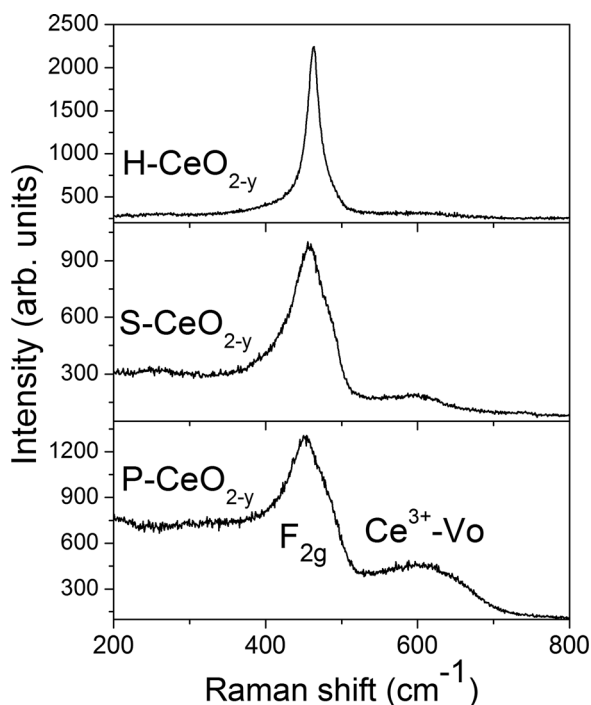
FIG. 2. Room-temperature Raman spectra of differently synthesized CeO_{2-y} nanocrystals.

successfully investigated by Raman spectroscopy.[21] In Fig. 2 are presented the Raman spectra of differently synthesized CeO_{2-y} nanocrystals in the spectral range 350–$750\,cm^{-1}$, where the F_{2g} mode and oxygen-vacancy-related Raman modes are positioned. The F_{2g} mode frequency and linewidth are essentially determined by the particle size, size distribution, and the presence of defects like oxygen vacancies.[22–24] In a case of $H{-}CeO_{2-y}$ sample, with the largest crystallite size, the F_{2g} mode is narrow and positioned at $463\,cm^{-1}$, very close to the value for bulk CeO_2 sample ($464.4\,cm^{-1}$).[23] In the case of $S{-}CeO_{2-y}$ and $P{-}CeO_{2-y}$ samples, with much smaller crystallite size, the F_{2g} peak is very broad, asymmetric, and shifted to lower frequencies ($458\,cm^{-1}$ and $454\,cm^{-1}$, respectively).

The other mode positioned around $600\,cm^{-1}$ originates from $Ce^{3+}{-}$oxygen vacancy (V_O) complexes. The intensity of this mode is proportional to the concentration of oxygen vacancies.[24–26] From Fig. 2, it can be seen that $P{-}CeO_{2-y}$ sample has the highest intensity of vacancy mode, implying

that this sample contains the highest concentration of oxygen vacancies. In the case of $S{-}CeO_{2-y}$ sample, the concentration of oxygen vacancies is lower, whereas $H{-}CeO_{2-y}$ sample has the lowest concentration of oxygen vacancies, because the corresponding Raman mode is barely visible. The observed behavior of the oxygen vacancy mode in investigated samples is expected, having in mind that $P{-}CeO_{2-y}$ sample has the smallest average crystallite size and consequently, the highest concentration of defects is expected to be found in this sample.

The STM/STS measurements present powerful tool for direct investigation of the electronic structure of nanomaterials. Using Raman spectroscopy, we have observed significant variations in the oxygen vacancy concentration in analyzed samples. Having in mind that defect states are abundant on the surface of nanoparticles, we applied STM/STS technique to examine how the presence of defects influences the electronic structure of synthesized ceria samples. Electronic band structure of stoichiometric CeO_2 is composed of O2p valence band states and 5d conduction band (CB) states. Inside the O2p$-$Ce5d band gap, there is narrow and localized Ce 4f band composed of empty $4f^0$ states. By measuring the change in the tunneling current with the bias voltage, between the STM tip and ceria nanocrystals, information about the electronic density of states can be obtained.[27] Current vs. voltage spectra are shown in Fig. 3(a) for the $H{-}CeO_{2-y}$, $S{-}CeO_{2-y}$, and $P{-}CeO_{2-y}$ samples together with the STM images of individual nanocrystals on which the STS measurements were performed. The crystallite size of individual nanocrystals was in good agreement with the average crystallite size obtained from XRD data.

In Fig. 3(b) are shown the differential conductance spectra (dI/dV) of investigated samples.

For the negative bias voltage, the information about the occupied electronic states can be obtained. The most prominent occupied band around $-3\,V$, in all investigated samples from the Fig. 3(b), corresponds to the O2p band.[28,29] When the oxygen vacancies are formed, part of Ce^{4+} atoms is reduced to Ce^{3+} atoms, resulting in a partial filling of the Ce 4f states. As a consequence, the Ce 4f band splits into occupied $4f^1$ and unoccupied $4f^0$ states. The occupied $4f^1$ states in CeO_2, detected by XPS measurements, were positioned around 1.2–$1.5\,eV$ above the top of the valence band.[30] In all investigated samples, $4f^1$ states appear about 0.7–$1eV$ above
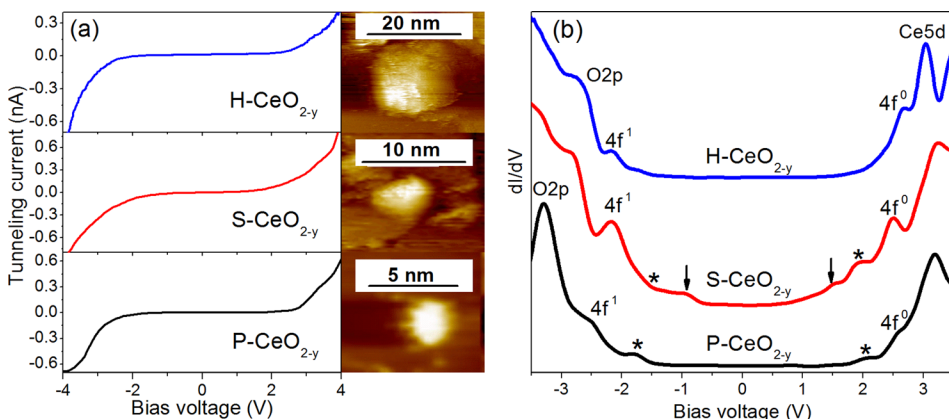

FIG. 3. (a) Current vs. voltage curves together with STM images of single ceria nanocrystals. Images were taken at $V_{bias} = 3\,V$ and $I = 100$–$300\,pA$. (b) Differential conductance spectra (dI/dV) for $H{-}CeO_{2-y}$, $S{-}CeO_{2-y}$, and $P{-}CeO_{2-y}$ samples. Arrows and asterisks indicate the position of dI/dV maxima which belong to F^+ and F^0 center defect states.

the valence band. In the case of S–CeO$_{2-y}$ and P–CeO$_{2-y}$ samples, besides the $4f^1$ states, we have detected another occupied defect electronic states marked with arrows and asterisks in Fig. 3(b). In the S–CeO$_{2-y}$ sample, these states appear as dI/dV peaks, approximately at -1 V and -1.5 V. For the P−CeO$_{2-y}$ sample, occupied states appear at -1.7 V, whereas no similar states are detected for H−CeO$_{2-y}$ sample. According to the paper of Jerratsch *et al.*,[31] two peaks above the valence band in the differential conductance spectra of defective CeO$_2$ films were ascribed to the splitting of the occupied $4f^1$ band. On the other side, the DFT calculations performed by Han *et al.*[32] on defective CeO$_2$ structure revealed that for increasing vacancy concentration, the electrons are localized not only on $4f$ states but also on the vacancy sites. This is manifested as further splitting of the gap states into empty and full states. Therefore, the gap states have substantial contributions from the electrons on the oxygen vacancy site in the case of high oxygen deficiencies.[32]

Surface defects like oxygen vacancies can trap two, one, or none electrons forming F^0, F^+ and F^{++} centers. F^0 and F^+ centers form localized occupied and empty states in the band gap, whereas F^{++} centers form only localized empty states near the conduction band. These types of defects are registered in various oxide nanomaterials, such as MgO,[33] HfO$_2$,[34] and TiO$_2$.[35] The STS measurements performed on defect rich surface of MgO[33] showed that the additional states were formed in the band gap of MgO. These states were ascribed to empty and occupied F center defect states. The appearance of these states in MgO supports our findings in ceria samples. In our recently published paper,[36] we have demonstrated that ceria nanocrystals synthetized by SPRT and precipitation methods exhibited different luminescence properties which originated from different F center defect states. PL spectra have shown that F^+ centres were dominant in the CeO$_2$ sample synthesized by SPRT method, whereas F^0 centres were the major defects in CeO$_2$ sample synthesized by precipitation method. Furthermore, the EPR analysis of these samples confirmed the existence of paramagnetic F^+ centers only in ceria samples produced by SPRT method.[36]

For positive bias voltage, the information about the empty electronic states can be obtained. The most prominent empty state around 3 V corresponds to the Ce 5d states which presents the upper part of the CB.[29] At approximately 2.5 V, we have $4f^0$ states which form the lower part of CB. Just below the $4f^0$ state, additional defect electronic states emerge in S−CeO$_{2-y}$ and P−CeO$_{2-y}$ samples which are marked with arrows and asterisks in Fig. 3(b). These peaks correspond to the empty states of F centers. The appearance of oxygen vacancy related empty electronic state, at similar energy, was detected by STS measurements performed on defect rich surface of ZnO nanorods.[37] Continuous rise of differential conductance spectrum for S−CeO$_{2-y}$ sample, starting from 1 V, indicates significant presence of unoccupied electronic trap states which can originate from different kinds of F center states, i.e., from F^0, F^+ or F^{++} centers. In the case of P−CeO$_{2-y}$ sample, there is one visible empty state at 2 V and in a case of H−CeO$_{2-y}$ sample, there are no visible empty states below the $4f^0$ band.

Another effect which can lead to the appearance of the peaks in the differential conductance spectra of metal and semiconductor nanoparticles is the so called Coulomb charging effect, where electron transport between the STM tip and nanocrystal is governed by electron-electron repulsion inside the spatially confined nanostructures.[38,39] This phenomena manifest as staircase behavior in the I(V) curves. The I/V curves of our investigated samples are flat and the absence of Coulomb staircases is evident.

Spectroscopic ellipsometry is a complementary technique to the STS measurements for the investigation of the electronic band structure and defect electronic states in nanomaterials. Additional motivation for using ellipsometry in this study lies in the fact that it is very sensitive method to the changes in the surface structure of the nanocrystals, where most of the defects are concentrated.

Optical properties of differently synthesized cerium dioxide nanocrystals were investigated using spectroscopic ellipsometry in the 2–5 eV spectral region. From the measurements of ellipsometric angles Ψ and Δ, by using the two-phase model approximation (CeO$_{2-y}$ nanoparticles/air), we have obtained the pseudo-dielectric function spectra.[40] The measurement of pseudo-dielectric function enables direct determination of real and imaginary parts of the complex dielectric function $\varepsilon(E) = \varepsilon_1(E) + i\varepsilon_2(E)$. The standard critical points (CPs) model for the dielectric function, in the case of 1D and 3D CPs (m $\neq$ 0), is given by[41–43]

$$\varepsilon(E) = C - A e^{i\varphi}(E - E_0 + i\Gamma)^m, \qquad (4)$$

and for 2D, CPs (m $=$ 0) can be written as

$$\varepsilon(E) = C - A e^{i\varphi}\ln(E - E_0 + i\Gamma), \qquad (5)$$

where A, E_0, Γ, and φ are the amplitude, energy threshold, broadening, and the excitonic phase angle of CP, respectively. The factor m determines the dimensionality of the critical point (m $= -1/2$ for 1D, m $= 0$ for 2D and m $= 1/2$ for 3D CP). To perform a line-shape analysis of the structures in the $\varepsilon(E)$ and to obtain the parameters of the critical points for ceria nanocrystals, we used the expressions from the articles of Albornoz *et al.*[44] and León *et al.*[45] to fit the second derivative spectra of the imaginary part of the dielectric function (d$^2\varepsilon_2$/dE^2).

The second derivative spectra of ε_2 (E) (open symbols) for all investigated samples are shown in Fig. 4(a), together with numerical fits (solid lines) based on CP model. An appropriate level of smoothing was applied in order to suppress the noise in the derivative spectra without distorting the line shape. We have used six critical points to describe the observed features in the spectra and the obtained parameters are presented in Table I.

The value of excitonic phase angle φ, for each CP, was obtained as the best-fit parameter. The obtained φ values were non-integer multiples of $\pi/2$ ($0 \leq \varphi \leq \pi/2$ for 3D and 1D CP and $0 \leq \varphi \leq 3\pi/2$ for 2D CP), due to the excitonic effects[43,44] which are expected to be more pronounced in confined systems like ceria nanocrystals.

Numerical modeling of ellipsometry data was carried out having in mind that defect structure of ceria nanocrystals can be well described by the core-shell model.[20] According
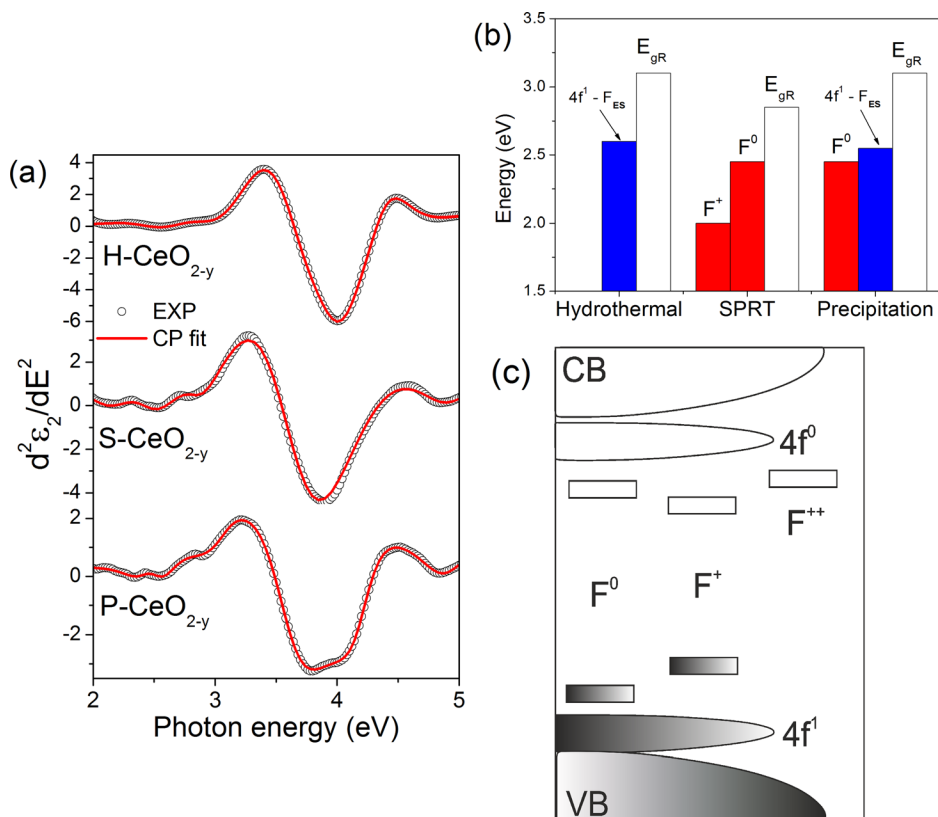
FIG. 4. (a) Numerical fits of the $d^2\varepsilon_2/dE^2$ spectra (open symbols) using the CP lineshape analysis is given by solid (red) lines, (b) energy values of the reduced band gap and defect electronic states transitions obtained from CP model fitting, and (c) schematic representation of the electronic band gap structure of CeO_{2-y} nanocrystals.

to this model, the surface shell of ceria nanocrystals is defect rich,[20] whereas the core is essentially bulk-like CeO_2. Therefore, the interband transitions related to the fundamental band gap features were well fitted with 3D line shape. The interband transitions which originate from defect shell were best fitted with 2D line shape, whereas for the electronic transition related to the surface oxygen species, 1D line shape yielded slightly better fit than 2D line shape.

The most prominent peak at around 4 eV in the $d^2\varepsilon_2/dE^2$ spectra of the synthesized samples from Fig. 4(a) corresponds to the optical band gap of bulk cerium dioxide, i.e., the transition from O 2p to the Ce $4f^0$ states.[29] This transition is split into two states ($^2F_{5/2}$ and $^2F_{7/2}$), because of the spin−orbit interaction,[46] so we fitted the main peak with two CPs (peaks 4 and 5 in Table I). The first CP is located at

3.6 eV for $S-CeO_{2-y}$ and $P-CeO_{2-y}$ and at 3.73 eV for $H-CeO_{2-y}$ sample. Obtained energy values match the energy of optical band gap transition in CeO_2.[47] Second CP of this transition, at 4.2 eV for $S-CeO_{2-y}$ and $P-CeO_{2-y}$ samples and at 4.27 eV for $H-CeO_{2-y}$ sample, corresponds to the transition from O 2p states into the upper part ($^2F_{7/2}$) of the $4f^0$ states. We can observe from fitting parameters that spin−orbit splitting in the $S-CeO_{2-y}$ and $P-CeO_{2-y}$ samples ($\Delta_{SO} = 0.6$ eV) is higher than for bulk sample ($\Delta_{SO} = 0.25$ eV), probably due to the strong electron confinement in nanocrystals.[48] The $O2p \rightarrow 4f^0$ transition is characteristic transition for bulk CeO_2 so it was treated as 3D CP.

In the lower energy region from the main peak in Fig. 4(a), additional structures appear in the $d^2\varepsilon_2/dE^2$ spectra which originate from the presence of defect electronic states in the CeO_{2-y} gap. The assignments of these CPs are given as follows:

- *F center states*

The CPs at the lowest energies (2–2.45 eV) from Table I were ascribed to different F center types of defects. F centers are characteristic for defect-rich shell of ceria nanocrystals and in a case of interband transitions which correspond to F center states, the best fits were obtained with 2D line shape.

In a case of $S-CeO_{2-y}$ sample, CP at 2 eV corresponds to the transition marked with arrows in Fig. 3(b). Previous results on HfO_2 (Ref. 34) and TiO_2 (Ref. 35) have pointed out that singly occupied vacancies (F^+ centers) introduce electronic states deeper in the band gap. Therefore, we ascribed CP at 2 eV to the F^+ center type of defect. These deep localized states appear only in $S-CeO_{2-y}$ sample. In a

TABLE I. Fit parameters of the CPs.

CP	$H-CeO_{2-y}$	$S-CeO_{2-y}$	$P-CeO_{2-y}$
E_1 (eV)	…	2	2.45
Γ_1 (eV)	…	0.32	0.2
E_2 (eV)	2.6	2.44	2.55
Γ_2 (eV)	0.25	0.3	0.24
E_3 (eV)	3.2	2.86	3.1
Γ_3 (eV)	0.46	0.24	0.28
E_4 (eV)	3.73	3.6	3.59
Γ_4 (eV)	0.36	0.58	0.43
E_5 (eV)	4.27	4.2	4.2
Γ_5 (eV)	0.24	0.67	0.24
E_6 (eV)	4.8	4.95	4.96
Γ_6 (eV)	0.4	0.45	0.36

case of P$-$CeO$_{2-y}$ sample, the CP at 2.45 eV corresponds to the transition marked with asterisk in Fig. 3(b). This interband transition can correspond to F^0 type of defects for which the characteristic is that the occupied/empty electronic states lie closer to the valence/conduction band.[34] For H$-$CeO$_{2-y}$ sample, there are no pronounced CP peaks which can correspond to F$^+$ or F^0 states and we have not observed any additional states in the differential conductance spectra of this sample too. Therefore, it is reasonable to assume that the concentration of the F centers is very low, which is in accordance with the Raman spectrum of this sample.

- *4f^1 – F center empty states (4f^1 – Fes)*
  Second CP from Table I at energies 2.55 (2.6) eV for P$-$CeO$_{2-y}$ (H$-$CeO$_{2-y}$), can correspond to the transition from 4f^1 state to the empty states of F centers (Fes). Since this transition involves electronic states characteristic for the defect-rich shell of ceria nanocrystals, the best fit was obtained with 2D line shape.

  In the case of S$-$CeO$_{2-y}$ sample, the second CP in the d$^2\varepsilon_2$/dE^2 spectra at 2.44 eV (marked with asterisk in Fig. 3(b)) can correspond to the transition between full and empty electronic states of F^0 type of defects. This transition is already seen in the STS spectrum of P$-$CeO$_{2-y}$ sample.

- *4f^1 → 4f^0 transition*
  The critical-point energies at 2.85 eV, 3.1 eV, and 3.2 eV for S$-$CeO$_{2-y}$, P$-$CeO$_{2-y}$, and H$-$CeO$_{2-y}$ samples can originate from 4f^1 → 4f^0 transition. The 2D line shape yielded the best fit for this transition. The appearance of 4f^1 and F center defect states reduces the band gap of CeO$_{2-y}$ samples[49,50] and shifts the absorption edge more towards the visible region. Such behavior is contrary to the quantum confinement model predictions (increase in energy gap (E$_g$) with decreasing particle size). Although the confinement effect is present, particularly for S$-$CeO$_{2-y}$ and P$-$CeO$_{2-y}$ nanocrystalline samples, the dominant role in the band gap behavior with decreasing particle size comes from the formation of 4f^1 and F center defect states in the gap.[50] As 4f^1 → 4f^0 transition reduces the optical band gap of ceria, we named it as reduced band gap (E$_{gR}$). According to the selection rules for dipole transition such a transition would be generally forbidden or would have low oscillator strength. However in nanosystems, this transition can be allowed due to the breaking of the selection rules in confined nanocrystals.

Finally, the critical-point energies at 4.8 eV, 4.95 eV, and 4.96 eV, in the d$^2\varepsilon_2$/dE^2 spectra of H$-$CeO$_{2-y}$, S$-$CeO$_{2-y}$, and P$-$CeO$_{2-y}$ samples, may be assigned to the oxygen species adsorbed on the surface of CeO$_{2-y}$ nanocrystals.[51] The electronic transitions ascribed to adsorbed oxygen were slightly better fitted with 1D than 2D lineshape. The adsorbed oxygen probably form linear chains on the ceria surface, similar to the one-dimensional Pt oxide chains formed when the atomic oxygen covered the Pt(111) surface.[52] Critical point analysis of chain-like structures can be well described with 1D CPs.[53]

In Fig. 4(b) presented are the reduced band gap value energies together with the corresponding energies of F center defect electronic states transitions obtained from CP model fitting, whereas in Fig. 4(c), proposed is the schematic representation of the electronic band structure of defective CeO$_{2-y}$ nanocrystals. It is important to mention here that there is some discrepancy in the critical point energies observed in ellipsometric spectra and energies between the corresponding peaks in the differential conductance spectra. This can be explained by the fact that STS measurements were carried out on a single CeO$_{2-y}$ nanocrystals, whereas the ellipsometric measurements were performed on the nanocrystalline samples composed of different crystallite sizes which contribute to the final CP energy with different weights.

It is known from the literature that the formation of the F centers in ceria nanostructures is responsible for the appearance of very interesting effect, the ferromagnetism (FM) at room temperature. Extensive studies have been performed on the magnetic properties of ceria nanostructures and the results have demonstrated that charge state of oxygen vacancy is crucial for the establishment of the ferromagnetism in CeO$_2$.[9,54–58] It is already shown[56,57] that F$^+$ center type of defects mediates ferromagnetic ordering in CeO$_{2-y}$, whereas in a case of F^0 centers, electrons are in a singlet (S = 0) state and can only mediate weak antiferromagnetic interaction. In order to support the obtained results and the arguments on the formation of F centers in our samples, we have measured the magnetization vs. magnetic field for P$-$CeO$_{2-y}$ and S$-$CeO$_{2-y}$ samples at room temperature and compared it with bulk CeO$_2$ sample. These spectra are presented in Fig. 5. The bulk sample shows weak diamagnetic response, what is expected for stoichiometric cerium dioxide with Ce^{4+} ions in the 4f^0 electronic configuration. On the other hand, S$-$CeO$_{2-y}$ sample exhibits ferromagnetism at room temperature indicating that majority of oxygen vacancies, as the main mediators of FM ordering, is in the F$^+$ charge state. For P$-$CeO$_{2-y}$ sample, magnetization behavior is very similar to the bulk sample leading us to conclude that majority of oxygen vacancies is in the F^0 charge state. These findings are in complete agreement with conclusions from Ref. 36.
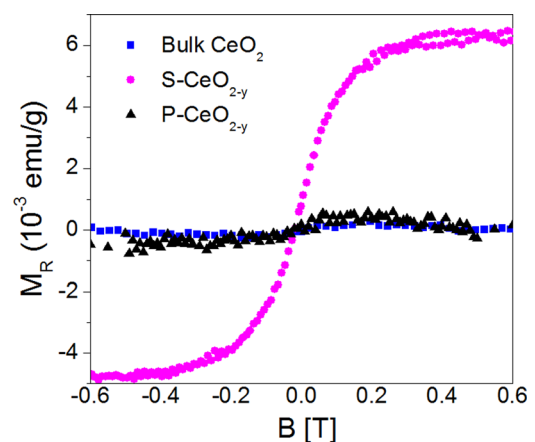

FIG. 5. Room temperature magnetization versus magnetic field for bulk, P$-$CeO$_{2-y}$, and S$-$CeO$_{2-y}$ samples.

This study has demonstrated that several types of F centers can be formed in the nanocrystals depending on the synthesis method. Particle size has important influence on the formation of F centers, since we have seen that $H-CeO_{2-y}$ sample with the largest crystallite size has the lowest concentration of F center defects. In a case of samples with much lower crystallite sizes ($S-CeO_{2-y}$ and $P-CeO_{2-y}$), the charge state of oxygen vacancies, i.e., the type of F centers formed, has significant influence on the energy band structure and magnetic properties of defective CeO_{2-y} nanomaterials.

IV. SUMMARY

The CeO_{2-y} nanopowders were synthesized by hydrothermal, SPRT, and precipitation methods. XRD and Raman spectroscopy measurements showed that ceria sample produced by hydrothermal method had the largest crystallite size, whereas the CeO_{2-y} samples produced by SPRT and precipitation methods, had much smaller crystallite size. The highest oxygen vacancy concentration was found in the sample produced by precipitation method. Combined STM/STS and ellipsometry measurements revealed that different types of F center defects were formed in the band gap of CeO_{2-y} samples. In the case of $S-CeO_{2-y}$ sample, both F^0 and F^+ centers were formed inside the gap, whereas for $P-CeO_{2-y}$ sample, only F^0 centers were detected. In the $H-CeO_{2-y}$ sample, no similar defect states were detected. Magnetic measurements confirmed our findings. By summarizing the obtained results, we have concluded that not only the concentration but also the charge state of oxygen vacancies, i.e., the formation of different types of F centers has significant impact on the band structure and optical and magnetic performance of the synthesized ceria nanocrystals.

ACKNOWLEDGMENTS

[1]H. C. Yao and Y. F. Yu Yao, J. Catal. **86**, 254 (1984).

[2]E. C. Su, C. N. Montreuil, and W. G. Rothschild, Appl. Catal. **17**, 75 (1985).

[3]B. E. Gillman and S. D. Jacobs, Appl. Opt. **37**, 3498 (1998).

[4]A. Walkenhorst, M. Schmitt, H. Adrian, and K. Petersen, Appl. Phys. Lett. **64**, 1871 (1994).

[5]S. Kanakaraju, S. Mohan, and A. K. Sood, Thin Solid Films **305**, 191 (1997).

[6]H. J. Beie and A. Gneorich, Sens. Actuators, B **4**, 393 (1991).

[7]B. C. H. Steele, Solid State Ionics **129**, 95 (2000).

[8]B. C. H. Steele and A. Heinzel, Nature (London) **414**, 345 (2001).

[9]X. Chen, G. Li, Y. Su, X. Qui, L. Li, and Z. Zou, Nanotechnology **20**, 115606 (2009).

[10]A. Thurber, K. M. Reddy, V. Shutthanandan, M. H. Engelhard, C. Wang, J. Hays, and A. Punnoose, Phys. Rev. B **76**, 165206 (2007).

[11]L. Truffault, Q. W. Yao, D. Wexler, I. P. Nevirkovets, K. Konstantinov, T. Devers, and S. Nightingale, J. Nanosci. Nanotechnol. **11**, 4019 (2011).

[12]A. Corma, P. Atienzar, H. García, and J.-Y. Chane-Ching, Nature Mater. **3**, 394 (2004).

[13]M. Lira-Cantu and F. C. Krebs, Sol. Energy Mater. Sol. Cells **90**, 2076 (2006).

[14]A. Verma, A. K. Bakhshi, and S. A. Agnihotry, Sol. Energy Mater. Sol. Cells **90**, 1640 (2006).

[15]F. Chen, Y. Cao, and D. Jia, Appl. Surf. Sci. **257**, 9226 (2011).

[16]P. Ji, J. Zhang, F. Chen, and M. Anpo, Appl. Catal., B **85**, 148 (2009).

[17]X. Liu, S. Chen, and X. Wang, J. Lumin. **127**, 650 (2007).

[18]N. Shehata, K. Meehan, I. Hassounah, M. Hudait, N. Jain, M. Clavel, S. Elhelw, and N. Madi, Nanoscale Res. Lett. **9**, 231 (2014).

[19]G. K. Williamson and W. Hall, Acta Metall. **1**, 22 (1953).

[20]L. Wu, H. J. Wiesmann, A. R. Moodenbaugh, R. F. Klie, Y. Zhu, D. O. Welch, and M. Suenaga, Phys. Rev. B **69**, 125415 (2004).

[21]Z. V. Popović, Z. D. Dohčević-Mitrović, N. Paunović, and M. Radović, Phys. Rev. B **85**, 014302 (2012).

[22]W. H. Weber, K. C. Hass, and J. R. McBride, Phys. Rev. B **48**, 178 (1993).

[23]J. E. Spanier, R. D. Robinson, F. Zhang, S. W. Chan, and I. P. Herman, Phys. Rev. B **64**, 245407 (2001).

[24]J. R. McBride, K. C. Hass, B. D. Poindexter, and W. H. Weber, J. Appl. Phys. **76**, 2435 (1994).

[25]M. D. Hernandez-Alonso, A. B. Hugria, A. Martinez-Arias, J. M. Coronado, J. C. Conesa, J. Soria, and M. Fernandez-Garcia, Phys. Chem. Chem. Phys. **6**, 3524 (2004).

[26]Z. D. Dohčević-Mitrović, M. Grujić-Brojčin, M. Šćepanović, Z. V. Popović, S. Bošković, B. Matović, M. Zinkevich, and F. Aldinger, J. Phys.: Condens. Matter **18**, S2061 (2006).

[27]N. Yao and Z. L. Wang, *Handbook of Microscopy for Nanotechnology* (Kluwer Academic Publisher, Boston, 2005).

[28]D. D. Koelling, A. M. Boring, and J. H. Wood, Solid State Commun. **47**, 227 (1983).

[29]N. V. Skorodumova, R. Ahuja, S. I. Simak, I. A. Abrikosov, B. Johansson, and B. I. Lundqvist, Phys. Rev. B **64**, 115108 (2001).

[30]M. A. Henderson, C. L. Perkins, M. H. Engelhard, S. Thevuthasan, and C. H. F. Peden, Surf. Sci. **526**, 1 (2003).

[31]J. F. Jerratsch, X. Shao, N. Nilius, H. J. Freund, C. Popa, M. V. Ganduglia-Pirovano, A. M. Burow, and J. Sauer, Phys. Rev. Lett. **106**, 246801 (2011).

[32]X. Han, J. Lee, and H. I. Yoo, Phys. Rev. B **79**, 100403(R) (2009).

[33]T. König, G. H. Simon, H. P. Rust, G. Pacchioni, M. Heyde, and H. J. Freund, J. Am. Chem. Soc. **131**, 17544 (2009).

[34]D. Muñoz Ramo, J. L. Gavartin, A. L. Shluger, and G. Bersuker, Phys. Rev. B **75**, 205336 (2007).

[35]N. Serpone, J. Phys. Chem. B **110**, 24287 (2006).

[36]S. Aškrabić, Z. D. Dohčević-Mitrović, V. D. Araújo, G. Ionita, M. M. de Lima, Jr., and A. Cantarero, J. Phys. D: Appl. Phys. **46**, 495306 (2013).

[37]M. Herrera-Zaldívar, J. Valenzuela-Benavides, and U. Pal, Opt. Mater. **27**, 1276 (2005).

[38]W. Lu, B. Wang, K. Wang, X. Wang, and J. G. Hou, Langmuir **19**, 5887 (2003).

[39]T. Baron, P. Gentile, N. Magnea, and P. Mur, Appl. Phys. Lett. **79**, 1175 (2001).

[40]H. Fujiwara, *Spectroscopic Ellipsometry Principles and Applications* (John Wiley and Sons Ltd., Chichester, 2003).

[41]P. Lautenschlager, M. Garriga, S. Logothetidis, and M. Cardona, Phys. Rev. B **35**, 9174 (1987).

[42]S. Logothetidis, P. Lautenschlager, and M. Cardona, Phys. Rev. B **33**, 1110 (1986).

[43]L. Viña and M. Cardona, Phys. Rev. B **34**, 2586 (1986).

[44]J. G. Albornoz, R. Serna, and M. León, J. Appl. Phys. **97**, 103515 (2005).

[45]M. León, S. Levcenko, A. Nateprov, A. Nicorici, M. Merino, R. Serna, and E. Arushanov, J. Phys. D: Appl. Phys. **40**, 740 (2007).

[46]M. Marabelli and P. Wachter, Phys. Rev. B **36**, 1238 (1987).

[47]S. Guo, H. Arwin, S. N. Jacobsen, K. Järrendahl, and U. Helmersson, J. Appl. Phys. **77**, 5369 (1995).

[48]O. Voskoboynikov, C. P. Lee, and O. Tretyak, Phys. Rev. B **63**, 165306 (2001).

[49]I. Kosacki and H. U. Anderson, Ionics **6**, 294 (2000).

[50]P. Patsalas, S. Logothetidis, L. Sygellou, and S. Kennou, Phys. Rev. B **68**, 035104 (2003).

[51]A. Bensalem, J. C. Muller, and F. Bozon-Verduraz, J. Chem. Soc. Faraday Trans. **88**, 153 (1992).

[52]S. P. Devarajan, J. A. Hinojosa, Jr., and J. F. Weaver, Surf. Sci. **602**, 3116 (2008).

[53]S. Loughin, R. H. French, L. K. De Noyer, W.-Y. Ching, and Y.-N. Xu, J. Phys. D: Appl. Phys. **29**, 1740 (1996).

[54]A. Sundaresan, R. Bhargavi, N. Rangarajan, U. Siddesh, and C. N. R. Rao, Phys. Rev. B **74**, 161306(R) (2006).

[55]A. Tiwari, V. M. Bhosle, S. Ramachandran, N. Sudhakar, J. Narayan, S. Budak, and A. Gupta, Appl. Phys. Lett. **88**, 142511 (2006).

[56]L. R. Shah, B. Ali, H. Zhu, W. G. Wang, Y. Q. Song, H. W. Zhang, S. I. Shah, and J. Q. Xiao, J. Phys.: Condens. Matter **21**, 486004 (2009).

[57]N. Paunović, Z. Dohčević-Mitrović, R. Scurtu, S. Aškrabić, M. Prekajski, B. Matović, and Z. V. Popović, Nanoscale **4**, 5469 (2012).

[58]V. Fernandes, P. Schio, A. J. A. de Oliveira, W. A. Ortiz, P. Fichtner, L. Amaral, I. L. Graff, J. Varalda, N. Mattoso, W. H. Schreiner, and D. H. Mosca, J. Phys.: Condens. Matter **22**, 216004 (2010).

Infrared study of plasmon–phonon coupling in pure and Nd-doped CeO$_{2-y}$ nanocrystals

You may also be interested in:

Infrared study of plasmon–phonon coupling in pure and Nd-doped CeO₂₋$_y$ nanocrystals

M Radović[1], **Z Dohčević-Mitrović**[1], **N Paunović**[1], **S Bošković**[2], **N Tomić**[1]
N Tadić[3] **and I Belča**[3]

[1] Center for Solid State Physics and New Materials, Institute of Physics, University of Belgrade, 11080 Belgrade, Serbia
[2] Institute for Nuclear sciences 'Vinča', Materials Science Laboratory, University of Belgrade, Belgrade, Serbia
[3] Faculty of Physics, University of Belgrade, 11000 Belgrade, Serbia

E-mail: marrad@ipb.ac.rs

CrossMark

Abstract

Plasmon-longitudinal-optical (LO) phonon interaction in pure and Nd-doped CeO_{2-y} nanocrystals was investigated by measuring far–infrared reflectivity spectra in the 100–700 cm^{-1} spectral range at room temperature. Analysis of the obtained results revealed that the presence of free charge carriers becomes significant with the particle size decrease to nanometer range and increase of lattice defects. The free charge carriers were found to be responsible for a plasmon mode which coupled strongly with two LO phonon modes of ceria. The presence of more pronounced low-frequency Drude tail and the screening of the phonon modes in Nd-doped CeO_{2-y} nanocrystals implied that the Plasmon-LO phonon interaction increased with doping. Factorized and additive dielectric function models were applied to deduce about the coupled and decoupled LO phonon frequencies and the structure of the decoupled plasmon mode in pure and Nd-doped CeO_{2-y} nanocrystals. These models were combined with Bruggeman effective medium approximation in order to properly describe the influence of porosity on the infrared reflectivity spectra. With increasing dopant content, the decoupled plasmon mode exhibited redshift and damping decrease implying that doping induced semiconductor–to–metalic state transition took place.

Keywords: Nd-doped ceria nanocrystals, infrared spectroscopy, plasmon–phonon interaction

(Some figures may appear in colour only in the online journal)

1. Introduction

Cerium dioxide (CeO_2, ceria) is a wide band gap semiconductor with ionic and partially covalent bonding nature [1, 2], which has received considerable interest due to the variety of applications in advanced technologies. CeO_2-based solid solutions have been acknowledged to be the most promising electrolytes for intermediate temperature solid oxide fuel cells, exhibiting excellent ionic conductivity at intermediate temperatures ($500 - 800°$C) [3, 4], much better than traditional ionic conductors like yttria-stabilized zirconia [3]. With a reduction of particle size, ceria becomes a mixed ionic–electronic conductor [5], because the presence of defects and unsaturated surface bonds leads to the increase

of the free carrier contribution to the overall conductivity. The electrical conductivity of nanocrystalline ceria based materials can be attributed to the small polaron hopping mechanism [6, 7]. It was shown [8, 9] that the electrical conductivity, measured at different temperatures and oxygen partial pressures, is increased with the decreasing size of nanoparticles and is almost 10^4 times greater than in microcrystalline materials [8, 9]. This property can be utilized for gas sensor applications [10].

The influence of free carrier collective excitations (plasmons) on the optical phonon spectra of nanocrystalline ceria, i.e. plasmon–phonon coupling, has not been studied. The infrared (IR) spectroscopy is a nondestructive and widely applied spectroscopic technique for the investigation of the

mechanism of plasmon–phonon coupling in different materials. From the IR reflection spectra of polar semiconductors, both phonon and plasmon excitations can be registered, enabling the direct investigation of the plasmon − phonon interaction mechanism.

In the present paper, the plasmon − phonon interaction in pure and Nd-doped CeO_{2-y} nanocrystals has been investigated by analyzing the IR reflection spectra of these samples. The application of factorized and additive forms of the dielectric function, together with Bruggeman effective medium approximation, allowed the determination of coupled (decoupled) phonon frequencies, damping parameters and the structure of decoupled plasmon mode with doping. Better insight into the plasmon − phonon coupling mechanism in nanocrystalline ceria can be very important because the plasmon − phonon interaction can influence the ceria electrical conductivity properties.

2. Experimental

Undoped CeO_{2-y} nanopowders were prepared using the self-propagating room temperature synthesis and the detailed preparation procedure is described elsewhere [11, 12]. The as-prepared samples were calcinated at 600 and 800°C for 2 h, in order to induce the growth of crystalite size. The Nd-doped samples were doped with 10, 15, 20 and 25 wt% Nd. X-ray diffraction (XRD) technique was used for the characterization of structural properties and the degree of crystallinity of the synthesized nanopowders. Diffraction patterns were recorded over the 2θ range from 20 to 80° on a Siemens D-5000 diffractometer, using Cu Kα radiation The external standard correction was performed using LaB_6 (NIST) powder. Atomic force microscope (AFM) images were taken using the Omicron B002645 SPM PROBE VT AFM 25 in noncontact mode. The IR reflectivity spectra were measured at room temperature in the far-IR region (100–700 cm^{-1}) on a Bomem DA8 spectrometer using the DTGS detector.

3. Models

In this section, a brief overview of the theoretical models used to analyze the measured IR spectra will be presented.

The IR reflectivity spectra of the ionic crystals where large splitting between transverse-optical (TO) and longitudinal-optical (LO) modes is observed [13, 14], are usually fitted with a dielectric function given by the expression [15]:

$$\varepsilon_M = \varepsilon_\infty \prod_j \frac{\omega_{LOj}^2 - \omega^2 + i\omega\gamma_{LOj}}{\omega_{TOj}^2 - \omega^2 + i\omega\gamma_{TOj}}, \qquad (1)$$

where ε_∞ is the high frequency dielectric constant and $\omega_{TO(LO)j}$ and $\gamma_{TO(LO)j}$ are the TO and LO phonon frequencies and damping rates of the corresponding IR mode. This model introduces four adjustable parameters for each TO-LO mode and is used for description of pure phonon properties. In further text it will be named the Lattice Vibrations model (LV). The main disadvantage of this model results from the fact that it does not

take into account the contribution from the electronic excitations i.e. the plasmons and plasmon–phonon coupling.

Most semiconductors have a significant portion of free carriers and a complete description of the far-IR optical properties of semiconductor materials has to take both phonon and plasmon contributions into account. The coexistence of phonons and plasmons usually leads to a strong coupling between plasmons and LO phonons. This effect is most pronounced when the plasma frequency (ω_P) is in the vicinity of the LO phonon frequency. In that case the plasmon–phonon interaction can be described with the factorized form of the dielectric function given by [16, 17]:

$$\varepsilon_M = \varepsilon_\infty \frac{\prod_{j=1}^{m+n} \left(\omega^2 + i\omega\gamma_{LOj} - \omega_{LOj}^2\right)}{\omega^m \prod_{j=1}^{m} \left(\omega + i\gamma_{Pj}\right) \prod_{j=1}^{n} \left(\omega^2 + i\omega\gamma_{TOj} - \omega_{TOj}^2\right)}, \qquad (2)$$

where ω_{TOj} and γ_{TOj} are frequencies and damping rates of the TO modes and γ_P is the plasma damping. This expression gives directly the coupled plasmon-LO phonon frequencies ω_{LOj} and damping rates γ_{LOj} and in further text will be named as the Coupled Plasmon − Phonon (CPP) model.

The extension of the Drude model which has been used to fit the IR reflectivity spectra of conducting oxides is known in the literature as the Double-damping extended Drude model [18]. The additive form of the dielectric function in which the plasmon contribution is expressed by Double-damped Drude term, is composed of two terms:

$$\varepsilon_M = \varepsilon_\infty \left(\prod_j \frac{\omega_{LOj}^2 - \omega^2 + i\omega\gamma_{LOj}}{\omega_{TOj}^2 - \omega^2 + i\omega\gamma_{TOj}} - \frac{\omega_P^2 + i(\gamma_P - \gamma_0)\omega}{\omega(\omega - i\gamma_0)} \right). \qquad (3)$$

The first term represents the phonon contribution and the second term is the plasmon contribution. The $\omega_{TO(LO)j}$ and $\gamma_{TO(LO)j}$ are TO(LO) frequencies and dampings of decoupled phonon modes, whereas the ω_P, γ_P and γ_0 are the plasma frequency and dampings at $\omega = \omega_P$ and $\omega = 0$. This model allows the decoupling of phonon and plasmon contributions and enables to make a difference between the damping (γ_P) at the plasma frequency and the static damping at zero frequency (γ_0). The second term in equation (3) becomes the classical Drude formula for $\gamma_P = \gamma_0$. The application of this model offers more flexibility in numerical fitting and more precise description of the dielectric function response [18]. In further text this model will be named the Decoupled Plasmon − Phonon (DPP) model.

In order to properly analyze the IR spectra of porous nanomaterials, one of the most commonly used models is the Bruggeman effective medium approximation [19, 20]. For the inhomogeneous, binary material, composed of material (ε_M) and air ($\varepsilon_{air} = 1$) with the volume fractions f_M and $1 - f_M$ respectively, the empirical relation for the effective dielectric function (ε_{eff}) can be written as [20]:

$$\left(\frac{\varepsilon_M - \varepsilon_{eff}}{\varepsilon_M + 2\varepsilon_{eff}}\right) f_M + \left(\frac{1 - \varepsilon_{eff}}{1 + 2\varepsilon_{eff}}\right)(1 - f_M) = 0. \qquad (4)$$

J. Phys. D: Appl. Phys. **48** (2015) 065301

M Radović *et al*

Therefore, the effective dielectric function (ε_{eff}) from equation (4) of a pure and Nd-doped CeO_{2-y} porous nanocrystalline sample can be expressed in terms of the dielectic function of material (ε_M) given by equations (1), (2) or (3) and volume fractions of material and air.

The theoretical reflectivity is obtained by using the Fresnel formula:

$$R_{\text{calc}} = \left| \frac{\sqrt{\varepsilon_{\text{eff}}} - 1}{\sqrt{\varepsilon_{\text{eff}}} + 1} \right|^2 . \tag{5}$$

The least-squares fitting procedure between the theoretical (R_{calc}) and experimental (R_{exp}) reflectivity was carried out until the chi-squared value:

$$\chi^2 = \frac{1}{N} \sum_i^N \left(R_{i,\text{exp}} - R_{i,\text{calc}} \right)^2 \tag{6}$$

was minimized, where N is the number of measured points.

4. Results and discussion

A detailed analysis of the XRD spectra of undoped and Nd-doped samples has been already given in [11, 12]. The Nd-doped samples crystallized into a fluorite type structure of CeO_2 with Nd^{3+} ions entering substitutionally into a ceria lattice. The presence of amorphous or any other phase was not detected, even for the highest Nd concentration [11, 12]. The synthesized samples were composed of very small particles in the nanometric range (3–4 nm) [11, 12]. Additionally, the undoped CeO_{2-y} sample was calcinated at 600 and 800°C for 2h in air, in order to compare the structural and vibrational properties of thermally treated and non-treated samples. The XRD spectra of thermally treated samples are given in figure 1(*a*). Characteristic Miller indices are denoted for main diffraction peaks. The average crystallite size and strain values were calculated using the Williamson–Hall method [21, 22] and the obtained values for each sample are presented in figure 1(*a*). In the inset of figure 1(*a*) is presented the Williamson–Hall plot of an as-prepared CeO_{2-y} sample. The calcinated samples exhibited sharper diffraction lines as a consequence of increased crystallite size and much better degree of crystallinity. The XRD pattern of the sample calcinated at 800°C is similar to the XRD spectrum of polycrystalline CeO_2. In figures 1(*b*) and (*c*) are presented AFM images of a ceria sample calcinated at 800°C and of an as-prepared CeO_{2-y} sample. The size of nanocrystals was in good agreement with the average crystallite size obtained from the XRD data.

Bearing in mind that ceria phonon properties are very much dependent on the crystallite size, we first investigated the influence of the particle size on the infrared reflectivity spectra of as-prepared and calcinated samples of CeO_{2-y}. In figure 2 are presented the IR reflectivity spectra of a bulk CeO_2 sample (reconstructed according to the literature data [2]) and calcinated ceria samples with different crystallite sizes, determined from XRD spectra from figure 1. Factor-group analysis for a fluorite type CeO_2 structure, predicts only one triple-degenerate IR active phonon mode of the F_{2u} symmetry, with TO and LO mode frequencies at 218 and 597 cm^{-1}, respectively [2]. In the IR spectrum of the bulk sample, wide reststrahlen band, characteristic for the ionic bond nature, is observed.

With decreasing crystallite size, the reststrahlen band splits into two broad TO-LO modes in the $200 - 550$ cm^{-1} region. The splitting and redshift of both LO modes become more distinct in the sample with the smallest crystallite size (4.2 nm). A similar behavior was previously observed for pure and doped ceria powders [23] and for other nanostructured materials such as porous SiC films [20] and Mn_2O_3 nanocrystals [24]. It is reasonable to expect that the vibrational properties of nanomaterials are changed due to the increased concentration of structural defects (such as oxygen vacancies in ceria) and large number of dangling bonds at the nanoparticles surface, which leads to crystal symmetry breakdown. The lifting of the F_{2u} mode degeneracy in CeO_{2-y} nanocrystals can be ascribed to the long-range Coulomb field which splits the degeneracy of the polar modes in nanocrystals [24]. Another possible explanation for the observed splitting of the restrahlen band was ascribed to the multiphonon (anharmonic) effects [23].

From figure 2, for the CeO_{2-y} sample with the smallest crystallite size, it can be seen that the phonon modes are significantly damped and that the plasmonic background becomes prominent. The presence of lattice defects in the form of oxygen vacancies and consequently free charge carriers, is responsible for the appearance of the plasmonic background. The formation of an oxygen vacancy in the ceria lattice is followed by the localization of two electrons into empty Ce $4f^0$ orbitals [25], causing the change in the valence state of neighboring Ce ions from 4^+ to 3^+. With decreasing particle size, the concentration of oxygen vacancies increases. The electrons tend to be localized not only on the Ce sites, but also on the vacancy sites, giving rise to the formation of the *F*-center defect states [26, 27]. The electrons localized on vacancy sites behave like free charge carriers, which can significantly contribute to the increasing of ceria electrical conductivity as the crystallite size decreases [10]. Our previous Raman spectroscopy analysis of nonstoichiometric nanosized ceria [28] have demonstrated that anomalous broadening of the Raman F_{2g} mode can be ascribed to the electron-molecular vibrational coupling effect due to the increased concentration of charge carriers at the Fermi surface. It was shown that the delocalization of electrons onto oxygen vacancies causes semiconductor–to–metallic state transition in highly oxygen deficient nanosized ceria. Therefore, the electronic contribution to the dielectric function has to be properly taken into account in the analysis of the IR reflectivity spectra of the nanocrystalline CeO_{2-y} samples.

The IR reflectivity spectrum of CeO_{2-y} nanocrystals, with the smallest crystallite size (4.2 nm in figure 2), was analyzed using two models for plasmon − phonon interaction. The first one was the CPP model, (equation (2)), which enables to directly obtain coupled plasmon − phonon frequencies and dampings. The second one was the DPP model which was used to obtain the LO mode parameters of the decoupled phonons and plasmons, (equation (3)). These two models were

J. Phys. D: Appl. Phys. **48** (2015) 065301

M Radović *et al*
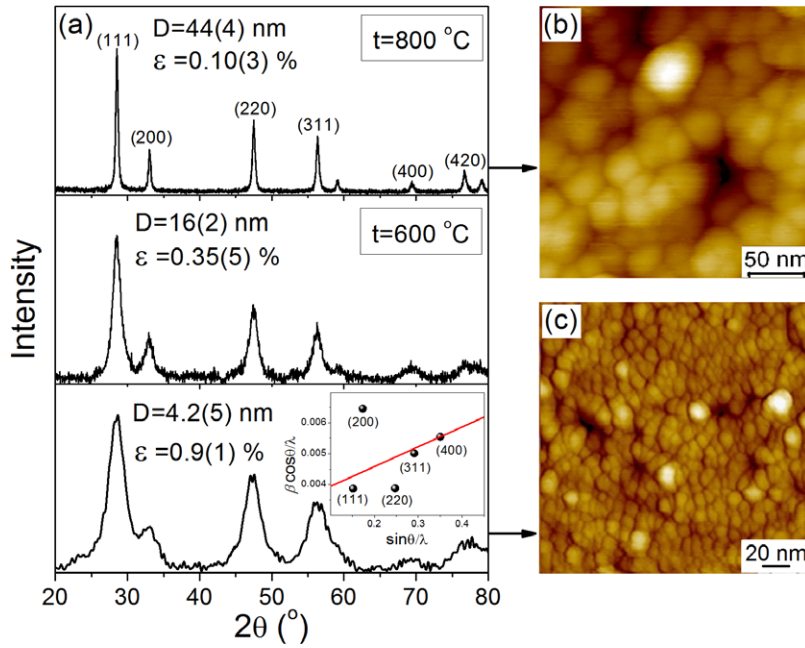
Figure 1. (*a*) XRD patterns of as-prepared and thermally treated CeO_{2-y}, together with the crystallite size (*D*) and strain (*ε*) values. The inset presents the Williamson–Hall plot of as-prepared CeO_{2-y}. AFM images of (*b*) CeO_{2-y} sample calcinated at 800°C and (*c*) as-prepared CeO_{2-y} sample.
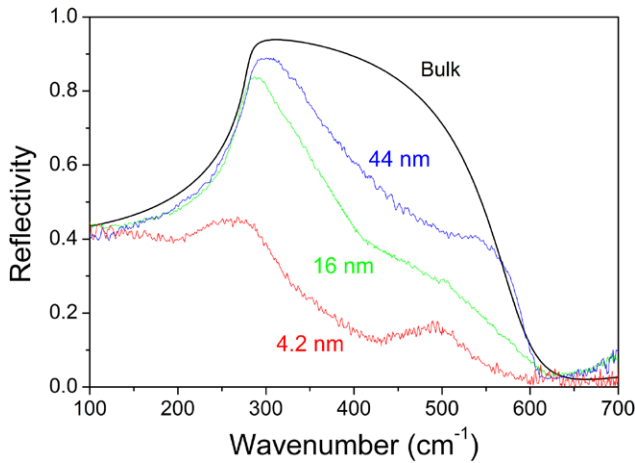
Figure 2. IR reflectivity spectra of CeO_{2-y} nanocrystals with different crystallite sizes and theoretical curve for bulk sample according to the data taken from [2].

combined with Bruggeman effective medium approximation (equation (4)) in order to properly include the influence of material porosity f_M on the resulting IR spectra. The dielectric function model which takes into account only the pure lattice vibrations (LV model given by equation (1)) was also applied. A comparison between the theoretical models and the experimental spectrum for a CeO_{2-y} sample is shown in figure 3. In all applied models, the reflectivity spectrum of the CeO_{2-y} sample was fitted with two oscillators (due to the observed splitting of the restsrahlen band).

From figure 3, it can be seen that LV model did not give a good fit of the experimental data in the frequency region bellow $200\,cm^{-1}$, because of the contribution of free charge carriers. On the contrary, both the CPP and DPP models gave satisfactory fits of the reflectivity data.
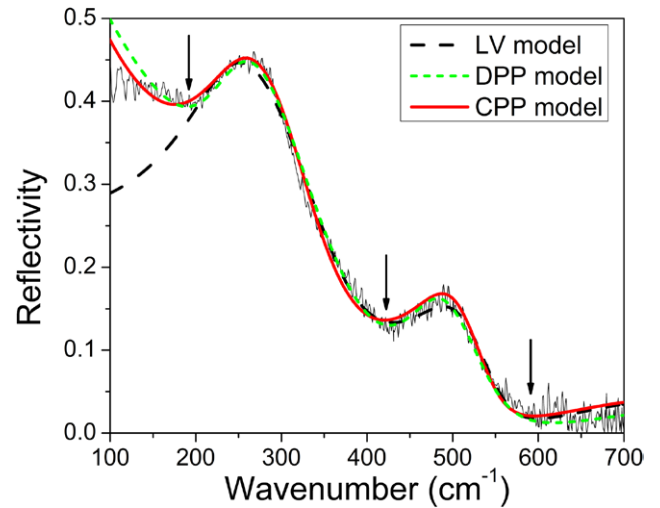
Figure 3. IR reflectivity spectrum of a CeO_{2-y} nanocrystalline sample (crystallite size 4.2 nm), together with theoretical fits using the LV, DPP and CPP models. The arrows mark the reflectivity minima.

The plasmon-LO phonon coupling in the nanocrystalline CeO_{2-y} sample was analyzed by the CPP model, assuming that the plasmon mode is coupled with two LO phonon modes of the nanocrystalline CeO_{2-y} sample. In that case, the equation (2) becomes [17]:

$$\varepsilon_M = \varepsilon_\infty \frac{\left(\omega^2 - \omega_{LO1}^2 + i\omega\gamma_{LO1}\right)\left(\omega^2 - \omega_{LO2}^2 + i\omega\gamma_{LO2}\right)\left(\omega^2 - \omega_{LO3}^2 + i\omega\gamma_{LO3}\right)}{\omega\left(\omega + i\gamma_P\right)\left(\omega^2 - \omega_{TO1}^2 + i\omega\gamma_{TO1}\right)\left(\omega^2 - \omega_{TO2}^2 + i\omega\gamma_{TO2}\right)}.$$

(7)

From this model, the reflection spectrum minima occur for the eigenfrequencies ω_{LOj} (*j* = 1–3) [16], where the coupling between plasmon and two LO phonons manifests as the appearance of an additional longitudinal plasmon − phonon mode.

Table 1. Fitting parameters obtained by using the Coupled Plasmon–Phonon (CPP) model. The estimated errors are given in parenthesis.

Sample	f_M	γ_P	ω_{TO1}	γ_{TO1}	ω_{LO1}	γ_{LO1}	ω_{TO2}	γ_{TO2}	ω_{LO2}	γ_{LO2}	ω_{LO3}	γ_{LO3}	χ^2
	(± 0.03)	(± 10)	(± 5)	(± 10)	(± 5)	(± 15)	(± 5)	(± 10)	(± 5)	(± 15)	(± 5)	(± 15)	
CeO_{2-y}	0.8	210	248	120	370	155	492	105	545	75	210	290	0.0012
10%Nd	0.72	208	248	107	360	180	480	250	549	150	210	290	0.0013
15%Nd	0.61	118	240	176	336	110	477	210	552	190	185	205	0.001
20%Nd	0.56	90	244	95	343	165	480	130	546	110	193	108	0.0023
25%Nd	0.81	130	245	175	332	159	485	180	546	150	173	120	0.0041

Table 2. Fitting parameters obtained by using the Decoupled Plasmon–Phonon (DPP) model. The estimated errors are given in parenthesis.

Sample	f_M	ω_P	γ_P	γ_0	ω_{TO1}	γ_{TO1}	ω_{LO1}	γ_{LO1}	ω_{TO2}	γ_{TO2}	ω_{LO2}	γ_{LO2}	χ^2
	(± 0.03)	(± 5)	(± 15)	(± 15)	(± 5)	(± 10)	(± 5)	(± 15)	(± 5)	(± 10)	(± 5)	(± 15)	
CeO_{2-y}	0.8	450	360	330	245	100	300	45	479	100	505	75	0.0017
10%Nd	0.72	440	360	330	243	98	319	25	477	195	500	145	0.0015
15%Nd	0.61	315	289	151	243	190	273	78	475	190	515	110	0.001
20%Nd	0.56	310	180	83	246	97	299	110	475	110	515	107	0.0021
25%Nd	0.81	238	140	103	249	148	290	145	480	130	509	115	0.0042

In our case, this new mode, ω_{LO3}, corresponds to the reflection minimum at ~200 cm^{-1} in the reflectivity spectrum of the CeO_{2-y} sample. From the CPP model, the plasma frequency can be determined using the following equation [16, 17]:

$$\omega_P = \frac{\omega_{LO1}\omega_{LO2}\omega_{LO3}}{\omega_{TO1}\omega_{LO2}}, \tag{8}$$

and the frequencies of the coupled plasmon − phonon mode can be obtained by putting $\varepsilon_M = 0$ in the equation (7) [16, 17]:

$$\Omega_{LOj} = \sqrt{\omega_{LOj}^2 + \frac{1}{4}\gamma_{LOj}^2}. \tag{9}$$

The fitting parameters obtained from the CPP model, which yielded the best fit to the reflectivity spectrum for the CeO_{2-y} sample, are presented in table 1. The best fit parameters obtained from DPP model are presented in table 2. The values of plasma frequency (ω_P) and coupled plasmon–phonon modes (Ω_{LO1}, Ω_{LO2}) obtained from equations (8) and (9) are given in table 3. The value of the high frequency dielectric constant $\varepsilon_\infty = 4$, for nanocrystalline CeO_{2-y}, was used in both applied theoretical models. The reduced chi-squared values are given in the last column of tables 1 and 2.

From the fit parameters for the CeO_{2-y} sample, it can be concluded that the eigenfrequencies of the coupled (ω_{LO1} and ω_{LO2}) plasmon-LO phonon modes are shifted to higher energies with respect to the decoupled LO phonon frequencies (ω_{LO1} and ω_{LO2}). The frequency shift and increased damping of the coupled longitudinal modes can be assigned to the strong plasmon–phonon interaction. The TO frequencies of the corresponding modes are not affected by plasmon − phonon interaction, as expected.

Further, we investigated how Nd doping influences the plasmon–phonon interaction in CeO_{2-y} nanocrystals. In the IR refelctivity spectra of Nd-doped samples, presented in figure 4, the low frequency Drude tail and the screening of the phonon modes became pronounced. Therefore, the IR spectra of doped samples were fitted by using the CPP and
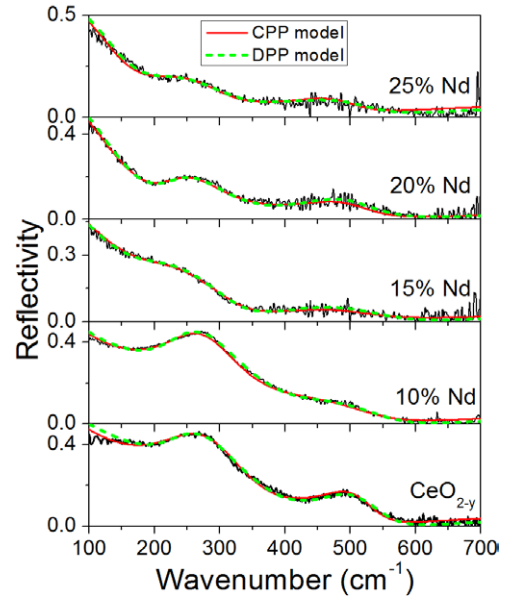
Figure 4. IR reflectivity spectra of pure and Nd-doped samples, together with theoretical fits obtained by CPP and DPP models.

DPP dielectric function models as previously in the case of the undoped CeO_{2-y} sample. In figure 4 are shown the IR reflectivity spectra of undoped and Nd-doped CeO_{2-y} nanocrystals together with theoretical fits obtained by the applied models.

The best fit parameters for Nd-doped samples, obtained from the CPP and DPP models, are given in tables 1 and 2. The materials volume fraction f_M decreased with Nd doping up to 20% of Nd, after which approaches the value for pure CeO_{2-y}. The estimated f_M is in good correlation with specific surface area (S_{BET}) measurements performed earlier on Nd-doped samples. It was found that doping with Nd cations had increased the porosity of ceria nanocrystals except for the sample doped with 25% of Nd for which the porosity decreased [12]. It is worth mentioning that the increased porosity can be also a reason for lower reflectivity of pure and

J. Phys. D: Appl. Phys. 48 (2015) 065301

M Radović *et al*

Table 3. Calculated values of the plasma frequency and coupled plasmon–phonon modes. The estimated errors are given in parenthesis.

Sample	ω_P	Ω_{LO1}	Ω_{LO2}
	(±5)	(±5)	(±5)
CeO_{2-y}	347	378	546
10%Nd	349	371	554
15%Nd	300	340	560
20%Nd	308	353	549
25%Nd	264	341	551

doped nanocrystalline ceria samples compared to the reflectivity of the bulk counterpart.

From the reflectivity spectra of Nd-doped samples it can be seen that with an increase of the dopant concentration (more than 10% of Nd) the low frequency Drude tail becomes more prominent and a pronounced screening of the phonon modes takes place. Such a behavior implies that with Nd doping the concentration of the free charge carriers increases. The presence of free charge carriers can be explained by the fact that with increasing Nd content in the ceria lattice, the number of oxygen vacancies increases. According to the paper of Han *et al* [26] in nonstoichiometric ceria, with increasing vacancy concentration the amount of electrons which are localized near the vacancy sites increases too, giving rise to the formation of *F*-center defects in different charge states ([27] and the references within). These electrons are loosely bound and behave more like free charge carriers. Additionally, in the paper of Chen and Wang [29] it was shown that in Nd-doped ZnO nanowires the formation of vacancies near the Nd cations, can induce an increase of concentration of free (delocalized) electrons. In a recent paper of Choudhury *et al* [30], using Hall effect measurements, it was demonstrated that in Nd-doped ceria nanopowders, with increasing Nd content up to 4%, the number of free carriers increased. The increased free carrier concentration caused the widening of the band gap due to Burstein–Moss shift. The above mentioned theoretical and experimatal works support our finding that the plasmon − phonon interaction in Nd-doped ceria samples become stronger.

By analyzing the fitting parameters of the doped samples from tables 1 and 2, we can see that TO frequencies are not much affected by doping, whereas the eigenfrequencies of the plasmon-LO phonon coupled modes (ω_{LO1} and ω_{LO2} from table 1) are notably shifted with respect to decoupled LO modes (ω_{LO1} and ω_{LO2} from table 2). It can be also noticed that the damping parameter γ_{LO1} is significantly increased for doped samples.

In figure 5(*a*) are presented the frequencies of the coupled plasmon–phonon modes (Ω_{LO1}, Ω_{LO2}) and the decoupled LO phonon modes (ω_{LO1} and ω_{LO2} from table 2) as a function of Nd content. From figure 5(*a*) it is obvious that frequencies of the coupled modes are shifted to higher energies. Since the plasma frequency ω_P in doped samples is much closer to the frequency of the Ω_{LO1} mode than to the frequency of the Ω_{LO2} mode (see table 3), it is expected that the plasmon–phonon coupling would be stronger for the Ω_{LO1} mode. The

observed decrease of the Ω_{LO1} frequency with increasing Nd content confirms that this mode is more strongly coupled with plasmon.

In figure 5(*b*) is presented the variation of the plasma frequency ω_P with doping concentration in the case of both applied models. As can be seen from figure 5(*b*), we have obtained similar behavior of the plasma frequency from both models. The plasma frequency shifts towards lower energies as Nd concentration increases. Similar behavior of plasma frequency was found for crystalline and amorphous GaAs [31] when a metal-like phase appeared in these materials.

From the table 2 one can deduce that the plasmon mode is overdamped ($\gamma_P/\omega_P > 1/\sqrt{2}$) for the undoped CeO_{2-y} sample and samples doped up to 15% of Nd. This is a feature of conducting oxides, in particular cuprates [18]. For higher doping content (20 and 25% of Nd), the γ_P/ω_P ratio decreases ($\gamma_P/\omega_P \sim 0.5$). The decreasing trend of the γ_P/ω_P ratio is characteristic for the metallic state [18].

The plasmon dielectric function, according to the Double-damping extended Drude model, can be written in the form [18, 32]:

$$\epsilon_{pl} = \epsilon_\infty \left(1 - \frac{\omega_p^2 + i(\gamma_p - \gamma_0)\,\omega}{\omega\left(\omega - i\gamma_0\right)} \right) \qquad (10)$$
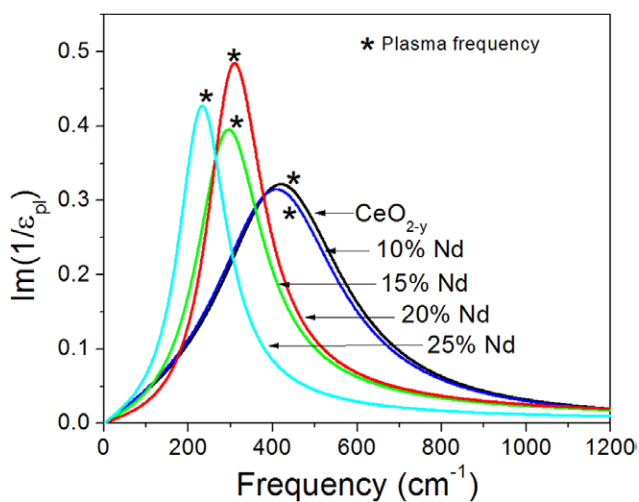
The decoupled plasmon mode structure can be extracted from the imaginary part of the inverse plasmon dielectric function, $Im(1/\epsilon_{pl})$ [32]. The decoupled plasmon mode structure with Nd doping is presented in figure 6, where the positions of the plasma frequencies (table 2) are marked with (*).

As can be seen from figure 6, with increased Nd doping the plasmon mode shifts towards lower energies, as well as the plasma frequency. The shift of the plasma frequency to lower energies is found in perovskite-type oxides like $BaPb_{1-x}Bi_xO_3$ [33] and $Ba_{1-x}K_xO_3$ [34], when these materials undergo semiconductor–to–metal transition. Bearing in mind that the plasma frequency ω_P is proportional to n_e/m^*, where n_e is the free carrier concentration and m^* is the electron effective mass, we can deduce that doping not only influences the free carrier concentration, but also changes the electron effective mass. In fact, our results for plasma frequency (plasmon mode) behavior suggest that the effective mass of free electrons increases with doping. Our conclusion is supported by the results performed on $Ba_{1-x}K_xO_3$ and InN films [34, 35] in which it was found a pronounced increase in the electron effective mass with increasing concentration of free carriers followed by a semiconductor–metal transition [34].

In order to verify how the plasmon–phonon interaction changes in thermally treated Nd-doped samples, the 15% and 25% Nd samples were calcinated in the same manner as it was done for the undoped ceria sample from figure 2. The IR refelectivity spectra of thermally treated 15% (25%) Nd-doped samples together with the corresponding untreated samples are presented in figure 7. As can be seen, the IR spectra of the calcinated samples are very similar to the bulk counterpart (figure 2), as the plasmonic background vanished and TO (LO) frequencies approached the bulk values. The disappearance of the Drude tail is expected, bearing in

J. Phys. D: Appl. Phys. 48 (2015) 065301

M Radović *et al*
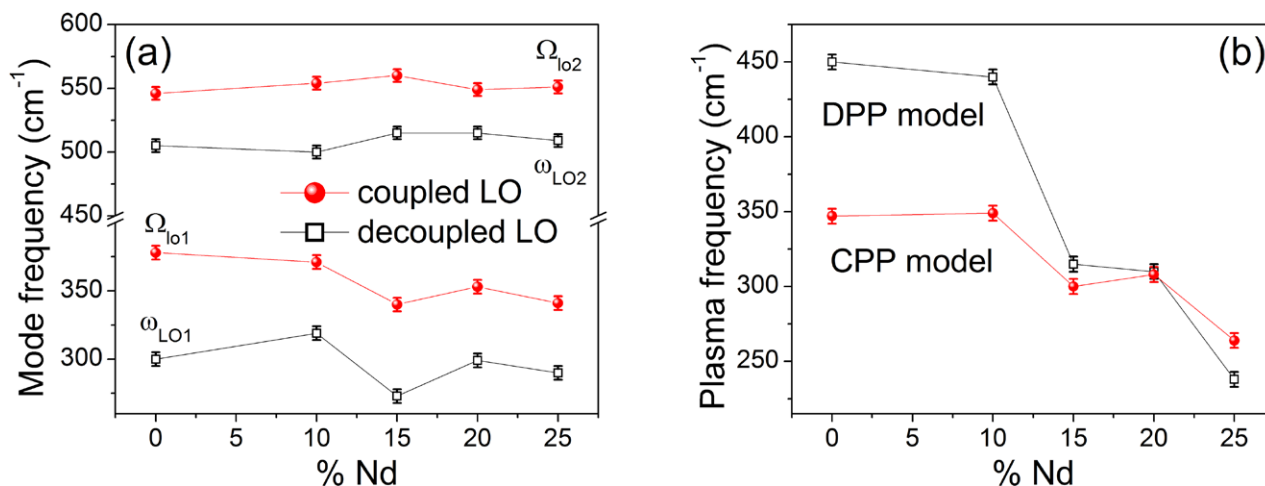
Figure 5. (*a*) Variation of the coupled and decoupled LO mode frequencies and (*b*) plasma frequency variation with Nd dopant concentration, obtained by using the CPP and DPP models.
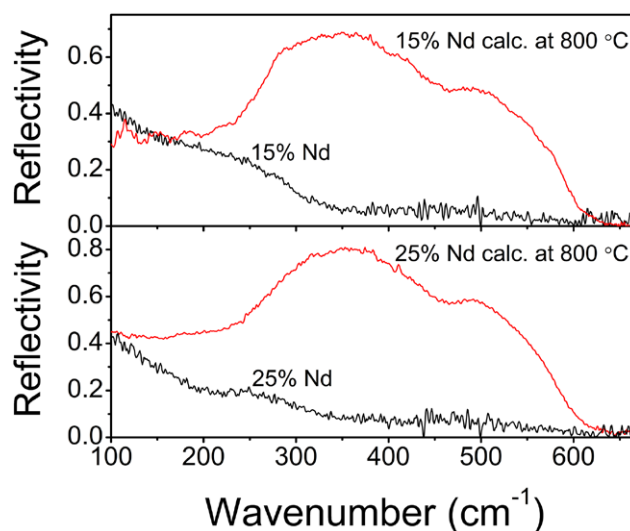

Figure 6. Decoupled plasmon mode structure in undoped and Nd doped samples. The positions of the plasma frequencies are marked with (*).

Figure 7. IR reflectivity spectra of untreated and thermally treated 15% (25%) Nd-doped samples.

mind that with temperature treatment in air, the nanosize effects become less pronounced with increasing crystallite size and that the concentration of the *F*-center defects and free carriers decreases.

Therefore, we can conclude that with increasing Nd content the plasmon–phonon interaction becomes stronger and at higher doping content (≥15% Nd) our samples undergo doping induced semiconductor–to–metallic state transition. With temperature treatment in air, it was demonstrated that the plasmonic background disappeared and the IR reflectivity spectra became similar to the bulk counterpart. The influence of doping on the n/m^* ratio and the estimation of the electron effective mass in pure and doped ceria nanocrystals will be the subject of our further work.

5. Conclusions

The influence of particle size decrease and Nd doping on the plasmon–phonon interaction in CeO_{2-y} nanocrystals

was investigated. Analysis of the infrared reflection spectra of CeO_{2-y} nanocrystalline sample revealed that with decreasing of particle size the contribution of free charge carriers becomes significant, resulting in the appearance of the plasmon mode. The plasmon mode coupled strongly with two LO modes of ceria. The appearance of more pronounced low frequency Drude tail and screening of the phonon modes suggested that doping further increased the plasmon–phonon coupling. The plasmon–phonon interaction in undoped and doped CeO_{2-y} samples was investigated by using factorized and additive models combined with Bruggeman effective medium approximation. The factorized model based on plasmon-two LO phonon interaction has proven to fit the experimental data successfully. From this model, the coupled plasmon-LO phonon frequencies and dampings were derived. The application of the additive form for the dielectric function enabled to obtain decoupled LO phonon frequencies and to deduce about the decoupled plasmon mode structure. The red-shift of the plasmon mode, plasma damping decrease and

pronounced screening of the phonon modes with increasing Nd content in ceria nanocrystalline samples pointed out that doping induced semiconductor–to–metallic state transition took place.

Acknowledgments

References

[1] Nakamatsu H, Mukoyama T and Adachi H 1995 *Chem. Phys. Lett.* **247** 168
[2] Marabelli F and Wachter P 1987 *Phys. Rev. B* **36** 1238
[3] Steele B C H and Heinzel A 2001 *Nature* **414** 345
[4] Suzuki T, Funahashi Y, Yamaguchi T, Fujishiro Y and Awano M 2008 *J. Power Sources* **183** 544
[5] Knauth P 2006 *Solid State Ion.* **177** 2495
[6] Lapplainen J, Tuller H L and Lantto V 2004 *J. Electroceram.* **13** 129
[7] Tschöpe A, Bäuerle C and Birringer R 2004 *J. Appl. Phys.* **95** 1203
[8] Chiang Y-M, Lavik E B, Kosacki I, Tuller H L and Ying J Y 1996 *Appl. Phys. Lett.* **69** 185
[9] Suzuki T, Kosacki I, Anderson H U and Colomban P 2001 *J. Am. Ceram. Soc.* **84** 2007
[10] Jasinski P, Suzuki T and Anderson H U 2003 *Sensors Actuators B-Chem.* **95** 73
[11] Matović B, Dukić J, Devečerski A, Bošković S, Ninić M and Dohčević-Mitrović Z 2008 *Sci. Sintering* **40** 63
[12] Bošković S, Djurović D, Dohčević-Mitrović Z, Popović Z, Zinkevich M, Aldinger F 2005 *J. Power Sources* **145** 237
[13] Gervais F and Servoin J-L 1993 *Phys. Rev. B* **47** 8187
[14] Gonzalez R J, Zallen R and Berger H 1997 *Phys. Rev. B* **55** 7014
[15] Gervais F 1983 *Infrared and Millimeter Waves* vol 8 ed K J Button (New York: Academic) pp 279–339
[16] Kukharskii A A 1973 *Solid State Commun.* **13** 1761
[17] Kim O K and Spitzer G 1979 *Phys. Rev. B* **20** 3258
[18] Gervais F 2002 *Mater. Sci. Eng.* R **39** 29
[19] Webman I, Jortner J and Cohen M H 1977 *Phys. Rev. B* **15** 5712
[20] Spanier J E and Herman I P 2000 *Phys. Rev. B* **61** 10437
[21] Williamson G K and Hall W 1953 *Acta Metall.* **1** 22
[22] Zhou X-D and Huebner W 2001 *Appl. Phys. Lett.* **79** 3512
[23] Santha N I, Sebastian M T, Mohanan P, Alford N McN, Sarma K, Pullar R C, Kamba S, Pashkin A, Samukhina P and Petzelt J 2004 *J. Am. Ceram. Soc.* **87** 1233
[24] Chen Z W, Lai J K L and Shek C H 2006 *J. Non-Cryst. Solids* **352** 3285
[25] Skorodumova N V, Simak S I, Lundqvist B I, Abrikosov I A and Johansson B 2002 *Phys. Rev. Lett.* **89** 166601
[26] Han X, Lee J and Yoo H I 2009 *Phys. Rev. B* **79** 100403(R)
[27] Aškrabić S, Dohčević-Mitrović Z D, Araújo V D, Ionita G Jr, de Lima M M and Cantarero A 2013 *J. Phys. D: Appl. Phys.* **46** 495306
[28] Popović Z V, Dohčević-Mitrović Z D, Paunović N and Radović M 2012 *Phys. Rev. B* **85** 014302
[29] Chen Q and Wang J 2013 *Phys. Chem. Chem. Phys.* **15** 17793
[30] Choudhury B and Choudhury A 2013 *Curr. Appl. Phys.* **13** 217
[31] Callan J P, Kim A M-T, Roeser C A D and Mazur E 2001 *Phys. Rev. B* **64** 073201
[32] Baumard J-F and Gervais F 1977 *Phys. Rev. B* **15** 2316
[33] Tajima S, Uchida S, Masaki A, Takagi H, Kitazawa K and Tanaka S 1985 *Phys. Rev. B* **32** 6302
[34] Goodenough J B and Cooper S L 2001 *Localized to Itinerant Electronic Transition in Perovskite Oxides* vol 98 ed J B Goodenough (Heidelberg: Springer-Verlag) pp 184–5
[35] Wu J, Walukiewicz W, Shan W, Yu K M, Ager J W III, Haller E E, Lu H and Schaff W J 2002 *Phys. Rev. B* **66** 201403
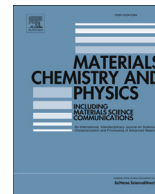
Photocatalytic degradation of alprazolam in water suspension of brookite type TiO₂ nanopowders prepared using hydrothermal route

N. Tomić [a], M. Grujić-Brojčin [a, *], N. Finčur [b], B. Abramović [b], B. Simović [c], J. Krstić [d], B. Matović [e], M. Šćepanović [a]

[a] Center for Solid State Physics and New Materials, Institute of Physics, University of Belgrade, Pregrevica 118, 11080 Belgrade, Serbia
[b] Department of Chemistry, Biochemistry and Environmental Protection, Faculty of Sciences, University of Novi Sad, Trg D. Obradovića 3, 21000 Novi Sad, Serbia
[c] Institute for Multidisciplinary Research, University of Belgrade, Kneza Višeslava 1, 11030 Belgrade, Serbia
[d] Institute of Chemistry, Technology and Metallurgy, Department of Catalysis and Chemical Engineering, University of Belgrade, Njegoševa 12, 11000 Belgrade, Serbia
[e] Institute of Nuclear Sciences "Vinča", University of Belgrade, 11001 Belgrade, Serbia

HIGHLIGHTS

- Brookite-type TiO₂ powders synthesized by combined sol—gel—hydrothermal method.
- Powders investigated by XRD, SEM, EDS, BET, SE and Raman spectroscopy.
- Photocatalytic degradation of alprazolam under UV radiation.
- Photocatalytic activity attributed to high content of brookite phase.
- High photocatalytic efficiency of pure brookite sample, comparable to Degussa P25.

ARTICLE INFO

ABSTRACT

Two series of nanocrystalline brookite-type powders have been synthesized by using combined sol—gel—hydrothermal method with titanium tetrachloride (TiCl₄) as a precursor and hydrothermal temperature and reaction time varied in the range of 120—200 °C and 12—48 h, respectively. The effects of chosen synthesis parameters on structural, morphological and optical properties of synthesized powders have been investigated by the XRPD, SEM, EDS and BET measurements, as well Raman spectroscopy and spectroscopic ellipsometry. The XRPD results have shown that pure brookite phase, with mean crystallite size of ~33 nm, has been obtained only in the sample synthesized at 200 °C, after 24 h of hydrothermal process. In all other samples anatase phase also appears, whereas rutile and sodium titanate phases have been noticed in the samples synthesized at lower temperatures. The presence of different titania phases has also been confirmed and analyzed by Raman scattering measurements. The SEM measurements have shown spindle-like particles in brookite-rich samples synthesized at 200 °C, whereas BET measurements have detected mesoporous structure in these samples. The properties of synthesized powders have been correlated to their photocatalytic efficiency, tested in degradation of alprazolam, one of the 5th generation benzodiazepines. The sample consisted of pure brookite has shown the highest efficiency in the photodegradation of alprazolam, practically equal to the activity of Degussa P25.

© 2015 Elsevier B.V. All rights reserved.

1. Introduction

Titanium dioxide (titania, TiO₂) is known as a polymorphic material with three naturally occurring crystalline modifications: anatase, rutile and brookite. These structures are composed of TiO₆ octahedra, with edge and corner sharing organized in a different way, which is also characteristic of various titanate materials [1—4]. Brookite is the rarest of the natural TiO₂ polymorphs. As opposite to anatase and rutile, common titania polymorphs easily synthesized by a variety of techniques from different titanium compounds, the

brookite occasionally appears as a by-product obtained together with either anatase or rutile or both of these phases. Consequently, the brookite has been much less characterized phase in comparison to anatase and rutile [2,5]. The investigation of properties and potential applications has been limited due to difficulties in synthesis of pure brookite phase [2,6–11], related mainly to narrow range of synthesis conditions, which allow brookite phase to be produced [5,12]. However, the interest in brookite has been increased in recent years and pure brookite has been observed as an interesting candidate in photocatalytic applications [5,13–15].

Titania may be generally obtained by thermolysis, hydrothermal synthesis and sol–gel process [10]. Well-crystallized titania nanoparticles have been produced by using hydrothermal method [6], which has been proven as necessary in synthesizing brookite as major phase [10]. Since this treatment with titanium tetrachloride as a precursor and the addition of NaOH into reaction solution can lead to all three polymorphs of titania, the control of synthesis parameters, such as hydrothermal temperature [16] and reaction time [14] is of a great importance. Also, under these hydrothermal conditions, certain solution pH (high basicity) and particular amounts of Na cations are necessary to produce pure brookite phase [2,4,17] (and references therein). Therefore brookite type nanopowders, investigated in this study, have been prepared by combined sol–gel–hydrothermal method with TiCl$_4$ as a precursor, in alkaline environment, with hydrothermal temperature and time varied. The effects of chosen synthesis parameters on the crystallite size, structure and phase composition of the synthesized nanopowders have been investigated by X-ray powder diffraction (XRPD), energy-dispersive X-ray spectroscopy (EDS), and Raman scattering measurements. The morphological properties of samples have been studied by scanning electron microscopy (SEM) and the Brunauer–Emmett–Teller (BET), whereas their optical properties have been investigated by the spectroscopic ellipsometry (SE) measurements.

The properties of synthesized brookite-type titania nanopowders have been correlated to their photocatalytic efficiency, tested in degradation of alprazolam and compared to the efficiency of commercial Degussa P25 under the same conditions. Alprazolam is one of the 5th generation benzodiazepines [18,19], a group of psychiatric substances acting on the central nervous system [19–21] and, similarly to the other pharmacological groups, occurring in the environment in the range of ng/l–μg/l [22]. The presence of these compounds in the ecosystems might have a significant effect on non-target organisms [23]. In the research investigating the stability of the benzodiazepines under the influence of simulated solar irradiation, only alprazolam has shown high resistance to photodegradation [24]. Having in mind continuous input of this kind of pharmaceuticals in the environment and their persistence, there is a great interest to find new methods for their removal.

2. Experimental

2.1. Synthesis of brookite-type powders

Brookite type nanoparticles have been prepared by using combined sol–gel–hydrothermal method with TiCl$_4$ (99.0% pure, Merck) as a precursor. An appropriate amount of TiCl$_4$ has been dissolved in 150 ml of distilled water under vigorous stirring on the ice-bath. In order to obtain the hydrogel, the aqueous solution of NaOH has been added under careful control of the pH value of the solution (9.3). After aging in the mother liquor for 5 h, as-prepared hydrogel has been placed in a steel pressure vessel (autoclave) under a controlled temperature. After treatment, filtration and washing with distilled water until complete removal of chloride

ions, were carried out. The last step was drying at 105.5 °C for 72 h. Two series of samples have been produced by varying the hydrothermal temperature and reaction time. In the first series the reaction time was 24 h at different temperatures: 120, 160, and 200 °C. The second series of samples was prepared by keeping the temperature at 200 °C, while the time of treatment was 12, 24, and 48 h. The labels assigned to samples, concerning the hydrothermal temperature and reaction time are listed in Table 1.

2.2. Characterization methods

The X-ray powder analysis was used to identify the crystalline phases, as well as to calculate lattice parameters of brookite phase in synthesized powders. The XRPD patterns of all samples were recorded on Rigaku (Ultima IV) X-ray Powder Diffractometer with Cu K$\alpha_{1,\,2}$ radiation (λ = 1.54178 Å). The measurements were performed in the 2θ range from 10° to 80° with the step of 0.02° and scanning time of 2 s/min. The calculation of the volume–weighted mean crystallite size (D) was performed on the basis of the full width at half maximum intensity of the all reflections for brookite phase by using Scherrer's formula [25].

Morphology of the synthesized nanopowders has been studied on SEM type JEOL JSM-6460LV with the operating voltage of 20 keV. The composition/quality has also been analyzed by using the same SEM instrument equipped with an EDS INCAx-sight detector and "INAx-stream" pulse processor (Oxford Instruments).

Adsorption–desorption isotherms were obtained by nitrogen adsorption at 77 K using a Sorptomatic 1990 Thermo Finnigan device. Prior to adsorption, the samples were outgassed for 1 h under vacuum at room temperature and, additionally, at 110 °C and the same residual pressure, for 16 h. The specific surface areas (S_{BET}) of samples is calculated from the linear part of the adsorption isotherm by applying the Brunauer–Emmet–Teller (BET) equation [26]. The total pore volumes (V_{tot}) were obtained from the N$_2$ adsorption, expressed in liquid form, by using the Gurvitsch rule [27]. The micropore volume (V_{mic}) has been estimated by the Dubinin–Radushkevich method [28]. The mesopore volume (V_{mes}), as well as mesopore size distribution have been estimated by the Barrett, Joyner and Halenda (BJH) method from the desorption branch of the isotherms [29].

The Raman scattering measurements on brookite-type powders pressed into pellets were performed using a TriVista TR557 triple spectrometer with the 900/900/1800 grooves/mm gratings combination, equipped with a nitrogen-cooled charge coupled device (CCD) detector. All spectra have been collected in backscattering micro-Raman configuration at room temperature in the air. The 488 nm line of a mixed Ar$^+$/Kr$^+$ gas laser was used as an excitation source with an output power of less than 10 mW to avoid local heating due to laser irradiation.

The ellipsometric spectra of the brookite-type nanopowders have been measured by SOPRA GES-5 variable angle ellipsometer in rotating polarizer configuration. The data were collected at room temperature, in the range from 1.5 to 6.2 eV with resolution of 0.04 eV and incidence angle of 65°.

3. Photocatalytic measurements

The photocatalytic activity of the nanopowders was evaluated

Table 1
The parameters of hydrothermal synthesis.

	B$_{120/24}$	B$_{160/24}$	B$_{200/24}$	B$_{200/12}$	B$_{200/48}$
Treatment temperature (°C)	120	160	200	200	200
Hydrothermal reaction time (h)	24	24	24	12	48

by the removal of the solution of alprazolam (8-chloro-1-methyl-6-phenyl-4H-[1,2,4]triazole[4,3,-α]-[1,4]-benzodiazepine, CAS No. 28981-97-7, $C_{17}H_{13}ClN_4$, $M_r = 308.765$). The photocatalytic study was carried out in a cell made of Pyrex glass (total volume of ca. 40 cm^3), with a plain window on which the light beam was focused, equipped with a magnetic stirring bar and a water circulating jacket. Irradiation in the UV range was performed using a 125 W high-pressure mercury lamp (Philips, HPL-N, emission bands in the UV region at 304, 314, 335 and 366 nm, with maximum emission at 366 nm), together with an appropriate concave mirror. Initial alprazolam concentration was 0.03 mM and the catalyst loading was 1.0 mg/cm^3. Experiments were carried out using 20 cm^3 of alprazolam solution. The aqueous suspension was sonicated (50 Hz) in the dark for 15 min before illumination, to uniformly disperse the photocatalyst particles and attain adsorption equilibrium. The suspension thus obtained was thermostated at 25 ± 0.5 °C in a stream of O_2 (3.0 cm^3/min), and then irradiated. During irradiation, the suspension was stirred at a constant rate under continuous O_2 flow. The kinetics of the alprazolam removal was monitored with liquid chromatography with diode array detection (UFLC−DAD) at 222 nm (wavelength of alprazolam maximum absorption [30]). Commercially available TiO_2 Degussa P25 (75% anatase and 25% rutile, with average particle size about 20 nm, according to the producer's specification), was used for comparison.

4. Results

4.1. X-ray powder diffraction

The XRPD has been used to determine the percentage of brookite phase in synthesized nanopowder samples. Corresponding diffraction patterns are presented in Fig. 1. The existence of brookite phase has been clearly evidenced from the presence of the (121) peak at $2\theta = 30.81°$ in the patterns of all samples, but brookite content significantly varies depending on the synthesis condition. Lower content of brookite (~12.6 and ~31.6%) has been registered in the samples treated at lower temperatures ($B_{120/24}$ and $B_{160/24}$, respectively), as listed in Table 2. In the samples synthesized at 200 °C, the content of brookite is significantly increased, but it varies with the hydrothermal time. The lowest content (~65%) of brookite is estimated in the sample treated for shortest time ($B_{200/12}$). In the samples treated for longer time the amount of brookite is increased: 95% in $B_{200/48}$ and 100% of brookite phase in the sample $B_{200/24}$.

The lattice parameters of brookite phase in all synthesized samples are listed in Table 3. Their values are similar to orthorhombic bulk structure of brookite ($a_0 = 9.184$ nm, $b_0 = 5.447$ nm, $c_0 = 5.145$ nm [31]). The values of mean crystallite size and strain of brookite phase have been estimated by Scherrer's method [25] only for the samples synthesized at 200 °C (Table 3). The attempt to obtain reliable size and strain data in the other samples has failed, most probably due to more disordered brookite phase produced at lower temperatures (120, 160 °C). As can be seen from the Table 3, the decrease of the average brookite crystallite size from 58 nm to ~30 nm with the increase of the hydrothermal reaction time from 12 to 48 h has been noticed, whereas maximal strain has been observed in pure brookite sample $B_{200/24}$.

In addition to the brookite diffraction peaks, the peaks corresponding to anatase phase have also been noticed in all XRPD patterns, except the one of the sample $B_{200/24}$ (Table 2). Note that the main (101) diffraction peak of anatase at $2\theta = 25.28°$ is partially overlapped with the (120) and (111) peaks of brookite at $2\theta = 25.34°$ and 25.69°, respectively [5,7,32,33]. According to results given in Table 2, in the sample treated for the shortest time ($B_{200/12}$) almost 35% of anatase phase is synthesized, whereas much
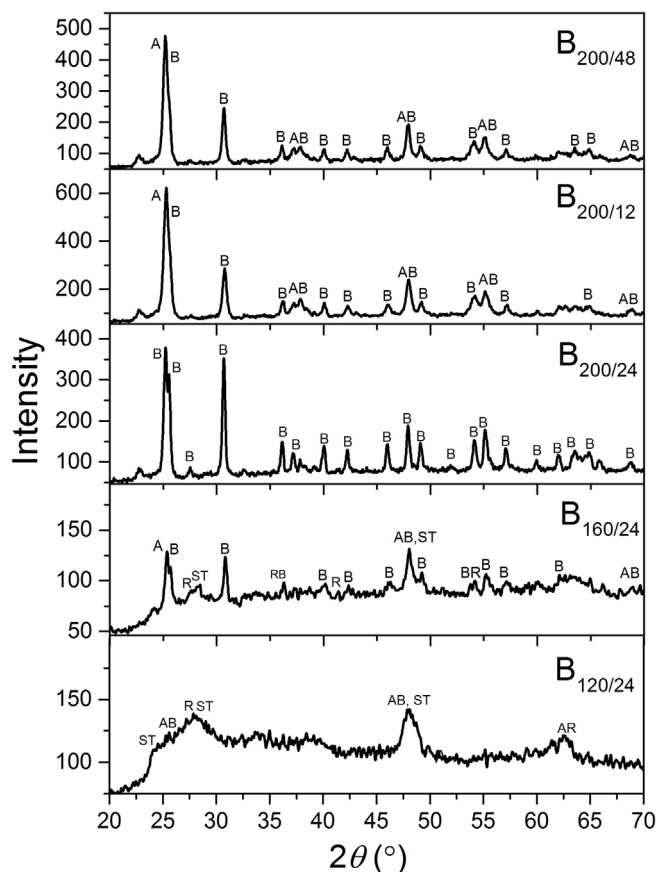

Fig. 1. XRPD patterns of titania nanopowders, with characteristic diffraction peaks of brookite, anatase, rutile and sodium titanate phase, denoted by corresponding letters.

smaller amount of anatase (~5−8%) is present in the samples treated for longer time, as can be seen from the Table 2.

Beside the brookite and anatase diffraction peaks, the XRPD patterns of the samples synthesized at lower temperatures (120 and 160 °C) exhibit low intensity and relatively broad peaks which may be related to rutile phase (~14 and ~6%, respectively) [33] and sodium trititanate in significant content (more than 50%) (Table 2), with the characteristic peaks at 24°, 28.1° and 48° [16,34]. However, the XRPD patterns of these two samples have pronounced background with the humps, especially in the pattern of the sample synthesized at the lowest temperature ($B_{120/24}$), suggest the presence of amorphous phase.

4.2. SEM

The SEM images of nanopowders are presented in Fig. 2. The differences in powder morphology, originated from different phase content, may be clearly observed. The samples synthesized at lower temperatures ($B_{120/24}$ and $B_{160/24}$), rich in sodium titanate phase, have nanoparticles (~50 nm) of dominantly spherical shape, with

Table 2
The volume fraction (%) of brookite, anatase, rutile and sodium titanate phases estimated from XRPD patterns of synthesized powders.

Sample	$B_{120/24}$	$B_{160/24}$	$B_{200/24}$	$B_{200/12}$	$B_{200/48}$
Brookite %	12.4	31.6	100	65.2	95
Anatase %	7.7	7.6	–	34.8	5.0
Rutile %	14.0	6.3	–	–	–
Na-titanate %	65.9	54.5	–	–	–

Table 3
The lattice parameters (*a*, *b*, *c*), average crystallite size (*D*) and average strain (*ε*) of brookite phase in synthesized powders.

Sample		$B_{120/24}$	$B_{160/24}$	$B_{200/24}$	$B_{200/12}$	$B_{200/48}$
Brookite	*a* (nm)	9.1782	9.1347	9.1673	9.1362	9.2470
	b (nm)	5.5591	5.5591	5.4382	5.4578	5.4698
	c (nm)	5.1091	5.1090	5.1303	5.1398	5.1634
	D (nm)	–	–	33	58	29.6
	ε	–	–	0.0351	0.0049	0.0040

pronounced agglomeration (Fig. 2(a and b)). The spindle-like particles are predominating in the pure brookite sample ($B_{200/24}$), with longer dimensions estimated up to ~300 nm, and shorter less than 100 nm (Fig. 2(c)). In the samples with mixture of anatase and brookite ($B_{200/12}$ and $B_{200/48}$), shown in Fig. 2(d and e), most of the particles are smaller than in the pure brookite sample, with elongated structure retained.

4.3. EDS

The chemical composition of synthesized nanopowders has been estimated by EDS method. The EDS spectra are collected from corresponding framed areas of SEM micrographs, shown together in Fig. 3. The oxygen weight percent in all samples is estimated in the range ~45–48 wt.% (Table 4), above the value corresponding to stoichiometric TiO_2 (40 wt.%). The Na content has been detected in sodium titanate rich samples, treated at lower temperatures (120 and 160 °C).

4.4. Nitrogen physisorption

In order to study the influence of the hydrothermal temperature and reaction time on the pore structure and adsorption abilities of synthesized powders nitrogen sorption isotherms have been measured. The isotherms of brookite-rich samples ($B_{200/12}$, $B_{200/24}$, and $B_{200/48}$) are presented in Fig. 4(a). The curves may be interpreted as type IV [35], typical for mesoporous materials, with an H_2-type hysteresis loop, indicating the presence of pore networks. Corresponding information on specific surface areas (S_{BET}) and the total pore (V_{tot}), micropore (V_{mic}) and mesopore (V_{mSSeso}) volumes are summarized in Table 5. According to these results, the specific surface area in the pure brookite sample ($B_{200/24}$) is the smallest ($S_{BET} = 69.5$ m^2/g), whereas S_{BET} is larger in the samples consisting of both anatase and brookite phase is higher (97.9 and 76.5 m^2/g in $B_{200/12}$ and $B_{200/48}$, respectively). Such reverse dependency

between the S_{BET} of brookite-rich powders and brookite content has been already noticed in the literature [36,37]. It should be also noted that in our samples synthesized at lower temperatures ($B_{120/24}$ and $B_{160/24}$) very high values of specific surface area (>250 m^2/g), with significant microporous contribution, have been measured.

The BJH method was used to evaluate the mesopore size distribution in brookite-rich samples from the desorption branch of the isotherm curves. The distributions are shown in Fig. 4(b), whereas the values of the most frequent pore diameter (D_p), corresponding to the maximum of the mesopore size distribution, are listed in Table 5. The highest value of D_p is estimated in the pure brookite sample.

4.5. Raman scattering measurements

The Raman spectroscopy, as a powerful technique to distinguish titania modifications in samples consisting of mixed phases, has been used for independent structural analysis, providing data on phase purity and crystallinity. The Raman spectra of all synthesized nanopowders are shown in Fig. 5. It can be noticed that the spectra of nanopowders synthesized at 200 °C are dominated by brookite modes (denoted by "B" in the figure). Moreover, all Raman features in the spectrum of the sample $B_{200/24}$ can be ascribed to brookite phase, as shown in Fig. 6. These brookite modes are assigned and listed in the Table 6, together with bulk reference values [11]. Almost all of these modes are also registered in the spectra of the samples at the same temperature, but for different time ($B_{200/12}$ and $B_{200/48}$), as shown in Table 6. The frequencies of the most intensive brookite Raman modes are slightly shifted towards higher values in comparison to the values of bulk brookite [11]. This shift is most pronounced in the spectrum of the sample $B_{200/48}$.

In the Raman spectra of the samples hydrothermally treated at 200 °C ($B_{200/12}$ and $B_{200/48}$), besides brookite modes, the most intensive anatase E_g mode ~144 cm^{-1} is clearly observed (Fig. 5). The other anatase modes have also been detected in these
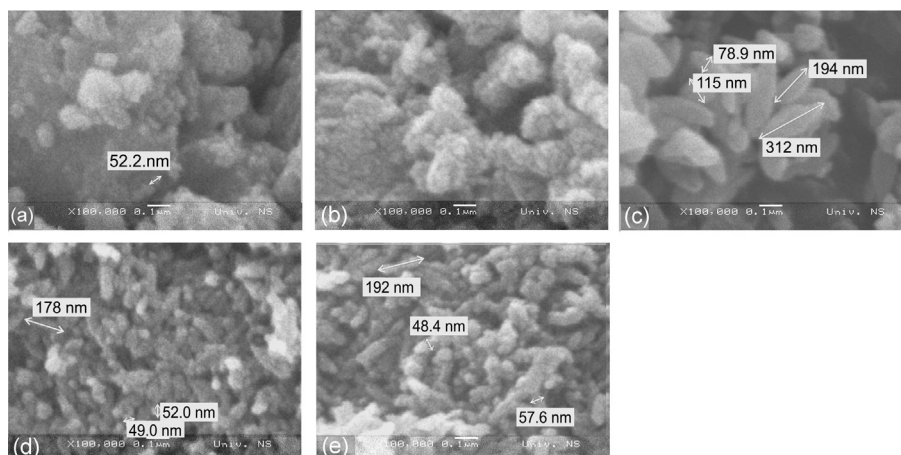
Fig. 2. The SEM micrographs of synthesized nanopowders: (a) $B_{120/24}$, (b) $B_{160/24}$, (c) $B_{200/24}$, (d) $B_{200/12}$, and (e) $B_{200/48}$.
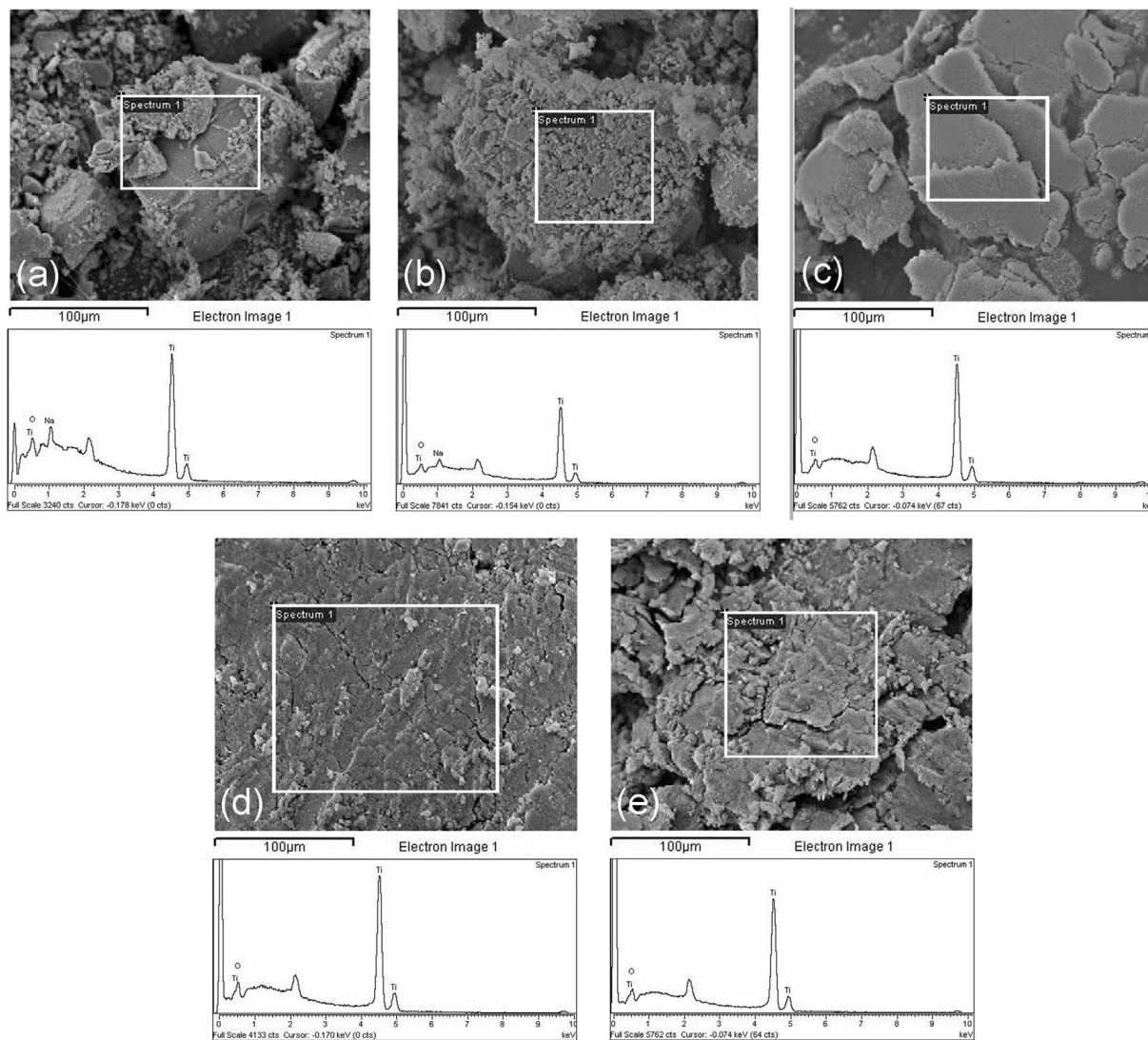
Fig. 3. EDS spectra of hydrothermally synthesized titania samples: (a) $B_{120/24}$, (b) $B_{160/24}$, (c) $B_{200/24}$, (d) $B_{200/12}$, and (e) $B_{200/48}$, with corresponding area shown in SEM images.

spectra: A_{1g} (~399 cm^{-1}) and $A_{1g} + B_{1g}$ (~520 cm^{-1}), with E_g mode at ~637 cm^{-1} partially overlapping with brookite A_{1g} mode at ~640 cm^{-1}.

The Raman spectra of samples treated at lower temperatures ($B_{120/24}$ and $B_{160/24}$) are dominated by the broad features which can be ascribed to amorphized sodium titanate structure [16,38] as follows: ~123, 385, 440, 582, 665, 710, 754, 815, and 911 cm^{-1}. These modes are more pronounced in the spectrum of the sample $B_{120/24}$. Note also that in the spectra of these samples very low intensity modes A_{1g} at ~445 cm^{-1} and E_g at ~610 cm^{-1} corresponding to rutile phase have also been registered.

The Raman spectra of all synthesized samples in the region of 80–230 cm^{-1}, fitted by the sum of Lorentzian functions

Table 4
EDS results for hydrothermally synthesized titania nanopowders.

Sample	O (wt.%)	Ti (wt.%)	Na (wt.%)	Total (wt.%)
$B_{120/24}$	46.26	44.43	9.31	100.00
$B_{160/24}$	45.21	48.78	6.01	100.00
$B_{200/24}$	45.46	54.54	–	100.00
$B_{200/12}$	48.09	51.91	–	100.00
$B_{200/48}$	47.22	52.78	–	100.00

corresponding to the modes of anatase, brookite and sodium titanate, are shown in Fig. 7. This region, containing the most intensive Raman modes of anatase and brookite, has been used as reliable fingerprint, which may give insight into the phase composition and crystallinity of synthesized nanopowders.

The spectra of the samples synthesized at lower temperatures ($B_{120/24}$ and $B_{160/24}$) in this region are characterized by the most intensive A_{1g} brookite mode (B) and broad features corresponding to sodium titanate modes (ST), covering anatase modes (A) and the other, less intensive brookite modes, positioned in the vicinity (marked as ST + B). Thereby, the intensity ratio of the brookite to sodium titanate Raman modes is much higher in the spectrum of the sample synthesized at higher hydrothermal temperature ($B_{160/24}$).

Raman modes corresponding to brookite phase positioned at ~129, 155, and 215 cm^{-1} have been clearly distinguished in specified region of all Raman spectra of the samples synthesized at 200 °C (Fig. 7). However in the spectra of the samples $B_{200/12}$ and $B_{200/48}$, characteristic anatase mode E_g at ~144 cm^{-1} is the most intensive. Slightly higher integrated intensity ratio of this anatase E_g mode to the most intensive brookite A_{1g} mode is found in the spectrum of the sample treated for shorter time ($B_{200/12}$).

Fig. 4. (a) Nitrogen physisorption isotherms of brookite-rich samples ($B_{200/12}$, $B_{200/24}$, $B_{200/48}$) at 77 K. The filled symbols represent adsorption points and empty symbols represent desorption points. (b) The mesopore size distribution calculated by BJH method.

4.6. Spectroscopic ellipsometry

Electronic band structure of brookite is rarely studied in comparison to other titania polymorphs. Basically, there are experimental and theoretical studies providing different and also conflicting bandgap energies, both direct and indirect, as well as larger and smaller than bandgap of anatase phase ([3,7,13] and references therein). In general, the reason for lack of unambiguous opinion on the bandgap of brookite is anisotropy of such complex semiconductor material. Therefore the values of energy related to direct or indirect transition is surely dependent on the structural and morphological properties of brookite material, determined by different synthesis conditions.

The spectroscopic ellipsometry has been used to investigate optical and electronic properties of synthesized brookite-type nanopowders. The complex pseudo-dielectric functions of these powders have been determined from SE data by using a two-phase (ambient/substrate) model. No correction for overlayers and surface roughness has been made. The absorption coefficient for all synthesized powders has been evaluated as $\alpha(\lambda) = 4\pi k(\lambda)/\lambda$, where λ is the wavelength of incident light and the spectral dependence of the extinction coefficient $k(\lambda)$ has been calculated from the real and the imaginary part of the pseudo-dielectric function.

Table 5
The porous properties of brookite-rich nanopowders and Degussa P25 obtained from BET measurement: specific surface area (S_{BET}), total pore volume (V_{tot}), meso- and micro-pore volume (V_{meso} and V_{mic}, respectively), and the most frequent pore diameter (D_p).

Sample	S_{BET} (m²/g)	V_{tot} (cm³/g)	V_{meso} (cm³/g)	V_{mic} (cm³/g)	D_p (nm)
$B_{200/12}$	97.9	0.244	0.247	0.032	5.78
$B_{200/24}$	69.5	0.241	0.201	0.024	6.64
$B_{200/48}$	76.5	0.286	0.280	0.026	5.91
Degussa P25	53.2	0.134	0.108	0.017	2.09
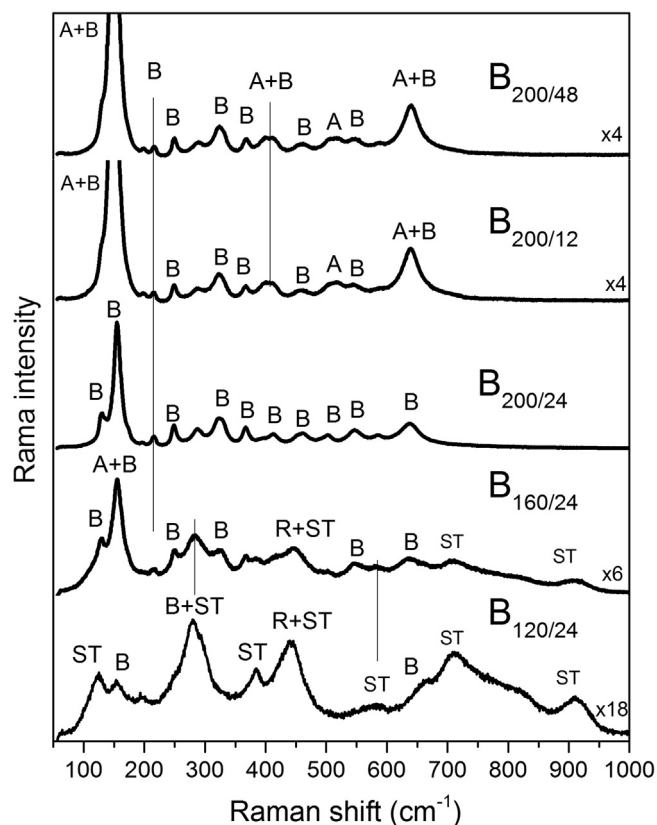
Fig. 5. The Raman spectra of hydrothermally synthesized powders, with the most intensive modes assigned to brookite (B), anatase (A), rutile (R), and sodium titanate (ST).
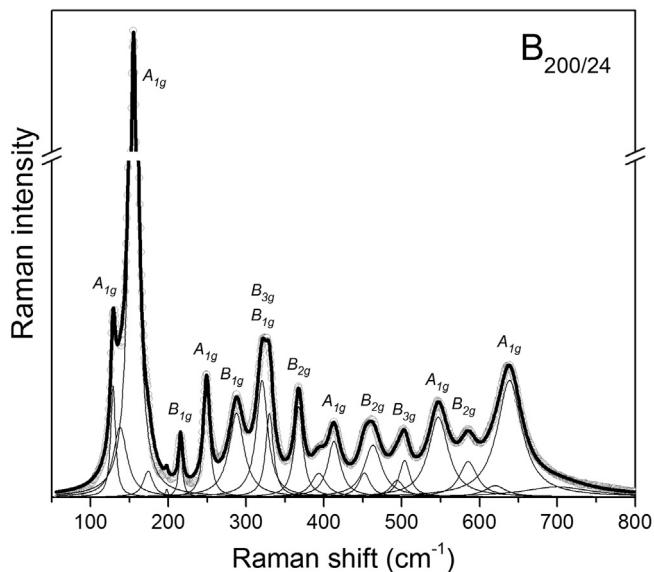
Fig. 6. The Raman spectrum of nanopowder B$_{200/24}$ fitted by the sum of Lorentzians corresponding to brookite modes (only the most intensive modes are assigned).

Table 6
The brookite Raman modes of the brookite-type nanopowders samples. The assignation has been performed according to Iliev et al. [11].

Assign.	Raman modes (cm^{-1})					
	B$_{120/24}$	B$_{160/24}$	B$_{200/24}$	B$_{200/12}$	B$_{200/48}$	Ref. [11]
A$_{1g}$	128	125	129	129	130	125 m
	155	154	155	155	156	152 vs
	195	197	198	199	200	194 w
	244	249	249	249	250	246 s
	–	–	–	–	–	324 w
	–	418	413	413	413	412 w
	–	–	494	–	–	492 w
	–	549	547	546	547	545 s
	–	635	639	638	640	640 s
B$_{1g}$	168	–	174	170	179	169 m
	218	215	215	215	215	212 m
	289	285	288	287	290	283 s
	–	–	330	–	–	327 m
	–	–	–	–	–	381 vw
	–	–	–	–	–	–
	–	451	452	–	–	449 m
	–	–	625	–	–	622 w
B$_{2g}$	–	–	–	–	–	160 s
	–	–	–	–	–	254 vw
	–	–	–	–	–	325 m
	–	366	367	367	368	366 s
	–	–	393	399	399	391 w
	–	–	463	460	460	460 s
	–	586	585	587	583	584 m
B$_{3g}$	–	–	137	–	–	132 m
	–	–	–	–	–	212 w
	322	325	320	323	324	318 s
	–	–	–	–	–	416 w
	506	500	504	508	505	500 m

The absorption coefficient α is assumed to follow well-known dependence $\alpha E \approx A(E-E_g)^{\gamma}$, where E is the photon energy, A is a sample-dependent constant parameter, whereas γ is a constant equal to 1/2 and 2 for direct and indirect allowed transitions, respectively. The dependence of $(\alpha E)^{1/2}$ plots on the photon energy for an indirect transition, as well as the $(\alpha E)^2$ plots for a direct transition, are shown in Fig. 8(a) and (b) respectively. The energies of direct and indirect transition in pure brookite sample (B$_{200/24}$) are determined by extrapolating the straight-line portions of these plots to the photon energy axis [39]. For this sample the values of ~2.5 eV for indirect and ~3.85 eV for direct transition energy have been obtained by this procedure. The curves presented in Fig. 8 suggest lower values of the energy both for direct and indirect transition in other samples synthesized at 200 °C (B$_{200/12}$ and B$_{200/48}$) consisted from anatase and brookite. On the contrary, in the powders synthesized at lower temperatures (B$_{120/24}$ and B$_{160/24}$), with sodium titanate as dominant phase, the energies of direct and indirect transition seem to be higher than in pure brookite sample. However, the values of transition energy for the samples other than pure brookite have not been refined by the procedure described above, having in mind that two-phase model is not fully appropriate to calculate the dielectric function of the material consisted of several phases with different bandgap energies. Therefore more elaborate analysis of the ellipsometric data, should be performed in the future research.

4.7. Photocatalytic efficiency

The influence of the hydrothermal temperature and time of the synthesis process on photocatalytic activity of produced powders have been studied through the photocatalytic removal of alprazolam under UV light irradiation. The effect of the treatment temperature on the photocatalytic activity of powders synthesized during 24 h, presented in Fig. 9(a), has been studied. Photocatalytic activity of powders treated at 120 and 160 °C have shown very low photocatalytic activity, whereas the one treated at 200 °C has exhibited a significant increase in the alprazolam photodegradation efficiency. The kinetics curve of alprazolam removal using the most frequently used oxide semiconductor for photodegradation, Degussa P25 is also shown in Fig. 9(a). As can be seen from the

figure, photocatalytic activity of the sample B$_{200/24}$ is practically equal to Degussa P25.

The effect of hydrothermal reaction time (12, 24 and 48 h) on photocatalytic activity of the samples synthesized at 200 °C has also been studied. The kinetics curves for the samples are presented in Fig. 9(b). Among these samples, all active in degradation of alprazolam, the sample B$_{200/24}$ have shown the highest activity. On the basis of these kinetic curves from Fig. 9(b), the kinetics parameters (reaction rate constant and reaction rate) were also calculated by fitting a pseudo-first order kinetic model to each set of results. Linear regression coefficients were in the range from 0.9968 to 0.9989 (Table 7), confirming the adequacy of the pseudo-first order model to describe the kinetics of alprazolam degradation. According to this analysis, the lowest photocatalytic efficiency has been registered in nanopowder B$_{200/12}$, whereas the sample B$_{200/24}$ has been the most effective in the degradation of alprazolam.

5. Discussion

The intention of this work is to analyze the influence of structure and morphology of brookite-type powders on photocatalytic efficiency in removal of alprazolam, as pharmaceutical rarely studied in terms of photocatalytic degradation. Two series of nanocrystalline brookite-type powders have been synthesized by using combined sol–gel–hydrothermal method with TiCl$_4$ as a precursor, with the hydrothermal temperature and reaction time varied. By comparing the synthesis conditions and the properties of produced samples of these two series, optimal hydrothermal parameters for producing pure brookite phase have been determined.

The first series of samples has been obtained at different temperatures (120, 160 and 200 °C) during 24 h. The XRPD and Raman
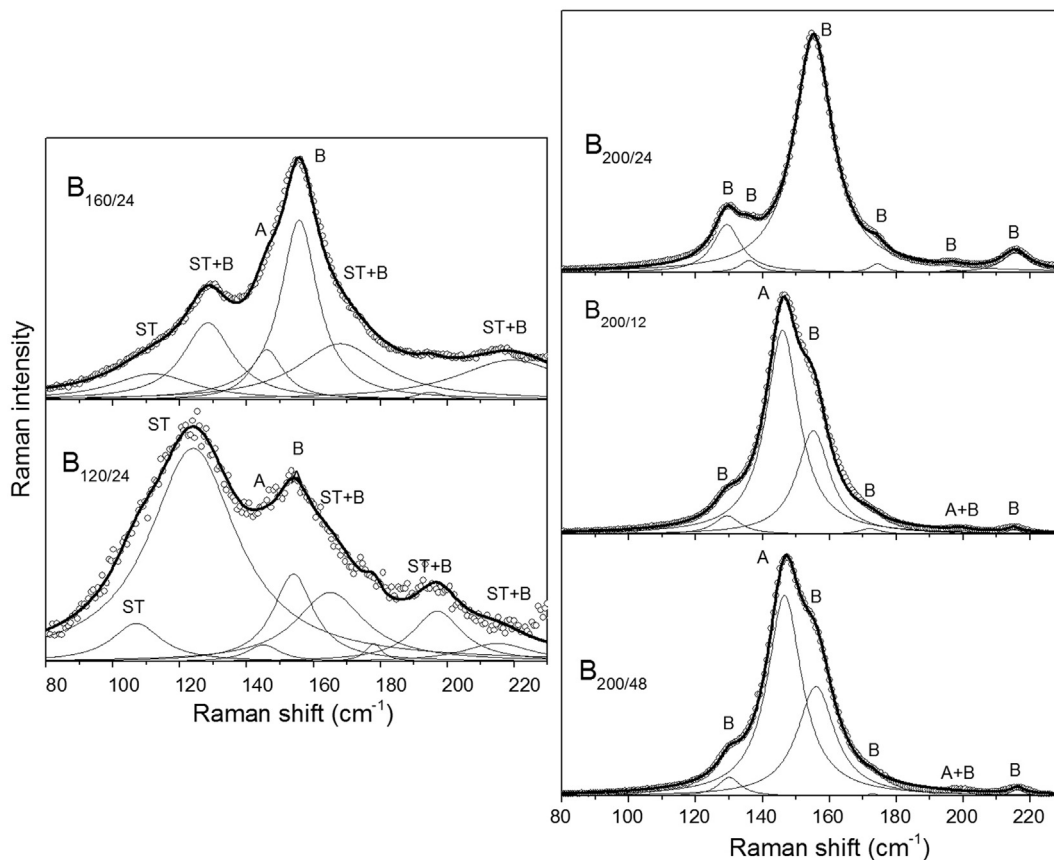
Fig. 7. The Raman spectra of nanopowder samples in the range from 80 to 230 cm^{-1} fitted by the sum of Lorentzians corresponding to the modes of anatase, brookite and sodium titanate, denoted by A, B, and ST respectively.

scattering measurements have shown that temperatures lower than 200 °C in such hydrothermal process are insufficient to synthesize brookite-rich samples. Namely, the samples synthesized at lower temperatures (B$_{120/24}$ and B$_{160/24}$) are abundant in amorphous sodium titanate phase, whereas all titania phases (rutile, anatase, and brookite) are represented in a much smaller percentage. The SEM measurements have shown that these powders

consisted of agglomerated nanoparticles with dominantly spherical shape. Also, in these samples, synthesized at lower temperatures, a large specific surface areas, with great microporous contribution, have been measured by BET. With hydrothermal temperature increased to 200 °C, specific surface area has decreased, and mesoporous samples have been synthesized. Pure brookite sample with spindle-like particles has been obtained at the temperature of
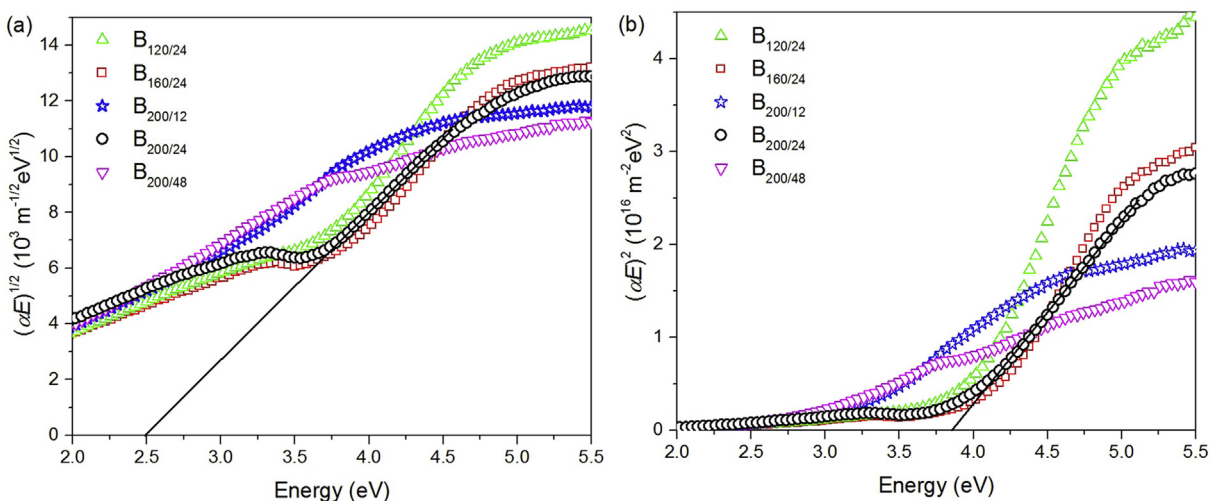
Fig. 8. (a) The plot of $(\alpha E)^{1/2}$ versus E for indirect bandgap transition in synthesized powders; (b) The plot of $(\alpha E)^2$ versus E for direct bandgap transition in the same samples with characteristic tangent lines for pure brookite sample.
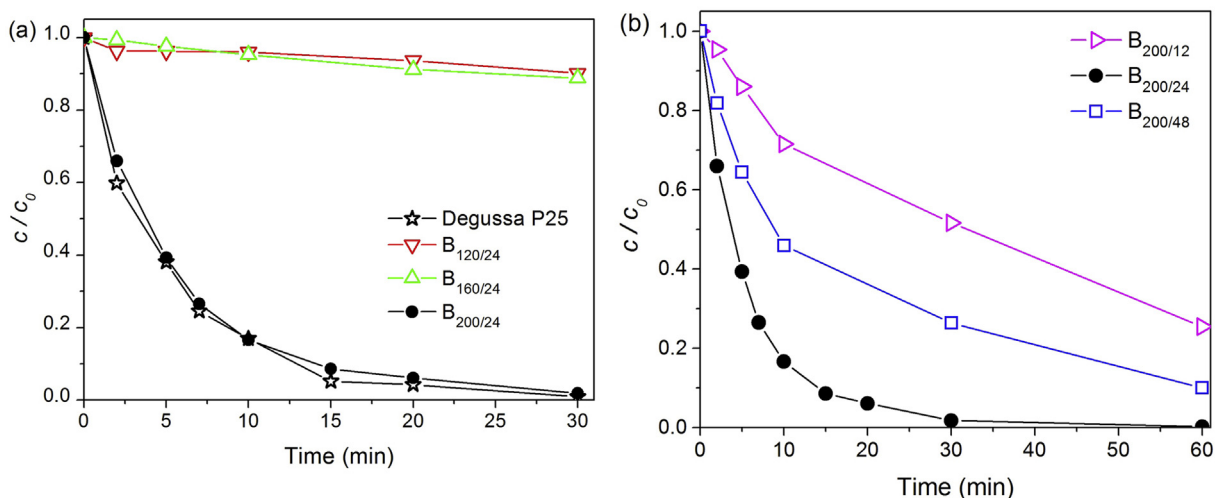
Fig. 9. The influence of different synthesis conditions on the photocatalytic efficiency of synthesized powders in the removal of alprazolam (c_0 = 0.03 mM): (a) the samples synthesized at different temperatures (120, 160, and 200 °C) during 24 h, and (b) the samples synthesized at 200 °C during different hydrothermal reaction time (12, 24, and 48 h).

200 °C for 24 h of hydrothermal procedure, as mentioned in the previous sections.

In another series of the samples the influence of the hydrothermal time on the properties of powders synthesized at 200 °C has been studied. Beside the sample synthesized during 24 h at 200 °C, included in the series described above, two more powders with hydrothermal reaction times of 12 and 48 h have been produced. According to the XRPD analyses average crystallite size of brookite phase has decreased with the increase of hydrothermal reaction time. The results obtained by Raman scattering measurements have also pointed to higher crystallinity of brookite phase in the sample synthesized for 12 h than in the one synthesized for 48 h. Namely, similar Raman spectra obtained for the samples $B_{200/12}$ and $B_{200/48}$, with different brookite content (according to XRPD), may be the consequence of lower crystallinity of brookite phase in the sample with higher brookite content ($B_{200/48}$). It should be noted that these results are opposite to those presented in the study of Xie et al. [6] where, with $Ti(SO_4)_2$ used as precursor, more crystalline, larger particles of brookite phase have been produced by increasing the hydrothermal reaction time.

In the samples $B_{200/12}$ and $B_{200/48}$ the anatase phase has also been revealed by the XRPD and Raman scattering measurements, in addition to the brookite phase. In both of these samples spindle-like particles recorded by the SEM are ascribed to brookite phase, whereas particles with dominant anatase phase are most likely spherical. The anatase has been synthesized not only in the sample treated for time shorter than 24 h (~35%), but also in the one treated for the 48 h (~5% of anatase phase), confirming that by described hydrothermal procedure pure brookite may be synthesized in relatively narrow range of reaction time [12]. Note also that in hydrothermal synthesis of mixed titania phase, produced with $TiCl_3$

Table 7
Kinetic parameters for the photocatalytic removal of alprazolam (c_0 = 0.03 mM) in presence of synthesized TiO_2 nanopowders.

	$k^a \times 10^2$ (min^{-1})	$R^b \times 10^3$ (mM/min)	r^c
$B_{200/12}$	3.39	1.02	0.9976
$B_{200/24}$	17.9	5.38	0.9989
$B_{200/48}$	7.68	2.30	0.9968

[a] Reaction rate constant determined for the first 10 min of irradiation.
[b] Reaction rate determined for the first 10 min of irradiation.
[c] Linear regression coefficient.

as precursor and NaOH added to the reaction solution, the decrease of pH value of solution, followed by the decrease of brookite content, has been registered with increase of hydrothermal time [17]. Having in mind that high basicity is required for the formation of brookite phase in this type of hydrothermal synthesis [4,17], reappearance of anatase phase after hydrothermal reaction time longer than 24 h, as in the sample $B_{200/48}$ here, may be attributed to the decrease in the pH value of the solution due to increased reaction time. The BET measurements have shown that all brookite-rich samples were mesoporous, with the specific surface area of the samples decreasing and maximum of the mesopore size distribution slightly increasing with the increase of brookite content. The results of spectroscopic ellipsometry have pointed that the presence of anatase phase in the samples synthesized at 200 °C is decreasing the energy of direct and indirect transitions. This observation is in accordance with effective increase of the bandgap energy of the brookite in comparison to that of the anatase phase, due to cathodic shift of conduction band of brookite [36].

Regarding the photocatalytic activity, pure brookite sample $B_{200/24}$ has shown the highest efficiency, removing more than 98% of alprazolam completely in the first 30 min of photocatalytic reaction. This sample has shown activity practically equal to commercial Degussa P25. The samples $B_{200/12}$, and $B_{200/48}$, consisted of both brookite and anatase phases, have removed ~75% and ~90% of alprazolam within 60 min of exposure. The sodium-titanate-powders synthesized at lower temperatures ($B_{120/24}$ and $B_{160/24}$) have performed very low activity.

In general, the dependence of photocatalytic activity of titania-based materials on many factors, such as crystallinity and crystallite size, phase composition, morphology and porous structure, bandgap energy, etc., is a complex question [7,37,40–42]. The photocatalytic activity of two or three phases titania mixture is often reported higher than of pure polymorphs [7,43,44], but the majority of studies have been related to anatase-based photocatalysts [[7] and references therein]. Several authors have pointed out an optimum ratios between anatase and brookite corresponding to the highest photoactivity in particular degradation processes [7,44]. On the other side, the nature of brookite-based photocatalysts is still matter of discussion, as pure brookite samples of different structures have been reported as both more and less active than other titania polymorphs or mixtures of brookite with other titania phases [5,14,15].

In photocatalytic degradation of alprazolam, presented in this work, the samples consisted of brookite-anatase mixed phase have shown increasing efficiency with decreasing of anatase in favor of brookite content. Among brookite-rich samples the pure brookite has performed the highest efficiency in degradation of alprazolam. This efficiency could not be related to the properties often pointed out as preferable in photocatalysis, such as small particle size and/or large specific surface area. Namely, neither the specific surface area of the pure brookite sample is the largest (on the contrary, it has minimal value, ~69.5 m^2/g), nor its brookite crystallites are the smallest (see Table 3). High brookite content as decisive factor for higher photocatalytic efficiency of brookite/anatase mixtures, rather than crystallite size or surface area, has been previously noticed and explained by the cathodic shift of the conduction band of brookite in comparison to anatase phase [36,37]. This shift should facilitate the interfacial electron transfer to molecular oxygen and thus accelerate the overall photocatalytic process [36,40]. Having in mind this consideration, the energy of direct and indirect transition registered in pure brookite sample, higher than in brookite/anatase mixtures, may provide better photocatalytic efficiency in degradation of alprazolam. Beside this, improved efficiency in photodegradation of relatively large molecule of alprazolam (with molecular size estimated as $1.27 \times 1.13 \times 0.85$ nm) may also be influenced by a slight increase of most frequent pore diameter with the increase of brookite content in the samples.

6. Conclusion

The influence of composition and morphology of brookite-type powders on their photocatalytic efficiency in removal of alprazolam under UV light irradiation has been studied. Two series of nanocrystalline brookite-type powders have been synthesized by using combined sol−gel−hydrothermal method with TiCl$_4$ as a precursor, with the hydrothermal temperature and reaction time varied. Optimal hydrothermal parameters for producing pure brookite phase have been determined. The brookite-rich powders, synthesized at 200 °C, have shown high photocatalytic efficiency, whereas the powders consisted dominantly of sodium-titanate, produced at lower temperatures (120 and 160 °C), have been almost photocatalytically inactive in degradation of alprazolam. Pure brookite sample has performed the highest efficiency, removing more than 98% of alprazolam in the first 30 min of photocatalytic reaction. Improved photocatalytic efficiency in photodegradation of alprazolam has been mainly ascribed to increased amount of brookite phase in the hydrothermally synthesized TiO$_2$ samples, rather than brookite crystallite size and specific surface area of nanopowders. Such improvement may be related to higher energy of direct and indirect transitions in pure brookite sample, as well as a slight increase of most frequent pore diameter with the increase of brookite content in brookite-rich samples.

Acknowledgment

References

[1] H. Liu, E.R. Waclawik, Z. Zheng, D. Yang, X. Ke, H. Zhu, R.L. Frost, TEM investigation and FBB model explanation to the phase relationships between titanates and titanium dioxides, J. Phys. Chem. C 114 (2010) 11430−11434.

[2] J.G. Li, T. Ishigaki, Brookite − rutile phase transformation of TiO$_2$ studied with monodispersed particles, Acta Mater. 52 (2004) 5143−5150.

[3] D. Reyes-Coronado, G. Rodríguez-Gattorno, M.E. Espinosa-Pesqueira, C. Cab, R. de Coss, G. Oskam, Phase-pure TiO$_2$ nanoparticles: anatase, brookite and rutile, Nanotechnology 19 (2008) 145605 (1−10).

[4] Y. Zheng, E. Shi, S. Cui, W. Li, X. Hu, Hydrothermal preparation of nanosized brookite powders, J. Am. Ceram. Soc. 83 (10) (2000) 2634−2636.

[5] A. Di Paola, M. Bellardita, L. Palmisano, Brookite, the least known TiO$_2$ photocatalyst, Catalysts 3 (1) (2013) 36−73.

[6] J. Xie, X. Lü, J. Liu, H. Shu, Brookite titania photocatalytic nanomaterials: synthesis, properties, and applications, Pure Appl. Chem. 81 (12) (2009) 2407−2415.

[7] A. Di Paola, G. Cufalo, M. Addamo, M. Bellardita, R. Campostrini, M. Ischia, R. Ceccato, L. Palmisano, Photocatalytic activity of nanocrystalline TiO$_2$ (brookite, rutile and brookite-based) powders prepared by thermohydrolysis of TiCl$_4$ in aqueous chloride solutions, Colloid. Surf. A 317 (2008) 366−376.

[8] B.I. Lee, X. Wang, R. Bhave, M. Hu, Synthesis of brookite TiO$_2$ nanoparticles by ambient condition sol process, Mater. Lett. 60 (2006) 1179−1183.

[9] J.H. Lee, Y.S. Yang, Synthesis of TiO$_2$ nanoparticles with pure brookite at low temperature by hydrolysis of TiCl$_4$ using HNO$_3$ solution, J. Mater. Sci. 41 (2006) 557−559.

[10] R.C. Bhave, B.I. Lee, Experimental variables in the synthesis of brookite phase TiO$_2$ nanoparticles, Mater. Sci. Eng. A 467 (2007) 146−149.

[11] M.N. Iliev, V.G. Hadjiev, A.P. Litvinchuk, Raman and infrared spectra of brookite (TiO$_2$): experiment and theory, Vib. Spectrosc. 64 (2013) 148−152.

[12] Y. Morishima, M. Kobayashi, V. Petrykin, S. Yin, T. Sato, M. Kakihana, K. Tomita, Hydrothermal synthesis of brookite type TiO$_2$ photocatalysts using a water soluble Ti-complex coordinated by ethylenediaminetetraacetic acid, J. Ceram. Soc. Jpn. 117 (3) (2009) 320−325.

[13] M. Koelsch, S. Cassaignon, J.F. Guillemoles, J.P. Jolivet, Comparison of optical and electrochemical properties of anatase and brookite TiO$_2$ synthesized by the sol−gel method, Thin Solid Films 403−404 (2002) 312−319.

[14] H. Lin, L. Li, M. Zhao, X. Huang, X. Chen, G. Li, R. Yu, Synthesis of high-quality brookite TiO$_2$ single-crystalline nanosheets with specific facets exposed: tuning catalysts from inert to highly reactive, J. Am. Chem. Soc. 134 (2012) 8328−8331.

[15] M. Zhao, H. Xu, H. Chen, S. Ouyang, N. Umezawa, D. Wang, J. Ye, Photocatalytic reactivity of {121} and {211} facets of brookite TiO$_2$ crystals, J. Mater. Chem. A Mater. Energy Sustain. 3 (2015) 2331−2337.

[16] T.-D. Nguyen-Phan, E. Jung Kim, S. Hong Hahn, W.-J. Kim, E. Woo Shin, Synthesis of hierarchical rose bridal bouquet- and humming-top-like TiO$_2$ nanostructures and their shape-dependent degradation efficiency of dye, J. Colloid Interface Sci. 356 (1) (2011) 138−144.

[17] S. Okano, S. Yamamuro, T. Tanaka, Synthesis of brookite-typed titania from titanium chloride solution, Sci. China. Ser. E Tech. Sci. 52 (1) (2009) 190−192.

[18] B. Castañeda, W. Ortiz-Cala, C. Gallardo-Cabrera, N. Sbarbati Nudelman, Stability studies of alprazolam tablets: effect of chemical interaction with some excipients in pharmaceutical solid preparations, J. Phys. Org. Chem. 22 (2009) 807−814.

[19] P. Pérez-Lozano, E. García-Montoya, A. Orriols, M. Miñarro, J.R. Ticó, J.M. Suñé-Negre, Development and validation of a new HPLC analytical method for the determination of alprazolam in tablets, J. Pharm. Biomed. Anal. 34 (2004) 979−987.

[20] K. van der Ven, W. Van Dongen, B.U.W. Maes, E.L. Esmans, R. Blust, W.M. De Coen, Determination of diazepam in aquatic samples by capillary liquid chromatography−electrospray tandem mass spectrometry, Chemosphere 57 (2004) 967−973.

[21] C. Gallardo Cabrera, R. Goldberg de Waisbaum, N. Sbarbati Nudelman, Kinetic and mechanistic studies on the hydrolysis and photodegradation of diazepam and alprazolam, J. Phys. Org. Chem. 18 (2005) 156−161.

[22] J.P. Bound, K. Kitsou, N. Voulvoulis, Household disposal of pharmaceuticals and perception of risk to the environment, Environ. Toxicol. Phar. 21 (2006) 301−307.

[23] V. Calisto, V.I. Esteves, Psychiatric pharmaceuticals in the environment, Chemosphere 77 (2009) 1257−1274.

[24] V. Calisto, M.R.M. Domingues, V.I. Esteves, Photodegradation of psychiatric pharmaceuticals in aquatic environments − kinetics and photodegradation products, Water Res. 45 (2011) 6097−6106.

[25] B.D. Cullity, S.R. Stock, Elements of X-ray Diffraction, third ed., Prentice Hall, New Jersey, 2001.

[26] S. Brunauer, P.H. Emmett, E. Teller, Adsorption of gases in multimolecular layers, J. Am. Chem. Soc. 60 (1938) 309−319.

[27] S.J. Gregg, K.S.W. Sing, Adsorption, Surface Area and Porosity, Academic Press, London, 1982, p. 126.

[28] F. Rouquerol, J. Rouquerol, K. Sing, Adsorption by Powders and Porous Solids, Academic Press, London, 1999, p. 111.

[29] E.P. Barret, L.G. Joyner, P.P. Halenda, The determination of pore volume and area distributions in porous substances. I. Computations from nitrogen isotherms, J. Am. Chem. Soc. 73 (1951) 373−380.

[30] A. Golubović, N. Tomić, N. Finčur, B. Abramović, I. Veljković, J. Zdravković, M. Grujić-Brojčin, B. Babić, B. Stojadinović, M. Šćepanović, Synthesis of pure and La-doped anatase nanopowders by sol−gel and hydrothermal methods and their efficiency in photocatalytic degradation of alprazolam, Ceram. Int. 40 (2014) 13409−13418.

[31] S.-D. Mo, W.Y. Ching, Electronic and optical properties of three phases of titanium dioxide: rutile, anatase, and brookite, Phys. Rev. B 51 (1995) 13023−13032.

[32] W. Hu, L. Li, G. Li, C. Tang, L. Sun, High-quality brookite TiO_2 flowers: synthesis, characterization, and dielectric performance, Cryst. Growth Des. 9 (2009) 3676–3682.

[33] S. El-Sherbiny, F. Morsy, M. Samir, O.A. Fouad, Synthesis, characterization and application of TiO_2 nanopowders as special paper coating pigment, Appl. Nanosci. 4 (2014) 305–313.

[34] B.C. Viana, O.P. Ferreira, A.G. Souza Filho, J. Mendes Filho, O.L. Alves, Structural, morphological and vibrational properties of titanate nanotubes and nanoribbons, J. Braz. Chem. Soc. 20 (1) (2009) 167–175.

[35] J. Rouquerol, D. Avnir, C.W. Fairbridge, D.H. Everett, J.H. Haynes, N. Pemicone, J.D.F. Ramsay, K.S.W. Sing, K.K. Unger, Recommendations for the characterization of porous solids (Technical Report), Pure Appl. Chem. 66 (1994) 1739–1758.

[36] T.A. Kandiel, A. Feldhoff, L. Robben, R. Dillert, D.W. Bahnemann, Tailored titanium dioxide nanomaterials: anatase nanoparticles and brookite nanorods as highly active photocatalysts, Chem. Mater. 22 (2010) 2050–2060.

[37] A.A. Ismail, T.A. Kandiel, D.W. Bahnemann, Novel (and better?) titania-based photocatalysts: brookite nanorods and mesoporous structures, J. Photochem. Photobiol. A 216 (2010) 183–193.

[38] B.C. Viana, O.P. Ferreira, A.G. Souza Filho, A.A. Hidalgo, J. Mendes Filho, O.L. Alves, Alkali metal intercalated titanate nanotubes: a vibrational spectroscopy study, Vib. Spectrosc. 55 (2011) 183–187.

[39] M.C. Ferrara, L. Pilloni, S. Mazzarelli, L. Tapfer, Hydrophilic and optical properties of nanostructured titania prepared by sol–gel dip coating, J. Phys. D. Appl. Phys. 43 (2010) 095301 (1–9).

[40] T.A. Kandiel, L. Robben, A. Alkaima, D. Bahnemann, Brookite versus anatase TiO_2 photocatalysts: phase transformations and photocatalytic activities, Photochem. Photobiol. Sci. 12 (2013) 602–609.

[41] M. Grujić-Brojčin, S. Armaković, N. Tomić, B. Abramović, A. Golubović, B. Stojadinović, A. Kremenović, B. Babić, Z. Dohčević-Mitrović, M. Šćepanović, Surface modification of sol–gel synthesized TiO_2 nanoparticles induced by La-doping, Mat. Char. 88 (2014) 30–41.

[42] M. Šćepanović, B. Abramović, A. Golubović, S. Kler, M. Grujić-Brojčin, Z. Dohčević-Mitrović, B. Babić, B. Matović, Z.V. Popović, Photocatalytic degradation of metoprolol in water suspension of TiO_2 nanopowders prepared using sol–gel route, J. Sol–Gel Sci. Technol. 61 (2012) 390–402.

[43] S. Bakardjieva, V. Stengl, L. Szatmary, J. Subrt, J. Lukac, N. Murafa, D. Niznansky, K. Cizek, J. Jirkovskyc, N. Petrova, Transformation of brookite-type TiO_2 nanocrystals to rutile: correlation between microstructure and photoactivity, J. Mater. Chem. 16 (2006) 1709–1716.

[44] V. Iancu, M. Baia, L. Diamandescu, Zs Pap, A.M. Vlaicu, V. Danciu, L. Baia, Weighting the influence of TiO_2 anatase/brookite ratio in TiO_2-Ag porous nanocomposites on visible photocatalytic performances, Mater. Chem. Phys. 141 (2013) 234–239.

WO₃/TiO₂ composite coatings: Structural, optical and photocatalytic properties

Zorana Dohčević-Mitrović[a,*], Stevan Stojadinović[c], Luca Lozzi[d], Sonja Aškrabić[a], Milena Rosić[e], Nataša Tomić[a], Novica Paunović[a], Saša Lazović[b], Marko G. Nikolić[b], Sandro Santucci[d]

[a] Center for Solid State Physics and New Materials, Institute of Physics Belgrade, University of Belgrade, Pregrevica 118, 11080 Belgrade, Serbia
[b] Institute of Physics Belgrade, University of Belgrade, Pregrevica 118, 11080 Belgrade, Serbia
[c] Faculty of Physics, University of Belgrade, Studentski Trg 12-16, 11000 Belgrade, Serbia
[d] Department of Physical and Chemical Sciences, University of L'Aquila, Via Vetoio 67100, L'Aquila, Italy
[e] Laboratory for Material Science, Institute of Nuclear Sciences, Vinča, University of Belgrade, P.O. Box 522, 11001 Belgrade, Serbia

ARTICLE INFO

ABSTRACT

WO₃/TiO₂ and TiO₂ coatings were prepared on titania substrates using facile and cost-effective plasma electrolytic oxidation process. The coatings were characterized by X-ray diffraction, scanning electron microscopy, Raman, UV–vis diffuse reflectance spectroscopy, and X-ray photoelectron spectroscopy. With increasing duration of PEO process, the monoclinic WO₃ phase became dominant and new monoclinic WO₂.₉₆ phase appeared. The optical absorption edge in the WO₃/TiO₂ samples, enriched with WO₃/WO₂.₉₆ phase, was shifted to the visible region. The photocatalytic efficiency of WO₃/TiO₂ and pure TiO₂ samples was evaluated by performing the photodegradation experiments in an aqueous solution of Rhodamine 6G and Mordant Blue 9 under the visible and UV light. The WO₃/TiO₂ catalysts are much more efficient than pure TiO₂ under visible light and slightly better under UV light. The improvement of photocatalytic activity in the visible region is attributed to better light absorption, higher adsorption affinity and increased charge separation efficiency.

1. Introduction

Among semiconductor materials, titanium dioxide (TiO₂) in anatase phase has been shown as excellent and widely used photocatalyst for the degradation of different organic contaminants, because of its physical and chemical stability, high oxidative power, high catalytic activity, long-term photostability, low cost and ease of production. Many organic compounds can be decomposed in an aqueous solution in the presence of TiO₂, illuminated by photons with energies greater than or equal to the band gap energy of titanium dioxide (3.2 eV for anatase TiO₂) [1–6]. The major drawback for TiO₂ commercial use lies in its wide band gap, and relatively high recombination rate of photoinduced electron-hole pairs. The modification of TiO₂ by doping with metals and non-metals [7–12] or by Ti³⁺ self-doping [13,14] have been extensively performed in order to improve its photocatalytic activity under the visible irradiation.

Another very promising approach is the combination of TiO₂ with metal oxides like V₂O₅, ZnS, InVO₄, WO₃ [15–19] or graphene [20]. Among the metal oxides, WO₃ has smaller band gap (2.8 eV) than TiO₂ and better absorbs visible light. Moreover, WO₃ has a suitable conduction band potential and acts as a trapping site for photoexcited electrons from TiO₂. The photogenerated holes from the valence band of WO₃ move towards and accumulate in the valence band of TiO₂. In such a way the efficiency of charge separation is increased, enhancing at the same time the photocatalytic acivity of TiO₂ [21]. Additionally, the formation of WO₃ monolayer on TiO₂ increases the acidity of the WO₃/TiO₂ surface enabling the adsorption of greater amount of hydroxyl groups and organic reactants on the surface [21,22]. In recent years, WO₃/TiO₂ composites were synthesized using different methods such as sol-gel, ultrasonic spray pyrolysis, ball milling, hydrothermal, sol-precipitation, and impregnation to improve photocatalytic activity of TiO₂ under the visible light [23–28]. Thin films of TiO₂/WO₃ have also been prepared by dip and spin coating [29,30] or by one-step oxidation method [31]. In most of these reports it was demonstrated that WO₃/TiO₂ composites were found to have much

* Corresponding author
E-mail address: zordoh@ipb.ac.rs (Z. Dohčević-Mitrović).

higher photocatalytic activity under the visible light than pure TiO_2 [24,26,28,31]. Therefore, the combination of these two materials can lead to increased charge carrier lifetime and improved photocatalytic activity under the visible irradiation. Among different synthesis routs, plasma electrolytic oxidation (PEO) process is very facile, cost-effective and environmentally benign process for producing of well-adhered and crystalline oxide films, but the studies on structural and photocatlytic properties of WO_3/TiO_2 films (coatings), produced by PEO process, are limited [32–34].

In this study WO_3/TiO_2 coatings were synthetized on titanium substrate by using PEO process. Structural and optical properties of the coatings were fully characterized by XRD, SEM, Raman, XPS, and diffuse reflectance spectroscopy. The aim of this work was to tailor the band gap energy of WO_3/TiO_2 coatings towards the visible spectral region, varying the time of PEO process and to explore the photocatalytic properties of the coatings. The photocatalytic efficiency of WO_3/TiO_2 coatings was tested under the visible and UV light irradiation using Rhodamine 6G and Mordant Blue 9 as model pollutants. We demonstrated that this approach provides an efficient route for the formation of cost-effective and improved visible-light-driven photocatalysts.

2. Experimental

2.1. Preparation of WO_3/TiO_2 coatings

WO_3/TiO_2 coatings were prepared on titanium substrate using plasma electrolytic oxidation (PEO) process. PEO process is an anodizing process of lightweight metals (aluminum, magnesium, zirconium, titanium, etc.) or metal alloys above the dielectric breakdown voltage, when thick, highly crystalline oxide coating with high corrosion and wear resistance, and other desirable properties are produced. During the PEO process, numerous small sized and short-lived discharges are generated continuously over the coating's surface, accompanied by gas evolution. Due to increased local temperature, plasma-chemical reactions are induced at the discharge sites modifying the structure, composition, and morphology of such oxide coatings. The oxide coatings formed by PEO process usually contain crystalline and amorphous phases with constituent species originating both from metal and electrolyte. WO_3/TiO_2 coatings were formed on the rectangular titanium samples (99.5% purity, Alfa Aesar) of dimensions 25 mm $\times$ 10 mm $\times$ 0.25 mm, which were used as working electrodes in the experiment. The working electrodes were sealed with insulation resin leaving only an area of 1.5 cm^2 as an active surface. Before starting the PEO process, titanium samples were degreased in acetone, ethanol, and distilled water, using ultrasonic cleaner and dried in a warm air stream. The anodic oxidation process was conducted in an aqueous solution of 10^{-3} M 12-tungstosilicic acid ($H_4SiW_{12}O_{40}$), at constant current density (150 mA/cm^2). During PEO process, the electrolyte circulated through the chamber–reservoir system. The temperature of the electrolyte was kept fixed at (20 ± 1) °C. Detailed description of PEO process is given in the ref. [33].

After plasma electrolytic oxidation, the samples were rinsed in distilled water to prevent additional deposition of electrolyte components during drying. The WO_3/TiO_2 samples were obtained by varying the time of PEO process from 90 s up to 300 s. The pure TiO_2 sample was obtained after 300 s of PEO process.

2.2. Characterization of WO_3/TiO_2 coatings

The crystal structure of WO_3/TiO_2 samples was analyzed by X-ray diffraction (XRD), using a Rigaku Ultima IV diffractometer in Bragg-Brentano geometry, with Ni-filtered CuKα radiation ($\lambda = 1.54178$ Å). Diffraction data were acquired over the scattering angle 2θ from 15° to 75° with a step of 0.02° and acquisition rate of 2°/min. The XRD spectra refinement was performed with the software package Powder Cell. The TCH pseudo-Voigt profile function gave the best fit to the experimental data.

Scanning electron microscope (SEM) JEOL 840A equipped with an EDS detector was used to characterize the morphology and chemical composition of formed oxide coatings.

Micro-Raman scattering measurements were performed at room temperature in a backscattering geometry, using a Jobin-Yvon T64000 triple spectrometer system and Nd:YAG laser line of 532 nm as an excitation source. The incident laser power was kept less than 10 mW in order to prevent the heating effects.

UV-vis diffuse reflectance spectra were acquired using the Specord M40 Carl Zeiss spectrometer.

X-ray photoelectron spectroscopy (XPS) was used for the surface composition analysis of WO_3/TiO_2 coatings. XPS was carried out on a VG ESCALAB II electron spectrometer with a base pressure in the analysis chamber of 10^{-8} Pa. The X-ray source was monochromatized AlKα radiation (1486.6 eV) and the instrumental resolution was 1 eV. The spectra were calibrated using the C 1 s line (284.8 eV) of the adventitious carbon and corrected by subtracting a Shirley-type background.

2.3. Photocatalytic experiments

The photocatalytic activity of WO_3/TiO_2 samples was evaluated by monitoring the decomposition of Rhodamine 6G (R6G) and Mordant Blue 9 (MB9) under the irradiation of two different light sources: fluorescent and UV lamps. The photocatalytic measurements on R6G solution (initial concentration in water: 10 mg/L) have been performed using a 36 W visible fluorescent lamp (Hyundai eagle), whose emission spectrum, compared to sunlight spectrum, is given in Ref. [9]. The cuvette (3 mL) was placed at about 5 cm from the lamp. The evolution of the rhodamine concentration was followed by measuring the variation of the intensity of main absorption peak at ~525 nm. UV–vis absorption measurements as a function of the light exposure time were performed by using USB2000 spectrometer by Ocean Optics. The solution was placed in the dark for 60 min to reach the adsorption/desorption equilibrium before visible light exposure.

The photocatalytic activity of WO_3/TiO_2 samples under UV light irradiation was evaluated using aqueous solution of MB9 as a model pollutant. Batch type experiments were performed in an open thermostated cell (at 25 °C). The cell was equipped with a water circulating jacket to maintain the solution at room temperature. A mercury lamp (125 W) was used as a light source and was placed 13 cm above the surface of the dye solution. The initial concentration of MB9 in an aqueous suspension was 50 mg/L and the working volume was 25 mL. Before the lamp was switched on, the cell was kept in dark for 60 min in order to achieve the adsorption-desorption equilibrium. At regular time intervals the aliquots were taken and the concentration of the dye was determined by UV–vis spectrophotometer (Super Scan) at $\lambda_{max} =$ 516 nm. The photocatalytic experiments were conducted at the natural pH of the dyes (pH = 7 in a case of R6G solution and at pH = 6 in a case of MB9 solution). All photocatalytic measurements were repeated at least twice to check their reproducibility.

In order to detect the formation of free hydroxyl radicals (OH$^\bullet$) on the UV illuminated WO_3/TiO_2 surface, photoluminescence (PL) measurements were performed using terephthalic acid, which is known to react with OH$^\bullet$ radicals and produces highly fluorescent 2-hydroxyterephthalic acid. The experiment was conducted at ambient temperature. The WO_3/TiO_2 photocatalyst (TW300) was placed in open termostated cell filled with 20 mL of the 5×10^{-4} mol L^{-1} terephthalic acid in a diluted NaOH aqueous solution with

a concentration of 2×10^{-3} mol L^{-1}. UV lamp (125 W) was used as a light source. Sampling was performed after 15, 30, 60 and 90 min. PL spectra of reaction solution, using excitation wavelength of 315 nm, were measured on a Spex Fluorolog spectrofluorometer system at wavelength of 425 nm for which the 2-hydroxyterephthalic acid exhibits intense PL peak.

3. Results and discussion

3.1. Crystal structure and morphology

XRD patterns of the WO$_3$/TiO$_2$ samples obtained for 90 (TW90), 120 (TW120), and 300 s (TW300) of PEO process are presented in Fig. 1. The diffraction peaks which appear in TW90 sample at $2\theta = 23.3°$, $33.4°$, $54.2°$ belong to (002), (022) and (042) planes of monoclinic WO$_3$ phase, which crystallizes in $P2_1/c$ (No. 14) space group. Besides these XRD peaks, the XRD pattern also shows peak at $25.3°$ which belongs to TiO$_2$ anatase crystal phase (space group $I4_1/amd$ (No. 141)) and intense peaks of elemental Ti (space group $P6_3$/mmc (No. 194)). This indicates that Ti substrate is not completely oxidized to form TiO$_2$ during the PEO process. With increasing duration of PEO process, for the TW120 and TW300 samples, the XRD peaks of WO$_3$ phase became more intense. The spectra refinement, using Powder Cell program, showed that besides WO$_3$ phase a monoclinic WO$_{2.96}$ phase appeared (space group $P2/c$ (No. 13)). Furthermore, the intensities of XRD peaks which belong to TiO$_2$ phase and elemental Ti decreased implying that the WO$_3$/TiO$_2$ coatings were enriched with WO$_3$/WO$_{2.96}$ phase. According to the JCPDS database for WO$_3$, WO$_{2.96}$, TiO$_2$, and elemental Ti (JCPDS: 43-1035 (WO$_3$), 30-1387 (WO$_{2.96}$), 16-0934 (TiO$_2$) and 44-1294 (elemental Ti)) very good agreement is obtained between experimental and calculated diffraction patterns of the WO$_3$/TiO$_2$ samples. In Fig. 1 are marked main XRD peaks of WO$_3$ and WO$_{2.96}$ phases for clarity. The lattice parameters and the estimated volume fractions (%) of different phases for the WO$_3$/TiO$_2$ samples are given in Table 1.

In Fig. 2 are presented SEM images of WO$_3$/TiO$_2$ samples. In the TW90 sample produced with shorter PEO time, certain number of microdischarge channels together with molten regions was present because of the rapid cooling of the electrolyte. With increasing time of PEO process, when the thickness of the oxide coating was increased, the number of microdischarge channels and

Table 1
Phase fraction (vol%) and cell parameters (Å) of WO$_3$/TiO$_2$ samples.

Phase	TW90	TW120	TW300
WO$_3$	$a = 7.4060$ $b = 7.6400$ $c = 7.6455$ 29.6%	$a = 7.3026$ $b = 7.5398$ $c = 7.6933$ 29.1%	$a = 7.4060$ $b = 7.5177$ $c = 7.5920$ 54.5%
WO$_{2.96}$	/	$a = 11.9006$ $b = 3.8258$ $c = 59.6312$ 36.70%	$a = 11.8000$ $b = 3.8098$ $c = 59.7400$ 20.90%
TiO$_2$	$a = 3.7778$, $c = 9.4440$, 66.0%	$a = 3.7841$, $c = 9.5105$, 32.2%	$a = 3.7790$, $c = 9.4124$, 23.8%
Ti	$a = 2.9481$ $c = 4.7325$ 4.3%	$a = 2.9594$ $c = 4.7254$ 2.0%	$a = 3.0510$ $c = 4.7820$ 0.9%

micropores decreased followed by increased roughness of the coating's surface.

The quantitative elemental analysis confirmed the presence of Ti, O and W and the elemental composition of the samples is shown in Table 2. EDS analysis confirmed the increasing trend of W content with increasing of PEO time.

3.2. Raman and diffuse reflectance spectra

The Raman spectra of WO$_3$/TiO$_2$ samples produced for different duration of PEO process are shown in Fig. 3a. Several modes originating from two crystalline oxide phases can be identified (marked on Fig. 3a as T and W).
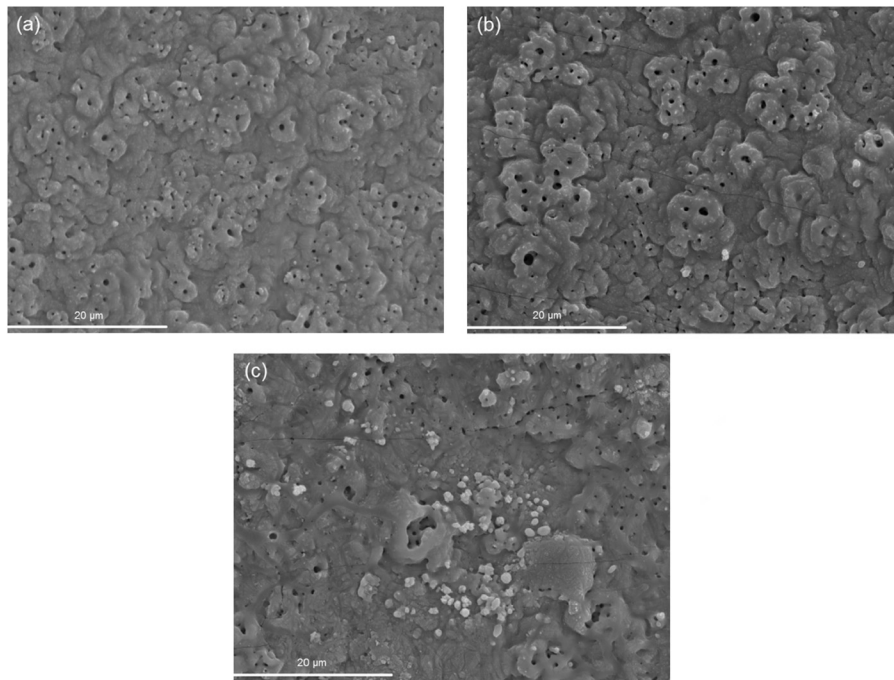
The Raman modes positions were determined using Lorentzian fit procedure and the deconvoluted spectra of TW90, TW120 and TW300 samples are presented in Fig. 3b. Besides the modes at about 144 cm^{-1} (E$_{g(1)}$), 197 cm^{-1} (E$_{g(2)}$), 393 cm^{-1} (B$_{1g(1)}$), 516 cm^{-1} (A$_{1g}$, B$_{1g(2)}$) and 638 cm^{-1} (E$_{g(3)}$) which belong to anatase phase of TiO$_2$ [35], several modes characteristic for monoclinic WO$_3$ phase are present [22,36,37]. The broad band at ~703 cm^{-1} and strong band at ~793 cm^{-1} are assigned to the stretching (O–W–O) modes of the bridging oxygen of the WO$_6$ octahedra. The bands observed at ~272 cm^{-1} and at ~316 cm^{-1} are assigned to the bending (O—W—O) vibrations of bridging oxygen in monoclinic m-WO$_3$ [22,37]. The band positioned at ~989 cm^{-1} is assigned to the dioxo (W=O)$_2$ symmetric vibration of the isolated surface WO$_4$ structure, whereas its weak shoulder at ~942 cm^{-1} represents asymmetric vibration of the same atomic group [22,37]. The low frequency mode at 58 cm^{-1} belongs to the to lattice modes of monoclinic WO$_3$ phase [38].

Further, from the Lorentzian fit procedure it was obtained that the ratio between the intensity of the peak positioned at 639 cm^{-1} and the sum of the intensities of the 703 cm^{-1} and 793 cm^{-1} peaks decreased with the increase of PEO time. This fact supports the XRD results that WO$_3$ content increases with prolonged duration of PEO process.

In Fig. 4 are presented the Raman spectra of TW90, TW120 and TW300 samples in the C—H and O—H region. The Raman band at around 2885 cm^{-1} originates from the overlapped CH$_3$ and CH$_2$ stretching vibrations [39]. Broad Raman peak in the 3000–3600 cm^{-1} frequency range can be assigned to the O—H stretching vibration of water molecules adsorbed on the surface of the WO$_3$/TiO$_2$ coatings [3,5].

The absorption spectra of TW90, TW120 and TW300 samples are given in Fig. 5a. With increasing content of WO$_3$ phase the absorption edge shifts to higher wavelengths. In the spectra of TW120 a structure around 380–400 nm can be observed, which is

Fig. 1. XRD patterns of TW90, TW120 and TW300 samples formed in various stages of PEO process, together with the XRD spectrum of Ti-substrate. In the inset is given XRD spectrum of anatase TiO$_2$ obtained on Ti-substrate after 300 s of PEO process.

Fig. 2. SEM micrographs of WO$_3$/TiO$_2$ samples formed in various stages of PEO process: (a) TW90, (b) TW120 and (c) TW300 sample.

very pronounced in the TW300 sample. The appearance of this absorption structure can be attributed to the electronic population of WO$_3$ conduction band [40]. From the absorption spectra from Fig. 4a, applying the same procedure as Ghobadi in his work [41], the band gap energies for pure TiO$_2$ and WO$_3$/TiO$_2$ samples were estimated. In Fig. 5b are presented the Tauc plots for indirect transition, as TiO$_2$ and WO$_3$ are indirect band gap semiconductors [26]. The band gap (E$_g$) energies are 3.19 eV for pure TiO$_2$, and 2.84, 2.77 and 2.6 eV for TW90, TW120 and TW300 samples, respectively. It is obvious that with increasing WO$_3$ content the band gap decreases compared to pure TiO$_2$ and shifts to the visible spectral range. Patrocinio et al. [40] have shown that in TiO$_2$/WO$_3$ films, the WO$_3$ conduction band introduces new low lying electronic levels with respect to the conduction band of TiO$_2$, causing the lowering of the band gap energy of composite samples compared to pure TiO$_2$. This finding is in accordance with the band gap behavior of our WO$_3$/TiO$_2$ samples from Fig. 5b.

3.3. XPS analysis

The XPS study was further used to confirm the chemical binding states of W 4f. The W 4f XPS spectra of the TW90 and TW300 samples and the results of their decomposition into peaks are shown in Fig. 6. The W 4f spectrum of TW90 sample (Fig. 6a) can be deconvoluted into one doublet with binding energies of 35.8 (W 4f$_{7/2}$) and 38.1 eV (W 4f$_{5/2}$), respectively. The energy position of this doublet corresponds to the W^{6+} oxidation state [42].

In the TW300 sample (Fig. 6c) the contribution of W^{5+} states from nonstoichiometric oxide phase can be seen. The W 4f

spectrum can be deconvoluted with two doublets. The first two characteristic peaks at 36 (W 4f$_{7/2}$) and 38.3 eV (W 4f$_{5/2}$) correspond to W^{6+} state as in the case of TW90. The binding energies of these peaks are somewhat higher than that for TW90 sample. The up-shift in binding energy can be ascribed to the presence of defects and OH-groups on the surface [43], existence of
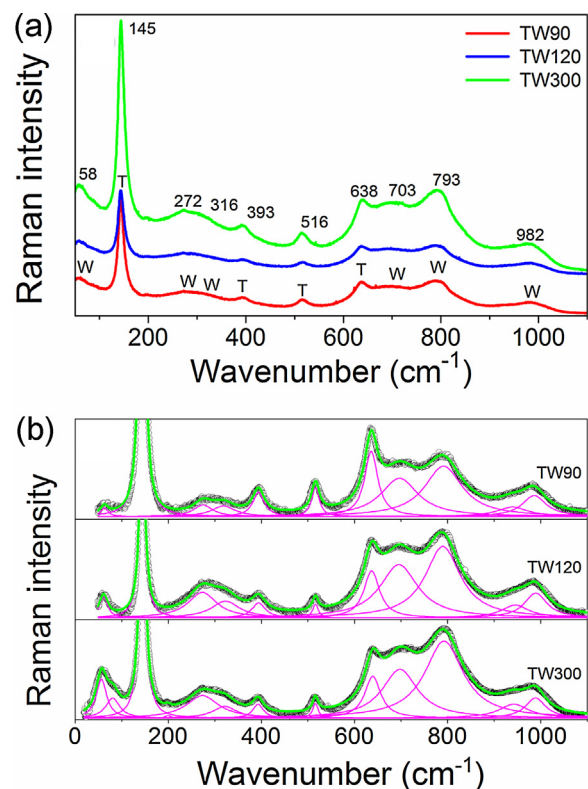
Fig. 3. Room-temperature Raman spectra of WO$_3$/TiO$_2$ samples (a). The TiO$_2$ and WO$_3$ Raman modes are marked as T and W. Deconvoluted Raman spectra of TW90, TW120 and TW300 samples (b).

Table 2
EDS analysis of the WO$_3$/TiO$_2$ composites.

Sample	EDS data			
	Ti (at%)	W (at%)	O (at%)	W/Ti
TW90	6.98	14.17	78.85	2.03
TW120	6.22	16.12	77.66	2.59
TW300	4.09	17.16	78.75	4.1
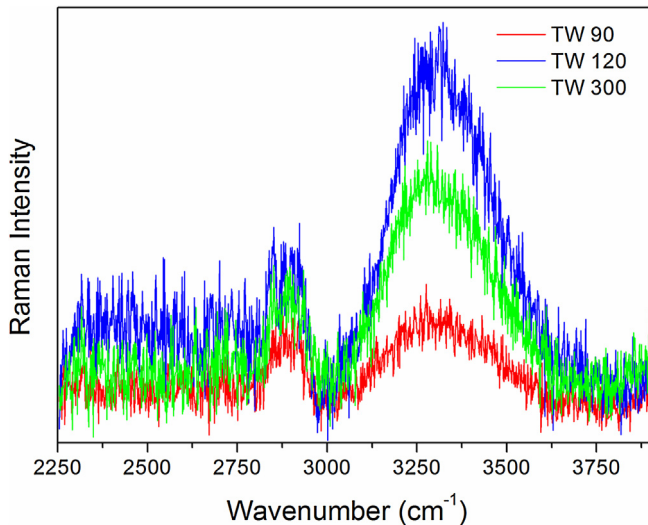
Fig. 4. Raman spectra of WO_3/TiO_2 samples in the C–H and O–H spectral region.

which is confirmed by Raman analysis (Fig. 4). The binding energies of the second doublet at 34.5 (W $4f_{7/2}$) and 36.5 eV (W $4f_{5/2}$) correspond to W^{5+} state [42]. These results are in accordance with XRD analysis.

The O 1s spectra of TW90 and TW300 samples (Fig. 6b, d) are decomposed into three peaks. The major peak at binding energy of 531.2 eV can be assigned to the oxygen atoms in WO_3 and to the OH-groups present on the surface [32,44]. The second peak observed at 530.6 eV has been attributed to oxygen bound to Ti [26], whereas the binding energy of the third peak at 533.1 eV corresponds to the oxygen in water molecules bound in the coating's structure or adsorbed on its surface [45]. The relative intensity of the XPS peaks at 531.2 eV and 533.1 eV was increased in the TW300 sample. The intensity increase of these peaks can be related to the presence of sub-stoichiometric WO_{3-x} phase ($WO_{2.96}$). Similar behavior was reported in the paper of Shpak et al. [44] in which these peaks were more intense in WO_{3-x} oxides than in stoichiometric WO_3. This finding is also supported by the Raman spectrum of TW300 sample (Fig. 4), for which the intensity of the Raman mode, corresponding to the water molecules adsorbed on the surface, is higher than in TW90 sample.

3.4. Photocatalytic performances of WO_3/TiO_2 coatings

Fig. 7a shows the kinetics of degradation of R6G for pure TiO_2 and WO_3/TiO_2 samples under the visible light. No detectable degradation of R6G was registered without the presence of WO_3/TiO_2 samples (black circles on Fig. 7a). As can be seen from Fig. 7a, both TiO_2 and WO_3/TiO_2 coatings adsorbed the dye in the equilibrium period of 60 min before the exposure to visible light. It is known from the literature that the zero point charge (pH_{zpc}) of TiO_2 lies between 6 and 6.8 [46–48], whereas the isoelectric point of WO_3 is even lower and lies in the range 1.5–2.5 [49]. At higher pH values than these WO_3 and TiO_2 surfaces should be negatively charged. Therefore, the adsorption of the R6G as cationic dye at pH = 7, points out that the surfaces of WO_3/TiO_2 and TiO_2 coatings are negative and attract the positively charged R6G. The dye adsorption ability can be crucial for the high catalytic activity of the catalyst, because it can enhance the electron/hole transfer efficiency and contact with photogenerated active species.

When TiO_2 and WO_3/TiO_2 samples were subjected to visible radiation, composite coatings have shown much better photo-efficiency and demonstrated to be far superior than pure TiO_2. The highest activity was observed for the TW90 and TW120 samples for which the photodegradation of R6G reached almost 80% after 60 min. With further increase of WO_3 content, the photocatalytic efficiency slightly decreased, but is still much higher than for pure TiO_2.

Further, the photocatalytic activity of WO_3/TiO_2 coatings for degradation of MB9 was tested under the UV light. In Fig. 7b is presented the photodegradation of MB9 in the presence of WO_3/TiO_2 samples. In the dark, WO_3/TiO_2 coatings showed no adsorption of MB9. The absence of adsorption can be explained by highly anionic character of MB9 and electrostatic repulsion between the dye and negatively charged surface of WO_3/TiO_2 coatings.

The photocatalytic activity of WO_3/TiO_2 samples was improved with increased content of WO_3 phase, and the TW300 sample exhibited better activity than pure TiO_2. As can be seen from Fig. 7b, after 240 min more than 80% of dye was degraded in the presence of WO_3/TiO_2 coatings.

Photocatalytic degradation of both dyes can be well described by first-order kinetic equation, $ln(C/C_o) = kt$, where C_o is the initial dye concentration and C is the dye concentration at time t. The first order kinetic constant k is obtained from the slope of the $ln(C/C_o)$ versus t for both dyes. In Table 3 are given the first order rate constants for R6G and MB9 (k_{R6G}, k_{MB9}), together with the corresponding linear correlation coefficient (R^2). In a case of R6G degradation under the visible light, the highest k value (k_{R6G}) was obtained for the TW90 sample. In a case of MB9 degradation under UV light, value of k_{MB9} increased with increasing amount of WO_3.

The degradation rate constant k of WO_3/TiO_2 coatings under visible light is almost five times higher than that of TiO_2, whereas its value under UV light are comparable with TiO_2, suggesting that

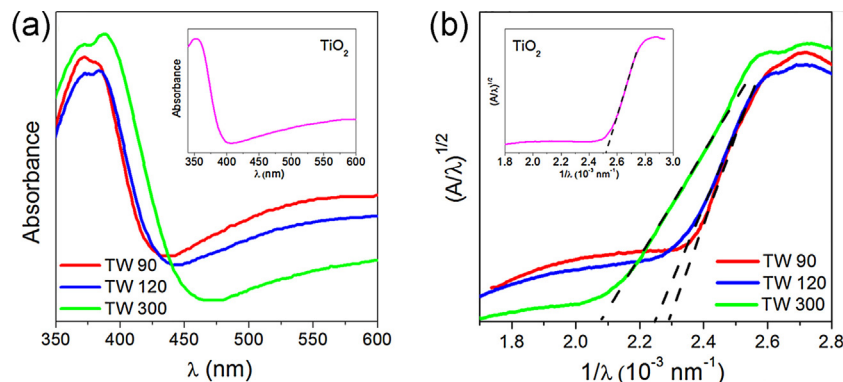**Fig. 5.** Absorbance spectra (a) and Tauc plots for indirect band gap for WO_3/TiO_2 samples (b). In the inset is given Tauc plot for indirect band gap for pure TiO_2.

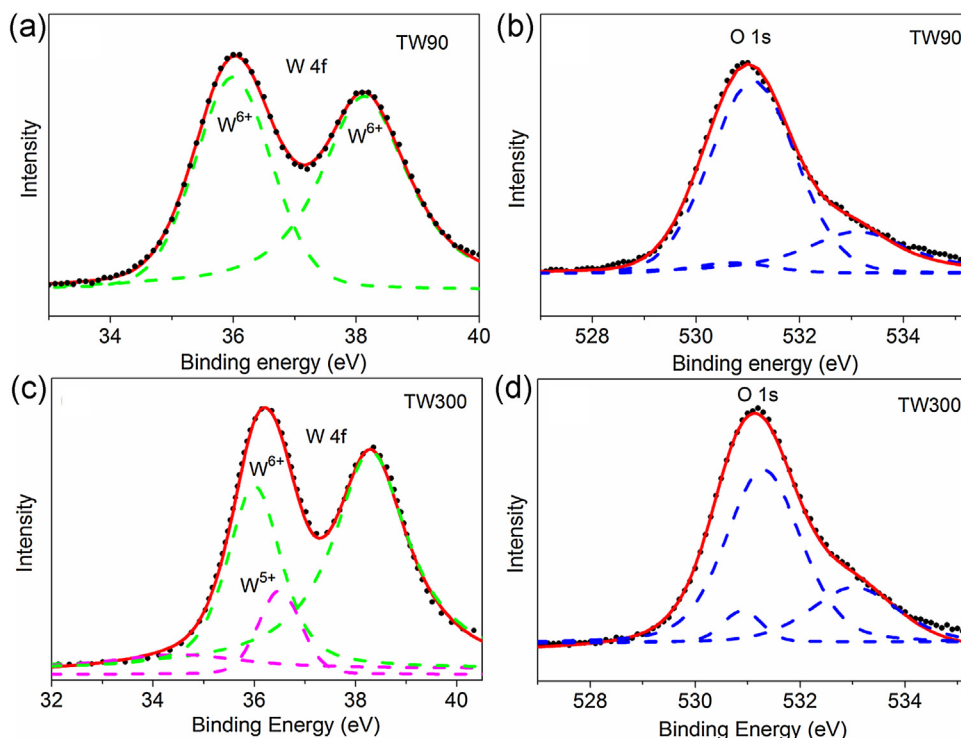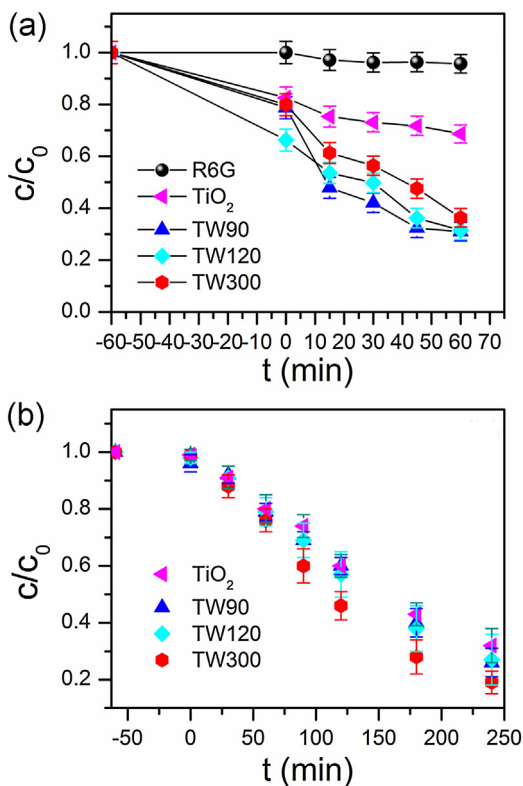**Fig. 6.** XPS spectra of W 4f and O 1s regions for TW90 and TW300 samples.

composite coatings are very efficient photocatalysts under visible light.

3.5. Hydroxyl radical analysis

The formation of free hydroxyl radicals ($OH^{\bullet}$) was tested on the surface of TW300 photocatalyst under UV irradiation and detected by PL method. Applying similar procedure as described in the paper of Su et al. [50], TW300 sample was placed in terephthalic acid solution and illuminated by UV light. PL spectra of the reaction solution were measured at room temperature after 15, 30, 60 and 90 min, and these spectra are presented in Fig. 8. The terephthalic acid reacts with $OH^{\bullet}$ producing 2-hydroxyterephthalic acid, which exhibits PL peak at 425 nm [51]. The intensity of this peak is proportional to the amount of $OH^{\bullet}$ produced in water [50,51]. As can be seen from Fig. 8, gradual increase of PL intensity at 425 nm with prolonged illumination time points at increasing amount of $OH^{\bullet}$ radicals produced at the surface of TW300 sample.

3.6. Mechanism of the reaction

The photocatalytic degradation of R6G or MB9 is initiated by the photoexcitation of the WO_3/TiO_2 coatings when the electron-hole pairs are formed on the catalyst's surface. According to the

Fig. 7. Photocatalytic degradation of R6G under visible light (a) and MB9 under UV light (b) in the presence of WO_3/TiO_2 and TiO_2 coatings.

Table 3
The pseudo-first rate constants for R6G and MB9 together with R^2.

Sample	$k_{R6G} \times 10^{-2}$ (min^{-1})	R^2	$k_{MB9} \times 10^{-2}$ (min^{-1})	R^2
TW90	1.52	0.975	0.44	0.990
TW120	1.24	0.957	0.47	0.982
TW300	1.20	0.963	0.65	0.966
TiO_2	0.28	0.888	0.41	0.963
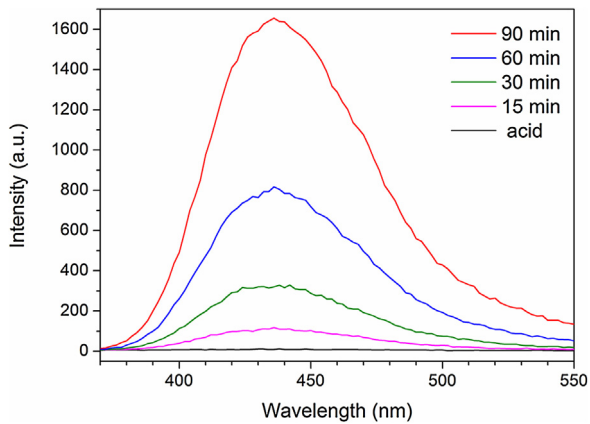
Fig. 8. PL spectral changes observed during UV illumination of TW300 sample in the solution of terephthalic acid after 15, 30, 60 and 90 min. The PL spectra of pure terephthalic acid is also presented.

generally accepted photoexcitation mechanism, electrons from the conduction band of TiO_2 can easily diffuse into the conduction band of WO_3 [40,52]. Since W(VI) can be easily reduced to W(V), WO_3 acts as an acceptor of conduction band electrons from TiO_2, whereas the photogenerated holes migrate in the opposite direction, i.e. from the lower-lying valence WO_3 band to the valence band of TiO_2. In such a way the charge separation efficiency can be increased.

In Fig. 9 is given an illustration of photo-induced electron-hole separation and reacting radicals formation. The presence of holes in the dye solution permits a direct oxidation of the dye, due to high oxidative potential of the holes (h^+):

$$h^+ + dye \rightarrow dye^{\bullet+} \rightarrow oxidation\ of\ the\ dye \qquad (1)$$
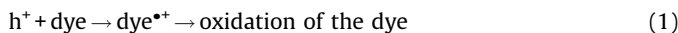
Further, hydroxyl radicals ($OH^\bullet$) are usually formed by the reaction between the holes and OH^- or water molecules present on the surface of the catalyst. The $OH^\bullet$ radicals attack the dye in aqueous solution leading to its degradation:

$$OH^\bullet + dye \rightarrow photodegradation\ of\ the\ dye \qquad (2)$$
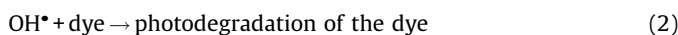
The photo-induced electrons can also react with dissolved oxygen to form superoxide ions ($O_2^{-\bullet}$) which in contact with H_2O molecules form OH^- ions and finally $OH^\bullet$ radicals.

It is known from the literature that WO_3 is almost 15 times more acidic than TiO_2 [21,22,31], so it is expected that the surface of PEO produced WO_3/TiO_2 coatings is more acidic than that of TiO_2, and has a higher affinity for chemical species having unpaired electrons. Because of higher acidity, the surface of WO_3/TiO_2 coatings can absorb more H_2O and OH^- generating more $OH^\bullet$ radicals. The XPS and Raman spectra of WO_3/TiO_2 composite coatings gave an evidence that adsorbed H_2O and hydroxyls are present on the surface of WO_3/TiO_2 coatings, existence of which is important for the formation of $OH^\bullet$ radicals. PL measurements, performed on TW300 sample, (Fig. 8) clearly demonstrated that with increasing illumination time the increasing amount of $OH^\bullet$ radicals is formed on the surface of photocatalysts, which manifests through higher photocatalytic activity of TW300 sample.

The absorption measurements have shown that the band gap energy of TiO_2 is higher than that of WO_3/TiO_2 coatings. Namely, with prolonged time of PEO process, the WO_3 content increases followed by an appearance of $WO_{2.96}$ phase. As the conduction band of nonstoichiometric WO_{3-x} oxides is lower with respect to WO_3 and TiO_2 (Fig. 9) [53], the presence of $WO_{2.96}$ phase will further reduce the band gap of WO_3/TiO_2 samples towards the visible spectral range, as already noticed from the Tauc plots from Fig. 5. As a result, the electron-hole recombination will be more difficult and more reactive radicals can be produced at the WO_3/TiO_2 surface. Therefore, WO_3/TiO_2 coatings should be more efficient as catalysts under the visible light. The photocatalytic degradation of R6G and kinetics of the reaction confirmed that WO_3/TiO_2 coatings are efficient photocatalysts in the visible region. Slight decrease of photocatalytic activity of TW300 sample in a case of R6G photodegaradation (Fig. 7a) can be explained by the occurrence of photochromism [27,40]. Namely, the electron accumulation at the WO_3 conduction band can be more pronounced with increased WO_3 content. The accumulated electrons can react with $OH^\bullet$ radicals forming OH^- ions or can reduce the number of superoxide radicals [27,40] degrading at some extent the photocatalytic activity of WO_3/TiO_2 coatings. The presence of pronounced absorption feature around 380–400 nm in the absorbance spectrum of TW300 sample confirms this assumption. Another reason can be found in the formation of small polarons, appearance of which is characteristic for WO_3 and WO_{3-x} phases. The photoexcited electron-hole pairs can be rapidly quenched by recombination of photoexcited holes with electrons from localized polaron states, whereas photoexcited electrons
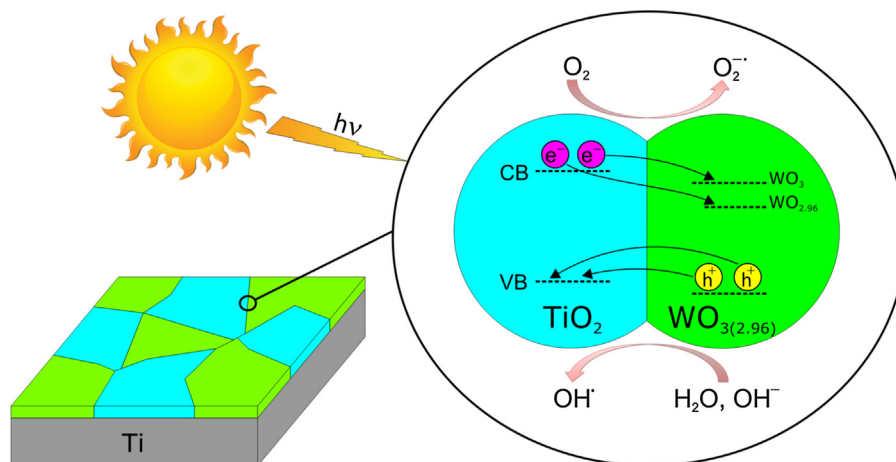
Fig. 9. Schematic diagram of electron-hole pairs separation and proposed mechanism of photodegradation over WO_3/TiO_2 photocatalysts.

populate polaron states [54], reducing on the other side the photocatalytic efficiency of the catalyst.

4. Conclusion

WO_3/TiO_2 composite and pure TiO_2 coatings have been prepared on titania substrates using facile and cost-effective PEO process. The structural, morphological, optical properties and chemical composition of these samples were investigated by different methods such as XRD, SEM, Raman, UV–vis diffuse reflectance spectroscopy and XPS. XRD and Raman analysis revealed that the coatings are mainly composed of monoclinic WO_3 and anatase TiO_2. With increasing duration of PEO process the crystallinity of the samples was improved, the WO_3 phase become dominant and a certain amount of monoclinic $WO_{2.96}$ phase appeared. XPS analysis confirmed the XRD results and revealed the presence of OH-groups and adsorbed H_2O on the surface of WO_3/TiO_2 coatings. The increasing amount of $WO_3/WO_{2.96}$ phase caused a decrease of optical band gap, i.e. shift from near UV to visible spectral region. The photocatalytic activity of WO_3/TiO_2 samples has been measured by monitoring photodecolouration of two model pollutants in aqueous solution, R6G under visible and MB9 under UV light irradiation. The WO_3/TiO_2 samples have shown enhanced photocatalytic activity compared to pure TiO_2 under the visible light irradiation. Slight decrease of photocatalytic activity under the visible light in the sample enriched with $WO_3/WO_{2.9}$ phase can be ascribed to the occurrence of photochromism and/or small polaron formation. Under the UV light, the WO_3/TiO_2 photocatalysts have shown slightly better photocatalytic activity than pure TiO_2. PL mesurements demonstrated the correlation between photoactivity and the formation rate of OH• radicals under UV light irradiation, i.e. higher amount of OH• radicals formed, the better photoactivity of WO_3/TiO_2 photocatalysts was achieved. The kinetics of the reaction in the case of both azo dyes followed the pseudo-first order. The degradation rate constant k of WO_3/TiO_2 coatings under the visible light is almost five times higher than that of TiO_2. Much better photocatalytic activity of the WO_3/TiO_2 samples compared to pure TiO_2 in the visible range can be attributed to better light absorption, higher adsorption affinity and increased charge separation efficiency with increasing content of $WO_3/WO_{2.96}$ phase.

Acknowledgements

References

[1] L. Ren, Y. Li, J. Hou, X. Zhao, C. Pan, ACS Appl. Mater. Interfaces 6 (2014) 1608–1615.
[2] F. Ruggieri, A.A. D'Archivio, M. Fanellia, S. Santucci, RSC Adv. 1 (2011) 611–618.
[3] M. Šćepanović, B. Abramović, A. Golubović, S. Kler, M. Grujić-Brojčin, Z. Dohčević-Mitrović, B. Babić, B. Matović, Z.V. Popović, J. Sol-Gel Sci. Technol. 61 (2012) 390–402.
[4] A. Golubović, B. Abramović, M. Šćepanović, M. Grujić-Brojčin, S. Armaković, I. Veljković, B. Babić, Z. Dohčević-Mitrović, Z.V. Popović, Mater. Res. Bull. 48 (2013) 1363–1371.
[5] S. Watson, D. Beydoun, J. Scott, R. Amal, J. Nanoparticle Res. 6 (2004) 193–207.
[6] A.N. Banerjee, Nanotechnol. Sci. Appl. 4 (2011) 35–65.
[7] M. Xing, D. Qi, J. Zhang, F. Chen, Chem. Eur. J. 17 (2011) 11432–11436.
[8] Y. Niu, M. Xing, J. Zhang, B. Tian, Catal. Today 201 (2013) 159–166.
[9] F. Ruggieri, D. Di Camillo, L. Maccarone, S. Santucci, L. Lozzi, J. Nanopart. Res. 15 (2013) 1–11.
[10] W. M. Xing, Y. Li, J. Wu, X. Gong Zhang, J. Phys. Chem. C 115 (2011) 7858–7865.
[11] M. Janus, B. Tryba, E. Kusiak, T. Tsumura, M. Toyoda, M. Inagaki, A.W. Morawski, Catal. Lett. 128 (2009) 36–39.
[12] M. Takeuchi, M. Matsuoka, M. Anpo, Res. Chem. Intermed. 38 (2012) 1261–1277.
[13] X. Chen, L. Liu, P.Y. Yu, S.S. Mao, Science 331 (2011) 746–750.
[14] W. Fang, M. Xing, J. Zhang, Appl. Catal. B: Environ. 160–161 (2014) 240–246.
[15] Y. Wang, J. Zhang, L. Liu, C. Zhu, X. Liu, Q. Su, Mater. Lett. 75 (2012) 95–98.
[16] Y. Xiaodan, W. Qingyin, J. Shicheng, G. Yihang, Mater. Charact. 57 (2006) 333–341.
[17] J. Rashid, M.A. Barakat, S.L. Pettit, J.N. Kuhn, Environ. Technol. 35 (2014) 2153–2159.
[18] B. Gao, Y. Ma, Y. Cao, W. Yang, J. Yao, J. Phys. Chem. B 110 (2006) 14391–14397.
[19] X. Luo, F. Liu, X. Li, H. Gao, G. Liu, Mat. Sci. Semicon. Proc. 16 (2013) 1613–1618.
[20] N.R. Khalid, E. Ahmed, Z. Hong, M. Ahmad, Y. Zhang, S. Khalid, Ceram. Int. 39 (2013) 7107–7113.
[21] Y. Li, P.C. Hsu, S.M. Chen, Sensor. Actuat. B-Chem. 174 (2012) 427–435.
[22] K.K. Akurati, A. Vital, J.P. Dellemann, K. Michalowa, T. Graule, D. Ferri, A. Baiker, Appl. Catal. B: Environ. 79 (2008) 53–62.
[23] D. Ke, H. Liu, T. Peng, X. Liu, K. Dai, Mater. Lett. 62 (2008) 447–450.
[24] H. Song, H. Jiang, X. Liu, G. Meng, J. Photoch. Photobio. A 181 (2006) 421–428.
[25] C. Shifu, C. Lei, G. Shen, C. Gengyu, Powder Technol. 160 (2005) 198–202.
[26] F. Riboni, L.G. Bettini, D.W. Bahnemann, E. Selli, Catal. Today 209 (2013) 28–34.
[27] J. Yang, X. Zhang, H. Liu, C. Wang, S. Liu, P. Sun, L. Wang, Y. Liu Catal, Today 201 (2013) 195–202.
[28] S. Bai, H. Liu, J. Sun, Y. Tian, S. Chen, J. Song, R. Luo, D. Li, A. Chen, C.-C. Liu, Appl. Surf. Sci. 338 (2015) 61–68.
[29] A. Rampaul, I.P. Parkin, S.A. O'Neill, J. DeSouza, A. Mills, N. Elliott, Polyhedron 22 (2003) 35–44.
[30] J.H. Pan, W. In Lee, Chem. Mater. 18 (2006) 847–853.
[31] M. Long, B. Tan, P. Hu, B. Zhou, Y. Zhou, J. Mater. Chem. A 3 (2015) 10195–10198.
[32] J. He, Q. Luo, Q.Z. Cai, X.W. Li, D.Q. Zhang, Mater. Chem. Phys. 129 (2011) 242–248.
[33] S. Stojadinović, N. Radić, R. Vasilić, M. Petković, P. Stefanov, Lj. Zeković, B. Grbić, Appl. Catal. B: Environ. 126 (2012) 334–341.
[34] S. Petrović, S. Stojadinović, Lj. Rožić, N. Radić, B. Grbić, R. Vasilić, Surf. Coat. Technol. 269 (2015) 250–257.
[35] T. Ohsaka, F. Izumi, Y. Fujiki, J. Raman Spectrosc. 7 (1978) 321–324.
[36] Y. Djaoued, S. Balaji, N. Beaudoin, J. Sol-Gel Sci. Technol. 65 (2013) 374–383.
[37] C. Santato, M. Odziemkowski, M. Ulmann, Jan Augustynski, J. Am. Chem. Soc. 123 (2001) 10639–10649.
[38] E. Cazzanelli, C. Vinegoni, G. Mariotto, A.J. Purans, Solid State Ionics 123 (1999) 67–74.
[39] Y. Yu, K. Lin, X. Zhou, H. Wang, S. Liu, X. Ma, J. Phys. Chem. C 111 (2007) 8971–8978.
[40] A.O.T. Patrocinio, L.F. Paula, R.M. Paniago, J. Freitag, D.W. Bahnemann, ACS Appl. Mater. Interfaces 6 (2014) 16859–16866.
[41] N. Ghobadi, Int. Nano Let. 3 (2013) 1–4.
[42] K. Senthil, K. Yong, Nanotechnology 18 (2007) 395604 (1–7).
[43] H. Ling, J. Lu, S. Phua, H. Liu, L. Liu, Y. Huang, D. Mandler, P.S. Lee, X. Lu, J. Mater. Chem. A 2 (2014) 2708–2717.
[44] A.P. Shpak, A.M. Korduban, V.O. Medvedskij, J. Electron. Spectrosc. Relat. Phenom. 156–158 (2007) 172–175.
[45] H.Y. Wong, C.W. Ong, R.W.M. Kwok, K.W. Wong, S.P. Wong, W.Y. Cheung, Thin Solid Films 376 (2000) 131–139.
[46] A.A. Khodja, A. Boulkamh, C. Richard, Appl. Catal. B: Environ. 59 (2005) 147–154.
[47] C.C. Wang, J.Y. Ying, Chem. Mater. 11 (1999) 3113–3120.
[48] M.D. Hernández-Alonso, F. Fresno, S. Suarez, J.M. Coronado, Energy Environ. Sci. 2 (2009) 1231–1257.
[49] M. Anik, T. Cansizoglu, J. Appl. Electrochem. 36 (2006) 603–608.
[50] T.M. Su, Z.L. Liu, Y. Liang, Z.Z. Qin, J. Liu, Y.Q. Huang, Catal. Comm. 18 (2012) 93–97.
[51] K. Ishibashi, A. Fujishima, T. Watanabe, K. Hashimoto, Electrochem. Commun. 2 (2000) 207–210.
[52] H. Park, A. Bak, T.H. Jeon, S. Kim, W. Choi, Appl. Catal. B: Environ. 115–116 (2012) 74–80.
[53] A.K.L. Sajjad, S. Shamaila, B. Tian, F. Chen, J. Zhang, Appl. Catal. B: Environ. 91 (2009) 397–405.
[54] M.B. Johansson, G.A. Niklasson, L. Österlund, J. Mater. Res. 27 (2012) 3130–3140.

PAPER

Check for updates

Nitrate-assisted photocatalytic efficiency of defective Eu-doped Pr(OH)₃ nanostructures†

S. Aškrabić,*[a] V. D. Araújo,[b] M. Passacantando,[c] M. I. B. Bernardi,[d] N. Tomić,[a] B. Dojčinović,[e] D. Manojlović,[f] B. Čalija, [iD][g] M. Miletić[a] and Z. D. Dohčević-Mitrović*[a]

Pr(OH)₃ one-dimensional nanostructures are a less studied member of lanthanide hydroxide nanostructures, which recently demonstrated an excellent adsorption capacity for organic pollutant removal from wastewater. In this study, $Pr_{1-x}Eu_x(OH)_3$ (x = 0, 0.01, 0.03, and 0.05) defective nanostructures were synthesized by a facile and scalable microwave-assisted hydrothermal method using KOH as an alkaline metal precursor. The phase and surface composition, morphology, vibrational, electronic and optical properties of the as-prepared samples were characterized by X-ray diffraction (XRD), X-ray photoelectron spectroscopy (XPS), inductively coupled plasma optical emission spectrometry (ICP-OES), transmission electron microscopy (TEM), field emission scanning electron microscopy (FE-SEM), Raman, infrared (IR), photoluminescence (PL), and diffuse reflectance spectroscopy (DRS). It was deduced that the incorporation of Eu^{3+} ions promoted the formation of oxygen vacancies in the already defective Pr(OH)₃, subsequently changing the Pr(OH)₃ nanorod morphology. The presence of KNO₃ phase was registered in the Eu-doped samples. The oxygen-deficient Eu-doped Pr(OH)₃ nanostructures displayed an improved photocatalytic activity in the removal of reactive orange (RO16) dye under UV-vis light irradiation. An enhanced photocatalytic activity of the Eu-doped Pr(OH)₃ nanostructures was caused by the synergetic effect of oxygen vacancies and Eu^{3+} (NO_3^-) ions present on the Pr(OH)₃ surface, the charge separation efficiency and the formation of the reactive radicals. In addition, the 3% Eu-doped sample exhibited very good adsorptive properties due to different morphology and higher electrostatic attraction with the anionic dye. $Pr_{1-x}Eu_x(OH)_3$ nanostructures with the possibility of tuning their adsorption/photocatalytic properties present a great potential for wastewater treatment.

Introduction

Nanocrystalline rare earth hydroxides have started to draw attention in the recent years because they are relatively facile

[a] *Center for Solid State Physics and New Materials, Institute of Physics Belgrade, University of Belgrade, Pregrevica 118, 11080 Belgrade, Serbia. E-mail: sonask@ipb.ac.rs, zordoh@ipb.ac.rs*

[b] *Unidade Acadêmica do Cabo de Santo Agostinho, Universidade Federal Rural de Pernambuco, Cabo do Santo Agostinho, PE, Brazil*

[c] *Department of Physical and Chemical Sciences, University of L'Aquila, Via Vetoio, 67100 Coppito L'Aquila, Italy*

[d] *Instituto de Física de São Carlos, Universidade de São Paulo, São Carlos, SP, Brazil*

[e] *Center of Chemistry, Institute of Chemistry, Technology and Metallurgy, University of Belgrade, Njegoševa 12, 11000 Belgrade, Serbia*

[f] *Faculty of Chemistry, University of Belgrade, Studentski trg 12-16, 11000 Belgrade, Serbia*

[g] *Faculty of Pharmacy, University of Belgrade, Vojvode Stepe 450, 11221 Belgrade, Serbia*

† Electronic supplementary information (ESI) available. See DOI: 10.1039/c7cp06440c

to synthesize and usually do not require high-temperature annealing. As all rare earth compounds, lanthanide hydroxides display an interesting catalytic, optical, magnetic and adsorptive properties.[1–5] They also represent a straightforward approach for obtaining rare earth oxides since these hydroxides can be transformed to the corresponding oxides by annealing at higher temperatures. Rare earth hydroxides in the form of one-dimensional nanostructures were synthesized by different methods such as precipitation, hydrothermal or microemulsion method or electrodeposition.[2–9] It is known that lanthanide hydroxides most often crystallize into one-dimensional (1D) structures, such as nanorods, nanobundles or nanobelts. These 1D porous structures have the potential for applications in water pollutant removal since their dimensionality makes them much more accessible to the pollutant molecules. Moreover, it is expected that the abundance of –OH groups (inherent in these materials) can have a significant impact on their photocatalytic and adsorptive properties. As the 1D nanostructures are expected to have a better surface activity if the total surface

31756 | *Phys. Chem. Chem. Phys.*, 2017, **19**, 31756–31765

This journal is © the Owner Societies 2017

to volume ratio is higher, it is of interest to obtain nanorods/ nanowires with a high length-to-diameter ratio. The 1D geometry (the aspect ratio of longer to shorter dimension) can be tuned in the hydrothermal synthesis process by changing the molar ratios of $[OH^-]/[Ln^{3+}]$, where OH^- ions originate from the hydroxide precursor and Ln^{3+} ions from lanthanide salt or oxide, but this ratio is also dependent on the choice of alkaline metal hydroxide. In the case of $Eu(OH)_3$, it was shown that with increasing ratio of $[OH^-]/[Eu^{3+}]$, the aspect ratio of the 1D nanostructures decreased when NaOH was used,[4] but increased when KOH was used.[10]

Among nanocrystalline lanthanide hydroxides, the electrochemically prepared 1D $Pr(OH)_3$ nanostructures were shown to possess the excellent adsorptive properties regarding the dye removal from water.[6,7] Electrodeposition was also used to produce the 1D $Pr(OH)_3$ nanostructures that demonstrated good adsorption of phosphates.[8] Furthermore, the 1D porous $Pr(OH)_3$ nanowire bundles synthesized by a template-free electrochemical deposition method demonstrated good ferromagnetic properties.[2] In addition, the toxicity studies of the porous $Pr(OH)_3$ nanostructures demonstrated their great potential as the environmentally friendly adsorbent materials.[7]

There are only a few papers dedicated to the investigation of the 1D $Pr(OH)_3$ nanostructures[2,6–9] and a majority of them concerned the adsorptive properties of this material. To the best of our knowledge, the photocatalytic properties of pure or doped $Pr(OH)_3$ have not been investigated up till date. This is probably due to the relatively large band gap of these materials (4.7 eV) and their consequent insufficient efficiency in the absorption of the solar radiation. However, a recent study by Dong *et al.*[3] showed that oxygen vacancies can create the electronic states within the band gap of $La(OH)_3$ nanorods, extending their photoresponse range and making them very efficient photocatalysts. In addition, doping of $La(OH)_3$ nanorods with lanthanides, Ln^{3+}, drastically improved their photocatalytic activity; Eu^{3+} was one of the dopants that produced the best results in this direction.[11]

In this study, $Pr(OH)_3$ nanorods and $Pr_{1-x}Eu_x(OH)_3$ ($x = 0.01$, 0.03, and 0.05) nanostructures were obtained by a microwave-assisted hydrothermal method. We demonstrated that Eu doping influences the changes in the $Pr(OH)_3$ morphology, the adsorption affinity, and can substantially increase the photocatalytic activity of $Pr(OH)_3$ nanorods towards the dye degradation. In addition, the doping changes the content of oxygen vacancies, which, together with synthesis-introduced nitrates and morphology, determine whether the resulting nanostructures are dominantly photocatalysts or adsorbents. The facile and scalable synthesis, the high photocatalytic activity of Eu-doped $Pr(OH)_3$ nanostructures and the possibility of tuning the ratio of their adsorptive/photocatalytic activity present a great potential for their application in the efficient and cost-effective pollutant removal.

Experimental

Preparation of pure and Eu-doped $Pr(OH)_3$ nanostructures

$Pr_{1-x}Eu_x(OH)_3$ ($x = 0$, 0.01, 0.03, and 0.05) nanostructures were prepared by the microwave-assisted hydrothermal method

from the precursor oxides, Pr_6O_{11} and Eu_2O_3. The synthesis procedure included the following steps: first, the precursors were dissolved in aqueous HNO_3; subsequently, 0.02 mol of the dissolved Pr- and Eu-precursors (0, 1%, 3% and 5% at. Eu) were added into 50 mL of distilled water. Following this, 50 mL of a 10 M KOH solution was added rapidly under vigorous stirring. KOH was chosen as a precursor for the hydrothermal synthesis of pure and doped $Pr(OH)_3$ nanorods in this study, as it has been shown that it enhances the formation of 1D nanorods with a higher ratio of length to diameter.[10] The mixed solution was placed in a 110 mL Teflon autoclave (filling 90% of its volume), which was sealed and placed in a microwave-assisted hydrothermal system; 2.45 GHz of microwave radiation was applied at a maximum power of 800 W. The temperature was measured with a temperature sensor (type K thermocouple) inserted into the vessel. Each of the as-prepared solutions was subjected to the microwave hydrothermal synthesis and heated to a temperature of 140 °C for 10 min. The products were then air-cooled to room temperature. The as-obtained precipitate powder was washed several times with distilled water and isopropyl alcohol and then dried on a hot plate at 60 °C for 24 h.

Characterization

The powder X-ray diffraction (XRD) characterization was performed using a Shimadzu diffractometer (Model XRD-7000, CuKα radiation ($\lambda = 1.54$ Å), 40 kV and 30 mA). The scanning range was between 5 and 120° (2θ) with a step size of 0.02° and a step time of 5.0 s. The Rietveld analysis was performed using the Rietveld refinement program GSAS.[12] A pseudo-Voigt profile function was used. The specific surface area (S_{BET}) was estimated from the N_2 adsorption/ desorption isotherms at liquid nitrogen temperature following the multipoint BET procedure using a Micromeritics ASAP 2000. The determination of the concentrations of europium in the doped samples was performed by inductively coupled plasma optical emission spectrometry (ICP-OES) using an iCAP 6500 Duo ICP (Thermo Fisher Scientific, Cambridge, UK) spectrometer and RACID86 charge injector device (CID) detector with iTEVA operational software. The quantification of europium in the solutions was performed at the following emission wavelength: Eu II 381.967 nm. The morphology of the nanostructures was characterized by transmission electron microscopy (TEM) and field emission scanning electron microscopy (FE-SEM). The TEM characterization was conducted on a Philips CM 300 microscope operating at 300 kV. The SEM measurements were carried out on a Tescan MIRA3 field emission gun at 10–20 kV under high vacuum. The SEM working distance was between 3.3 and 4 mm. The room-temperature micro-Raman spectra of $Pr_{1-x}Eu_x(OH)_3$ nanostructures were excited using solid state Nd:YAG laser line of 514 nm. Low laser power ($\sim$2 mW) was applied to prevent the thermal degradation of the sample. Tri Vista 557 triple spectrometer coupled to the nitrogen-cooled CCD detector was employed for the spectra collection at room temperature. X-ray photoelectron spectroscopy (XPS) measurements were performed using the PHI ESCA system equipped with a non-monochromatic Al X-ray source (1486.6 eV) with a hemispherical analyzer. The infrared transmission spectra (IR) were obtained on a Thermo

This journal is © the Owner Societies 2017

Phys. Chem. Chem. Phys., 2017, **19**, 31756–31765 | 31757

Nicolet 6700 Fourier transform infrared spectrophotometer at room temperature. Diffuse reflectance spectra (DRS) were acquired using a Specord M40 Carl Zeiss spectrometer. The room-temperature PL measurements were performed on a Spex Fluorolog spectrofluorometer using a 340 nm excitation wavelength.

Photodegradation tests

The photocatalytic activity of $Pr_{1-x}Eu_x(OH)_3$ nanostructures under UV light irradiation was evaluated by monitoring the decomposition of reactive orange (RO16) as a model pollutant. The batch-type experiments were performed in an open thermo-stated cell (at 25 °C) equipped with a water circulating jacket to maintain the solution at room temperature. A mercury lamp (125 W) was used as a light source. The initial concentration of RO16 in an aqueous suspension was 50 mg L^{-1} and the working volume was 25 mL. Before the photocatalytic experiment, the cell was kept in dark for 60 min in order to achieve the adsorption–desorption equilibrium. At regular time intervals, the aliquots were taken and the dye concentration was monitored by measuring the variation of the intensity of absorption peak at λ_{max} = 494 nm using a Varian Super Scan 3 UV-vis spectrophotometer. The photo-catalytic experiments were conducted at the natural pH of the RO16 dye (pH = 4.7). In order to detect the formation of the photo-generated hydroxyl radicals (OH$^{\bullet}$), the photoluminescence (PL) measurements were performed using terephthalic acid, which is known to react with OH$^{\bullet}$ radicals and produce highly fluorescent 2-hydroxyterephthalic acid. The experiment was conducted at ambient temperature and the photocatalyst was placed in an open thermostated cell filled with 20 mL of 5×10^{-4} mol L^{-1} terephthalic acid in a diluted NaOH aqueous solution with a concentration of 2×10^{-3} mol L^{-1}. A UV light source was used and a sampling was performed after 5, 10, and 15 min. The PL spectra of the reaction solution, using an excitation wavelength of 315 nm, were measured on a Spex Fluorolog spectrofluoro-meter system following the changes of the PL peak at 425 nm, at which the 2-hydroxyterephthalic acid exhibits an intense PL peak.

Results and discussion

The structural characterization of the obtained $Pr_{1-x}Eu_x(OH)_3$ (x = 0, 0.01, 0.03, and 0.05) nanostructures was performed using XRD analysis and the diffraction patterns are shown in Fig. 1. All diffraction peaks of the as-synthesized samples can be perfectly indexed to the hexagonal $P6_3/m$ space group (ICSD No. 200487 or JCPDS No. 83-2304).[13] The secondary peaks (marked with (*) in Fig. 1) at 23.5°, 33.9° and 43.7° were detected in the Eu-doped samples and ascribed to KNO_3 that was formed from the precursors.[14] The lattice parameters (a and c) and oxygen occupancy factor (O_{occup}) calculated from the Rietveld refinement and the quality factors (R_{exp} and R_{Bragg}) of the refinement are summarized in Table 1.

The lattice parameters slightly decreased with Eu doping due to the substitution of the larger Pr^{3+} ion (radii = 1.179 Å) by the smaller Eu^{3+} ion (radii = 1.12 Å)[15] except for the 3%

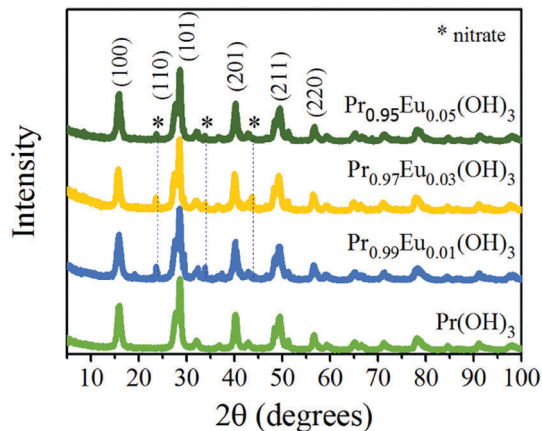**Fig. 1** XRD patterns obtained for $Pr_{1-x}Eu_x(OH)_3$ nanostructures ($0 \leq x \leq 0.05$). The positions of the diffraction peaks assigned to KNO_3 are marked with asterisks.

Table 1 Specific surface area (S_{BET}), lattice parameters (a) and (c), oxygen occupancy factor (O_{occup}), and density (ρ) of $Pr_{1-x}Eu_x(OH)_3$ nanostructures

Sample	S_{BET} (m^2 g^{-1})	a^a (Å)	c^a (Å)	O_{occup}^a	ρ^a (g cm^{-3})	R_{exp} (%)	R_{Bragg} (%)
$Pr(OH)_3$	130.52	6.453(4)	3.769(9)	0.84(8)	4.45	11.6	6.0
1% Eu	83.24	6.453(4)	3.768(9)	0.80(2)	4.39	12.6	7.0
3% Eu	63.05	6.461(1)	3.769(0)	0.66(6)	4.22	13.0	8.5
5% Eu	82.77	6.449(0)	3.763(4)	0.74(5)	4.34	11.9	6.0

^{a} Calculated *via* the Rietveld refinement.

Eu-doped sample. The decrease in O_{occup} with Eu doping signifies an increase in oxygen vacancy content. From Table 1, it can be seen that the 3% Eu-doped sample has the smallest O_{occup}, *i.e.*, the highest content of oxygen vacancies, the presence of which can be responsible for the observed lattice expansion in this sample.[16] In Table 1, the BET specific surface area and the density of the as-synthesized samples are also presented. Clearly, the specific surface area (S_{BET}) decreased in the doped samples compared to that of the pure hydroxide and was the lowest in the 3% Eu-doped sample.

The type of dopant and its incorporation influence the properties of the obtained materials to a great extent. Therefore, it is important to determine precisely the amount of the incorpo-rated Eu in $Pr_{1-x}Eu_x(OH)_3$ ($0.01 \leq x \leq 0.05$) nanopowders. In that sense, the ICP analysis was performed and the results reveal that the content of the incorporated Eu is slightly lower than its nominal content for each doped sample (see Table 2).

The morphology of pure and Eu-doped nanostructures was characterized by TEM and FE-SEM. Fig. 2 shows the TEM images of pure and Eu-doped $Pr(OH)_3$ nanostructures, while the SEM images are shown in Fig. S1 in the ESI.† Pure $Pr(OH)_3$ dominantly consists of well-dispersed nanorods with diameters ranging between 5 and 10 nm (Fig. 2(a)). With the increase of the Eu dopant content, the morphology of the obtained nanomaterials changed and besides nanorods, the increasing presence of irregularly shaped grains that do not have the nanorod morphology was also observed. This can be explained

Paper

Table 2 Measured Eu content of $Pr_{1-x}Eu_x(OH)_3$ nanostructures by ICP-OES

Sample	Theoretical Eu content (mg g^{-1})	Measured Eu content (mg g^{-1})	Atomic concentration (%)
$Pr_{0.99}Eu_{0.01}(OH)_3$	7.91	6.45	0.82
$Pr_{0.97}Eu_{0.03}(OH)_3$	23.72	20.50	2.59
$Pr_{0.95}Eu_{0.05}(OH)_3$	39.48	32.64	4.13
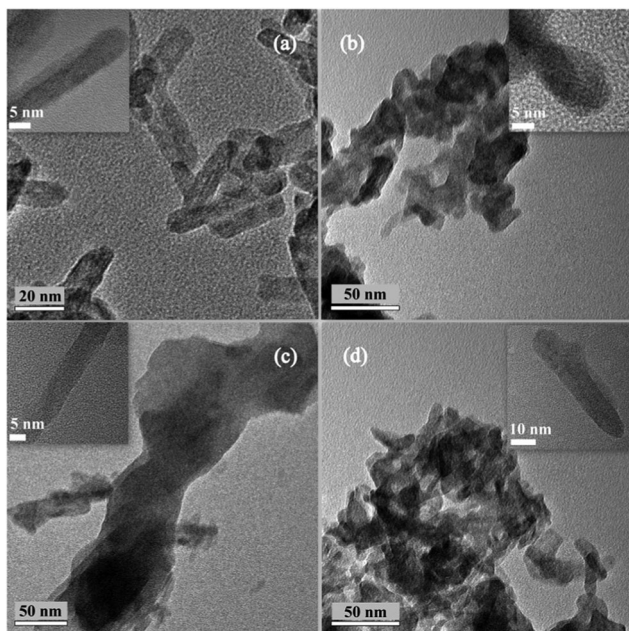
Fig. 2 TEM images of (a) $Pr(OH)_3$, (b) $Pr_{0.99}Eu_{0.01}(OH)_3$, (c) $Pr_{0.97}Eu_{0.03}(OH)_3$, and (d) $Pr_{0.95}Eu_{0.05}(OH)_3$ nanostructures. The insets are the magnified images of individual nanorods.

Fig. 3 Room-temperature Raman spectra of $Pr_{1-x}Eu_x(OH)_3$ nanostructures.

by the known fact that the dopant atoms can change the crystallization directions and act as the nucleation centers,[17,18] thus changing the resultant morphology of the sample. It is also worth to mention that in the case of the 3% Eu-doped $Pr(OH)_3$ sample, two types of nanorods were formed–narrow nanorods with diameters in the range 7–15 nm (similar to pure $Pr(OH)_3$) and wider nanorods, with diameters of the order of 50 nm (shown in the inset of Fig. S1(c), ESI†).

The nature of the Eu ion incorporation was further studied by Raman spectroscopy through analyzing the influence that Eu doping has on the vibrational properties of the starting material, $Pr(OH)_3$. The crystal symmetry of $Pr(OH)_3$ is hexagonal with a symmetry group $P6_3/m$, for which the group theory predicts 11 Raman active modes: $4A_g$, $2E_{1g}$ and $5E_{2g}$ modes.[19,20] In Fig. 3, the room-temperature Raman spectra of pure and Eu-doped $Pr(OH)_3$ are shown. The main Raman modes of $Pr(OH)_3$ are present in the spectra of the pure and doped samples and are positioned at the energies: 140 cm^{-1} (peak 1), 240 cm^{-1} (peak 2), 294 cm^{-1} (peak 3), 359 cm^{-1} (peak 4), and 465 cm^{-1} (peak 5). The modes positioned at 240 cm^{-1} and 294 cm^{-1} are ascribed to the E_{1g} and E_{2g} lattice vibrations of OH$^-$ anion, whereas the E_{2g} lattice vibrational mode of heavier
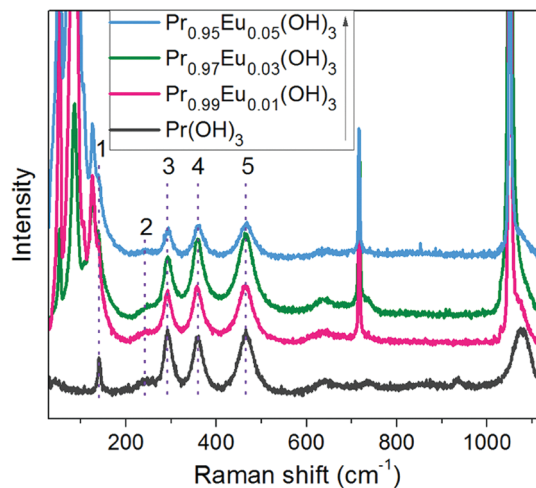
Pr^{3+} ions is positioned at a lower energy of 140 cm^{-1}. The vibration frequencies of the OH$^-$ atomic group are positioned at 359 cm^{-1} and 465 cm^{-1} (E_{2g} and E_{1g} modes).[19,20] The Raman peaks 3, 4 and 5 shifted slightly to higher wavenumbers in the $Pr_{0.95}Eu_{0.05}(OH)_3$ spectrum, which can be explained by a certain degree of Eu substitutional incorporation onto the Pr sites as these peaks are positioned at higher wavenumbers in $Eu(OH)_3$ compared to $Pr(OH)_3$.[20] Several low-frequency modes at ~ 53 cm^{-1}, ~ 85 cm^{-1}, ~ 107 cm^{-1}, ~ 127 cm^{-1}, and ~ 137 cm^{-1} are present in the Raman spectra of the Eu-doped samples. These modes correspond to nitrates, in the form of either nitrate monohydrate layers interconnected with hydrogen bonds[21,22] or KNO_3.[23,24] Both of these compounds can be formed from the unreacted nitrate ions originating from the precursor. The sharp Raman modes positioned at 715 cm^{-1} and 1050 cm^{-1} correspond to the vibrations of NO_3^- ions.[23,24] Based on the results of Raman spectroscopy and keeping in mind the X-ray diffraction results, we can conclude that some amount of the crystalline KNO_3 phase is present in the Eu-doped $Pr(OH)_3$ samples. The XPS measurements of the $Pr_{1-x}Eu_x(OH)_3$ samples enabled the elucidation of changes in the chemical composition and electronic structures with Eu doping and determined the valence states of various species present in the pure and doped samples.

Fig. 4(a) shows the survey XPS spectra of the $Pr_{1-x}Eu_x(OH)_3$ samples, while the Pr 3d, Eu 3d, O 1s, and K 2p/C 1s XPS spectra are shown in Fig. 4(b). The Pr 3d spectra (Fig. 4(b), upper left) contain two spin–orbit doublets, labeled c/c' and b/b' with approximate energies of 929/949 eV and 933/954 eV, respectively. These doublets represent the $3d_{5/2}$ (c, b) and $3d_{3/2}$ (c', b') components of the Pr 3d spectra. An additional structure t is present in the $3d_{3/2}$ component and its presence can be explained by multiple effects. The doublets c/c' and b/b' are found both in Pr^{4+} and Pr^{3+}, so they cannot be used to distinguish between these two valence states of Pr. The small peaks observed at ~ 923 eV and ~ 943 eV are identified as X-ray satellites, originating from the non-monochromatic X-ray source. From the Eu 3d spectra (Fig. 4(b), upper right), we can observe that the
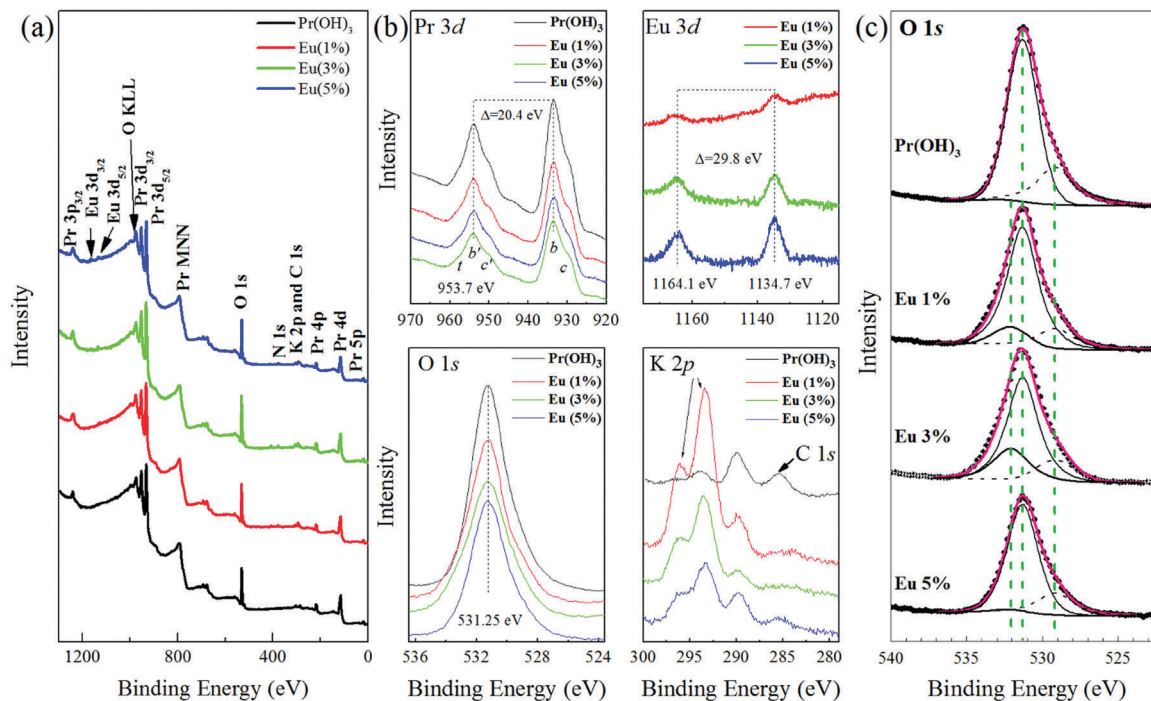
Fig. 4 XPS spectra of Pr$_{1-x}$Eu$_x$(OH)$_3$ nanostructures: (a) survey spectra, (b) high-resolution spectra of Pr 3d, Eu 3d, O 1s and K 2p/C 1s regions and (c) deconvolution of O 1s region into three peaks.

components Eu 3d$_{5/2}$ and 3d$_{3/2}$ are positioned at ∼1134.7 eV and ∼1164.1 eV, respectively. These values correspond to the Eu^{3+} valence state. When compared to the literature values for Eu$_2$O$_3$ (1133.7),[25] Eu(OH)$_3$ (1134.3)[26] and Eu(NO$_3$)$_3$ (1136.4),[25] it can be observed that these peaks are closest to those of Eu(OH)$_3$, which confirms the substitutional incorporation of Eu^{3+} and the absence of europium oxide/nitrate. More evidence indicating that Eu$_2$O$_3$ is not present in these samples is the fact that the strong Raman mode of Eu$_2$O$_3$ at ∼330 cm^{-1} was not registered in the Raman spectra. The K 2p states are particularly prominent in the 1% and 3% Eu-doped samples (see Fig. 4(b)) and originate from the KNO$_3$ phase, as already observed in the XRD and Raman spectra of the doped samples. A low-intensity C 1s peak (see Fig. 4(b)) originates from the surface impurity carbons, while the N1s states are characterized by very low-intensity peaks visible in the survey XPS spectra. The O 1s peaks of Pr$_{1-x}$Eu$_x$(OH)$_3$ samples (Fig. 4(c)) are asymmetric and have been deconvoluted into three components positioned at ∼529 eV, ∼531 eV, and ∼532 eV. The vertical dashed lines shown in Fig. 4(c) indicate the binding energy (BE) position of these three components. The latter two are generally ascribed to the lattice oxygen and adsorbed –OH groups, possibly from water,[25–27] while the peak at ∼529 eV can be ascribed to the surface oxygen vacancies.[20]

The elemental composition of the investigated samples obtained by XPS measurements is represented in Table 3. The atomic concentrations, shown in Table 3, were obtained considering the sensitivity factors of PHI (Physical Electronics) and the peak features of Pr(3d$_{5/2}$), O(1s) and Eu(3d$_{5/2}$) (Fig. 4). It can be noticed that the relative atomic concentrations of Eu,

Table 3 Elemental composition of Pr(OH)$_3$, pure and Eu-doped as determined by XPS

| Sample | Atomic concentration (%) | | | | |
	Pr	O	Eu	Eu/(Eu+Pr)	Vacancy/lattice
Pr(OH)$_3$	24.501	75.499	0.000		0.16
1% Eu	21.674	77.846	0.480	2.0%	0.20
3% Eu	19.189	78.369	2.441	11.3%	0.22
5% Eu	21.213	75.030	3.757	15.0%	0.26

calculated as Eu/(Eu + Pr), were higher than the nominal stoichiometric concentrations of this element. This can be a consequence of the segregation of the dopant atoms on the materials surface as already registered by XPS in other rare earth nanocomposites.[28] This finding suggests that Eu^{3+} ions are segregated at the surfaces of nanocrystals, but mostly connected to oxygen ions as deduced from the Eu 3d binding energies. From the peak area fitting data of the components that belong to lattice oxygen and oxygen vacancies, we have calculated the oxygen molar ratio, which is also summarized in Table 3. Although XPS provides the information about the surface stoichiometry, the obtained ratio is in agreement with the XRD results (see Table 1), confirming that the Eu-doped samples are more oxygen deficient.

Infrared spectroscopy (IR) was employed to evidence the presence of the –OH groups as well as other organic and inorganic species. The IR transmission spectra of the pure and Eu-doped Pr(OH)$_3$, obtained in the range 500–4000 cm^{-1}, are shown in Fig. 5. The peak at 670 cm^{-1} represents the Pr–O–H lattice vibration.[13,20] The prominent broad peaks at 1382 cm^{-1}

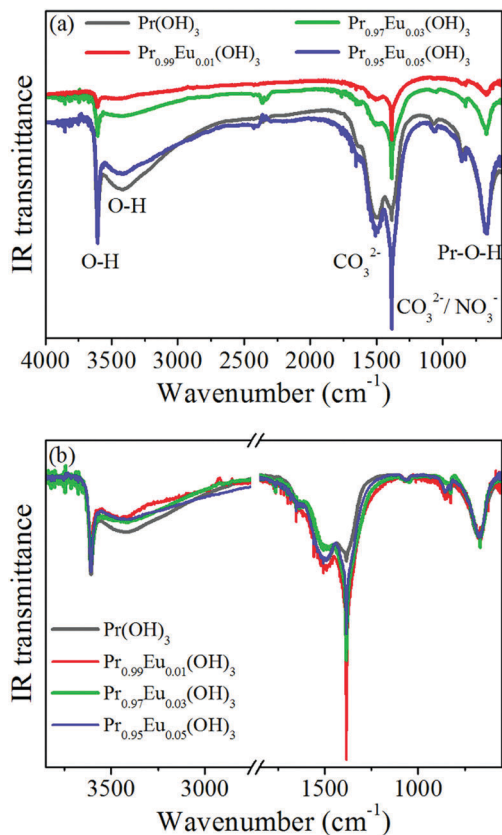Fig. 5 (a) IR transmission spectra and (b) normalized IR spectra of pure and Eu-doped $Pr(OH)_3$ nanostructures.

Fig. 6 (a) Absorption spectra and (b) Tauc plots of $(Ah\nu)^{1/2}$ vs. $(h\nu)$ for $Pr_{1-x}Eu_x(OH)_3$ nanostructures.

and 1505 cm^{-1} belong to the symmetric and asymmetric COO$^-$ vibrations[29] due to the adsorbed carbon species. Another sharp peak at 1385 cm^{-1} with a much higher intensity in the spectra of the doped samples is observed. This sharp peak can be ascribed to the NO$_3^-$ vibrations[30] together with the observed low-intensity peak at ∼828 cm^{-1}, which also corresponds to the NO$_3^-$ vibrations and is present only in the doped samples.[30] The intensity of this sharp peak (1385 cm^{-1}) is very high in the 1% Eu-doped sample and decreases with the increase in the dopant concentration as shown in the normalized IR spectra in Fig. 5(b) (normalized to the Pr–OH vibration peak), which is in agreement with the XPS K 2p spectra of the pure and doped samples. Another sharp peak at 3600 cm^{-1} represents the vibrations of the OH$^-$ groups from $Pr(OH)_3$/$Eu(OH)_3$, while the broad peak at 3400 cm^{-1} corresponds to the delocalized OH$^-$ vibrations from the adsorbed H_2O on the sample surface.[29,31]

The UV-vis absorption spectra of $Pr_{1-x}Eu_x(OH)_3$ are presented in Fig. 6(a). A strong absorption band can be observed in the region below 270 nm, corresponding to the band gap, and is shifted to a lower wavelength for the Eu-doped samples compared to that in the $Pr(OH)_3$ spectrum. Several sharper peaks at 446 nm, 462 nm, 470 nm, 583 nm and 591–597 nm represent the Pr^{3+} electronic transitions. These peaks were observed in both pure and doped samples.

There are no peaks that can be ascribed to the intraband 4f–4f Eu^{3+} electronic transitions due to the fact that the doping percentage is l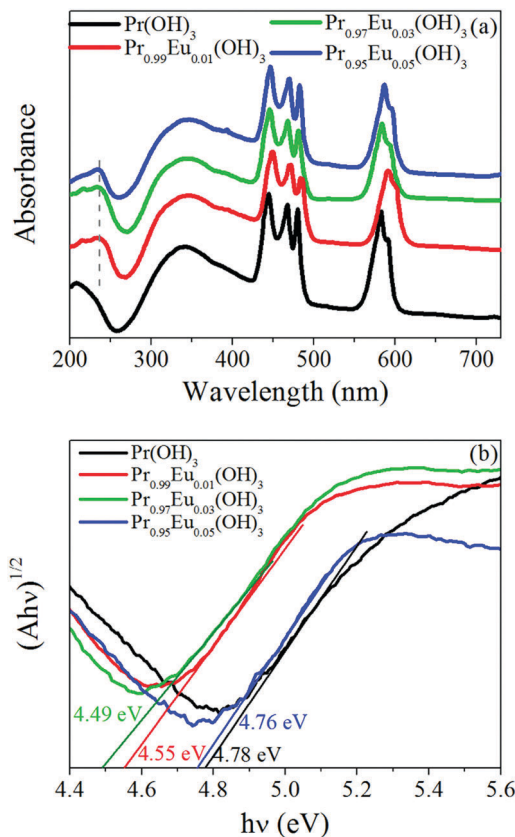ow. Another very broad absorption peak at ∼340 nm can be ascribed to the formation of oxygen-vacancy impurity levels within the band gap. These states are already seen in the defective $La(OH)_3$ nanorods (with the absorption around 280 nm) and ascribed to the surface oxygen vacancy states formed during the synthesis process.[3]

From the absorption spectra shown in Fig. 6(a), by applying the absorption spectra fitting method for the indirect electronic transitions,[32] the band gap of these materials was estimated. Fig. 6(b) presents the Tauc plots[33] for the indirect transition of the $Pr_{1-x}Eu_x(OH)_3$ samples. It was deduced that the pure $Pr(OH)_3$ band gap of ∼4.78 eV was shifted to ∼4.5 eV in $Pr_{0.99}Eu_{0.01}(OH)_3$ and $Pr_{0.97}Eu_{0.03}(OH)_3$, while it increased again in $Pr_{0.95}Eu_{0.05}(OH)_3$, approaching the $Pr(OH)_3$ value. The lower gap of the 1% and 3% Eu-doped samples can be explained by the presence of a higher amount of the KNO_3 phase in these samples, which have a lower band gap[14,34] compared to that of $Pr(OH)_3$.

In order to probe the intraband defect states, the PL measurements were performed using a 340 nm excitation light with the purpose of exciting the states corresponding to the broad peak centered at 340 nm in the absorption spectra (see Fig. 6(a)). The PL spectra of $Pr_{1-x}Eu_x(OH)_3$ samples shown in Fig. S2 (ESI†) consist of an intense PL peak centered at 430 nm and several lower intensity Pr^{3+} emission peaks that are red-shifted, compared to those of their counterparts in the

absorption spectra. The characteristic Eu^{3+} peaks are not observed because of the presence of the hydroxyl groups, which act as the luminescence quenching centers and can increase the non-radiative processes.[35] The intensive blue emission peak can be attributed to the deep level oxygen vacancy defect states and originates from the recombination of an electron occupying the vacancy and the photogenerated holes.[3,36] The intensity of this peak increases in the 3% and 5% Eu-doped samples. This is in accordance with the XPS and XRD results, which showed that the oxygen deficiency increased with increased Eu content.

Although the determined band gap values of $Pr_{1-x}Eu_x(OH)_3$ nanostructures are relatively high, the sub-band gap state observed from the PL and UV-vis absorption spectra (see Fig. 6(a) and Fig. S2, ESI†) allows for these structures to be tested as the potential photocatalysts in the UV region. Therefore, the photocatalytic degradation of the RO16 dye was tested for $Pr_{1-x}Eu_x(OH)_3$ nanostructures under UV light.

The kinetics of the degradation of RO16 under UV light is shown in Fig. 7(a). It is evident that RO16 can be effectively removed by the $Pr_{1-x}Eu_x(OH)_3$ nanostructures. The pure $Pr(OH)_3$ sample showed a moderate adsorption in the dark and its photocatalytic removal efficiency was more than 90% after 180 min. A pronounced adsorption in the equilibrium period of 60 min before the exposure to UV light was seen in the 3% Eu-doped sample. On the contrary, the 1% and 5% Eu-doped samples showed no adsorption. The iso-electric point of a photocatalyst influences the adsorption process to a great extent. Therefore, the zeta potentials for pure, 1%, and 3% Eu-doped $Pr(OH)_3$ (shown in Fig. 8(b)) were measured in the pH
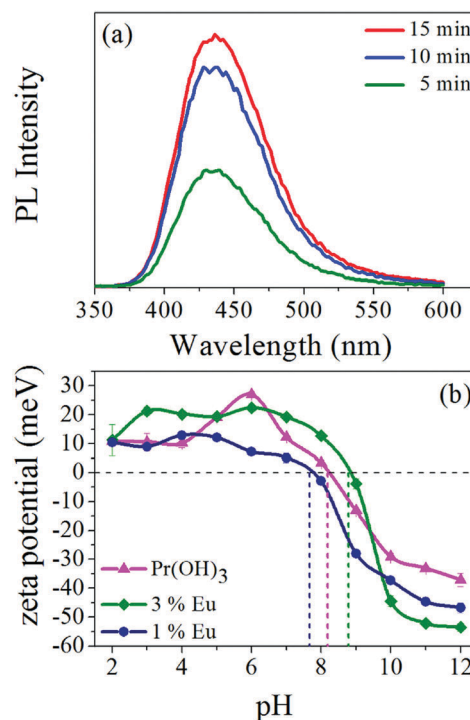
Fig. 8 (a) PL spectral changes observed during UV illumination of the $Pr_{0.95}Eu_{0.05}(OH)_3$ sample in the solution of terephthalic acid after 5, 10, and 15 min and (b) zeta potential dependence on pH value for pure, 1%, and 3% Eu-doped $Pr(OH)_3$.

range of 2.0–12.0 and their iso-electric points were 8.2, 7.6 and 8.8 respectively. At pH = 4.7, which was the natural pH value of the solution, the surface charge of the catalysts is positive in the following order: 3% Eu > $Pr(OH)_3$ > 1% Eu. As the RO16 dye molecule is negatively charged, the best adsorption is expected in the 3% Eu-doped sample due to the stronger electrostatic interaction between the adsorbent and the adsorbate. A slightly weaker adsorption is expected in $Pr(OH)_3$ and the lowest is in the 1% Eu-doped $Pr(OH)_3$ sample. This is in good agreement with the experimental results. The changes in the morphology of the 3% Eu-doped $Pr(OH)_3$ (*i.e.* the existence of two types of nanorods with diameters of the orders of magnitude ∼10 nm and ∼50 nm as shown in Fig. S1(c), ESI†) and the increased amount of oxygen vacancies (deduced from the Rietveld analysis) in this sample can be additional reasons for the enhanced adsorption.

The Eu-doped $Pr(OH)_3$ nanostructures exhibited a much faster removal efficiency than pure $Pr(OH)_3$ and a faster dye removal at the beginning of the reaction (Fig. 7(a)). A rapid removal of RO16 was observed in the first 30 min and after 70 min, the dye was almost completely removed. Under the similar conditions, the Eu-doped $Pr(OH)_3$ nanostructures demonstrated a much better photocatalytic activity than Degussa.[37,38] The photocatalytic degradation of RO16 followed the first-order kinetics (Fig. 7(b)), expressed by the equation $\ln(C/C_0) = kt$, where C_0 is the initial dye concentration and C is the dye concentration at time t. The first-order rate constant k values, obtained from the slope of $\ln(C/C_0)$ vs. t, for the $Pr_{1-x}Eu_x(OH)_3$ samples are presented in Fig. 7(b).

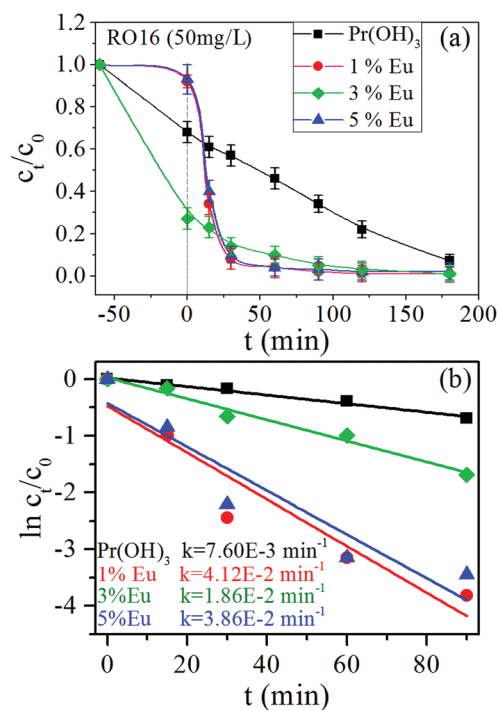

Fig. 7 (a) Degradation of RO16 dye under UV light in the presence of the pure and Eu-doped $Pr(OH)_3$ nanostructures and (b) the first-order reaction kinetics and constant k values.

It can be deduced that the Eu-doped samples have significantly higher k values than that of pure $Pr(OH)_3$, confirming that these samples are better photocatalysts than the pure $Pr(OH)_3$ sample.

The XRD, XPS and UV-vis absorption spectra have revealed that the $Pr_{1-x}Eu_x(OH)_3$ samples are oxygen deficient. In addition, the XRD results have confirmed that the oxygen deficiency increases with Eu doping. The XPS measurements suggested the high segregation of Eu ions on the surface of the doped nanostructures. The presence of lattice defects such as oxygen vacancies (V_O) and Eu^{3+} ions, particularly on the surface of Eu-doped nanostructures, can influence, to a great extent, the photocatalytic activity of the $Pr_{1-x}Eu_x(OH)_3$ samples.

The photo-generated electrons or holes can be captured by V_O, which forms impurity levels inside the band gap and serves as charge carrier trap, suppressing the e–h recombination process.[39] Moreover, the vacancies facilitate the charge transfer to the adsorbed species on the catalyst surface such as O_2 or H_2O, forming reactive radicals (superoxide radical ($O_2^{\bullet-}$) or $OH^\bullet$), the existence of which is important for a fast and successful photocatalytic degradation of organic dyes. It is well-documented that at the surface of oxide nanostructures such as TiO_2 or CeO_2, water dissociation takes place exclusively on the oxygen vacancy defect sites, where every surface V_O enables the formation of two hydroxyl groups.[40–43] The infrared study of $Pr_{1-x}Eu_x(OH)_3$ nanostructures confirmed the presence of hydroxyl groups from water.

The formation of the $OH^\bullet$ radicals was tested on the surface of the $Pr_{0.95}Eu_{0.05}(OH)_3$ photocatalyst under UV irradiation and detected by the PL method. The PL spectra of the reaction solution were measured at room temperature and are presented in Fig. 8(a). Terephthalic acid reacts with the $OH^\bullet$ radicals producing 2-hydroxyterephthalic acid, which exhibits a PL peak at 425 nm.[44] The intensity of this peak is proportional to the amount of $OH^\bullet$ radicals produced in the solution.[44,45] As shown in Fig. 8(a), a substantial increase of the intensity of the 425 nm peak with prolonged illumination time indicates the increasing amount of $OH^\bullet$ radicals produced at the surface of the $Pr_{0.95}Eu_{0.05}(OH)_3$ sample.

The existence of the surface and subsurface vacancies also enables better adsorption of O_2, which can capture the photo-generated electrons or electrons located on V_O, producing the superoxide radical groups.[41,46] In addition, due to a high oxidative potential of the holes, they can directly attack the dye, leading to its oxidation (h^+ + dye → dye$^{\bullet+}$ → oxidation of the dye). Furthermore, the photogenerated holes can easily react with the surface-bound H_2O or hydroxyls (OH^-), forming the hydroxyl radicals ($OH^\bullet$). Although similar studies, to the best of our knowledge, have not been performed for the $Pr(OH)_3$ nanostructures, it is reasonable to assume that the oxygen vacancies have an important role in the photocatalytic process at the $Pr_{1-x}Eu_x(OH)_3$ surface. Furthermore, the recent papers of Dong et al.[3] and Wang et al.,[11] aimed at the investigation of the photocatalytic properties of the defective $La(OH)_3$ nanorods and $La(OH)_3$ nanorods doped with 4f elements, demonstrated the crucial role of oxygen vacancies in the photocatalytic degradation of dyes and strongly support our findings. The oxygen vacancy

states in the band gap were registered by the PL and absorption measurements.

Moreover, Eu^{3+} ions are often used as the dopants that can prevent rapid recombination of the photogenerated electrons and holes because they create the surface states that present a barrier for electrons.[47] The emission from these states was not observed in the PL spectra excited with 340 nm probably due to the OH bond quenching. However, since the Eu^{3+} states were registered by XPS, they can be responsible for the enhanced photocatalytic activity of the Eu-doped nanostructures due to the abovementioned electron trapping effect.

In the recent paper of Mahlalela et al., it was demonstrated that TiO_2 nanoparticles exhibited an enhanced photocatalytic activity in the presence of KNO_3. This was ascribed to the increased production of the hydroxyl radicals due to the presence of NO_3^- anions. The direct photolysis of nitrate ions (NO_3^-) during irradiation with $\lambda > 280$ nm can result in the formation of the $NO_2^\bullet$ and $O^{\bullet-}$ radicals. In the presence of water, the $O^{\bullet-}$ radicals can be protonated, leading to the formation of the hydroxyl radicals ($OH^\bullet$) and OH^- ions according to the following reaction:[48]

$$(NO_3^-) \xrightarrow{h} (NO_3^-)^* \rightarrow NO_2^\bullet + O^{\bullet-} + H_2O \rightarrow NO_2^\bullet + OH^\bullet + OH^-$$

(1)
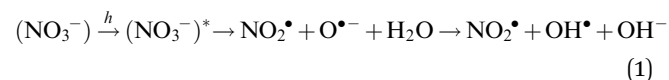
In this way, the concentration of the $OH^\bullet$ radicals is increased, thus enhancing the photodegradation of the dyes. Furthermore, nitrate ions are good acceptors for the photoinduced electrons, forming the nitrogen trioxide anion radicals ($NO_3^{\bullet 2-}$). These radicals on reacting with water would form powerful nitrogen dioxide ($NO_2^\bullet$) anions, which are capable of oxidizing the dyes.[48]

The XPS, XRD and Raman analysis confirmed the presence of the KNO_3 phase in the Eu-doped samples. The presence of NO_3^- ions at the surface of the doped samples can additionally improve their photocatalytic properties due to the abovementioned radical formation. Considering all previously mentioned results, a mechanism of photocatalytic reactions in Eu-doped $Pr(OH)_3$ is proposed and presented in Fig. 9.

The photocatalytic stability was tested on the $Pr_{0.95}Eu_{0.05}(OH)_3$ sample. Fig. S3 (ESI†) shows the repeated photocatalytic runs under the UV light irradiation. Although there was a certain drop in the efficiency in the second run, these results indicated that the Eu-doped $Pr(OH)_3$ catalysts were stable. The drop in the efficiency after the first run is ascribed to the adsorbed dye molecules and the reduction of a number of the active sites since the catalyst is recycled by centrifugation and deionized water washing without any additional chemical treatment.

Therefore, an enhanced photocatalytic activity of the Eu-doped $Pr(OH)_3$ nanostructures can be explained by the presence of oxygen vacancies, Eu^{3+} trapping states and KNO_3-mediated hydroxyl radical production at the surface of our as-prepared samples. The synergy of these three factors resulted in the efficient separation of the photogenerated electrons and holes and their transfer to adsorbed species at the surface, thus enabling excessive formation of the reactive radicals and efficient dye degradation.
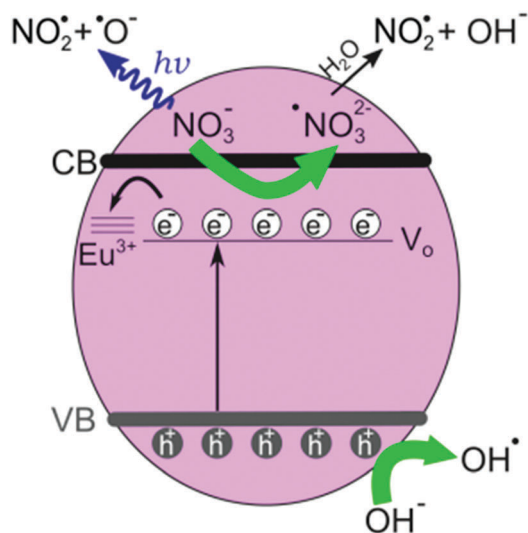
This journal is © the Owner Societies 2017

Phys. Chem. Chem. Phys., 2017, **19**, 31756–31765 | **31763**

Fig. 9 Illustration of the photocatalytic mechanism of Eu-doped Pr(OH)$_3$ under the UV light irradiation.

This study provides a new insight into the role of oxygen vacancies, 4f dopants and a proper choice of alkaline metal hydroxides in promoting the photocatalytic efficiency of Pr(OH)$_3$. Our future studies would be dedicated to the investigation of the influence of other 4f dopants on the morphology, the electronic structure and the photocatalytic performances of Pr(OH)$_3$ nanostructures.

Conclusions

In summary, the defective Pr$_{1-x}$Eu$_x$(OH)$_3$ nanostructures were synthesized by a simple microwave-assisted hydrothermal method and the comprehensive characterization has been performed by XRD, XPS, ICP-OES, FE-SEM, Raman, IR and DR spectroscopy. It is observed that Eu^{3+} doping promotes the formation of oxygen vacancies and changes the morphology of Pr(OH)$_3$ nanorods. Eu^{3+} ions also have a tendency to segregate at the surface of the nanostructure. Furthermore, the presence of KNO$_3$ phase is registered in the doped samples. The Eu-doped nanostructures exhibit an excellent photocatalytic activity towards the photo-degradation of an azo dye compared to that of pure Pr(OH)$_3$ nanorods. Oxygen vacancies, the change in the morphology and the presence of Eu^{3+} and NO$_3^-$ ions at the Pr(OH)$_3$ surface play a significant role in improving the photocatalytic properties of the Pr(OH)$_3$ nanostructures. The enhanced photocatalytic activity of the Pr$_{1-x}$Eu$_x$(OH)$_3$ nanostructures originates from the combined effect of oxygen vacancies and Eu^{3+} ions, which act as trapping centres, subsequently enabling the facile charge transfer to the adsorbed species. In this way, a fast electron–hole recombination can be suppressed and more reactive radicals can be formed. The presence of the KNO$_3$ phase in the Pr$_{1-x}$Eu$_x$(OH)$_3$ samples additionally improves the photocatalytic performances of Pr(OH)$_3$ nanostructures, *i.e.*, the presence of NO$_3^-$ ions can enhance the production of NO$_2^\bullet$ and OH$^\bullet$ radicals. Furthermore, the 3% Eu-doped sample exhibited very good adsorption properties due

to a higher electrostatic attraction of anionic dye and different morphology compared to those of other samples. The possibility of tuning the ratio of photocatalytic *versus* adsorptive activity of the Eu-doped Pr(OH)$_3$ nanostructures makes them desirable for environmental applications.

Conflicts of interest

There are no conflicts of interest to declare.

Acknowledgements

References

1 X. Wang and Y. Li, *Chem. – Eur. J.*, 2003, **9**, 5627–5635.
2 X. Ouyang, S. Yuan, Q. Qiu, W. Zeng, G. A. Hope and H. Li, *Inorg. Chem. Commun.*, 2014, **46**, 21–23.
3 F. Dong, X. Xiao, G. Jiang, Y. Zhang, W. Cui and J. Ma, *Phys. Chem. Chem. Phys.*, 2015, **17**, 16058–16066.
4 D. Zhang, T. Yan, L. Shi, H. Li and J. F. Chiang, *J. Alloys Compd.*, 2010, **506**, 446–455.
5 S. Zhang and C. Yao, *Mater. Lett.*, 2013, **94**, 143–146.
6 X. Sun, T. Zhai, X. Lu, S. Xie, P. Zhang, C. Wang, W. Zhao, P. Liu and Y. Tong, *Mater. Res. Bull.*, 2012, **47**, 1783–1786.
7 T. Zhai, S. Xie, X. Lu, L. Xiang, M. Yu, W. Li, C. Liang, C. Mo, F. Zeng, T. Luan and Y. Tong, *Langmuir*, 2012, **28**, 11078–11085.
8 J. Tang, J. Chen, W. Huang, D. Li, Y. Zhu, Y. Tong and Y. Zhang, *Chem. Eng. J.*, 2014, **252**, 202–209.
9 A. Dodd, *J. Colloid Interface Sci.*, 2013, **392**, 137–140.
10 X. Wang and Y. Li, *Angew. Chem., Int. Ed.*, 2002, **41**, 4790–4793.
11 Y. Wang, S. Liu, Y. Cai, S. Deng, B. Han, R. Han, Q. Li and Y. Wang, *Ceram. Int.*, 2014, **40**, 5091–5095.
12 A. C. Larson and R. B. Von Dreele, *Report LAUR 86-748*, Los Alamos National Laboratory, 2004.
13 D. F. Mullica, W. O. Milligan and G. W. Beall, *J. Inorg. Nucl. Chem.*, 1979, **41**, 525–532.
14 M. Hafez, I. S. Yahia and S. Taha, *Acta Phys. Pol., A*, 2015, **127**, 734–740.
15 R. Shannon, *Acta Crystallogr., Sect. A: Found. Crystallogr.*, 1976, **32**, 751–767.
16 S. Deshpande, S. Patil, S. V. N. T. Kuchibhatla and S. Seal, *Appl. Phys. Lett.*, 2005, **87**, 133113.

17 J. D. Bryan and D. R. Gamelin, *Prog. Inorg. Chem.*, John Wiley & Sons, Inc., 2005, ch. 2, pp. 47–126, DOI: 10.1002/0471725560.

18 C. Li, H. Liu and J. Yang, *Nanoscale Res. Lett.*, 2015, **10**, 1–6.

19 K. Ahrens, H. Gerlinger, H. Lichtblau, G. Schaack, G. Abstreiter and S. Mroczkowski, *J. Phys. C: Solid State Phys.*, 1980, **13**, 4545.

20 J.-G. Kang, Y. Jung, B.-K. Min and Y. Sohn, *Appl. Surf. Sci.*, 2014, **314**, 158–165.

21 R. M. Escribano, D. Fernández-Torre, V. J. Herrero, B. Martín-Llorente, B. Maté, I. K. Ortega and H. Grothe, *Vib. Spectrosc.*, 2007, **43**, 254–259.

22 H. Grothe, C. E. Lund Myhre and C. J. Nielsen, *J. Phys. Chem. A*, 2006, **110**, 171–176.

23 M. H. Brooker, *Can. J. Chem.*, 1977, **55**, 1242–1250.

24 D. Liu, F. G. Ullman and J. R. Hardy, *Phys. Rev. B: Condens. Matter Mater. Phys.*, 1992, **45**, 2142–2147.

25 F. Mercier, C. Alliot, L. Bion, N. Thromat and P. Toulhoat, *J. Electron Spectrosc. Relat. Phenom.*, 2006, **150**, 21–26.

26 H. Wu, Y. Zhang, M. Zhou, C. Yao and X. Ge, *Cryst. Res. Technol.*, 2016, **51**, 508–512.

27 J.-C. Dupin, D. Gonbeau, P. Vinatier and A. Levasseur, *Phys. Chem. Chem. Phys.*, 2000, **2**, 1319–1324.

28 N. Paunovic, Z. Dohcevic-Mitrovic, R. Scurtu, S. Askrabic, M. Prekajski, B. Matovic and Z. V. Popovic, *Nanoscale*, 2012, **4**, 5469–5476.

29 J.-G. Kang, Y.-I. Kim, D. Won Cho and Y. Sohn, *Mater. Sci. Semicond. Process.*, 2015, **40**, 737–743.

30 J. T. Kloprogge and R. L. Frost, Infrared and Raman spectroscopic studies of layered double hydroxides (LDHs), in *Layered double hydroxides: Present and future*, ed. V. Rives, Nova Science Publishers, Inc., New York, 2001, pp. 139–192.

31 F. Cui, J. Zhang, T. Cui, S. Liang, L. Ming, Z. Gao and B. Yang, *Nanotechnology*, 2008, **19**, 065607.

32 N. Ghobadi, *Int. Nano Lett.*, 2013, **3**, 2.

33 M. Wang, P. Guo, T. Chai, Y. Xie, J. Han, M. You, Y. Wang and T. Zhu, *J. Alloys Compd.*, 2017, **691**, 8–14.

34 M. K. Aydinol, J. V. Mantese and S. P. Alpay, *J. Phys.: Condens. Matter*, 2007, **19**, 496210.

35 Z. Zuo, D. Liu, J. Liu, H. Liu, S. Qin and F. Zheng, *Mater. Chem. Phys.*, 2010, **123**, 502–506.

36 D. Liu, Y. Lv, M. Zhang, Y. Liu, Y. Zhu, R. Zong and Y. Zhu, *J. Mater. Chem. A*, 2014, **2**, 15377–15388.

37 D. Mijin, M. Radulović, D. Zlatić and P. Jovančić, *Chem. Ind. Chem. Eng. Q.*, 2007, **13**, 179–185.

38 R. C. Hsiao, L. S. Roselin, H.-L. Hsu, R. Selvin and R. S. Juang, *Int. J. Mat. Eng. Innov.*, 2011, **2**, 96–108.

39 F. Kayaci, S. Vempati, I. Donmez, N. Biyikli and T. Uyar, *Nanoscale*, 2014, **6**, 10224–10234.

40 R. Schaub, P. Thostrup, N. Lopez, E. Lægsgaard, I. Stensgaard, J. K. Nørskov and F. Besenbacher, *Phys. Rev. Lett.*, 2001, **87**, 266104.

41 X. Pan, M.-Q. Yang, X. Fu, N. Zhang and Y.-J. Xu, *Nanoscale*, 2013, **5**, 3601–3614.

42 Z. Yang, Q. Wang, S. Wei, D. Ma and Q. Sun, *J. Phys. Chem. C*, 2010, **114**, 14891–14899.

43 N. M. Tomić, Z. D. Dohčević-Mitrović, N. M. Paunović, D. Ž. Mijin, N. D. Radić, B. V. Grbić, S. M. Aškrabić, B. M. Babić and D. V. Bajuk-Bogdanović, *Langmuir*, 2014, **30**, 11582–11590.

44 K.-i. Ishibashi, A. Fujishima, T. Watanabe and K. Hashimoto, *Electrochem. Commun.*, 2000, **2**, 207–210.

45 T.-M. Su, Z.-L. Liu, Y. Liang, Z.-Z. Qin, J. Liu and Y.-Q. Huang, *Catal. Commun.*, 2012, **18**, 93–97.

46 C. L. Muhich, Y. Zhou, A. M. Holder, A. W. Weimer and C. B. Musgrave, *J. Phys. Chem. C*, 2012, **116**, 10138–10149.

47 D. Yue, D. Chen, W. Lu, M. Wang, X. Zhang, Z. Wang and G. Qian, *RSC Adv.*, 2016, **6**, 81447–81453.

48 L. C. Mahlalela and L. N. Dlamini, *Surf. Interfaces*, 2016, **1–3**, 21–28.

ALEKSANDAR GOLUBOVIĆ[1]
IVANA VELJKOVIĆ[2]
MAJA ŠĆEPANOVIĆ[1]
MIRJANA GRUJIĆ-BROJČIN[1]
NATAŠA TOMIĆ[1]
DUŠAN MIJIN[3]
BILJANA BABIĆ[4]

[1]Institute of Physics, University of Belgrade, Belgrade, Serbia
[2]Institute for Multidisciplinary Research, University of Belgrade, Belgrade, Serbia
[3]Faculty of Technology and Metallurgy, University of Belgrade, Belgrade, Serbia
[4]Institute of Nuclear Sciences "Vinča", University of Belgrade, Belgrade, Serbia

INFLUENCE OF SOME SOL-GEL SYNTHESIS PARAMETERS OF MESOPOROUS TIO₂ ON PHOTOCATALYTIC DEGRADATION OF POLLUTANTS

Article Highlights
- Anatase nanopowders were synthesized by sol-gel method using tetrabutyl titanate as precursor
- XRPD data showed slight growth of crystallites in synthesized samples (from 24 to 35 nm)
- Raman scattering data confirmed the anatase as dominant TiO₂ phase
- The BET showed that specific surface area was greater at the lower temperature of calcination
- Photodegradations were comparable with Degussa P25 for C.I. Reactive Orange 16 and phenol

Abstract

Titanium dioxide (TiO₂) nanopowders were produced by sol-gel technique from tetrabutyl titanate as a precursor by varying some parameters of the sol-gel synthesis, such as temperature (500 and 550 °C) and the duration of calcination (1.5, 2 and 2.5 h). X-ray powder diffraction (XRPD) results have shown that all synthesized nanopowders were dominantly in the anatase phase, with the presence of a small amount of rutile in samples calcined at 550 °C. According to the results obtained by the Williamson-Hall method, the anatase crystallite size was increased with the duration of the calcination (from 24 to 29 nm in samples calcined at lower temperature, and from 30 to 35 nm in samples calcined at higher temperature). The analysis of the shift and linewidth of the most intensive anatase E_g Raman mode confirmed the XRPD results. The analysis of pore structure from nitrogen sorption experimental data described all samples as mesoporous, with mean pore diameters in the range of 5-8 nm. Nanopowder properties have been related to the photocatalytic activity, tested in degradation of the textile dye (C.I. Reactive Orange 16), carbofuran and phenol.

Keywords: nanostructures, anatase, X-ray diffraction, Raman scattering.

Photocatalysis is a well-known process mostly employed to degrade or transform organic and inorganic compounds, and the kinetics depend on catalyst surface area, availability of active sites, pore sizes, number and nature of trapped sites, as well as on adsorption/desorption characteristics. TiO₂ is an important photocatalyst mainly because of its strong oxidizing power, non-toxicity and long-term photostabi-

bility. Nanocrystalline TiO₂ is essentially a cheap and biocompatible wide band-gap semiconductor with an involving photogenerated holes and photocatalytic capabilities for organic pollutants [1-3]. Namely, many organic compounds can be decomposed in aqueous solution in the presence of TiO₂ powders or coatings illuminated with near ultraviolet (UV) or visible light. The structural, morphological, optical and photocatalytic properties of TiO₂ nanocrystals are strongly dependent on the synthesis process [4,5]. Among the various synthesis methods, the sol-gel method has recently attracted a lot of attention, since it is simple and cost-effective way of producing nanostructured anatase TiO₂ with tailored properties.

Many factors influence photocatalytic reactivity of TiO_2 which is documented by numerous publications in the last decades [6-11]. Generally, anatase is considered a desirable phase for photocatalysis application as it shows higher activity then rutile [8,12-13]. However, a mixture of anatase and rutile with a sintered interface, like commercial TiO_2 (Degusa P25), is claimed to be more active then pure anatase [14-17]. In order to obtain the highest performance, the main challenge is the synthesis of preferably nanocrystalline anatase TiO_2 that enables a balance between major influencing parameters: crystal structure, surface hydroxylation and crystallinity.

The sol-gel process represents a flexible chemical route to synthesize various high-performance nanostructured ceramic materials with controlled internal morphology and chemistry. Materials with designed internal nanostructure (entirely interconnected open nanoporosity, hierarchical, fractal or nanocrystalline solid network) and various possible chemical compositions (from organic to inorganic) can be obtained in large range of shapes (finely divided nanopowders, nanoparticles, thin and thick films, fibers, granular beds and monolithic materials). The sol-gel process is a solution-based technique, where the material structure is created through chemical reactions in the liquid state, giving the high flexibility of the process for easy application.

The photocatalytic efficiency of TiO_2 powder heavily depends on its microstructure and physical properties, which are in turn determined by the preparation conditions. Among these, the presence of mesopores gives rise to a large surface area, which offers abundant interaction sites with external molecules [18]. The photocatalytic process involves the separation of the electron-hole charge pair, their transport and trapping to/at the surface, and, finally, their reaction with the desired molecules. These processes always compete with the charge pair recombination. The nanostructure significantly affects these elemental processes based on several reasons. Apart from a high surface-to-volume ratio, which must be beneficial for all chemical processes, the first factor is the quantum confinement and improved reduction/oxidation power. The second factor is the practical absence of band bending and the consequent easier access of both charged particles to the surface [19].

TiO_2 nanopowders are very efficient compounds for the photodegradation of many pollutants [20,21]. In our investigations, we made a focus on degradation of organic pollutants having different chemical structure. Namely, a textile dye (C.I. Reactive Orange 16) [22,23], an insecticide (carbofuran [2,24-26]) and a phenol [27,28]. The commercial TiO_2 (Degussa P25) was applied in a number of photodegradation processes of pollutants, and we wanted to synthesize TiO_2 nanopowders using various parameters of synthesis and to compare the photocatalytic properties of such prepared catalysts. The mechanism of the photodegradation process is not completely defined, as many parameters are involved. According to this, our manuscript is a contribution in understanding of such a complex process. To the best of our knowledge, this study is original and it was not found in the literature.

Several methods of characterization, such as XRPD, Brunauer-Emmett-Teller (BET) measurements, and Raman scattering were employed in this study to correlate structural and morphological properties of synthesized TiO_2 nanopowders and their photocatalytic activity under UV light irradiation.

EXPERIMENTAL

Synthesis

The TiO_2 nanocrystals were prepared by a sol-gel method. All of the reagents were of analytical grade and were obtained from commercial sources and used without further purification. Tetrabutyl titanate (99%, Acros Organics, Belgium) was used as the precursor of titania, hydrochloride acid (36.2%, Zorka, Serbia) as the catalyst, ethanol (96%, denatured, Carlo Erba, Italy) as the solvent, and distilled water for hydrolysis. pH of the solution was 7. The reagent molar ratio was $Ti(OBu)_4$:HCl:EtOH:H_2O = = 1:0.3:15:4 according to [29], which enabled obtaining a stable gel. The process of gelation was carried out at 4 °C, where appropriate amounts of $Ti(OBu)_4$, HCl and EtOH were stirred one hour by magnetic stirrer. After that, an appropriate amount of distilled water was added in the mixture due to hydrolysis and formation of the gel. This gel was "aged" (the process of polycondensation) for two hours, the wet gels were dried at 80 °C, and then calcinated at 500 and 550 °C for 1.5, 2 and 2.5 h, to obtain TiO_2 nanocrystals. The heating and the cooling rates were 135 °C/h. According to the calcination conditions (various temperature of calcinations and duration of the calcinations), synthesized samples were labeled as: $T_{500/1.5}$, $T_{500/2}$, $T_{500/2.5}$, $T_{550/1.5}$, $T_{550/2}$ and $T_{550/2.5}$.

Characterization methods

Generally, instrumental broadening is negligible in the case of low crystallinity samples. Broadening of the peaks because of low crystallinity is dominant. These are fundamentals of X-ray powder analysis.

Structural analysis of prepared samples was done by XRPD on an Ital Structures APD2000 diffractometer, using CuKα radiation (λ = 1.5406 Å), angular range: $20° < 2\theta < 90°$. Data were collected at every 0.01° in the 20-90° 2θ using a counting time of 80 s/step. MDI Jade 5.0 software was used for calculation of the structural and microstructural parameters. The Williamson-Hall method [30] was applied for the determination of average microstrain and the mean crystallite sizes, $<D>$, of the prepared samples. The obtained values were compared to the mean crystallite sizes calculated by the Scherrer formula [31]. The Scheerer formula is an estimate of crystallite size calculated from FWHM of all diffractions collected during measurement.

Raman scattering measurements was performed in the backscattering geometry at room temperature in air, using Jobin-Yvon T64000 triple spectrometer, equipped with a confocal microscope and a nitrogen-cooled coupled device detector. The spectra, excited by 514.5 nm line of Ar^+/Kr^+ laser with output power less than 5 mW to avoid local heating due to laser irradiation, was recorded with high spectral resolution of about 0.7 cm^{-1}.

The porous structure of anatase samples is evaluated from adsorption/desorption isotherms of N_2 at -196 °C, using the gravimetric McBain method. The main parameters of the porosity, such as specific surface area and pore volume, have been estimated by BET method from α_s-plot [32]. The pore size distribution was estimated from hysteresis sorption data by the Barret-Joyner-Halenda (BJH) method [33].

Measurements of photocatalytic activity

UV irradiation of a suspension (an appropriate amounts of pollutant and TiO_2 powder as the catalyst) was performed in an open flask (100 ml volume) with an Osram Ultra-Vitalux® 300 W (UV-A) lamp placed 50 cm from the surface of the solution. The light intensity was 40 mW cm^{-2}, and it was measured on the Amprobe Solar-100, Solar Power meter, Beha-Amprobe, GmbH. The textile dye, C.I. Reactive Orange 16, was obtained from the company Bezema, Switzerland, as a gift (commercial name Bezaktiv Orange V-3R) and used without futher purification. Carbofuran (99.2 %) was obtained from FMC, USA. Phenol, p.a. grade, was purchased from Fluka. The photodegradation of organic pollutants was studied by preparing a solution containing known concentration of organic and appropriate amount of TiO_2. In a typical experiment, 25 ml of a solution was used, the quantity of TiO_2 was 50 mg, whereas the pollutants solution molarities were 8.1×10^{-5} M (C.I. Reactive Orange 16), 6.86×10^{-4} M (carbofuran), 4×10^{-4} M (phenol), respectively. Upon preparation of the solution, agitation was applied in dark by continuous stirring (magnetic stirrer) at 400 rpm to keep the suspension homogenous for 90 min. Then, the lamp was switched on and the suspension sampled after appropriate times of irradiation. The concentration of pollutants was determined after centrifugation of a sample on Mini Spin Eppendorf at 12000 rpm by a UV-Vis spectrophotometer (Shimadzu 1700) at appropriate wavelength.

RESULTS AND DISCUSSION

XRPD measurements

The XRPD measurement confirmed that sol-gel synthesis resulted with preparation of anatase modification of TiO_2, which is clearly indicated with the main anatase reflection at $2\theta \approx 25°$ (JCPDS card no. 21-1272). The samples calcinated at 500 °C were found to be phase-pure anatase (Figure 1), with crystallite sizes growing with increasing calcination time (Table 1), while the samples calcinated at 550 °C have small amount of rutile impurities, which are confirmed by small peaks at $2\theta \approx 27°$ in Figure 1 (JCPDS, card no. 21-1276). The presence of rutile in calcined anatase samples can be caused both by pH value and the temperature of the calcination [34]. In our case, the small amount of rutile in samples calcined at 550 °C is caused by the temperature of the calcination as pH value is the same (pH 7).
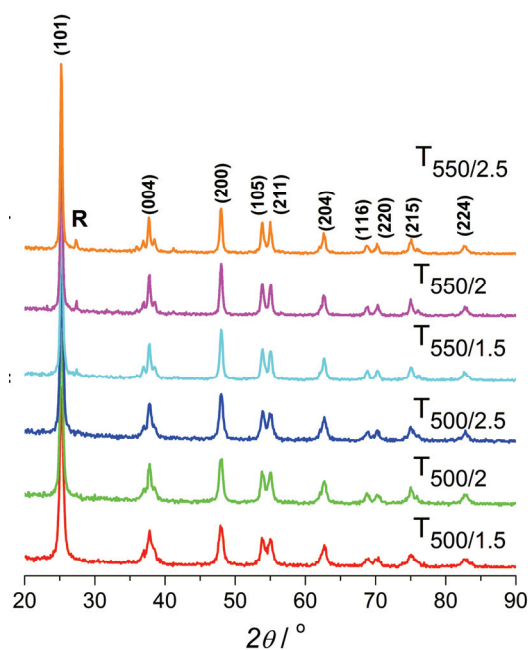

Figure 1. The XRPD patterns of TiO_2 samples, where rutile diffraction is denoted by "R".

Table 1. The unit cell parameters and unit cell volume, together with average crystallite size, <D>, of anatase and microstrain obtained by Scherrer and Williamson-Hall methods

Sample	Calcination conditions		Unit cell parameters	Scherrer method	Williamson-Hall method	
	Temperature, °C	Time, h	a and c in Å, V in Å^3	<D> / nm	<D> / nm	Microstrain, %
$T_{500/1.5}$	500	1.5	a = 3.784(3) c = 9.53(0) V = 136.4(8)	15	24	0.301
$T_{500/2}$	500	2.0	a = 3.789(9) c = 9.52(1) V = 136.7(5)	18	28	0.231
$T_{500/2.5}$	500	2.5	a = 3.789(2) c = 9.50(3) V = 136.4(5)	19	29	0.247
$T_{550/1.5}$	550	1.5	a = 3.789(1) c = 9.51(5) V = 136.6(1)	24	30	0.108
$T_{550/2}$	550	2.0	a = 3.788(7) c = 9.51(4) V = 136.5(7)	28	33	0.077
$T_{550/2.5}$	550	2.5	a = 3.789(1) c = 9.53(4) V = 136.8(9)	30	35	0.085

According to the Scherrer formula, the crystallite size for samples calcinated at lower temperature has been estimated in the range from 15 to 19 nm, while the samples calcinated at higher temperature have higher crystallinity, with crystallite size in the range from 24 to 30 nm, while for these estimated by Williamson-Hall method were in the range from 24 to 29 nm for lower temperature and from 30 to 35 nm for higher temperature. The analysis of XRPD data by the Williamson-Hall method has shown higher microstrain value in the samples calcinated at 500 °C compared to the samples calcinated at 550 °C. In all futher discussion, values of crystalline size evaluated by the Williamson-Hall method were used.

Raman scattering measurements

The Raman spectra of all synthesized nanopowders are dominated by anatase Raman modes [35,36]: $E_{g(1)}$ (~143 cm^{-1}), $E_{g(2)}$ (~199 cm^{-1}), B_{1g} (~399 cm^{-1}), $A_{1g}+B_{1g}$ (~518 cm^{-1}), and $E_{g(3)}$ (~639 cm^{-1}), as can be seen from the spectrum of two chosen samples shown in Figure 2. The most intensive Raman $E_{g(1)}$ mode is positioned between 142.8 and 143.5 cm^{-1}, with linewidths from 9 to 11.5 cm^{-1}. The dependence of Raman shift on linewidth of this mode is shown in Figure 3. The $E_{g(1)}$ Raman modes in the samples $T_{500/1.5}$, $T_{500/2}$ and $T_{500/2.5}$, calcinated at lower temperature (500 °C), are more shifted and more broadened then the mode in samples calcinated at higher temperature (550 °C). Having in mind the relatively large crystallite size in all samples registered
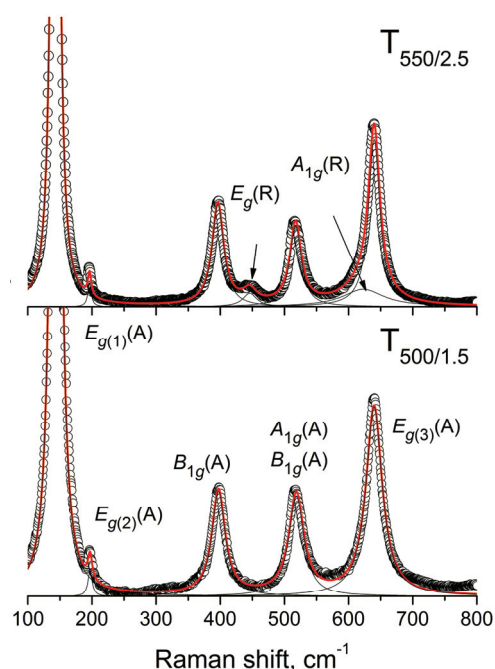

Figure 2. The Raman spectra of samples $T_{500/1.5}$ and $T_{550/2.5}$. The experimental spectra (circles) are fitted by the sum of Lorentzians (thin lines). Anatas modes are denoted by "A" and rutile by "R".

by XRPD (24-35 nm), slight shift and broadening relative to bulk anatase [33] may rather be ascribed to defects and disorder in anatase crystal structure, than to the phonon confinement effects. The smaller linewidth and the Raman shift of Degussa P25 compared

to the series of obtained samples can be explained as the least deffective and disordered anatase structure.
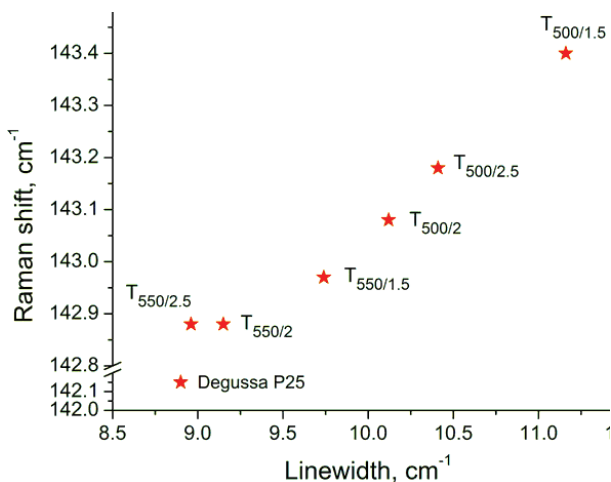

Figure 3. The experimental dependence of Raman shift on linewidth for the most intensive $E_{g(1)}$ mode of synthesized anatase samples and Degussa P25.

Some additional Raman features, detected in the sample $T_{550/2.5}$ shown in Figure 2, can be ascribed to the rutile modes [37] E_g (~445 cm^{-1}) and A_{1g} (~609 cm^{-1}). The Raman modes related to the brookite phase [38] in the synthesized samples were not detected.

Porosity

To investigate the effects of synthesis conditions parameters on the adsorption abilities and pore structure of TiO$_2$ samples, the nitrogen sorption isotherms measurements have been carried out. The specific surface area, pore volume and mean pore diameter calculated from both BET and BJH are listed in Table 2. The samples calcined at 500 °C (samples $T_{500/1.5}$, $T_{500/2}$ and $T_{500/2.5}$) are obviously more porous than those calcined at 550 °C (samples $T_{550/1.5}$ and $T_{550/2.5}$). Note that the parameters of porosity, determined from the α_s-plots [16,39], suggest that the samples are fully mesoporous ($S_{meso} = S_{BET}$), whereas in the sample

$T_{550/2}$ the porosity was very small (the pore concentration is within experimental error). The mean pore diameters obtained by BET and BJH method are in good agreement. The pore size distribution for synthesized anatase samples and Degussa P25, obtained by BJH method, are shown in Figure 4. It could be seen that in the rows $T_{500/1.5}$, $T_{500/2}$, $T_{500/2.5}$ and $T_{550/1.5}$, $T_{550/2}$, $T_{550/2.5}$ value of specific surface area had the highest value for the first member, lowest for the second and close to the first for the third member. The explanation for this tendency lies in the fact that the pores tranformed during the time of calcination. The tendency of microstrain in Table 1 was in accordance with the tendency of a pore evolution. Also, the pores in the samples calcined at 500 °C (mean pore diameter around 5-6 nm) are smaller than those in the samples calcined at higher temperature (7-8 nm), as can be seen in Table 2. From Figure 4 can be also
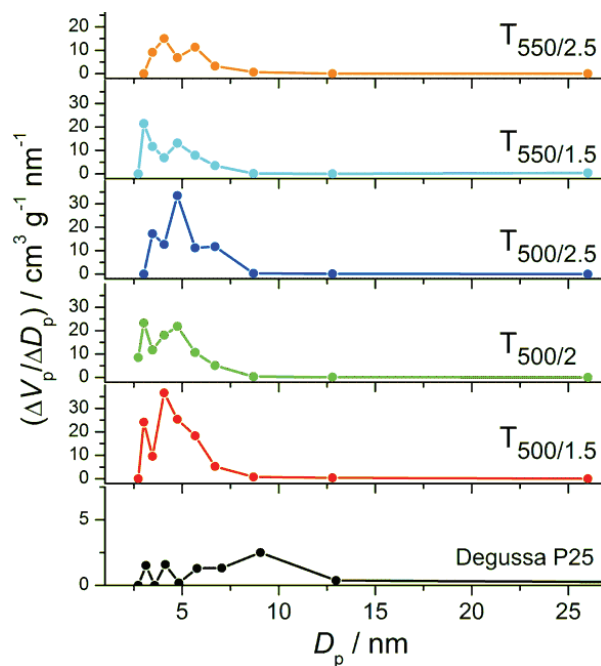

Figure 4. The pore size distribution for synthesized anatase sample and Degussa P25 obtained by BJH method.

Table 2. The porous properties of synthesized anatase samples, as well as Degussa P25: specific surface areas (S_{BET}, S_{BJH}), pore volumes (V_p, V_t), and mean pore diameters ($\bar{D}_{BET}$, $\bar{D}_{BJH}$) obtained by BET and BJH methods, respectively

Sample	$S_{BET} = S_{meso}$, in m^2/g	V_p / cm^3 g^{-1}	$\bar{D}_{BET}$ / nm	S_{BJH} / m^2 g^{-1}	V_t / cm^3 g^{-1}	$\bar{D}_{BJH}$ / nm
$T_{500/1.5}$	52	0.1063	5.3	52.0	0.1025	5.1
$T_{500/2}$	33	0.0757	5.9	34.2	0.0777	5.9
$T_{500/2.5}$	45	0.0922	5.3	45.9	0.0903	5.1
$T_{550/1.5}$	18	0.0580	8.3	18.5	0.0599	8.3
$T_{550/2}$	2	-	-	-	-	-
$T_{550/2.5}$	17	0.0454	6.9	18.3	0.0504	7.1
Degussa P25	13	0.0244	7.5	11.6	0.0214	7.4

seen that the pore distribution of Degussa 25 was almost uniform (except for the largest value of about 9 nm) and that could be the crucial fact why Degussa 25 was the powerful tool for the photocatalytic degradation.

Photocatalytic activity

The photocatalytic activity of synthesized catalyst was studied using three representatives of organic pollutants: C.I. Reactive Orange 16 (textile dye), carbofuran (pesticide) and phenol. The samples were (after mixing with pollutants, sorption and UV irradiation) withdrawn and analyzed on a UV-Vis spectrophotometer at 492.5 nm for C.I. Reactive Orange 16, 277 nm for carbofuran and 270 nm for phenol. The time after the agitation 90 min in dark is denoted as 0, and these concentrations are denoted as c_0. The reactions were performed using Degussa P25 TiO$_2$ for comparison. The results are shown in Figure 5.

In Figure 5a, the effectiveness of synthesized TiO$_2$ catalysts in photodegradation reaction of (C.I. Reactive Orange 16) is presented. In comparison to Degussa P25, the catalyst T$_{500/1.5}$ showed almost the same photodegradation effectiveness (99 and 98% after 90 min of UV irradiation, respectively), while the others samples, except T$_{550/1.5}$, showed similarly good photodegradation effectiveness. The photodegradation efficiency can be determined as:

$$\text{Efficiency} = 100\frac{c_0 - c}{c_0}$$

where c_0 is the initial concentration of pollutant sol-

ution and c is the concentration after irradiation with UV light. The efficiencies of the studied TiO$_2$ catalysts as well as the observed pseudo first reaction rate constants were presented in Table 3. The main difference between Degussa P25 and synthesized catalysts is the reaction rate as a result of pore distribution uniformity.

In case of carbofuran, Degussa P25 showed higher photodegradation efficiency than all synthesized samples (98% of carbofuran was photodegraded after 90 min). After 150 min of UV irradiation, the highest photodegradation efficiency was obtained by samples T$_{500/1.5}$ (75%), whereas the lowest efficiency were observed for the samples T$_{550/1.5}$ and T$_{550/2.5}$ (both 49%). The obtained results are in accordance with the pore distribution influence on the reaction rate. Photocatalitic degradation of carbofuran using synthesized of TiO$_2$ series and Degussa P25 as catalysts are presented in Figure 5b. Here, one can observe that the photocatalytic reaction rate is highest when Degussa P25 is used, while the differences between synthesized catalysts are much less pronounced. As given above, the observed reaction rate might be the result of the mean pore diameter range, and the combination of specific surface area and mean pore diameter.

Phenol [40] was also subjected to photodegradation using synthesized catalysts and the results are shown in Figure 5c. It appears that TiO$_2$ (both synthesized and Degussa P25) is able to remove phenol too, but it requires more time, since the concentrations continuously decrease. After 150 min of
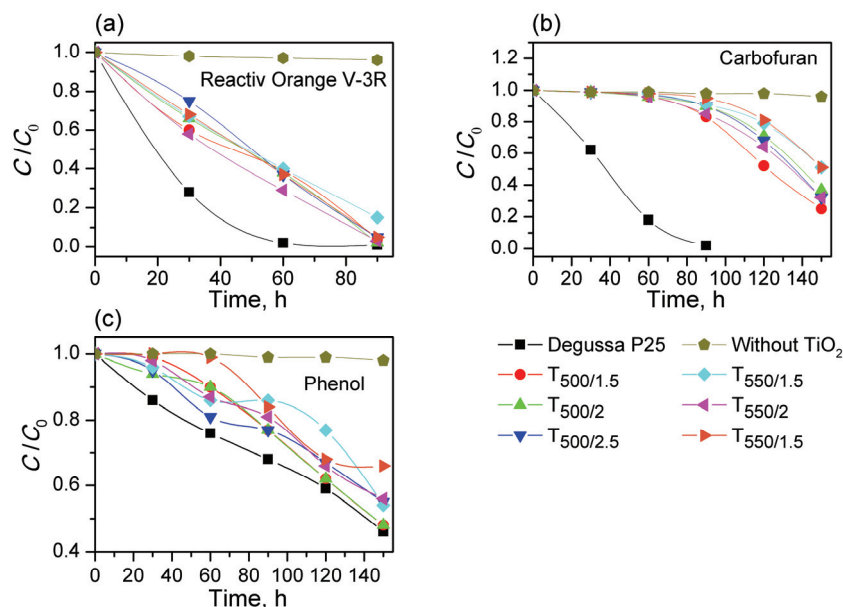

Figure 5. The kinetics of degradation of: a) C.I. Reactive Orange 16, b) carbofuran and c) phenol, under UV irradiation monitored in the presence of synthesized TiO$_2$ samples and Degussa P25.

Table 3. The efficiency, %, of the studied TiO₂ catalysts as well as the observed pseudo-first reaction rate constants

Time, min	Catalyst						
	P-25	$T_{500/1.5}$	$T_{500/2}$	$T_{500/2.5}$	$T_{550/1.5}$	$T_{550/2}$	$T_{550/2.5}$
	RO16						
0	0	0	0	0	0	0	0
30	72	40	34	25	33	42	32
60	98	61	62	63	60	71	63
90	99	96	98	95	85	97	95
k / min⁻¹	0.0546	0.0287	0.0335	0.0271	0.0189	0.0322	0.0271
	Carbofuran						
0	0	0	0	0	0	0	0
30	38	1	1	1	1	1	1
60	82	4	4	3	2	4	2
90	98	17	10	10	9	15	5
120		48	29	32	21	36	19
150		75	63	68	49	68	49
k / min⁻¹	0.0372	0.0062	0.0041	0.0027	0.0028	0.0049	0.0027
	Phenol						
0	0	0	0	0	0	0	0
30	14	1	6	5	4	2	0
60	24	10	10	19	14	13	1
90	32	23	23	23	14	19	16
120	41	38	38	33	23	34	32
150	54	52	52	45	46	44	34
k / min⁻¹	0.0048	0.004	0.004	0.0035	0.003	0.0033	0.0025

UV irradiation, Degussa P25 degraded 54%, almost the same value as for $T_{500/1.5}$ and $T_{500/2}$ (52%). Other samples ($T_{500/2.5}$, $T_{550/1.5}$ and $T_{550/2}$) degraded about 45% and $T_{550/2.5}$ showed the worst result (34%). Obtained photodegradation result for Degussa P25 is in accordance with results from de la Cruz Romero *et al.* [3] where phenol was not 100% photodegraded even with the UV irradiation of 10 h (only 60% under similar experimental conditions).

One would expect that the smaller molecule, phenol, can easily access the internal surface of Degussa sample giving higher degradation rate in comparison to other two organic pollutants. Namely, if only size of the molecule is important, than the reaction rate order would be: phenol > carbofuran > > RO16. On the contrary, the rate order is inverse, RO16 being most reactive. The main reason for such reaction rate is due to the different mechanisms of degradation and different part of molecules involved. If only one molecule is concerned, then the influence of the catalyst is more complex. Not only the mean pore diameter is important, but also the combination of specific surface area and mean pore diameter, giving Degussa an advantage when voluminous molecules are concerned.

CONCLUSIONS

The structural and morphological properties of TiO₂ powders were intentionally varied by the temperature and duration of the calcination. The analysis of XRPD data showed that rising of temperature and extending the duration of the calcination caused slight growth of crystallites in synthesized samples (from 24 to 35 nm), which was confirmed by Raman scattering. It was also noticed that the most intensive Raman E_g mode in the samples calcined at higher temperature (550 °C) is less broadened and blueshifted than in the samples calcined at 500 °C, pointing to less deffective and disordered anatase structure. The BET analysis showed that the greatest specific surface area was in the sample calcined for 1.5 h at 550 °C ($T_{550/1.5}$). The samples calcined at 500 °C displayed higher photocatalytic activity in the degradation in comparison with the samples calcined at 550 °C. The results of photodegradation of C.I. Reactive Orange 16 for the sample calcined 2 h at 500 °C (sample $T_{500/2}$) was comparable with Degussa P25. The samples calcined for 1.5 and 2 h at the same temperature (samples $T_{500/1.5}$ and $T_{500/2}$) showed comparable efficiency with Degussa P25 in photodegradation of phenol, while in

photodegradation of carbofuran Degussa P25 showed superior photocatalytic properties.

Acknowledgement

This work was financially supported by the Serbian Ministry of Education, Science and Technological Development, Projects No. III45018 and ON171032, as well as SASA project F-134.

REFERENCES

[1]   R. Pourata, A. R. Khataee, S. Aber, N. Daneshvar, Desalination 249 (2009) 301-307

[2]   M. Mahalakshmi, B. Arabindoo, M. Palanichamy, V. Murugesan, J. Hazard. Mater. 143 (2007) 240-245

[3]   D. de la Cruz Romero, G. Torres Torres, J. C. Arévalo, R. Gomez, A. Aguilar-Elguezabal, *J. Sol-Gel Sci. Technol.* 56 (2010) 219-226

[4]   Y. Wang, A. Zhou, Z. Yang, Mater. Lett. 62 (2008) 1930--1932

[5]   Hari-Bala,Y. Guo, X. Zhao, J Zhao, W. Fu, X. Ding, Y. Jiang, K. Yu, X. Lv, Z. Wang, Mater. Lett. 60 (2006) 494--498

[6]   W. Dong, Y. Sun, C. W. Lee, W. Hua, X. Lu, Y. Shi, S. Zhang, J. Chen, D. Zhao, J. Am. Chem. Soc. 129 (2007) 13894-13904

[7]   E. Stathatos, D. Papoulis, C. A. Aggelopoulos, D. Panagiotaras, A. Nikolopoulou, J. Hazard. Mater. 211-212 (2012) 68-76

[8]   T. Ohno, K. Sarukawa, M. Matsumura, New J. Chem. 26 (2002) 1167-1170

[9]   M. Inagaki, R. Nonaka, B. Tryba, A. W. Morawski, Chemosphere 64 (2006) 437-445

[10]   A. Sclafani, L. Palmisano, M. Schiavello, J. Phys. Chem. 94 (1990) 829-832

[11]   N. Serpone, D. Lawless, R. Khairutdinov, E. Pelizzetti, J. Phys. Chem. 99 (1995) 16655-16661

[12]   T. Ohno, K. Sarukawa, M. Matsumura, J. Phys. Chem., B 105 (2001) 2417-2420

[13]   K. Tanaka, M. F. V. Capule, T. Hisanaga Chem. Phys. Lett. 187 (1991) 73-76

[14]   D.C. Hurum, K.A. Gray, T. Rajh, M.C. Thurnauer, J. Phys. Chem., B 109 (2004) 977-980

[15]   J. Zhang, Q. Xu, Z. Feng, M. Li, C. Li, Angew. Chem. Int. Edit. 47 (2008) 1766-1769

[16]   T. Kawahara, Y. Konishi, H. Tada, N. Tohge, J. Nishii, S. Ito, Angew. Chem. Int. Edit. 41 (2002) 2811-2813

[17]   A. Zachariah, K. V. Baiju, S. Shukla, K. S. Deepa, J. James, K.G.K. Warrier, J. Phys. Chem., C 112 (2008) 11345-11356

[18]   W. Li, X. Guo, Y. Zhu, Y. Hui, K. Kanamori, K. Nakanishi, J. Sol-Gel Sci. Technol. 67 (2013) 639-645

[19]   M. Fernández-García, A. Martínez-Arias, J. C. Hanson, J. A. Rodriguez, Chem. Rev. 104 (2004) 4063-4104

[20]   S. Ahmed, M.G. Rasul, W.N. Martens, R. Brown, M.A. Hashib, Desalination 261 (2010) 3-18

[21]   S. Ahmed, M.G. Rasul, W.N. Martens, R. Brown, M.A. Hashib, Water Air Soil Pollut. 215 (2011) 3-29

[22]   C.-Y. Chen, Water Air Soil Pollut. 202 (2009) 335-342

[23]   D. Mijin, M. Radulović, D. Zlatić, P. Jovančić, Chem. Ind. Chem. Eng. Q. 13 (2007) 179-185

[24]   B. Lopez-Alvarez, R.A. Torres-Palma, G. Peñuela, J. Hazard. Mater. 191 (2011) 196-203

[25]   J. Fenoll, P. Hellín, P. Flores, C. M. Martínez, S. Navarro, J. Photochem. Photobiol., A 251 (2013) 33-40

[26]   F. Javier Benitez, J.L. Acero, F.J. Real, J. Hazard. Mater. 89 (2002) 51-65

[27]   M. Jesus, S. Benito, O. Aaron O, A.H. de Lasa, Chem. Eng. Sci. 78 (2012) 186-203

[28]   K. Majeda, W. Lijun, A.H. Al-Muhtaseb, A.B. Albadarin, G.M. Walker, Chem. Eng. J. 213 (2012) 125-134

[29]   Y.L. Du, Y. Deng, M.S. Zhang, J. Phys. Chem. Solids 67 (2006) 2405-2408

[30]   G.K. Williamson, W.H. Hall, Acta Metall. 1 (1953) 22-31

[31]   H.P. Klug, L.E. Alexander, X-Ray Diffraction Procedures: For Polycrystalline and Amorphous Materials, 2nd ed., Wiley-VCH, New York, 1974, p. 687

[32]   K. Kaneko, C. Ishii, H. Kanoh, Y. Hanzawa, N. Setoyama, T. Suzuki, Adv. Colloid Interfac. Sci. 76-77 (1998) 295--320

[33]   E.P. Barrett, L.G. Joyner, P.P. Halenda, J. Am. Chem. Soc. 73 (1951) 373-381

[34]   W. Zhang, S. Chen, S. Yu, Y. Yin, J. Cryst. Growth 308 (2007) 122-129

[35]   T. Ohsaka, F. Izumi, Y. Fujiki, J. Raman Spectrosc. 7 (1978) 321-324

[36]   M.J. Šćepanović, M. Grujić-Brojčin, Z. Dohčević-Mitrović, Z.V. Popović, Appl. Phys., A 86 (2007) 365-371

[37]   X. Wang, J. Shen, Q. Pan, J. Raman Spectrosc. 42 (2011) 1578-1582

[38]   Y.-H. Zhang, C. K. Chan, J. F. Porter, W. Guo, J. Mater. Res. 13 (1998) 2602-2609

[39]   A. Golubović, B. Abramović, M. Šćepanović, M. Grujić-Brojčin, S. Armaković, I. Veljković, B. Babić, Z. Dohćević-Mitrović, Z. V. Popović, Mater. Res. Bull. 48 (2013) 1363-1371

[40]   J. Moreira, B. Serrano, A. Ortiz, H. de Lasa, Chem. Eng. Sci. 78 (2012) 186-203.

ALEKSANDAR GOLUBOVIĆ[1]
IVANA VELJKOVIĆ[2]
MAJA ŠĆEPANOVIĆ[1]
MIRJANA GRUJIĆ-BROJČIN[1]
NATAŠA TOMIĆ[1]
DUŠAN MIJIN[3]
BILJANA BABIĆ[4]

[1]Institut za fiziku, Univerzitet u Beogradu, Pregrevica 118, 11080 Beograd, Srbija
[2]Institut za multidisciplinarna istraživanja, Univerzite u Beogradu, Kneza Višeslava 1, 11000 Beograd, Srbija
[3]Tehnološko-metalurški fakultet, Univerzitet u Beogradu, Karnegijeva 4, 11000 Beograd, Srbija
[4]Institut za nuklearne nauke „Vinča", Univerzitet u Beogradu, 11001 Beograd, Srbija

NAUČNI RAD

UTICAJ NEKIH PARAMETARA SOL-GEL SINTEZE MEZOPOROZNOG TIO$_2$ NA FOTOKATALITIČKU DEGRADACIJU ZAGAĐIVAČA

Nanoprahovi titan-dioksida (TiO$_2$) su proizvedeni sol-gel tehnikom iz tetrabutil-titanata kao prekursora, varirajući neke parametre sol-gel sinteze kao što su temperatura kalcinacije (500 i 550 °C) i dužina kalcinacije (1,5; 2 i 2,5 h). XRPD rezultati su pokazali da su svi sintetizovani nanoprahovi dominantno u anataz fazi sa prisustvom malih količina rutilne faze u uzorcima kalcinisanim na 550 °C. Saglasno rezultatima dobijenim Williamson-Hall metodom, kristaliti anataza rastu sa vremenom kalcinacije (od 24 do 29 nm u uzorcima kalcinisanim na nižoj temperaturi, i od 30 do 35 nm u uzorcima kalcinisanim na višoj temperaturi). Analize pomeraja i poluširine najintenzivnijeg Eg Ramanskog moda anataza su potvrdile XRPD rezultate. Parametri veličine pora dobijeni pomoću eksperimentalnih podataka sorpcije azota su ukazali na to da su svi uzorci mezoporozni, sa srednjom veličinom pora u opsegu 5-8 nm. Fotokatalitička aktivnost dobijenih nanoprahova je testirana na degradaciji tekstilne boje (C.I. Reactive Orange 16), karbofurana i fenola.

Ključne reči: nanostrukture, anataz, difrakcija X-zraka na prahu, rasipanje.